

NI

~~CONFIDENTIAL~~  
~~RESTRICTED DATA~~

UNCLASSIFIED

# THE EFFECTS OF ATMOSPHERIC RE-ENTRY ON GRAPHITIC PARTICLES -- ~~CONFIDENTIAL~~

January, 1964

Prepared For: Space Nuclear Propulsion Office  
Cleveland Extension  
21000 Brookpark Rd., Cleveland, Ohio

On: Contract SNPC-10 (GE Requisition 214-L28)

Prepared by: Space Sciences Laboratory  
Missile and Space Division  
General Electric Company  
P.O. Box 8555  
Philadelphia 1, Pennsylvania

*Declassified per  
letter from H.W. Dix, SNPO  
dated April 6, 1964*

FACILITY FORM 802	308	
	(ACCESSION NUMBER)	(THRU)
	308	0
	(PAGES)	(CODE)
	CR-84047	18
	(NASA CR OR TMX OR AD NUMBER)	(CATEGORY)

~~CONFIDENTIAL~~  
~~RESTRICTED DATA~~

UNCLASSIFIED

143915

~~CONFIDENTIAL~~  
~~RESTRICTED DATA~~  
THIS PAGE IS UNCLASSIFIED

This document consists of 308 pages,  
of which 89 are CONFIDENTIAL and  
219 are UNCLASSIFIED

No 54 of 50 Copies, Series A.

DIN: 214-L28E

## THE EFFECTS OF ATMOSPHERIC RE-ENTRY ON GRAPHITIC PARTICLES ~~CONFIDENTIAL~~

January, 1964

Prepared for: Space Nuclear Propulsion Office  
Cleveland Extension  
21000 Brookpark Rd., Cleveland, Ohio

On: Contract SNPC-10 (GE Requisition 214-L28)

Principal Contributors: M. J. Engel  
B. B. Hamel  
J. W. Metzger  
E. J. Nolan  
S. M. Scala  
R. A. Tanzilli

EXCLUDED FROM AUTO-  
MATIC REGRADING;  
DOD DIR 5200.10 DOES  
NOT APPLY.

### RESTRICTED DATA

This document contains restricted  
data within the meaning of the Atomic  
Energy Act of 1954. Its transmission  
or the revelation of its contents in any  
manner not authorized by that act, is  
prohibited by law.

Space Sciences Laboratory  
Missile and Space Division  
General Electric Company

LAN: 4730-02-1

~~CONFIDENTIAL~~  
~~RESTRICTED DATA~~  
UNCLASSIFIED



UNCLASSIFIED

UNCLASSIFIED

CONTENTS

	<u>Pages</u>
List of Tables	4
List of Figures	5
List of Symbols	9
Section: I. Preface	15
II. Theoretical Considerations	18
A. Introduction	18
B. Analysis of Aerothermochemical Interactions in Low Density Hypersonic Flow	20
1. Approach	20
2. Model	21
3. Free Molecular Solution	24
4. Results	27
C. Engineering Correlations	31
1. Drag	31
2. Heat Transfer	35
3. Mass Transfer	39
III. Experiment	46
A. Introduction	46
B. Experimental Equipment	47
1. Facility Description	47
2. Facility Operation and Control	50
3. Test Instrumentation and Specimens	50
3.1 Pyrometer	50
3.2 Total Calorimeter	51
3.3 Pressure Probe	52
3.4 Specimen Calorimeters	53
3.5 Test Specimens	54
3.6 Motion Pictures	56
3.7 General	56
C. Test Procedures	57
1. Specimen Location	57
2. Pyrometry <del>Test</del> <sup>HEAT</sup>	57
3. Specimen <del>Test</del> <sup>HEAT</sup> Transfer	59
4. Model Stagnation Pressure	60
D. Evaluation of Environment and Measurements	61
1. Evaluation of Flow Environment	61
2. Evaluation of Enthalpy	63
3. Evaluation of Data Correlation Factors	64
4. Evaluation of Mass Loss Data	67
5. Evaluation of Rate of Mass Loss	68
6. Evaluation of Integrated Mass Loss Models	69
7. Evaluation of Surface Temperatures	70
8. Evaluation of Calorimetric Measurements	72

UNCLASSIFIED

UNCLASSIFIED

DECLASSIFIED

	<u>Pages</u>
E. Discussion of Results	76
1. Oxidation of ATJ Graphite	76
2. Integrated Mass Loss - ATJ Graphite	81
3. Oxidation of Material "X"	86
4. Integrated Mass Loss - Material "X"	89
5. Comparison of Material "X" and ATJ Graphite	93
IV. Systems Study	99
A. Introduction	99
B. Trajectory Considerations	100
C. Transient Heat Conduction	102
1. One Dimensional Idealization	102
2. Multidimensional Considerations	104
D. Oxidation of Spheres	105
E. Oxidation of Cylinders	108
F. Oxidation of Spheres (Multi-Dimensional Approach)	109
V. Comparison: Theory-Analysis with Experiment	112
VI. Conclusions	119
Appendices:	
A. Low Density Effects on the Specification of Chemical Kinetics	121
B. Derivation of Combined Theoretical-Empirical Equations	122
C. Discussion and Presentation of Sample Calculations Regarding Data Reduction	125
D. Diffusion Control Level for Material "X"	130
E. Comparison of Exact and Numerical Heat Conduction Solutions for Spheres	133
F. Determination of Average Heat and Mass Transfer for Spheres and Cylinders	137
References	139
Tables	141
Figures	198

UNCLASSIFIED  
DECLASSIFIED

LIST OF TABLES

	<u>Pages</u>
1. Summary of Pressure Probe Measurements	141
2. Mass Loss Data - ATJ Graphite	142
3. Mass Loss Data - Material "X"	146
4. Comparison: Mass Loss Data - One Inch Cylinders	151
5. Integrated Mass Loss Data, Spheres - ATJ Graphite	152
6. Integrated Mass Loss Data, Spheres - Material "X"	153
7. Integrated Mass Loss Data, Cylinders - Material "X"	154
8. Summary of Total Calorimeter Enthalpy Measurements	155
9. Summary of Cold Wall Heat Transfer Meas. -Flat Face Specimens	156
10. Summary of Cold Wall Heat Transfer Meas. -Spherical Specimens	157
11-16. Mass Rate Data - ATJ Graphite	158
17-21. Mass Rate Data - Material "X"	181
22. Monotonically Shrinking Spheres	196
23. One Dimensional Cylinders	197

=

[REDACTED]

# UNCLASSIFIED

# DECLASSIFIED

## LIST OF FIGURES

	<u>Pages</u>
1. Oxidation of Graphite in Near Free Molecular Hypersonic Couette Flow	198
2. Curve of Correlation for Drag	199
3. Curve of Heat Transfer Correlation	200
4. Hypersonic Arc Heated Wind Tunnel	201
5. Characteristics of Hypersonic Arc Wind Tunnel	202
6. General Arrangement of the Tandem Gerdien Plasma Jet Apparatus	203
7. Model Rotating Sting Apparatus	204
8. Total Enthalpy Calorimeter	205
9. Model Stagnation Pressure Probe	206
10. Typical Mass Transfer Model Calorimeter	207
11. Typical Spherical Model Calorimeter (Before and After Exposure)	207
12. Models for Oxidation Study	208
13. Modifications of ATJ Graphite Specimens	209
14. Mass Rate Specimen, 1.0" Diameter	210
15. Mass Rate Specimen, 1/4" Diameter	210
16. Mass Rate Specimen, 1/16" Diameter	211
17. Integrated Mass Transfer Model, 1.0" Diameter Sphere	211
18. Integrated Mass Transfer Model, 1/4" Diameter Sphere	211
19. Typical Two Color Pyrometer Calibration Curves	212
20. Model Stagnation Pressure vs. Distance from Nozzle Exit	213
21. Heat Transfer as a Function of Specimen Configuration	214
22. Flow Regime Correlation Function	215
23. Effective Pressure vs. Shock Reynolds Number	216
24. Stationary Spheres, 1.0" Diameter - Ablated ATJ Specimens	217
25. Rotating Spheres, 1.0" Diameter - Ablated ATJ Specimens	218
26. Time-Temperature Profile, 1.0" Diameter ATJ Graphite Sphere	219
27. Random Selection of Typical Surface Temperatures, Cylindrical Mass Rate Specimens	220
28. Random Selection of Typical Surface Temperatures, Spheres of Material "X"	221
29. Surface Temperatures, Cylinders of Material "X" ( $L/d = 2$ )	222
30. Experimental Values of Heat Transfer	223
31. Heat Transfer to a 1.0" Sphere (Cold Wall Calorimetry)	224
32. Arrhenius Plot, Mass Rate Data of ATJ Graphite (Not Modified)	225
33. Arrhenius Plot, Mass Rate Data for ATJ Graphite (Data Modified for Reynolds Number Effects)	226
34. Normalized Mass Rates vs. Temperature, ATJ Graphite (Theory Curves Modified for Reynolds Number Effects)	227

UNCLASSIFIED  
DECLASSIFIED

	<u>Pages</u>
35. Normalized Mass Rates vs. Temperature, ATJ Graphite (Data Modified for Reynolds Number Effects)	228
36. Profiles of 1.0" Diameter Stationary Spheres of ATJ Graphite	229
37. Ablation of a Stationary Sphere as a Function of Time (1.0" Diameter, ATJ Graphite)	230
38. Ablation of a Stationary Sphere as a Function of Central Angle (1.0" Diameter, ATJ Graphite)	231
39. Profiles of 1.0" Diameter Rotating Spheres of ATJ Graphite	232
40. Ablation of a Rotating Sphere as a Function of Time (1.0" Diameter, ATJ Graphite)	233
41. Ablation of a Rotating Sphere as a Function of Central Angle (1.0" Diameter, ATJ Graphite)	234
42. Profiles of 1/4" Diameter Stationary Spheres of ATJ Graphite	235
43. Ablation of a Stationary Sphere as a Function of Time (1/4" Diameter, ATJ Graphite)	236
44. Ablation of a Stationary Sphere as a Function of Central Angle (1/4" Diameter, ATJ Graphite)	237
45. Profiles of 1/4" Diameter Rotating Spheres of ATJ Graphite	238
46. Ablation of a Rotating Sphere as a Function of Central Angle (1/4" Diameter, ATJ Graphite)	239
47. Comparison of Mass Loss Data, ATJ Graphite Spheres	240
48. Effective Rate of Heat Transfer, Spinning Sphere vs. Stationary Sphere	241
49. Effective Rate of Heat Transfer to a Sphere as a Function of Rotational Speed	242
50. Ablation of ATJ Graphite - Dimensional Changes at the Stagnation Points of Spheres	243
51. Relative Ablation, Spinning Spheres vs. Stationary Spheres, Stagnation Region	244
52. Arrhenius Plot, Mass Rate Data of Material "X" (Not Modified)	245
53. Arrhenius Plot, Mass Rate Data of Material "X" (Data Modified for Reynolds Number Effects)	246
54. Normalized Mass Rates vs. Temperature, Material "X" (Data Modified for Reynolds Number Effects)	247
55. Typical Specimens of Material "X" (After Exposure)	248
56. Profiles of 1.0" Diameter Stationary Spheres of Material "X"	249
57. Ablation of a Stationary Sphere as a Function of Central Angle (1.0" Diameter, Material "X")	250
58. Ablation of a Stationary Sphere as a Function of Time (1.0" Diameter, Material "X")	251
59. Profiles of 1.0" Diameter Rotating Spheres of Material "X"	252

UNCLASSIFIED

DECLASSIFIED

	<u>Pages</u>
60. Ablation of a Rotating Sphere as a Function of Central Angle (1.0" Diameter, Material "X")	253
61. Ablation of a Rotating Sphere as a Function of Time (1.0" Diameter, Material "X")	254
62. Profiles of 1/4" Diameter Stationary Spheres of Material "X"	255
63. Profiles of 1/4" Diameter Rotating Spheres of Material "X"	256
64. Ablation of a Stationary Sphere as a Function of Central Angle (1/4" Diameter, Material "X")	257
65. Ablation of a Rotating Sphere as a Function of Central Angle (1/4" Diameter, Material "X")	258
66. Ablation of Stationary and Rotating Spheres as a Function of Time (1/4" Diameter, Material "X")	259
67. Comparison of Mass Loss Data, Material "X" Spheres	260
68. Comparison of Surface Appearance of Material "X" and ATJ Graphite After Exposure	261
69. Relative Integrated Mass Loss of Rotating and Stationary Spheres, (1.0" and 1/4" Diameter, Material "X")	262
70. Integrated Mass Loss Data, Material "X" Cylinders ( $l/d=2$ )	263
71. Comparative Plots of Normalized Mass Rate vs. Temperature for ATJ Graphite and Material "X"	264
72. Motion of a Re-Entry Fragment (Analytical Model)	265
73. Monotonically Shrinking Sphere (Analytical Model)	266
74. One Dimensional Cylinder (Analytical Model)	266
75. Two Dimensional Sphere - Rotation Axis 90° to Flow (Analytical Model)	267
76. Two Dimensional Sphere - Rotation Axis Aligned to Flow (Analytical Model)	267
77. Percent Mass Loss vs. $W/C_{DA}$ for Spheres	268
78. Particle Size vs. Altitude for Spheres (Material "X")	269
79. Particle Size vs. Altitude for Spheres (Material $X_i$ )	270
80. Comparison of ATJ and "X" Particle Size vs. Altitude	271
81. Variation of % Mass Loss with Re-Entry Angle ( $X_i$ Spheres)	272
82. Variation of % Mass Loss with Averaging Factor ( $X_i$ Spheres)	273
83. Trajectory for ATJ Graphite Sphere	274
84. Mass Transfer Rate Variation with Re-Entry Time (ATJ Sph.)	275
85. Trajectory for Material "X" Sphere	276
86. Mass Transfer Rate Variation with Re-Entry Time ("X" Sph.)	277
87. Maximum Surface Temperature vs. $(W/C_{DA})_E$ for Spheres	278
88. Maximum Heat Transfer Rate vs. Integrated Heat Transfer Rate for Various $(W/C_{DA})$ 's and Re-Entry Angles	279
89. Maximum Temperature Gradients for Spheres and Cylinders	280
90. Variation of Re-Entry Trajectory with $W/C_{DA}$	281
91. Variation of Re-Entry Trajectory with Re-Entry Angle	282
92. Thermal Conductivity - ATJ Graphite	283
93. Specific Heat - ATJ Graphite	284
94. Thermal Conductivity and Specific Heat for Material "X"	285

UNCLASSIFIED

UNCLASSIFIED

DECLASSIFIED

	<u>Pages</u>
95. Percent Mass Loss vs. $(W/C_D A)_E$ for Cylinders	286
96. Particle Size vs. Altitude for Cylinders (Material $X_1$ )	287
97. Particle Size vs. Altitude for Cylinders (Material "X")	288
98. Trajectory for Maximum % Mass Loss Cylinder	289
99. Mass Transfer Rate Variation with Re-Entry Time ("X" Cyl.)	290
100. Maximum Heat Transfer Rate vs. Integrated Heat Transfer Rate for Cylinders ( $X_1$ )	291
101. Variation of Maximum Heat Transfer Rate and Surface Temperature with $(W/C_D A)_E$ for Cylinders ( $X_1$ )	292
102. Surface Temperature Variation at Stagnation Point ("X" Sph.)	293
103. Surface Temperature vs. Time (Uniform Heating Rate)	294
104. Heating Rate vs. Body Angle	295
105. Surface Temperature vs. Time (Variable Heating Rate)	296
106. Theoretical Ablation of a Stationary Sphere vs. Test Time	297
107. Theoretical Ablation of a Stationary Sphere vs. Central Angle	298
108. Predicted Surface Temperature of a Stationary Sphere vs. Test Time	299
109. Comparison of Theoretical and Experimental Ablation of a Stationary Sphere	390
110. Theoretical Ablation of a Rotating Sphere vs. Test Time	301
111. Theoretical Ablation of a Rotating Sphere vs. Central Angle	302
112. Predicted Surface Temperature of a Rotating Sphere vs. Test Time	303
113. Comparison of Theoretical and Experimental Ablation of a Rotating Sphere	304
114. Comparison of Theoretical and Experimental Heat Transfer Rate Distribution on a Sphere	305
115. Ratio, Theoretical to Experimental Heat Transfer as a Function of Central Angle	306
116. Theoretical Ablation and Surface Temperature Profiles for a Stationary Cylinder of Material "X"	307
117. Comparison of Theoretical and Experimental Ablation for a Stationary Cylinder of Material "X"	308

UNCLASSIFIED

# UNCLASSIFIED

# DECLASSIFIED

## LIST OF SYMBOLS

$a$	radius at the surface
$a_{ii}$	hard sphere cross-section for i-i collision
$a_{ij}$	hard sphere cross-section for i-j collision
$a_{B,L}$	boundary layer resistance to mass transfer
$A$	area
$A'/A$	normalized area
ATJ	ATJ grade graphite
$C$	diffusion-controlled mass transfer constant
$C_D$	drag coefficient, $D/(\rho_\infty V_\infty^2 / 2)$
$C_{Di}$	drag coefficient for inviscid flow
$C_H$	Stanton number
$C_p$	specific heat
$\overline{C}$	thermal velocity
$d$	plate spacing (Figure 1); diameter
$D$	drag force per unit area
$E$	activation energy
$E_k$	electrical power
$f$	distribution function; fractional ratio
$F$	distribution function (eq. II B-30)
$F_k$	generalized forces, also $F_r$ and $F_\theta$
$F_m$	mass transfer rate modification factor
$g_k$	generalized displacements



UNCLASSIFIED

DECLASSIFIED

$g_o$	gravity at sea level, 32.2 ft/sec <sup>2</sup>
$h_s$	stagnation enthalpy
$h_{w \text{ air}}$	static enthalpy of air evaluated at $T_w$
$H_e$	stagnation enthalpy
$H_{in}$	number flux into the surface
$H_{out}$	number flux out of the surface
$J_{ii}$	collision integral for i-i collisions
$J_{ij}$	collision integral for i-j collisions
$k$	Boltzman's constant
$k_o$	specific reactivity coefficient = $\sqrt{21}$ (effective collision frequency)
$k_w$	specific reaction rate
$K$	thermal conductivity coefficient
$Kn$	Knudsen number
$\ell$	length dimension
$L$	length dimension
$m$	molecular weight; mass; reaction order
$\dot{m}$	mass transfer rate of ablating(or oxidizing material) per unit area
$\dot{m}'$	unadjusted mass transfer rate per unit area
$\dot{m}_a$	mass flow rate of air
$M$	Mach number
$n$	number density; reaction order
$N$	ratio, $\dot{m}_R/\dot{m}_D$
$p$	pressure

UNCLASSIFIED

# UNCLASSIFIED

## DECLASSIFIED

$P_{O_2}$	pressure of oxygen
$P_e$	stagnation pressure
$\dot{q}$	heat transfer rate per unit area
$q^*$	heat of ablation, $\dot{q}/\dot{m}$
$Q$	heat transfer rate per unit area
$\int Q_T$	total heat transfer per unit area
$r$	altitude measured from center of earth
$R$	Boltzman's Constant/molecular weight, $k/m$ , as in $e^{-E/RT}$ ; radius of sphere
$R_B$	radius of body
$R_c$	radius of curvature at stagnation region
$Re$	Reynolds number
$Re_s$	shock Reynolds number
$RT_o$	enthalpy at ambient conditions (33.86 Btu/lb)
$S_i$	defining equation (eq. II B-14)
$S_\infty$	speed ratio
$t$	time
$T$	temperature
$\bar{T}$	kinetic energy
$u$	velocity
$v$	molecular velocity
$V$	macroscopic velocity
$W$	weight
$x$	space variable
$x^*/R$	normalized body dimension

UNCLASSIFIED  
DECLASSIFIED

"X"	Material "X"
$X_i$	designates a material initially postulated to be like "X"
$z$	height above sea level
$Z$	defining equation (eq. II B-18)

Greek Letters

$\alpha$	defining equation (eq. II C-1)
$\beta$	constant (in $L^{-1}$ units)
$\beta_{\text{Diff}}$	diffusion controlled mass transfer constant
$\gamma$	specific heat ratio; path angle
$\gamma_i$	reaction probability (eq. II B-6)
$\Delta$	difference or change
$\epsilon$	total hemispherical emittance
$\eta$	kinematic viscosity
$\theta$	angular position
$\lambda$	mean free path
$\mu$	micro or microns
$\mu_i$	defining equation (eq. II B-13b)
$\pi$	Buckingham theorem constant
$\rho$	density
$\phi$	angular position
$\omega$	angular velocity (spin rate of spheres)
$\Phi$	ratio of the average heat and mass transfer to stagnation value for one-dimensional analyses of spheres and cylinders

UNCLASSIFIED  
DECLASSIFIED

$\Phi_M$  ratio of the average heat and mass transfer for a rotating sphere (spin axis  $90^\circ$  to flow) to that of a stationary sphere (or a sphere with spin axis aligned with the flow)

Other

$\alpha$  proportional to

$\infty$  infinity

Subscripts

av average

ATJ ATJ graphite

b back face or internal

B. L. boundary layer

C carbon

D diffusion control

e earth

eff. effective

E re-entry initial conditions

f final; fixed

ff flat face

F. M. free molecular

H. R. high Reynolds number

i species i

$\ell$  local

L. R. low Reynolds number

m measured during total calorimetry experiments

UNCLASSIFIED  
DECLASSIFIED

n.f.m.    near free molecule  
o        stagnation point  
ox       total oxidation  
r        rotating  
R        reaction rate control  
sph      spherical  
U        uranium  
w        wall or surface  
X        Material "X"  
 $\infty$       free stream

Superscripts

(o)      free molecule  
1        upper plate  
11      lower plate  
·        time derivative,  $d ( )/dt$   
..      2nd time derivative,  $d^2 ( )/dt^2$

UNCLASSIFIED  
UNCLASSIFIED

## I. PREFACE

A thorough investigation encompassing theoretical study, experiment and systems analysis and founded upon an existing treatment of the oxidation of materials was made of ATJ graphite, a well characterized basic material, and a Material "X", a reactor material of special interest. The existing continuum theory is extended to cover non-continuum situations for graphitic materials. Based on approximate analytic relations, oxidation behavior is predicted for both reaction rate controlled and diffusion controlled oxidation for low Reynolds number continuum flow and molecular flow. Relations in the transition region between these two regimes are also determined. Behavior of the reacting surface is described in terms of drag, heat transfer and mass transfer for these flow conditions, which correspond to very high altitudes. The results of the analytical investigation are presented in forms suited to engineering calculations. They demonstrate that as a non-continuum environment develops, oxidation behavior departs from that of continuum. Further, the differences that are predicted depend upon whether oxidation is reaction rate or diffusion controlled and can be correlated with the shock Reynolds number corresponding to the flow conditions existing in the environment. The necessary correlating expressions are established and are presented in graphic form.

The experimental investigation provided extension and corroboration of existing experimental results based on the continuum theory.

UNCLASSIFIED

Additional experimental data were acquired through a range of conditions other than high Reynolds number continuum. The results of the experiments substantiated the theoretical findings and provided insight into the shape change behavior of spherical specimens of ATJ graphite and the designated Material "X". Extensive oxidation mass loss data were acquired for both materials. Values of reaction coefficients and activation energies were determined from the experimental data and a positive corroboration of the diffusion controlled regime was established for ATJ graphite. In the case of Material "X", the experimental results did not clearly define a region of constant mass rate corresponding to diffusion controlled oxidation. An estimated value for the diffusion controlled oxidation of this material was not confirmed.

Shape changes observed on spherical specimens were, in general, as anticipated. Locally, mass loss was dependent upon the local heat transfer rate and spin. In effect, spin reduces the local rates of heat transfer, resulting in lower mass loss on rotating bodies. In the case of Material "X", some peculiar transient variations in mass loss behavior were observed, as compared with graphite.

Using the analytical tools and appropriate experimental data, the re-entry of various sized spheres and axially oriented cylinders of Material "X" on specific trajectories was investigated by programmed machine computation. The basic trajectories, treated for bodies with variable  $W/C_D A$ , had parameters into which perturbations were introduced to study performance changes. The computations determined that all of the particle sizes investigated would readily survive the selected re-entry environments.

UNCLASSIFIED  
UNCLASSIFIED

Computations of oxidation performance under conditions approximating the test facility environments were carried out for several specimens. The results offer a comparison of theoretically founded computations with direct experimental evidence. It was found that mass losses and dimensional changes showed quantitatively mixed agreement, however the trends are quite well defined. Introduction of a suitable spin factor into the machine computation to predict losses from rotating specimens was necessary to provide comparison with the experimental results. The determined spin factor was satisfactory in that the computer data showed discrepancies completely analogous to those of the fixed sphere, when compared to the experimental data. Since the discrepancies can be adequately accounted for upon realization that the flight theory equations are only generally applicable to the description of the flow properties produced in an arc heated facility, it is fairly obvious that further iteration of the computer analyses to account for these differences could with relative ease converge the disparities. This was accomplished for the case of the stable axially oriented cylinder.

Additionally, some empirical correlations were determined from the results of tests on fixed and tumbling short cylinders such that useful comparisons can be made with respect to particle shape and spin rate.

UNCLASSIFIED



UNCLASSIFIED  
DECLASSIFIED

## II. THEORETICAL CONSIDERATIONS

### A. INTRODUCTION

In describing the entry burning of an object into the earth's atmosphere, it is necessary to describe three distinct flight regimes. At altitudes above 450,000 feet the object can be considered to be in the free molecule flow regime; a regime in which one can ignore inter-molecular collisions. As the object descends towards lower altitudes, particles which have been reflected from the vehicle will begin to collide with the hyperthermal free stream particles. The effect of these inter-molecular collisions will be to steepen density gradients and so give rise to the formation of a shock wave. This is referred to as the transition regime since it delineates the onset of the region in which macroscopic gas phenomena begin to dominate over microscopic phenomena in the bulk gas flow. At still lower altitudes, the intermolecular collisions become dominant and the physico-chemical phenomena that are present are best described by the equations of continuum gas dynamics -- this is referred to as the continuum regime.

An objective of this report is to give approximate analytic relations for the prediction of drag, heat transfer, and mass transfer over the entire spectrum of entry flight regimes for an ablating graphite object. These relations are presented as correlation equations which span the free molecular to continuum regimes, and are in a form which are quite accessible to engineering calculation. In the following sections, the formulation of these correlation relations are discussed,

UNCLASSIFIED

UNCLASSIFIED  
DECLASSIFIED

the approximations and assumptions are stated and the equations are presented in a form which facilitates their use in engineering calculations.

UNCLASSIFIED

UNCLASSIFIED

B. ANALYSIS OF AEROTHERMOCHEMICAL INTERACTIONS IN  
LOW DENSITY HYPERSONIC FLOW

1. Approach

In predicting the entry behavior of small graphite particles it is of critical importance to understand the oxidation processes that occur under conditions of rarefied gas flow. This is because the smaller particles will spend a significant portion of their entry time at the higher altitudes where the mean free path for intermolecular collisions will be large comparable to the particle size. To assess the effects of oxidation in these rarefied flow regimes it is, therefore, necessary to analyze the Boltzmann transport equation.

In this study, the method of Knudsen iteration, as proposed by Enoch (Ref. 1) for the hyperthermal regime, is applied to the problem of hyperthermal Couette flow with oxidation occurring at the stationary surface. The approach utilized involves expressing the free molecular distribution function as a delta function,  $n_1 \delta(\underline{v} - \underline{V}_\infty)$ , for the hyper-velocity particles, and a delta function,  $n_2 \delta(\underline{v})$  for those particles which leave the stationary surface. Using these approximating forms in the relevant collision integrals, Knudsen iteration may be performed with the full Boltzmann equation. Closed form expressions are then obtained for the heat and mass transfer as functions of Mach number, Knudsen number, molecular weight ratios and the relevant physicochemical surface parameters.

UNCLASSIFIED

## 2. Model

In order to clarify the oxidation processes that occur in rarefied flows, the simplest one-dimensional problem has been chosen -- that of hypervelocity Couette flow with oxidation at the stationary surface. In Figure 1, the flow under consideration is schematically shown. At the upper plate ( $x = d$ ), we consider a source for molecular oxygen, with density  $n_0$ ; oxygen is injected through the upper plate and is convected to the stationary bottom plate ( $x = 0$ ) where it reacts with the graphitic surface by means of the following two reactions:



to form the reactant products  $CO_2$  and  $CO$ . These products diffuse through the streaming oxygen molecules to the upper surface, which acts as a sink for the reactant products. The intent of the present investigation is to find the heat and mass transfer for a given surface temperature,  $T_w$ , plate velocity,  $V_\infty$ , and Knudsen number,  $Kn_\infty$ .

To formulate the model we assume that (i) thermal velocity of each component is much less than the upper plate velocity,  $V_\infty$  (ii) that the distance between the plates,  $d$ , is much larger than all relevant mean free paths, (iii) hard sphere intermolecular potential for all molecular interactions (iv) diffuse reflection for all species at the bottom plate.

With the above assumptions we can proceed to apply a generalized form of "Enoch's" model to the Couette flow. We first

consider the form of the distribution functions to be chosen for each gas.

For the molecular oxygen (with subscript 3) we write:

$$f_3^{(o)} = n_3^{(o)'} \delta(\underline{v} - \underline{V}_\infty) + n_3^{(o)''} \delta(\underline{v}) \quad (3)$$

where  $n_3^{(o)'} = \frac{n_o}{2}$ , with,  $n_o$ , the source density of oxygen, and  $n_3^{(o)''}$

is the free molecular density of unreacted oxygen molecules that leave the stationary surface.

For the reactant products CO (subscript 1) and CO<sub>2</sub> (subscript 2) we write:

$$f_1^{(o)} = n_1^{(o)''} \delta(\underline{v}) \quad (4)$$

$$f_2^{(o)} = n_2^{(o)''} \delta(\underline{v}) \quad (5)$$

where  $n_1^{(o)''}$  and  $n_2^{(o)''}$  represent the free molecular densities of reactant products that leave the oxidizing, stationary surface.

Using eqs. (4) and (5) we can now perform Knudsen iteration on the Boltzmann equation of each species. This can be symbolically written as:

$$\frac{df_i}{dt} = J_{ii} \left( f_i^{(o)}, f_i^{(o)} \right) + \sum_{\substack{j \neq i \\ j=1}}^3 J_{ij} \left( f_i^{(o)}, f_j^{(o)} \right) \quad (6)$$

Using the forms for  $f_i$  and  $f_j$  given in eqs. (4) and (5) the integrations specified by (6) are tractable. It can be noted upon inspection that:

$$J \left( \begin{smallmatrix} (o) \\ f_i \end{smallmatrix}, \begin{smallmatrix} (o) \\ f_i \end{smallmatrix} \right) = 0; \quad i = 1, 2 \quad (7)$$

$$J \left( \begin{smallmatrix} (o) \\ f_3 \end{smallmatrix}, \begin{smallmatrix} (o) \\ f_3 \end{smallmatrix} \right) = J \left( \begin{smallmatrix} (o)' \\ f_3 \end{smallmatrix}, \begin{smallmatrix} (o)'' \\ f_3 \end{smallmatrix} \right) + J \left( \begin{smallmatrix} (o)'' \\ f_3 \end{smallmatrix}, \begin{smallmatrix} (o)' \\ f_3 \end{smallmatrix} \right) \quad (8)$$

$$J \left( \begin{smallmatrix} (o) \\ f_i \end{smallmatrix}, \begin{smallmatrix} (o) \\ f_3 \end{smallmatrix} \right) = J \left( \begin{smallmatrix} (o) \\ f_i \end{smallmatrix}, \begin{smallmatrix} (o)' \\ f_3 \end{smallmatrix} \right); \quad i = 1, 2 \quad (9)$$

$$J \left( \begin{smallmatrix} (o) \\ f_3 \end{smallmatrix}, \begin{smallmatrix} (o) \\ f_i \end{smallmatrix} \right) = J \left( \begin{smallmatrix} (o)' \\ f_3 \end{smallmatrix}, \begin{smallmatrix} (o) \\ f_i \end{smallmatrix} \right); \quad i = 1, 2 \quad (10)$$

Using the results of Ref. 1 (Appendix A) we can write for the collision integrals:

$$J_{33} \left( \begin{smallmatrix} (o) \\ f_3 \end{smallmatrix}, \begin{smallmatrix} (o) \\ f_3 \end{smallmatrix} \right) = \frac{2 n_3^{(o)'} n_3^{(o)''} a_{33}^2}{v_3 V_\infty} \delta \left( \mu_3 - \frac{v_3}{V_\infty} \right) \times \quad (11)$$

$$\left( 1 + \operatorname{sgn} \left[ V_\infty - v_3 \right] \right) - n_3^{(o)'} n_3^{(o)''} \pi a_{33}^2 V_\infty \left[ \delta(v_3 - V_\infty) + \delta(v_3) \right]$$

$$J_{i3} \left( \begin{smallmatrix} (o) \\ f_i \end{smallmatrix}, \begin{smallmatrix} (o) \\ f_3 \end{smallmatrix} \right) = a_{i3}^2 n_i^{(o)} n_3^{(o)'} \delta \left( \mu_i - \frac{v_i}{V_\infty} \right) \times \quad (12)$$

$$\left( 1 + \operatorname{sgn} \left[ V_\infty - v_i \right] \right) - \pi a_{i3}^2 n_i^{(o)} n_3^{(o)'} V_\infty \delta(v_i); \quad i = 1, 2$$

$$J_{3i} \left( \begin{smallmatrix} (o) \\ f_3 \end{smallmatrix}, \begin{smallmatrix} (o) \\ f_i \end{smallmatrix} \right) = a_{i3}^2 n_1^{(o)} n_3^{(o)'} \delta \left( \mu_3 - \frac{v_3}{V_\infty} \right) \times \quad (13)$$

$$\left( 1 + \operatorname{sgn} \left[ V_\infty - v_3 \right] \right) - \pi a_{i3}^2 n_i^{(o)} n_3^{(o)'} V_\infty \delta \left( \frac{v_3}{V_\infty} - v_i \right) \quad i = 1, 2.$$

where:  $\mu_i = \frac{v_i \cdot V_\infty}{v_i V_\infty}, \quad \operatorname{sgn} x = \begin{cases} 1; & x \geq 0 \\ 0; & x < 0 \end{cases} \quad (13b)$

and  $2\pi a_{ij}^2$  represents the cross-section for intermolecular collisions.

One can therefore write:

$$v_{ix} \frac{df_i}{dx} = S_i(\underline{v}) = J_{i3} \left( \begin{smallmatrix} (o) & (o) \\ f_i & f_3 \end{smallmatrix} \right); \quad i = 1, 2 \quad (14)$$

$$v_{3x} \frac{df_3}{dx} = S_3(\underline{v}) = J_{33} \left( \begin{smallmatrix} (o) & (o) \\ f_3 & f_3 \end{smallmatrix} \right) + \sum_{i=1}^2 J_{3i} \left( \begin{smallmatrix} (o) & (o) \\ f_3 & f_i \end{smallmatrix} \right) \quad (15)$$

It is important to point out that for species 1 and 2 the only collisions considered in the model are those between species 1 and 2 and hypervelocity species 3 particles. In the hyperthermal limit ( $V_\infty \gg \bar{C}_{1,2,3}$ ) this class of collisions will be most important in determining the flux of species 1 and 2 leaving the stationary surface 3. However, it must be noted that if the molecular weights,  $m_1$  and  $m_2$  are disparate, there can be a significant difference between the velocities of the particles leaving the stationary surface, and collisions between these classes of particles can become important.

### 3. Free Molecular Solution

To obtain the values of  $n_1^{(o)}$ ,  $n_2^{(o)}$  and  $n_3^{(o)}$ , it is necessary to obtain the free molecular solution. As noted earlier, we consider both CO and CO<sub>2</sub> as being formed at the oxidizing surface. We further define reaction probabilities,  $\gamma_1$  and  $\gamma_2$  as:

$$\gamma_1 = \frac{H_{1 \text{ out}}}{H_{3 \text{ in}}}; \quad \gamma_2 = \frac{H_{2 \text{ out}}}{H_{3 \text{ in}}} \quad (16)$$

These rate constants are considered to be functions of surface temperature alone, and can be related to the experimental data for graphite oxidation at low pressures. To relate  $\gamma_1$  and  $\gamma_2$  to experiment, we require that  $\gamma_1$  and  $\gamma_2$  reproduce the experimentally determined relation for  $(\text{CO}/\text{CO}_2)_w$  (Ref. 2), as well as the experimentally determined rate relation (Ref. 3). Using a curve fit for the data of Ref. 2, one obtains the following relation for  $\gamma_1$  and  $\gamma_2$ :

$$\frac{\gamma_1}{\gamma_2} = \left( \frac{m_2}{m_1} \right)^{1/2} Z \quad (17)$$

$$\log_{10} Z = - \left( 2.47 / T^{\circ} \text{R} \right) + 2.1 \quad (18)$$

and then by considering the reaction as first order, one obtains a second relation between  $\gamma_1$  and  $\gamma_2$  since:

$$\dot{m}_{\text{ox}} = \left[ \frac{n_o \bar{C}_3}{4} m_3 \right] \left[ \gamma_1 + \gamma_2 \right] \quad (19)$$

and:

$$\dot{m}_{\text{ox}} = k_w p_3 \quad (20)$$

one obtains:

$$k_w = \frac{3}{4} \left( \frac{\gamma_1 + \gamma_2}{\bar{C}_3} \right) \quad (21)$$

Combining eqs. (17) and (21):

$$\gamma_2 = \frac{\frac{4}{3} k_w \bar{C}_3}{\left( \frac{m_2}{m_1} \right)^{1/2} Z + 1} \quad (22)$$



$$\gamma_1 = \frac{4}{3} k_w \bar{C}_3 \left[ \frac{\frac{m_2}{m_1}^{1/2} Z}{\frac{m_2}{m_1}^{1/2} Z + 1} \right] \quad (23)$$

where  $k_w$  is the experimentally determined specific reaction rate:

$$k_w = k_o \exp \left( -E/RT_w \right) \quad (24)$$

Using the values of  $\gamma_1$  and  $\gamma_2$  given in (22) and (23) one can easily make use of the defining relations for  $\gamma_1$  and  $\gamma_2$  to find  $n_3^{(o)}$ ,  $n_1^{(o)}$ ,  $n_2^{(o)}$ :

$$H_{3 \text{ in}} \gamma_i = H_i = \frac{m_i \bar{C}_i n_i^{(o)}}{8} ; i = 1, 2 \quad (25)$$

$$H_{3 \text{ in}} = \frac{n_o \bar{C}_3}{4} \quad (26)$$

Therefore:

$$n_i^{(o)} = \gamma_i \frac{n_o \bar{C}_3 m_3}{2 \bar{C}_i m_i} = \frac{n_o}{2} \gamma_i \left( \frac{m_3}{m_i} \right)^{1/2} ; i = 1, 2 \quad (27)$$

In addition, we have from the conservation of mass:

$$\frac{H_{3 \text{ out}}}{H_{3 \text{ in}}} = 1 - \gamma_1 - \gamma_2 \quad (28)$$

Therefore:

$$n_3^{(o)} = 2 n_o (1 - \gamma_1 - \gamma_2) \quad (29)$$

#### 4. Results

With the values of  $n_1^{(o)}$ ,  $n_2^{(o)}$  and  $n_3^{(o)''}$  determined, one can easily write the solution to eqs. (14) and (15):

$$f_i(\underline{v}, x) = \frac{x S_i(\underline{v})}{v_{ix}} + F_i(\underline{v}); i = 1, 2 \quad (30)$$

$$f_3(\underline{v}, x) = \frac{x S_3(\underline{v})}{v_{3x}} + F_3(\underline{v}) \quad (31)$$

To determine  $F_1(\underline{v})$ ,  $F_2(\underline{v})$  and  $F_3(\underline{v})$  we apply the following boundary conditions:

$$x = d, f_1 = f_2 = 0$$

$$f_3 = \frac{n_o}{\left(\frac{2\pi kT}{m_3}\right)^{1/2}} e^{-\frac{m_3(\underline{v} - V_\omega)^2}{2kT}}; v_x < 0 \quad (32)$$

$$x = 0, f_i = \frac{n_i}{\left(\frac{2\pi kT}{m_i}\right)^{1/2}} e^{-m_i v^2 / 2kT}; v_x > 0 \quad (33)$$

and  $n_1$ ,  $n_2$ ,  $n_3$  are to be determined by the specification of the interfacial kinetics of oxidation.

To determine  $n_1$  and  $n_2$  one employs the definitions of  $\gamma_1$  and  $\gamma_2$ :

$$\frac{m_i n_i \bar{C}_i}{4} = \gamma_i |H_{3 \text{ in}}|; i = 1, 2 \quad (34)$$

and for  $n_3$  using eq. (28):

$$\frac{\bar{C}_3 m_3 n_3}{4} = H_{3 \text{ in}} (\gamma_1 + \gamma_2 - 1) \quad (35)$$

where:

$$H_{3 \text{ in}} = \int_{v_x < 0} m_3 f_3(o, \underline{v}) v_x d^3 v \quad (36)$$

Using eqs. (34) and (35) one can write for  $F_3(\underline{v})$ :

$$F_3(\underline{v}) = n_o \left( \frac{m_3}{2\pi kT} \right)^{3/2} e^{-\frac{m_3(\underline{v} - \underline{V}_\infty)^2}{2kT}} \left[ \frac{1 - \text{sgn } v_x}{2} \right] \\ + n_3 \left( \frac{m_3}{2\pi kT} \right)^{3/2} e^{-m_3 v^2 / 2kT} \left[ \frac{1 - \text{sgn } v_y}{2} \right] \quad (37)$$

Substituting the results of eqs. (31) and (37) into (36):

$$\frac{H_{3 \text{ in}}}{(m_3 n_o \bar{C}_{3/4})} = 1 - \frac{\pi V_\infty n_o d}{\bar{C}_3} \left[ \left( \frac{m_3}{m_1} \right)^{1/2} \gamma_1 a_{31}^2 \right. \\ \left. + \left( \frac{m_3}{m_2} \right)^{1/2} \gamma_2 a_{32}^2 \right] \quad (38)$$

Using eq. (38), one can then write the expression for the oxidation rate with:

$$(Kn_\infty)^{-1} = d \cdot \left[ 2\pi a_{33}^2 n_o \right]; S_\infty = \frac{V_\infty}{\bar{C}_3} \quad (39a)$$

$$\frac{\dot{m}_{ox}}{(\gamma_1 + \gamma_2) n_o \bar{C}_3} = 1 - \frac{1}{2} \frac{S_\infty}{Kn_\infty} \left[ \left( \frac{a_{31}}{a_{33}} \right)^2 \gamma_1 \left( \frac{m_3}{m_1} \right)^{1/2} + \left( \frac{a_{32}}{a_{33}} \right)^2 \gamma_2 \left( \frac{m_3}{m_2} \right)^{1/2} \right] \quad (39b)$$

One can also compute the energy transfer to the surface from the definition:

$$Q_3 = \int_{v_{3x} < 0} f_3(\underline{v}, o) m_3 v_3^2 v_{3x} d^3 v_3 \quad (40)$$

$$Q_i = \int_{v_{ix} < 0} m_i f_i(\underline{v}, o) v_i^2 v_{ix} d^3 v_i ; i = 1, 2 \quad (41)$$

$$Q_{TOTAL} = Q_1 + Q_2 + Q_3 \quad (42)$$

Performing the computation indicated by eqs. (40 - 42):

$$\frac{Q_i}{\bar{C}_3 n_o m_i v_\infty^2 / 2} = \frac{1}{4} \frac{S_\infty}{Kn_\infty} \cdot \frac{3}{2} \gamma_i \left( \frac{m_3}{m_i} \right)^{1/2} a_{31}^2 \quad (43)$$

$$\frac{Q_3}{\bar{C}_3 n_o m_3 v_\infty^2 / 2} = 1 - \frac{1}{2} \frac{S_\infty}{Kn_\infty} [1 - \gamma_1 - \gamma_2] \quad (44)$$

UNCLASSIFIED

Therefore:

$$\frac{Q_{\text{TOTAL}}}{\bar{C}_3 n_o m_3 V_{\infty}^2 / 2} = 1 - \frac{1}{2} \frac{S_{\infty}}{Kn_{\infty}} \left[ 1 - \gamma_1 - \gamma_2 \right. \\ \left. + \frac{3}{4} \left\{ \gamma_1 \left( \frac{a_{31}}{a_{33}} \right)^2 \left( \frac{m_3}{m_1} \right)^{1/2} + \gamma_2 \left( \frac{a_{32}}{a_{33}} \right)^2 \left( \frac{m_3}{m_2} \right)^{1/2} \right\} \right] \quad (45)$$

UNCLASSIFIED

## C. ENGINEERING CORRELATIONS

### 1. Drag

The drag on an object entering the earth's atmosphere stems from essentially different phenomena in the free molecular and continuum regimes. In the free molecular regime, the momentum of the hyper-velocity free stream particles is transferred directly by impact of the particle with the surface. These particle impacts give rise to a momentum transfer to the surface per unit time and unit area of  $\rho_{\infty} V_{\infty}^2$ , which can be expressed in terms of a drag coefficient, i.e.,

$C_D = \frac{D}{\rho_{\infty} V_{\infty}^2 / 2} \approx 2$ . However, in the continuum regime, in the vicinity of the stagnation point of a blunt object, the drag on the body is caused by the local continuum pressure which is of order:  $\rho_{\infty} V_{\infty}^2 / 2$ , giving rise to  $C_D \approx 1$ . Therefore, in developing an approximate theory to bridge the free molecular and continuum regimes it is necessary to consider the drag as a combination of continuum, pressure type drag and free molecular, particle impact. Rott and Whitenbury (Ref. 4) have succeeded in expressing  $C_D$  as:

$$C_D = C_{D_i} + \alpha (C_{D_{F.M.}} - C_{D_i}) \quad (1)$$

where  $C_{D_i}$  represents the continuum value for  $C_D$  and  $C_{D_{F.M.}}$  the free molecular value. In eq. (1),  $\alpha$  represents the fraction of free stream particles that arrive at the surface and in general will be a function of the Reynolds and Mach numbers. In the free molecular

regime when  $\alpha = 1$ , one can note that  $C_D \rightarrow C_{D_{F.M.}}$  while in the continuum regime  $\alpha = 0$ , and  $C_D \rightarrow C_{D_i}$ . Eq. (1) suggests that one plot the sphere drag data with  $\frac{C_D - C_{D_i}}{C_{D_{F.M.}} - C_{D_i}}$  instead of the conventional  $C_D$ . Both Masson et. al (Ref. 5) and Geiger (Ref. 6) have plotted the data in this fashion (i. e.,  $\frac{C_D - C_{D_i}}{C_{D_{F.M.}} - C_{D_i}}$ ) and find the correlation applicable over a wide range of free stream Mach numbers and wall temperature ratios.

Therefore, to develop approximate analytic expressions for  $C_D$  which would be applicable between the free molecular and the continuum regimes and be useful over a large range of free stream Mach numbers and wall temperature ratios, a curve fit of the data presented in Ref. 6 was undertaken. These data are presented in the following form:

$$\frac{C_D - C_{D_i}}{C_{D_{F.M.}} - C_{D_i}} \text{ vs. } Re_s \quad (2)$$

where  $Re_s$  is the Reynolds number behind the shock. Since data is sparse for  $Re_s \leq 10$  it has been necessary to use the near free molecular theory of Willis (Ref. 7) in the near free molecular regime ( $Re_s \leq .1$ ) and then interpolate between this theory and the data shown in Ref. 6.

For reference one can write the near free molecular theory of Willis in the following form:

$$\frac{C_D}{C_{D_{F.M.}}} = 1 - Re_\infty \left[ .835 + 6.4 S_\infty^{-1} \right]$$

Equations 3a, 3b, 3c therefore represents a curve fit for the data shown in Geiger (Ref. 6), the near free molecule theory of Willis (Ref. 7) evaluated at a free stream Mach number of 12 and an interpolation between the two. It should be noted that all near free molecular theories depend only on the free stream Reynolds number, therefore when these theories are plotted vs.  $Re_s$  there will appear a weak dependence on free stream Mach number, so by taking a value of  $M_\infty = 12$ , the result will be a good approximation in the range from  $7 \leq M_\infty \leq 15$ .

For  $10^{-5} \leq Re_s \leq 1$ :

$$\frac{C_D - C_{D_i}}{C_{D_{F.M.}} - C_{D_i}} = -6.875 \times 10^{-3} (\log_{10} Re_s)^2 - 6.875 \times 10^{-2} \log_{10} Re_s + 0.84 \quad (3a)$$

For  $1 \leq Re_s \leq 3$ :

$$\frac{C_D - C_{D_i}}{C_{D_{F.M.}} - C_{D_i}} = -.319(\log_{10} Re_s)^2 - .136(\log_{10} Re_s) + 0.84 \quad (3b)$$

For  $3 \leq Re_s \leq 10^5$ :

$$\frac{C_D - C_{D_i}}{C_{D_{F.M.}} - C_{D_i}} = .7 e^{-.771(\log Re_s - .478)} \quad (3c)$$



Using a hard sphere intermolecular interaction and considering  $M_\infty$  large, one can write a relation between  $Re_\infty$  and  $Re_s$ :

$$Re_\infty = 0.57 Re_s M_\infty \quad (4)$$

From the experimental data cited in Ref. 3 the value of  $C_{D_i}$  appropriate to sphere drag in hypersonic, high Reynolds number flows is:

$$C_{D_i} = .918 \quad (5a)$$

In choosing a value of  $C_{D_{F.M.}}$ , attention must be given to the dependence of  $C_{D_{F.M.}}$  on  $M_\infty$ , and on the surface interaction between the hypervelocity free stream particles and the surface. In Ref. 8, Schamberg presents a model for the interaction of a hypervelocity particle and a surface is given. Using Ref. 8 one can write for  $C_{D_{F.M.}}$ :

$$C_{D_{F.M.}} = 2 \left\{ 1 + \left[ \Phi(\phi_o) \right] (S_\infty \sqrt{3})^{-1} \cdot f(\nu) \right\} \quad (5b)$$

where  $\Phi_o$  is the beam width of the molecules re-emitted from the surface, and  $\Phi(\phi_o)$  is the ratio of the axial momentum carried from the surface to the momentum that would be carried away if all molecules in the beam were aligned with the beam axis, while  $f(\nu)$  accounts for the body shape and reflection law assumed. For diffuse emission one has:

$$\phi_o = \pi/2, \quad \Phi(\pi/2) = \frac{2}{3} \quad (6)$$

$$\nu \rightarrow \infty, \quad f(\nu) = \frac{2}{3}$$

$$C_{D_{F.M.}} = 2 \left[ 1 + \frac{4}{9\sqrt{3}} S_\infty^{-1} \right] \quad (7)$$

To apply eq. 3 to blunt faced bodies ("cigarettes") we assume here that the geometry does not have a significant effect on the shape of the transition curve between the free molecular and continuum regimes. One can, therefore, use values of  $C_{D_i}$  and  $C_{D_{F.M.}}$  appropriate to a blunt faced body; these are:

$$\begin{aligned} C_{D_i} &= .918 \\ C_{D_{F.M.}} &= 2.06 \end{aligned} \quad (8)$$

In defining  $Re_s$  in eq. 1, one now uses  $d$ , the lateral dimension of the blunt face, instead of  $R_B$ , the sphere radius.

It is expected that the correlation equations developed here will give a reasonable account of sphere drag and cylinder drag over the entire range of free stream Reynolds numbers for  $M_\infty \geq 7$ , and will also, to a good approximation, account for wall temperature effects (Fig. 2).

## 2. Heat Transfer

In developing methods for calculating the heat transfer to an ablating graphitic surface over the entire range of Knudsen number from the free molecular to the continuum regime, one is not only faced with the usual difficulties encountered in the transition regime, but additionally, one has the complicating physicochemical processes which occur at the graphite surface.

Analyses of heat transfer to an ablating graphitic surface have been performed by Scala (Ref. 9) for the high Reynolds number regime and in Section (II-B) of the present work the very low Reynolds number

the near free and free molecular regimes have been investigated. These analyses indicate for the regimes considered the aerodynamic heat transfer in the absence of oxidation will give a good representation for the heat conducted into the graphite surface in both the rate and diffusion controlled regimes. Therefore, we assume here that over the entire range of Reynolds numbers the usual aerodynamic heat transfer will provide a good approximation to the energy conducted into the surface.

To obtain a correlation formula for the aerodynamic heat transfer we write:

$$Q = \left\{ \frac{[C_H \sqrt{Re_s}]_{L.R.}}{(C_H \sqrt{Re_s})_{H.R.}} \right\} Q_{B.L.} \quad (9)$$

where the ratio:  $[C_H \sqrt{Re_s}]_{L.R.} / (C_H \sqrt{Re_s})_{H.R.}$  represents the ratio of the Stanton numbers in the low and high Reynolds number regimes and  $Q_{B.L.}$  is the boundary layer heat transfer given by Scala (Ref. 9) as:

$$Q_{B.L.} = \left( \frac{P_e}{R_B} \right)^{1/2} \left( 33.3 + .0333 [H_e - h_{w_{air}}] \right) \frac{\text{Btu.}}{\text{ft.}^2 - \text{sec.}} \quad (10)$$

with  $R_B$  the nose radius in feet, and with  $P_e$  given by the modified Newtonian distribution as:

$$P_e = p_\infty \left[ 1.55 M_\infty^2 - .22 \right] \cos^2 \theta + p_\infty \sin^2 \theta \quad (11)$$

in units of atmospheres and  $\theta$  the angle on the sphere face:


(12)

and:

$$h_{w_{air}} = .3T_w \text{ (Btu./\#); with } T_w \text{ in } ^\circ\text{R.}$$

$$\frac{\text{Btu}}{\#} = H_e = .3T_\infty (1 + .2M_\infty^2); \text{ with } T_\infty \text{ in } ^\circ\text{R.}$$

It should be pointed out that the assumptions implicit in the choice of eq. (9) to calculate the heat transfer is that the ratio  $\frac{[C_H \sqrt{Re_s}] \text{ L.R.}}{(C_H \sqrt{Re_s}) \text{ H.R.}}$

is a function of  $Re_s$  alone. It is clear that for hypervelocity flow, the above ratio is almost independent of Mach number in the boundary layer ( $Re_s \geq 10^4$ ) and viscous layer ( $10^4 > Re_s \geq 10^2$ ) regimes; however, in the transition and near free molecule flow regimes there will be a dependence. The assumption here is that the dependence is weak.

To obtain a correlation, expressions are obtained for the Stanton number ratio in the various flow regimes and interpolations are employed where results are not available.

In the free and near free molecular flow regimes, the results of Willis (Ref. 7) may be applied. One can write, using the results of Ref. 7:

$$(C_H \sqrt{Re_s})_{n.f.m.} = \sqrt{Re_s} [1 - .53 Re_\infty] \quad (13)$$

This result was obtained by a Knudsen iteration of the integral equation which results from a modified Krook model. It is interesting to point out that one has a dependence on  $Re_{\infty}$  in this regime rather than  $Re_s$ , so that to cast eq. (13) as a function of  $Re_s$  alone requires assuming a specific free stream Mach number; for the purposes of this investigation we choose:  $M_{\infty} = 12$ .

In the low Reynolds regime we have the theory of Cheng (Ref. 10) for a perfect monatomic, non-dissociated gas and that of Goldberg and Scala (Ref. 11) for an equilibrium dissociated gas. By interpolating between these theories one approximately obtains the effects of non-equilibrium dissociation in the gas phase. Further, by interpolating between the results of Willis (Ref. 7) and Cheng (Ref. 10), one obtains an approximation to the transition regime of rarefied gas dynamics.

One can then write the correlation equations, employing the above theories and interpolations (See Figure 3):

$$I) \quad 10^{-3} \leq Re_s \leq 10$$

$$\frac{C_H \sqrt{Re_s} \text{ L.R.}}{(C_H \sqrt{Re_s}) \text{ H.R.}} = \frac{2.14}{2.2} \exp \left( .922 \left[ \log_{10} Re_s - 1 \right] \right) \quad (14a)$$

$$II) \quad 10 \leq Re_s \leq 10^3$$

$$\frac{C_H \sqrt{Re_s} \text{ L.R.}}{(C_H \sqrt{Re_s}) \text{ H.R.}} = \frac{1}{2.2} \left[ -.405 \left[ \log_{10} Re_s \right]^2 + 1.98 \log_{10} Re_s + .57 \right] \quad (14b)$$

$$\text{III) } 10^3 \leq \text{Re}_s \leq 10^5$$

$$\frac{C_H \sqrt{\text{Re}_s} \text{ L.R.}}{(C_H \sqrt{\text{Re}_s}) \text{ H.R.}} = \frac{1}{2.2} \left[ .055 (\log_{10} \text{Re}_s)^2 - .67 \log_{10} \text{Re}_s + 4.36 \right] \quad (14c)$$

It should be noted that the assumptions implicit in using the correlation are that  $M_\infty \geq 7$ , and that the wall temperature ratio not be too large. It is interesting to point out that the use of eqs. (9) and (10) in calculating the heat transfer away from the stagnation point implies a  $\cos \theta$  distribution over the entire range of  $\text{Re}_s$ . This is correct in both the free molecular and boundary layer limits and can be expected to be a reasonable assumption over a wide range of Reynolds numbers.

For the "cigarette" shaped bodies, one can employ eqs. (9) through (14) provided one sets  $\theta = 0$  in eq. (11) and uses the lateral dimension of the blunt face rather than  $R_B$  in defining  $\text{Re}_s$ . In addition it should be mentioned that for the "cigarette" we assume that no energy is transferred to the afterbody and that no mass loss takes place from the afterbody.

### 3. Mass Transfer

The calculation of the mass transfer from an oxidizing graphite surface over the entire range of Reynolds numbers is, in a sense, a far more difficult problem than the estimation of either the drag or heat transfer. This is because no theories or experiments had existed previously for mass

transfer at low Reynolds number, and additionally, the chemical kinetics of graphite oxidation has never been experimentally investigated in the hypervelocity, rarefied regime. These uncertainties will render the estimates that follow approximate, and do indicate the need for more extensive theoretical and experimental studies of mass transfer and interfacial chemical kinetics over the entire range of Reynolds numbers.

In discussing the mass transfer problem, it is necessary to clearly define the reaction rate and diffusion controlled regimes, since either regime may dominate at a given Reynolds number and Mach number.

If the reaction at the surface is proceeding at a slow enough rate, compared to the time necessary for convection of the reactant species to the surface, one is said to have a reaction controlled process. In this limit, the reactant species concentrations in the gas phase are generally unaffected by the interfacial kinetics and one can treat the surface reactions as being uncoupled from any diffusion processes in the gas phase. However, if the reaction rates at the surface are quite fast compared to species flow times to the surface, the oxidation process is said to be in a diffusion controlled regime. In this limit diffusion in the gas phase can be uncoupled from the interfacial kinetics.

For the oxidation of graphite, Scala (Ref. 9), in the high Reynolds limit, has solved the problem of diffusion controlled oxidation and has proposed a simple relation for providing a transition between the diffusion and reaction controlled limits. Scala obtains for the

diffusion controlled oxidation rate:

$$\dot{m}_{D_{B.L.}} = \frac{P_e^{1/2}}{R_B^{1/2}} \times 6.2 \times 10^{-3} \frac{\text{lb}}{\text{ft}^2 \cdot \text{sec.}} \quad (15)$$

where  $P_e$  is given by eq. 11 and for a sphere  $R_B$  in units of ft. is the nose radius, while for the blunt faced bodies  $R_B$  should be replaced by the lateral dimension of the blunt face. In section (III-B) of the present work expressions have been obtained for the diffusion controlled oxidation rate in the very low Reynolds number, free molecular and near free molecular regimes. In various calculations of oxidation rates downstream of the stagnation point performed in this laboratory it was found that the mass transfer rates could be correlated by assuming that,  $Q^*$ , the effective heat of ablation of graphite was a constant. Therefore, in order to construct a correlation for the diffusion controlled mass transfer which could bridge the free molecular and continuum regimes, it was decided to utilize the same assumption that the  $Q^*$  found by Scala (Ref. 9) for the high Reynolds number regime, could be applied over the entire range of free stream Reynolds numbers and Mach numbers. Since  $Q^*$  is defined as:

$$Q^* = \frac{Q}{\dot{m}_D} \quad (16)$$

one can therefore write:

$$\dot{m}_D = \frac{Q}{Q^*} \quad (17)$$

where  $Q$  is the aerodynamic heat transfer rate which may be calculated



from eqs. 9 and 14, and  $Q^*$  can be written from Ref. (9) as:

$$Q^* = 5370 + 5.37 (h_e - h_{w, air}) \text{ Btu/lb} \quad (18)$$

It should be noted that eqs. (17) and (18) can be put in a form which is more amenable to engineering calculations:

$$\dot{m}_D = \dot{m}_{B.L.} \left( \frac{(C_H \sqrt{Re_s})_{L.R.}}{(C_H \sqrt{Re_s})_{H.R.}} \right) \quad (19)$$

where  $\dot{m}_{B.L.}$  is given in eq. (15) and the correlation for the Stanton number ratio is given eq. (14).

It is interesting to note that for the free molecular regime eq. (19) reduces to the correct free molecular limit, this can be seen

by noting that:  $\frac{(C_H \sqrt{Re_s})_{F.M.}}{(C_H \sqrt{Re_s})_{H.R.}} = \frac{\sqrt{Re_s}}{2.2}$ , and  $\dot{m}_{B.L.} = \left[ \frac{\rho_\infty V_\infty}{Re_s} \right]^{2.2}$

so that  $(\dot{m}_D)_{F.M.} = \rho_\infty V_\infty$ , which is the correct limit. In addition for the near free molecular limit  $\dot{m}_D$  as predicted by (19) yields:

$$(\dot{m}_D)_{n.f.m.} = \rho_\infty V_\infty \left[ 1 - .53 Re_\infty \right] \quad (20)$$

which is to within a numerical factor the same result obtained in section II-B for the near free molecular oxidation of graphite. Since eq. 19 correctly reproduces the boundary layer, near free and free molecular regimes, it is not unreasonable to assume that it gives a good approximation to the diffusion controlled oxidation mass transfer over the entire range of Reynolds numbers.

In obtaining expressions for the reaction controlled regime one encounters large uncertainties which are attributable to the dearth of definitive experimental data on the oxidation of graphite when subjected to hypervelocity, rarefied flows.

The existing experimental information on graphite oxidation was obtained under gas kinetic conditions (i. e. oxygen molecules reach the surface with a thermal velocity  $\bar{C} = \left(8kT/\pi m\right)^{1/2}$ ), these data indicate a rate equation of the following form:

$$\dot{m}_R = k_w (p_{O_2})^n \quad (21)$$

where  $\frac{1}{2} \leq n \leq 1$  and  $k_w$  is a rate constant which is a function of surface temperature alone. Experimental and theoretical considerations seem to indicate that, under gas kinetic conditions:  $n = \frac{1}{2}$ , this being attributable to a pore mechanism for the oxidation process. During the entry of an object into the earth's atmosphere, gas kinetic conditions, are generally achieved at the stagnation point after a fully developed shock wave has formed. Therefore, for the high Reynolds number regime it seems reasonable to utilize eq. 21, with  $n = \frac{1}{2}$ , in the rate controlled regime, where  $p_{O_2} = .21 P_e$  (eq. 11) and  $k_w$  is an experimentally measured function of temperature. However, as the Reynolds number decreases and the oxygen molecules incident at the surface retain a significant fraction of their free stream velocities, there may be a transition from a pore type mechanism to a surface type mechanism which would be first order rather than half order. To clarify these

questions accurate molecular beam experiments are necessary in the hypervelocity rarefied regime. In the light of these uncertainties, we choose a rather simple rate equation for the entire range of Reynolds numbers, with the understanding that for  $Re_s < 100$ , the equation will become progressively more inaccurate. We write:

$$\dot{m}_R = k_w (.21 P_e)^{1/2} \quad (22)$$

To provide the transition between the reaction and diffusion controlled regimes, an addition rule is derived for the boundary layer regime and is used over the entire range of Reynolds numbers. We first write for the mass transfer:

$$\dot{m}_{a_{B.L.}} = \left( P_{O_2_e} - P_{O_2_w} \right)^n \quad (23)$$

where the concept of a boundary layer resistance  $a_{B.L.}$ , to mass transfer is introduced, and additionally a rate equation:

$$\dot{m} = k_w \left( P_{O_2_w} \right)^n \quad (24)$$

Since the mass transfer rate as expressed in (23) and (24) must be equal, we equate (23) and (24) and obtain the following constraint:

$$(1 - \zeta)^m = \eta \zeta^n \quad (25)$$

where:  $\zeta = P_{O_2_w} / P_{O_2_e}$  and  $\eta = k_w a_{B.L.} P_{O_2_e}^{n-m}$ .

Since  $0 < \zeta < 1$  we may rewrite  $\zeta$  as:

$$\zeta = \frac{1}{1 + \beta} ; \beta \geq 0 \quad (26)$$

Therefore (24) may be rewritten as:

$$\dot{m} = \frac{1}{\left[ \frac{1}{k_w^{1/n} p_{O_2e}} + \frac{\beta}{k_w^{1/n} p_{O_2e}} \right]^n} \quad (27)$$

since  $k_w^{1/n} p_{O_2e} \approx \dot{m}_R$  and  $p_{O_2e} = \dot{m}_D^{1/m} a_{B.L.}^{1/m}$  we can

rewrite (27) as:

$$\dot{m} = \frac{1}{\left[ \frac{1}{(\dot{m}_R)^{1/n}} + \frac{\beta}{k_w^{1/n} (\dot{m}_D)^{1/m} a_{B.L.}^{1/m}} \right]^n} \quad (28)$$

For the problem of graphite oxidation:  $m = n = 1/2$  and:

$$\zeta = \frac{1}{1 + \eta^2} \quad (29)$$

$$\beta = (K a_{B.L.})^2$$

Therefore:

$$\dot{m} = \frac{1}{\left[ \frac{1}{(\dot{m}_R)^2} + \frac{1}{(\dot{m}_D)^2} \right]^{1/2}} \quad (30)$$

So that eq. 19 can be used to calculate  $\dot{m}_D$ , eq. 22 can be used in the calculation of  $\dot{m}_R$  and finally eq. 30 determines the total oxidation mass transfer from the surface.

### III. EXPERIMENT

#### A. INTRODUCTION

That phase of the investigation with which the experimentation was associated takes no cognizance of the circumstances through which particles re-enter the atmosphere. The premise is adopted that such particles are re-entering and the investigation seeks to examine their behavior under controlled re-entry environment conditions. The general solution offered is a machine-computed evaluation of the ablation of particles of various sizes following selected re-entry trajectories and based on a particular model of the ablation mechanism--that of the oxidation of materials as proposed by Scala (Ref. 9). While the experimental program does not relate directly to the computer analysis for re-entering particles, it is designed to provide experimental confirmation of the analytical approach in two ways.

First, experiments were performed on ATJ graphite, a well characterized graphitic material, to supplement and extend the existing data of Diaconis (Ref. 12), which had been obtained in support of Scala's oxidation theory. Data were acquired for the reaction rate controlled regime of oxidation for both continuum flow and for non-continuum flow. Subsequently, similar mass rate data were acquired for a Material "X", furnished by SNPO, and comparisons of the performances of the two and with the theory were made by empirical evaluation of the test data.

Second, a study to determine the integrated ablation and the shape variation of spherical bodies of different sizes in both a fixed attitude and during rotation about an axis perpendicular to the flow was

conducted. As a secondary output of the computer program, predictions were obtained for the ablation of such spheres subjected to environments corresponding to that produced in the arc facility. The predicted values were then compared to those actually obtained experimentally for ATJ. Tests of several fixed and rotating short cylinders constructed from Material "X", were also performed. Again, with corresponding spherical specimens, direct comparison was made of the results of ATJ Graphite and Material "X" in terms of dimensional and mass changes. Further assessment of the computer analysis was derived through the machine programming of a one-dimensional axially oriented "X" cylinder given an input laboratory (arc facility) environment. A comparison of the output with corresponding experimental results was performed.

## B. EXPERIMENTAL EQUIPMENT

### 1. Facility Description

All tests scheduled for the study of ATJ Graphite and Material "X" were conducted in a GE-SSL Hypersonic Arc Tunnel. This system is comprised of a Tandem Gerdien arc heater, a conical nozzle through which the heated test gas is expanded into a continuously evacuated test section where the specimens are normally mounted, a diffuser aft of the test section, and a high speed mechanical vacuum pump. The tunnel is illustrated in Figures 4 and 5.

The principal element of the test facility combines two Gerdien arc units functioning together with a common arc column. The arrangement (Figure 6) is such that air is admitted tangentially to each Gerdien unit through vortex chambers located between the

electrode housings and the plenum chamber. Valving in the air system provides a method of dividing the incoming air flows into two portions which are subject to close control. The greater portion of the air is bled from the system through exhaust ports in the electrode housings. In the course of its passage from the inlets to exhaust ports, the exhaust air carries with it the carbon products produced from the graphite electrodes which would normally contaminate the test gas. The remaining portions of the air admitted (which constitute the test gas) pass into the plenum from both sides, acquiring energy from the arc column enroute. Contaminants, measured spectroscopically, constitute less than 100 parts per million of the test gas. The rotation induced in the air as it is admitted tangentially, is oppositely directed in the two halves of the arc, the opposed rotations tending to offset one another as the two flows enter the plenum and mix. The combined flow then passes from the plenum through the throat of the conical nozzle.

The nozzle is constructed in two parts, one of which is essentially an extension of the other. The up-stream section has an exit diameter of 1.2". It is at the exit of this short nozzle that tests at the higher model stagnation pressures are performed. The extension, when added to the short nozzle, provides a nozzle of 5" exit diameter. The juncture of the two sections is sealed and the internal surfaces form a smooth interface in order that the flow will not be disturbed. All parts of the arc hardware and the nozzle are cooled with pressurized high velocity water in order to provide them with maximum service life.

UNCLASSIFIED

The test section in which specimens are normally mounted has access ports on both sides, top and bottom. Windows mounted in the side ports are generally employed for visual observation, optical and radiation instrumentation, and in some instances, for motion picture camera coverage. The top port is used for camera coverage of conventionally mounted specimens. Both top and bottom openings are adaptable for auxiliary equipment as needed.

Normally, specimens are mounted on a water cooled sting which extends up-stream into the test section. The sting, operated pneumatically, is capable of holding a specimen in a retracted position, out of the flow of heated gases. The controls can be regulated to automatically inject sting and specimen into the center of the flow, and remove it after a programmed interval. The sting is designed to carry instrumentation leads from the specimen through its interior to a terminal board outside the tunnel.

A portion of this program required a special sting to support and drive the rotating specimens. This sting was inserted from the top port and connected to a motor drive through a gear system (Figure 7). Speeds of approximately one and two radians per second were provided by interchanging gears.

Downstream of the test section the system is fitted with a diffuser, through which the high velocity of the test flow decreases, with a corresponding recovery of pressure. A heat exchanger and a large mechanical vacuum pump complete the system. The pump is a 5000 cfm rotary mechanical booster vacuum pump with two stages, the large capacity of which is required to maintain low pressure ( $< 100 \mu$  Hg) in the facility under full flow conditions.

UNCLASSIFIED



## 2. Facility Operation and Control

The Tandem Gerdien arc heater is operated on rectified direct current from a 500 KW power supply. The power drawn from the supply is divided between a ballast resistor bank and the arc column, which are connected in series. Power delivered across the arc can be varied by changing the resistance of the ballast included in the electrical circuit. The resistance of the ballast can be changed (between runs) in minimum increments of 0.065 ohms, to a maximum of 1.300 ohms. Thus, the properties of the test gas can be altered in discrete steps as a function of the power reaching the arc. In addition, the plenum pressure, and consequently the gas enthalpy, can be adjusted by varying the mass flow of air admitted to the arc unit and the relative amounts which are permitted to exhaust or to enter the plenum. While not customarily done on test programs, it has been shown that continuous variation of test gas properties over limited ranges is possible by proper control of the mass flows.

Finally, a discrete change in enthalpy of the test gas can be obtained by altering the geometry of the arc plenum chamber or of the vortex chambers used in the system. In this program, the enthalpy of the test gas was approximately halved by introducing vortex chambers with constricting orifices of decreased diameter.

## 3. Test Instrumentation and Specimens

3.1 Pyrometer: The primary datum acquired on the specimen during actual test for this program is a continuous record of surface temperature. This is obtained with a recording two-color pyrometer. The pyrometer employs two phototubes with maximum responses at different wavelengths. One tube has maximum response in the red

portion of the spectrum, the other in the blue. The evaluation of the relative responses of the two tubes is interpreted as a color temperature. For models tested in the flow from the 5" diameter nozzle, the two color pyrometer views the specimens through a test section window. When the 1.2" diameter nozzle is employed, use is made of a special small port built into the arc heater mounting flange.

3.2 Total Calorimeter: To measure the enthalpy of the test gas, a total calorimeter was used. This device (Figure 8) consists of a cylindrical housing containing a labyrinth passage for the test gases. The adjacent walls are cooled with pressurized water to remove the heat transferred from the test gas. The calorimeter is affixed directly to the throat of the nozzle, located in the wall of the arc plenum. The heated test gas from the plenum is directed through the calorimeter where it transfers the bulk of its heat to the circulating water. The heat remaining in the gas as it leaves the calorimeter is monitored by a thermocouple. Similarly, the temperature rise and mass flow of the circulating water are measured continuously during a test. Several thermocouples are mounted in the copper structure of the calorimeter to evaluate the heat "stored" in the walls. The test is continued until all reporting thermocouples equilibrate. The evaluation of the reported data, essentially a heat balance between the calorimeter elements and the test gas, results in a measure of the total heat content of the gas. Since it is estimated that there are some minor heat losses which cannot be evaluated, the value of the enthalpy obtained will be slightly conservative.

It should further be noted that the enthalpy determined is a "mean" of any distribution of energies at an arbitrary cross section of the

nozzle. For example, the heat content of the core gases is not distinguished from those of the boundary layer. The latter, being adjacent to the cooled nozzle walls, will obviously be lower. In addition, other methods, such as spectroscopic evaluation of gas enthalpy, indicate that the energy in the core itself is not uniformly distributed. Spectroscopic measurements in the past have recorded enthalpies about six percent higher than those obtained by total calorimetry.

3.3 Pressure Probe: As part of the test program it was essential to obtain a measure of the model stagnation pressure at the various test locations. The principal probe employed to obtain these data was a copper blunt cone configuration with a 94 mil central orifice (Figure 9). Since under the conditions of the experiment, the stagnation pressure is independent of model shape, the same probe was used for all measurements. (Other slender conical probes, having flat frontal configurations corresponding to the diameters of the mass rate specimens and with smaller orifices, were run at the lowest density condition to ascertain whether these factors might be important to the measurement. Within the required experimental accuracy, they were not). The probe was not water cooled. Reliance was placed upon the heat sink characteristics of the massive copper body to insure its survival in the test environments. In exposure times up to 30 seconds, the probe remained intact.

From the probe, tubing transmitted the pressure to a universal manometer rack. The system incorporated an arrangement of vacuum valving which permitted both legs of the manometer employed to first be evacuated with a vacuum pump. Thus the manometer was

referenced to an absolute pressure of less than 10 microns. When the pressure probe was inserted into the flow, one leg of the manometer was valved into the connecting tubing and the pressure was read as an essentially absolute value from the displacement of the manometer fluid.

For the lower pressure test condition (5.0" exit nozzle), the manometer working fluid was a vacuum oil of 1.04 specific gravity and very low vapor pressure. For the higher pressure test condition mercury was the working fluid.

3.4 Specimen Calorimeters: The measurement of heat transfer to the specimen configuration, while not essential to the evaluation of mass rate data, is considered important in the understanding of the behavior of the specimens tested for shape change. This was especially true when correlations with the computer analyses were sought.

Calorimetric models corresponding to each of the test specimen configurations were exposed to each of their respective test environments. Typical calorimeters are shown in Figures 10 and 11. The calorimeter bodies were constructed from phenolic nylon, chosen for its low thermal conductivity. Into each of these, a copper cylinder (in the case of several of the spheres, more than one) was inserted. A thermocouple attached to the back face of the copper slug recorded the rise in temperature in the copper during exposure. By confining the slug within a poor thermal conductor, the heat transfer could be evaluated on the basis of a one-dimensional heat flow analysis. The one inch cylindrical and spherical specimens were equipped with 1/4" diameter slugs. The 1/4" bodies employed

1/8" diameter slugs.

To obtain heat transfer to the 1/16" diameter specimen, a rigid 60 mil copper rod was employed. In order to minimize lateral heat input, the rod was coated with a 2 to 3 mil layer of RTV rubber which is highly resistant to thermal conduction. The 1/16" calorimeter appeared to perform extremely well, but in order to provide a higher level of confidence in this technique, several calorimeters constructed from 1/4" diameter copper rod coated with a correspondingly thin RTV skin were tested. Results were comparable to the data obtained from the 1/4" phenolic nylon cylinders with 1/8" diameter copper inserts.

3.5 Test Specimens: Several sizes of cylindrical specimens were involved in the acquisition of mass rate data. Sizes included diameters of 1/16", 1/4" and 1". For the study of shape change characteristics, spherical specimens of one inch and 1/4" diameter were included, together with short cylinders having a length to diameter ratio ( $l/d$ )=2. The configurations and dimensions of the specimens are shown in Figure 12. Similar specimens were prepared from ATJ Graphite and Material "X" except that only the  $l/d=2$  cylinders of "X" were tested. The ATJ Graphite specimens were furnished by GE-SSL. A sample of the original block of ATJ material is available for property evaluation if required. In general, Material "X" was supplied in specimen form by SNPO.

During the course of the program, various circumstances arose which warranted the introduction of several modifications to the specimens. Variations were introduced principally to the 1/4"

diameter cylinders. It was found that during consecutive tests the surface temperatures of similarly constructed models equilibrated at temperatures that differed but little from one another. The results, therefore, obtained under these circumstances, were confined to a relatively narrow range of temperatures. In order to extend the temperature range, variations of test specimens retaining the basic 1/4" diameter cylindrical shape were constructed (Figure 13). Objectives sought by making such changes were (a) the alteration of the thermal conduction paths and (b) a change in the heat storage volume of the specimen adjacent to the exposed surface. These changes were introduced to the ATJ specimens only. The Material "X" specimens were tested in essentially their original configurations. While the modified specimens did provide an increase in the range of surface temperatures obtained, the effects were not as pronounced as expected. However, for the same reasons the 1/16" specimens were also tested in one other configuration (Figure 13) in addition to the original. In this case, the increase in temperature range was also relatively small.

When testing of the rotating spheres was initiated, it was immediately evident that the ceramic strut employed did not have adequate strength to provide support in the test flow. Consequently, a threaded graphite rod was substituted for the ceramic rod formerly used. The substitution required that the holes in the rotating specimens be deepened and threaded. Reworking of the rotating models was necessary for both ATJ and Material "X".

Both cylindrical specimens and spheres were mounted to the

sting assemblies with graphite holders of cylinder-cone configuration. Several model and holder assemblies are shown (Figures 14-18). The graphite holder was employed to give additional protection to the permanent test facility sting.

3.6 Motion Pictures: Color motion pictures (16 mm) were taken of many of the runs performed at the 5.0" station. In the place of a normal framing speed, time lapse sequences were obtained at the rate of one frame per second for some of the longer runs. Pictorially, the films may be used to provide qualitative information, to verify transient phenomena and to document the tests. However, their use for quantitative data reduction purposes is severely limited because of the excessive temperature gradients; halation effects create the illusion of model enlargement in intensely bright areas. A typical effect is the tapered appearance of the two parallel edges of cylindrical specimens. In cases where the camera was stopped down more, the heated end is more accurately depicted but the cooler regions of the specimen do not appear on the film.

3.7 General: The facility is instrumented to provide a continuous record of arc current and voltage and plenum pressure. Such information, together with the response curves of the two-color pyrometer and calorimeter thermocouple data are recorded on a Midwestern multi-channel oscillograph recorder. Mass flows of air are measured and monitored by Fischer and Porter float-type flowmeters; test flow pitot probe pressure are measured with a manometer system; and test cabin pressures are monitored with tilting McCleod gages. Pre-set electric timers program operating sequences. These and other incidental but pertinent data are hand recorded.

### C. TEST PROCEDURES

#### 1. Specimen Location

From the outset of the program, it was evident that two positions would be involved in testing specimens at the lower pressure (5" station) condition. The mass rate specimens, on the coaxial sting were adjustable, permitting them to be located at a standard 9/16" from the nozzle exit. However, the rotating sting assembly required that the axis of rotation be located 2.350" from the nozzle exit. Hence the leading faces of rotating one inch spheres were 1.850" from the exit and those of the 1/4" diameter rotating spheres, 2.225" from the nozzle exit.

When testing of the 1/16" diameter mass rate cylinders was begun, it became apparent that the fore-shortened elliptical image of the stagnation region resulting from the extremely acute viewing angle (circa  $5^{\circ}$ ) failed to cover completely the aperture of the two-color pyrometer. Since calibration was based on an image which was larger than the aperture in the pyrometer, another position (1.500") was established to accomodate the small specimens).

In the higher pressure (1.2" station) position all models were tested at a location 9/16" from the nozzle exit. The limited field of view through the viewing port made this location for the specimens mandatory. The field of view permitted a maximum of less than 1/2" of model erosion to be followed by the two-color pyrometer.

#### 2. Pyrometry

One difficulty experienced during testing was a persistant problem in aligning the two-color pyrometer to pick up the image of the test surface during the initial heating of the specimen. Frequently, it was



possible to record a trace only after a manual adjustment of the focussing lens, with a consequent loss of as much as sixty seconds from the time of model immersion.

The situation improved when it was discovered that the evacuation of the test section produced an appreciable shift in the position of the image. The effect was produced by the change in the medium through which the radiation passed, with a consequent alteration in the refractive angle between the test section and the glass of the facility window. When the shift was noted, corrective compensation resulted in an improved record of surface temperature from those acquired during the early portion of the tests.

The two-color pyrometer (Ref. 13) used to monitor surface temperatures of the test specimens was calibrated against a tungsten filament standard lamp. The lamp itself was calibrated with true temperature as a function of input current at constant voltage by the National Bureau of Standards. This direct method of establishing the filament temperature was employed in preference to an optical pyrometer calibration in order to avoid the possible human errors introduced in reading and in correcting the brightness temperature of the filament to a corresponding color temperature. All surface temperature data are recorded as color temperatures. In the case of ATJ Graphite, the color temperature may be expected to depart from true temperature by very little, since the existing emissivity data indicate that the spectral distribution approximates that of a gray body. While the radiative properties of Material "X" are unknown, its composition suggests that surface temperatures recorded for it are also good approximations of the true temperature.

A calibration exercise was necessitated by each major alteration of the geometry of the test arrangement. In all, twelve calibrations were performed in the course of the program. The responses of the two phototubes in the pyrometer were recorded on a Midwestern oscillograph. The deflection of each "pen" was measured and the ratio of red to blue deflection was calculated. The ratios were plotted against their respective temperatures. The resulting graph was used to evaluate ratios obtained from the test specimen traces. A typical calibration curve is shown in Figure 19. If the source radiation increases sufficiently, the tubes will reach saturation and the resulting traces will be meaningless. To avoid tube saturation, a series of neutral density filters are mounted turret-fashion in front of the pyrometer window. As the tube output approaches saturation, a filter is indexed to bring the signal down to an acceptable level. The calibration technique is, of course, employed with each of the filters.

### 3. Specimen Heat Transfer

Measurements of the heat transferred to a cold wall calorimeter of the transient type were obtained for specimen configurations corresponding to each of those employed for the acquisition of mass rate and shape change data. The appropriate calorimetric specimens were tested at both the lower and higher pressure test locations and in both high and low enthalpy environments. In addition to conventional stagnation point heat transfer rate determinations on flat faced and spherical surfaces, the distribution over a sphere was measured. With the 5" diameter exit nozzle, calorimetric measurements were made at several stations downstream of the exit, since

the positions of the several specimens were necessarily different.

The procurement of a heat transfer rate consists of immersing the calorimeter in the flow of hot gas for a very few seconds. Heat delivered to the copper insert of the calorimeter by convection is conducted the length of the insert to a chromel-alumel thermocouple, the response of which is recorded on the Midwestern Oscilligraph Recorder as a function of time. The linear portion of the time-temperature trace is evaluated by the method of Sutton and Miksch (Ref. 14). Each thermocouple is individually calibrated.

#### 4. Model Stagnation Pressure

Stagnation pressure values were required for each specimen location and operating condition. The probe, described previously, was exposed for a time sufficient to obtain a steady deflection of the manometer fluid. In general, less than ten seconds were required for the mercury, although oscillations in the vacuum oil were slower to dissipate. Test times of up to 30 seconds were used with the oil filled manometer. Pressures were measured at each test station and for each enthalpy level (Table 1). In the case of the 5" diameter nozzle and high enthalpy operation, values were obtained at several distances from the nozzle exit. These are plotted (Figure 20) for extrapolation purposes since the probe could not be retracted to positions as remote as were several of the spheres. Because similarity of distribution could be expected and the variation in pressure was small, the complete survey was not repeated for the lower enthalpy condition.

#### D. EVALUATION OF ENVIRONMENT AND MEASUREMENTS

##### 1. Evaluation of Flow Environment

Data taken from mass rate specimens of several sizes and at three operating conditions augmented and extended oxidation rate data previously acquired for ATJ graphite and provided comparable information on Material "X". To examine the effect of various flow regimes, these specimens were tested in facility environments which, when considered with the model sizes, simulated continuum flow including that of low Reynolds number as well as near free molecular flow. Differences in the rate of mass loss in the various regimes predicted from theoretical considerations were sought.

In order to determine the type of simulation performance which the test facility could deliver, it was necessary to define the conditions of flow provided at different conditions of operation. Based on facility evaluation tests previously conducted in the GE-SSL Hypersonic Arc Tunnel (Ref. 15), a series of computations were made to determine the Reynolds number at the several test conditions. Although the available spectrographic evidence indicates that the flow is in equilibrium as it leaves the plenum, sufficient evidence also exists that the flow may freeze very rapidly in the vicinity of the throat of the nozzle (Ref. 16). Calculation of both the equilibrium and frozen flow expansions through the nozzle according to the treatment in Ref. 15 showed that while the local free stream properties were quite different at the test locations, the Reynolds numbers for both frozen and equilibrium flow in the model

stagnation region were of approximately the same magnitude, from less than 15% for the lower values, to less than 8% for the higher, over the pertinent range 500 to 4100 per foot. Consequently, when it was necessary to introduce a Reynolds number, an average value was used for each set of conditions.

In understanding the character of the test flow environment, it is necessary that one be able to recognize the flow regime established. An estimate may be made as to whether the gases behave as a continuum or as an aggregate of independent particles based on the Knudsen number coupled with the Mach number. A knowledge of the Reynolds number is extremely useful in evaluating the Knudsen number applicable to the various sized specimens.

Some time ago, Tsien (Ref. 17) proposed an expression for mean free path in terms of kinematic viscosity, the specific heat ratio, density and sound velocity.  $\lambda = 1.255 \eta \sqrt{\gamma} / \rho u$ . He further showed, in effect, that the ratio of Knudsen number to Mach number was proportional to the reciprocal of Reynolds number. By introducing values from kinetic theory his expression can be rearranged into a convenient form.  $Kn/M = 1.25 \sqrt{\gamma} / Re$ . From this equation one may calculate a Knudsen number appropriate to either frozen ( $Kn = 6.5$ ) or equilibrium ( $Kn = 2.9$ ) flows, for the 1/16" diameter specimen. Both numbers are representative of conditions generally classified in vacuum practice as a region of transition to molecular flow. More recent investigators have advocated the ratio of  $Kn/M$  as a proper representation of the various flow regimes. The

corresponding values are, for  $Kn = 6.5$ ,  $Kn/M = 0.513$ , and for  $Kn = 2.9$ ,  $Kn/M = 0.604$ . Hence, it may be concluded that nominally, the same flow regime (near free molecular) is predicted regardless of the equilibrium, or lack of it, in the heated gas.

## 2. Evaluation of Enthalpy

The nominal magnitudes of total enthalpy of the test gases at the two basic operating conditions were measured by total calorimetry. Direct measure of enthalpy ( $h$ ) during each specimen test was impractical, however, evaluation of individual test enthalpies was performed in the following manner.

By employing dimensional analysis one obtains the dimensionless relationships among the important variables of arc operation. Such an analysis is made using electrical power ( $E_k$ ), density ( $\rho$ ), mass flow of air ( $\dot{m}_a$ ), nozzle throat area ( $A$ ), and plenum (total) pressure ( $p$ ). From the analysis the following pi equations are developed:

$$\pi_1 = \frac{h \dot{m}_a}{E_k}$$

$$\pi_2 = \frac{\rho E_k}{\dot{m}_a p}$$

$$\pi_3 = \frac{A p}{(E_k \dot{m}_a)^{1/2}}$$

Combining  $\pi_1$  and  $\pi_3$ , one obtains

$$h = \frac{\pi_1}{\pi_3} \left( \frac{A p E_k^{1/2}}{\dot{m}_a^{1/2}} \right)$$

For this program, where A is constant, the pi factors were eliminated by taking ratios with respect to the measured total calorimetric data,

$$h = h_m \left[ \frac{p}{p_m} \left( \frac{E_k}{E_{km}} \right)^{1/2} \left( \frac{\dot{m}_{am}}{\dot{m}_a} \right)^{1/2} \right]$$

The subscript m refers to values measured during total calorimetry. With the exception of h, all other variables were measured for every specimen test.

### 3. Evaluation of Data Correlation Factors

Scala's theory relates mass loss rate and model stagnation pressure to the characteristic properties of a material as affected by temperature in the rate controlled regime. Mass loss rate, stagnation pressure, and body radius are interrelated in the diffusion controlled regime and are relatively independent of temperature. The relationships may be conveniently correlated on a graph of  $\dot{m} \sqrt{\frac{R_B}{P_e}}$  vs  $T_w$ . The mass rates per unit area computed by differences must be "normalized" with respect to body radius and stagnation pressure in order to be represented on such a graph. The normalization of the mass rate data with respect to pressure consists of introducing that pressure appropriate to a given specimen as determined from the model stagnation pressure data.

The problem of applying an appropriate model radius is a little more involved. Geometrically, the flat faced specimen has an infinite radius. However, since the body radius enters such a stagnation point correlation as representative of the local velocity gradient, one can

interpret that parameter in terms of an effective radius. Boison and Curtiss (Ref. 18) have made a thorough experimental investigation of the stagnation point velocity gradients for model configurations varying from hemispheric to flat faced (and cusped). The results of their studies relate the velocity gradient ( $du_e/dx$ ) to the geometry of the models. Therefore, it is possible to construct from the Boison-Curtiss data a graph (Fig. 21) of heat transfer, normalized with respect to that on a hemisphere, versus body configuration. Note that for a flat faced specimen ( $x^*/R = 0$ ), the heat transfer ratio  $\dot{q}_{ff}/\dot{q}_{sph} = 0.637$ . Recalling that the heat transfer rate to a body varies inversely with the square root of its radius, it is a simple calculation to show the effective radius of the flat faced specimen to be 2.46 for  $R_{sph} = 1$ .

$$\frac{\sqrt{R_{sph}}}{\sqrt{R_{ff}}} = \frac{\dot{q}_{ff}}{\dot{q}_{sph}} = 0.637$$

assigning  $\dot{q}_{sph}$  a value of unity,

$$R_{ff} = \frac{1}{(0.637)^2} = 2.46$$

Simple computations are applicable to flat faced cylinders of different sizes. Note that the theoretical analysis in Sect. II C treats with this problem by replacing  $R_B$  with the body diameter for flat faced cylinder, thus

$$R_{B_{ff}}(\text{theory}) = \frac{2}{2.46} R_{B_{ff}}(\text{exper.})$$



Finally, it is necessary to correlate the mass rate data with respect to the local flow regime of the model specimens. A portion of the theoretical section of this report deals with the relationships by which the correlations are effected. The basic oxidation relationships derived by theoretical considerations are constructed for what is nominally called high Reynolds number flow. A series of expressions modify the fundamental diffusion controlled oxidation theory for various regimes of flow over a range of Reynolds numbers from  $10^{-3}$  to  $10^{+5}$ . The modification is expressed as a Stanton number ratio, designated  $(C_H \sqrt{Re_s})_{L.R.} / (C_H \sqrt{Re_s})_{H.R.}$ . For convenience, the functional relationship between  $Re_s$  and  $(C_H \sqrt{Re_s})_{L.R.} / (C_H \sqrt{Re_s})_{H.R.}$  has been plotted (Fig. 22). The values of the mass loss rates calculated from the experimental data reflect the flow conditions at which they were obtained. Hence, before they could be compared with theory, it was necessary to divide each value by the appropriate Stanton number ratio corresponding to the Reynolds number of the test flow in which the data were measured.

The Reynolds numbers per foot determined for the facility operating conditions were discussed earlier. Since values of  $Re_s$  /ft. were little different whether computed for frozen flow or for equilibrium flow, an intermediate value to both was used in determining the  $Re_s$  representative of each model size, for each operating condition.

For oxidation in the rate controlled regime, the data for low Reynolds number flow conditions are altered as a function of the effective

pressure of oxygen at the model stagnation point. The effective pressure, treated in Appendix A, can be represented in dimensionless form as a ratio to high Reynolds number pressure (Fig. 23) and used as a modifying factor to rate controlled mass loss data in a manner analogous to the Stanton number factor for diffusion controlled oxidation. In the region where transition between reaction rate and diffusion controlled oxidation occurred an appropriately weighted mean of the two ratio factors was employed.

#### 4. Evaluation of Mass Loss Data

The mass loss data acquired in this program was intended to provide experimental evaluation of Scala's theory of graphite oxidation. In order to demonstrate the universality of the theory, tests were conducted on cylindrical specimens of several sizes under several different conditions of operation. In all, 89 cylindrical specimens were tested. The results of the tests on the various groups of specimens are summarized in Tables 2 and 3.

The useful data obtained from the cylindrical specimens consisted of the difference in length resulting from exposure to the test environment. The differences were obtained from micrometer measurements taken before and after test. Length change at the stagnation point was used in preference to measured mass loss because it was impossible to give accurate consideration to mass lost from the side wall of the cylinder. Typically, the gross mass lost from a cylinder varied between two and three times the mass loss on the stagnation region of the specimen, as calculated from the length change, using the following expression:

UNCLASSIFIED

$$\Delta m = \rho A (\Delta l)$$

It is possible that some mass is driven from below the receding face of a specimen. Hence a comparative evaluation of mass rate based on length change and on mass loss over an area with protected side walls would be informative. Provision for such a comparison was made on the one inch diameter specimens tested during the program. Since the diameter was sufficient, a small insert (1/4" diameter) was press fitted into a centerline cavity in the one inch specimens. Accurate mass losses from the inserts were obtained using a semi-automatic analytical balance. These are included in the data on Table 4 where the ratio of mass loss per unit area based on length change to that calculated from actual mass loss for each specimen is shown. These results are discussed in Sect. III, E.5.

A few specimens showed a measurable decrease in diameter as a result of side wall mass losses. This was especially noticed on the 1/16" diameter models. The net effect of such diametral decrease is a tendency for the heat transfer rate at the stagnation point to increase slightly ( $\dot{q}_0 \propto 1/\sqrt{R}$ ). Hence, mass rates for the longer run times might be expected to be slightly larger.

##### 5. Evaluation of the Rate of Mass Loss

In order to present the results of the tests in a form comparable to the theoretical representation it is necessary to obtain the mass rate of oxidation for incremental temperatures. While it may be possible in theory to evaluate mass rate as a continuous function of surface

UNCLASSIFIED

temperature from motion film records of the tests and time resolved surface temperature recordings, the relatively small dimensional change in the specimen puts a prohibitive penalty on the accuracy attainable. The technique used in this program employed a system of length and time differences.

Specimens were exposed to the test environment for various intervals of time, resulting in incremental differences in length change. The calculation of rate of mass loss per unit area proceeded from taking differences between length losses and times among the various specimens in the following manner:

$$\dot{m}_w = \rho \left( \frac{\Delta t_2}{\Delta t_2} - \frac{\Delta t_1}{\Delta t_1} \right)$$

The calculated mass loss rate is considered to represent that existing at the average temperature for the two test points evaluated, i.e.:

$$(T_1 + T_2)/2.$$

#### 6. Evaluation of Integrated Mass Loss Models

Specimens of both ATJ graphite and of Material "X" were tested to study shape change behavior. Spheres 1/4" and 1" diameter of both materials were exposed in a fixed position and at two rotational speeds; short cylinders of Material "X" were also examined. The latter were studied in two fixed positions, coaxial to and perpendicular to the flow; and at two rotational speeds about an axis perpendicular to the flow.

Evaluation was possible by each of two approaches. First, comparison was possible on a gross weight loss basis. The weight loss from

UNCLASSIFIED

each specimen was determined and recorded (Tables 5-7), and since tests were conducted for different lengths of time, an approximation of mass loss with time was possible. Second, by studying the changes in shape, e.g. (Figs. 24 and 25), one may obtain insight into the corresponding behavior of re-entering particles. To obtain accurate shape change profiles, the ablated specimens were installed on the stage of a Jones and Lamson optical comparator. The projected image, magnified 31.25x was measured to determine the contour to which each shape had ablated. On the magnified scale available, dimensions could be estimated to values accurate to less than .001" (true scale).

#### 7. Evaluation of Surface Temperatures

Many of the surface temperature traces show a "steady-state" temperature which departs markedly from a conveniently uniform plateau. Variations may be explained by any of three mechanisms. It is probable that all three contribute to variations in the trace, and presently there appears no way to determine with certainty the primary cause of a given fluctuation in the trace.

First, one may expect the existence of real variations in the intensity and spectral quality of energy being radiated from the specimen. Local "hot spots" on models have been observed on numerous test runs. These intense pinpoints may well cause modification of the spectral distribution of the radiation during their relatively brief duration. Such "hot spots" are clearly visible in several of the motion pictures.

UNCLASSIFIED

A second source of recorded variation arises from the manual switching of filters on the pyrometer. Failure to act quickly when a build-up in excessive phototube current results in tube saturation and produces an interval during which the response curves are not following the calibrated values. In some cases, these regions could be determined from the original traces, but experience has shown that the tubes do indeed recover rapidly and the extra data reduction effort is not justified.

Finally, there is a possible source of error due to the resolution of the recording instrument. This source of error is potentially most pronounced at the low end of the signal outputs. Thus, when the thickness of the trace masks an apparently small deflection, an error in measurement can affect the reported temperature.

When the plateau temperature reported for the specimen is highly irregular, the best mean value of the temperature was estimated for the interval being investigated. In spite of the several sources of error, it is estimated that the temperatures used depart no more than  $100^{\circ}\text{K}$  from their actual values.

The validity of measured surface temperature was demonstrated dramatically for one ATJ graphite sphere. A tungsten-rhenium thermocouple was imbedded at the center of a one inch sphere tested at the lower enthalpy condition. The thermocouple temperature recorded during the entire test was compared with the two-color pyrometer temperature measured on the surface. The data plot (Fig. 26) shows

a comparatively constant gradient of about  $50^{\circ}\text{K}$  between the surface and center of the sphere after the specimen reached a steady state. Typical surface temperature traces are found on Figs. 27-29.

#### 8. Evaluation of Calorimetric Measurements

Total enthalpy of the test gas was measured for each of the two enthalpy levels at which the facility was operated. The results of the tests, using the total calorimeter have been summarized (Table 8). The evaluation process for data acquired from the calorimeter is a heat balance between a heat exchanger (the calorimeter) and the test fluid (air) after the system has reached steady state operation.

The measured value of model heat transfer (Tables 9 and 10) are significant because they reflect the changes in model size and configuration (Fig. 30). In comparing the measured heat transfer rates to an existing empirical correlation equation by Scala (Ref. 20), for flight stagnation heat transfer rates, the values measured in the Arc Tunnel were found to be significantly lower than the values predicted by the empirical equation. The difference in heat transfer rates may be attributed to differences between the environment of the Arc Tunnel and the flight environment for which the correlation equation was derived. The equation is based on analyses of the region of high Reynolds number continuum flow. The flow provided in the tunnel was at low Reynolds number. Indeed, facility conditions are such that the boundary layer may be fully merged with the shock for all test condition runs, as inferred by a calculation of theoretical boundary layer thickness and shock

detachment distance. This indicated departure from flow conditions represented by the heat transfer correlation and exemplified by the thick model boundary layer which could produce a reduced enthalpy gradient at the wall, probably contributes to the lower (than theory) measured heating rates.

The diminution of heat transfer may be augmented by the frozen flow which the tunnel has given evidence of producing. Although the model bow wave recompression will affect the gas state, it is not unreasonable to expect a non-equilibrium state in the model shock layer. Under these conditions the chemical reactions within the boundary layer among the diffusing species could result in incomplete recombination at the model calorimeter surface. Further, although the calorimeter material (copper) has high catalytic efficiency, minute oxidation of the surface could appreciably decrease this efficiency, again resulting in a decreased heat of recombination. The measured rates of heat transfer were below those predicted by approximately 35%.

With the exception of the 1/4" diameter spherical calorimeters, all values were plotted directly as calculated from the recorded traces by the method of Sutton and Miksch (Ref. 14). Aside from experimental errors, it has been ascertained that the values for the spherical one inch specimens are conservative by 7%. In attempting to determine apparent discrepancies in the heat transfer to the 1/4" spherical calorimeters, attention was directed to the size of the calorimeter insert with respect to the dimensions of the sphere. A 1/8" diameter slug was installed in



a 1/4" sphere, with its face contoured to form the continuous spherical surface. Since it represents such a large portion of the entire exposed hemisphere it must also sense local heat transfer rates which are less than those at the stagnation point. Hence the response of the thermocouple represents an average heat rate less than that incident at the stagnation point. The distribution of heat transfer rates on a spherical surface is well known. Indeed, as part of this program, the distribution on a one inch sphere was measured (Fig. 31). The mean heat rate recorded by the calorimeter was employed in the determination of the maximum, or true stagnation heat transfer rate. It was found that the experimental distribution of the heat transfer could be approximated reasonably by a Gaussian type expression:

$$\dot{q} = \dot{q}_o e^{-\beta \pi \ell}$$

which, when doubly integrated gave the average heat transfer rate:

$$\dot{q}_{av} = \frac{\int \int \dot{q}_o \ell \, d\ell \, d\theta}{\int \int \ell \, d\ell \, d\theta} = \frac{2 \dot{q}_o}{(\beta \pi \ell)^2} \left[ 1 - \beta \pi \ell e^{-\beta \pi \ell} - e^{-\beta \pi \ell} \right]$$

Using information from an experimental study of heat transfer to a hemispherical surface (Ref. 21) the constant  $\beta$  (dimension =  $L^{-1}$ ) was evaluated. The resulting equation was then used to calculate a stagnation point heat transfer rate from the "average value" reported by the calorimeter. The analysis showed that the average value was 53.5% that of stagnation. Similarly, on the one inch sphere, the average value was 93% that of stagnation with a 1/4" diameter slug insert.

The profile of heat transfer to a sphere (Fig. 31) was obtained by using several spherical calorimeter bodies tested on separate runs. The first has 1/4" diameter inserts installed at 0° (stagnation point), 60° and 120°. Others included 30°, 45° and 90°. The results of the tests, when combined, formed the complete profile. Note that several positions were tested twice and repeated the local value with fidelity. Considered collectively, the heat transfer measurements show some scattering which may be attributed to calibration error, thermocouple attachment variations, and trace readout error.

In spite of a reasonable agreement of heat rates obtained with the RTV silicone rubber coated 1/16" copper calorimeters with the empirical curve, serious doubts were raised as to the effectiveness of the RTV in inhibiting lateral heat input. As a check of this, several 1/4" copper inserts were coated with the silicone rubber and tested. Their reported heat transfer rates were comparable to those measured with calorimeters of 1/4" diameter phenolic nylon containing 1/8" diameter copper inserts, thus confirming the validity of the technique.

As a consequence of ablation, the spherical oxidation specimens gradually altered in shape. The departure from a sphere was most pronounced on the fixed specimens. To determine what effect the shape change had produced on the incident heat transfer rate, calorimetric bodies were made in the shape of the ablated spheres. A stagnation point calorimeter was installed and measurements indicated that on bodies which had suffered the maximum erosion, the effective heat transfer rate had decreased to the equivalent of a flat faced specimen.

The calorimeter bodies duplicating the ablated specimen were prepared by molding. First a plaster shell was formed around the ablated graphite sphere. In turn, a casting of RTV silicone rubber was made using the plaster shell. Before the rubber was poured, a dummy insert with connecting rod was affixed to the mold to provide for the later insertion of the copper insert and thermocouple. The casts faithfully reproduced all surface irregularities, so that the RTV calorimeter body was an exact replica of the original ablated graphite specimen.

## E. DISCUSSION OF RESULTS

### 1. Oxidation of ATJ Graphite

Once the numerous mass rate values had been computed (Tables 11 - 16), they were plotted as a function of reciprocal temperature with the objective of determining the activation energy (E) and the reaction rate coefficient ( $k_o$ ) for the equation.

$$\dot{m} = k_o \sqrt{P_e} e^{-E/RT}$$

For pure reaction rate controlled oxidation, the given equation can be rewritten in the form of the integrated Arrhenius equation, which requires that the natural log of  $\dot{m}'$  vs  $1/T$  shall be a straight line.<sup>1</sup>

Examination of the data plotted in this form (Fig. 32) revealed that they did not follow the predicted form of the Arrhenius equation.

1. In this report, direct reference to unadjusted mass rate data employs the symbol  $\dot{m}'$ ; corrected data is denoted by the conventional  $\dot{m}$ .

Since it was fully expected that some of the specimens would have been oxidized under conditions of diffusion control, a departure from a linear plot was not surprising. The deviation obtained tended to confirm the presence of the diffusion controlled activity. Coupled with the scatter of the data points, the narrow range of mass rates for which linearity might be assumed made it difficult to plot a straight line which could be considered properly representative of the reaction. In lieu of an estimated slope of great uncertainty it was decided that a value would be chosen which was typical of graphite materials. The slope is a measure of the activation energy. Consultation with the available literature led to a choice of 44.0 kilocalories as a good representative value. A straight line of this slope was constructed to pass through the bulk of data points estimated to be predominantly reaction rate controlled. Based on the constructed line, the reaction coefficient was determined:

$$k_o = 4.42 \times 10^5 \text{ lb./sec. ft.}^2 \text{ atm.}^{1/2}$$

The equation for the reaction rate oxidation of graphite thus determined, was combined with the theoretical diffusion controlled oxidation expression using the transition equation derived in the theoretical portion (Sec. II C. eq. 30). Curves were computed for each type specimen and test condition from the combined expressions (see Appendix B) and were overplotted on the data points (Figure 32). It was immediately evident that in the diffusion controlled regime, the data points were high with respect to the theory. With the knowledge that the test facility provided environments which were not characterized by high Reynolds number flows, these differences

were expected.

The theory developed by Scala (Ref. 9) to describe the oxidation of graphite was based on flow of high Reynolds number. In this report, that theory is extended to regions of low Reynolds number and to molecular flow. The extension provides that data of both rate controlled and diffusion controlled oxidation must be adjusted in order to compare it with high Reynolds number continuum based theory, or vice versa. In their final forms, the modifications consist of applying a Stanton number ratio correction factor to data in the diffusion controlled regime or an effective pressure ratio correction factor to data in the reaction rate controlled regime. Both these factors are functionally dependent upon the Reynolds numbers corresponding to the test flow conditions. From calculated nominal values of Reynolds number per foot, corresponding to the various test conditions, the shock Reynolds number for each model was determined. The appropriate correction factors for either oxidation process were then obtained from the graph of Stanton number ratio vs.  $Re_s$  (Figure 22) or the graph of  $\left[ p_{O_2} / .21 p_{\infty} V_{\infty}^2 \right]$  vs.  $Re_s$  (Figure 23). Data point values must be divided by the correction factors determined from these graphs.

In examining the mass rate plotted against  $1/T$ , it may be seen that many of the points lie near the transition region of the theory curves. For these points, correction factors are needed which are intermediate between those appropriate for diffusion control and for rate control. To accomodate these points, the theoretical expressions were examined

and the contribution of each factor was weighted for each point in the transition region. Refer to Appendix C. Once the appropriate correction factors were determined for all regions containing data, they were applied, each to its corresponding datum point, to determine the mass rates in terms of Scala's original theory (Tables 11-16).

A second graph of  $m$  vs.  $1/T$  was prepared showing the adjusted data overplotted on the theoretical curves (Figure 33 and Appendix B, eq. 4). It may be seen that the diffusion controlled data are decreased and conform reasonably well to the predicted performances. In general, the rate data are increased in value, although the changes in position with respect to the theory curves are less pronounced because of the near-vertical slope of the reaction rate portions of the curves.

It is interesting to note that when the data are corrected to correspond to the theory, the shift of reaction rate data may be sufficient to warrant the construction of a new, displaced, slope for the activation energy and alteration of the weighting factors in the transition region. Extrapolated to its extremity, this becomes an iterative process which ceases when the required degree of accuracy has been attained. In the present case, the scatter of the data points is sufficient to make further approximations unjustified.

Having shown that the mass loss rate data does indicate reasonable concurrence with the theory, the final step was to prepare a plot of the data normalized with respect to pressure and specimen radius. However, it was evident that data corrected to correspond to the theory

curves would tend toward a more crowded pattern. In order to better examine the relative correspondence of theory and experiment for the individual test conditions, the theory curves were modified as the correction factors dictated, while the original mass rate data were normalized with respect to pressure and body radius only, (Tables 11-16). The results were plotted ( $\dot{m}' = \sqrt{R_B/P_e}$  vs.  $T_w$ ; Figure 34) to provide a clearer picture of the degree to which theory and experiment agree (Appendix B, eq. 7).

Finally, the appropriate correction factor was applied to each datum point normalized with respect to pressure and specimen radius (Tables 11-16), and the computed results were incorporated into a plot ( $\dot{m} = \sqrt{R_B/P_e}$  vs.  $T_w$ ; Figure 35) in which the theory curves remain in the form calculated from the unmodified continuum theory (Appendix B, eq. 6). The theoretical curves predict a dependency of data on the body size only in the reaction rate controlled regime but independence with respect to both pressure and body size in the diffusion controlled regime. The methods employed in reducing the data are described in detail in Appendix C.

Aside from the scatter of data it may be seen that there is indeed a trend which places the 1/4" specimen data between the majority of one inch and of 1/16" specimen data. In addition, the data for all three model sizes are in approximately the proper relation to one another as predicted by the theory. Note also that the  $6.2 \times 10^{-3}$  lb./ft.<sup>3/2</sup> sec. atm<sup>1/2</sup> plateau is placed in the midst of the data points corresponding to diffusion controlled oxidation.

The experimental results assuredly concur with the theory when a mean value of the data is considered. The difficulty of controlling precisely the operating conditions during the course of a run produces appreciable scatter. Hence the exact reproduction of the theory curve by experimental evidence is exceedingly difficult, although continued experience with this type of experiment has led to improvements in performance.

## 2. Integrated Mass Loss - ATJ Graphite

To obtain integrated mass loss data and shape change information, tests were made on spherical specimens, (a) fixed with respect to the flow and (b) rotating at two different speeds about an axis normal to the flow. Data were obtained from measurement of the profiles of specimens exposed for incrementally varied time intervals and from determinations of the gross loss of mass experienced by each. Profiles were obtained from measurements of the images projected by an optical comparator.

Profiles of the several initially one inch diameter fixed spheres were constructed to scale (Figure 36). From these, a plot of dimensional change vs. central angle was constructed for each of the increments of test time (Figure 37). The central angles were measured with the stagnation point at the zero angle position. It was also convenient to construct a plot of dimensional change vs. time for particular central angles (Figure 38). Time was used as a parameter for this graph.

Examination of the length loss vs. central angle plot indicates that the removal of mass from the specimen reflects the variation of heat



UNCLASSIFIED

transfer to the spherical surface (Figure 31). It may be recalled that the theoretical portion of this study postulates a constant effective heat of ablation ( $q^*$ ). The experimental data obtained on the spherical specimens suggest that this is a valid assumption, since, if  $q^*$  is to be constant, the rate of heat transfer experienced at a point must be a constant ratio with respect to the mass lost at that point. Of course, as the model changes shape the level of heat flux will also change, decreasing as the spherical surface becomes flattened and increasing as it becomes reduced in size.

Profiles were constructed for the 1" diameter spheres rotated at 2 radians per second ( $\omega = 2 \frac{\text{rad.}}{\text{sec.}}$  Figure 39), for which sufficient time variation in the tests provided adequate data to define trends in performance. Three intervals of test time were available. The time dependent graph of length change (Figure 40) does not exhibit the double inflection that was observed on the stationary spheres, within the accuracy of the measurements. One may infer that the effective heat transfer rate on the stagnation region, being considerably reduced because model rotation distributes the accepted heat more equitably, prevents the increase in length loss from progressing fast enough to clearly define a change in slope. A tendency of the slope to decrease at the longer test times reflects the gradual flattening of the equatorial region of the sphere. The cross plot of length loss vs. central angle (Figure 41) shows the equatorial flattening more clearly. The final shape assumed by the rotating specimens was that of a prolate spheroid.

UNCLASSIFIED

The progression in shape with central angle again relates to the heat transfer curve, as was noted for the fixed spheres.

Similar data were acquired for the 1/4" diameter spheres, both stationary and rotating. Complete profiles of the stationary specimens (Figure 42) were constructed, and the plots of length change vs. time (Figure 43) and of length change vs. central angle (Figure 44) exhibit characteristics similar to those of the one inch spheres. One 1/4" diameter stationary specimen (not included on the preceding graphs) was tested for 398 seconds, resulting in virtual destruction in that time. Only a slender annular piece remained, attached to the ceramic model support.

When profile measurements of the 1/4" diameter spheres at two rotational speeds were made, it was found that the dimensional changes were essentially identical. Hence, the profile measurements were averaged and a composite profile was constructed (Figure 45). Despite the similarity in observed dimensional change, it is interesting to note that positive differences in mass loss were detectable. These will be discussed later. With only two increments of test time available, the length of the 1/4" rotating spheres were not plotted as a function of time. However, a plot of the measure of length vs. central angle (Figure 46) shows that length loss decreases as one progresses from the equator toward the pole ( $\theta = 0^\circ \rightarrow \theta = 90^\circ$ ), similar to that which was observed on the one inch spheres, but to a lesser degree.

Finally, a graph of integrated (gross) mass loss from the various

spherical bodies was prepared (Figure 47). Note that for clarity, the mass loss scale used for the one quarter inch specimen data is 16 times that used for the one inch specimen data in that their values were increased in inverse proportion to the 1/4" diameter spherical surface area compared to that of the one inch spheres. In several instances there were insufficient data points to define the shape of a curve. In these cases, the illustrated curve was constructed in a shape analogous to those which were well defined.

It may be seen that for both size models, there is a definite and consistent trend for the mass loss to decrease as the speed of rotation increases, although at a diminished rate at the higher speeds of spin. This suggests a method of approximating the degree to which spin rate will affect the effective rate of heat transfer. It is evident that the effect may be somewhat variable with time, since the bodies ablate to different shapes when fixed than when spinning. Assuming the plotted mass losses to be directly proportional to the heat transfer at any time ( $q^* = \text{constant}$ ), the apparent reduction in  $\dot{q}$  (spin factor) was determined (Figure 48) for the two spin rates employed. The value of  $\dot{q}$  on the fixed sphere was taken as unity.

Note that the ratios obtained tend to increase with time. This is obviously due to the decreased heat transfer rate (the reference  $\dot{q}_{\text{sph}}$  of our ratio) evolved on the fixed sphere, as it flattens during ablation. Later in time, the more slowly ablating rotators will also develop large flattened equatorial zones and hence the slope may be expected to decrease.

Given time for the fixed sphere to be ablated to beyond the original center, the slope would probably reverse, since the transverse diameter of the fixed specimen would start to decrease.

If one assumes the ratios may be extrapolated to zero time (dotted lines), the relative value of the spinning sphere to the fixed sphere, before the latter has suffered appreciable shape change, may be estimated. These values were obtained for both size spheres, and a cross plot of the ratios vs. the model rotation speeds (Figure 49) shows that the ratios quickly approach constant values at little more than  $\omega = 4$  radians/second.

There is yet another method of considering the effect of rotation. That is, one may look at the local mass loss per unit of area as reflected by local dimensional changes. At any instant after time zero, the stagnation point of the fixed sphere will have receded more than the stagnation "point" (of these, there are an infinite number) on the rotating sphere. To examine this method of presentation, the stagnation point length loss data of the fixed and the rotating spheres were plotted (Figure 50). Ratios of the length lost by the rotating sphere to the length lost by the fixed sphere for each size specimen were computed and plotted as a function of time (Figure 51). There was insufficient evidence to separate effects due to differing rotational speeds but the time dependence of the ratios were again evident. The similarity in shape of the two curves is fortuitous; considering the scatter of the experimental data, differently shaped curves would have

~~CONFIDENTIAL~~  
~~RESTRICTED DATA~~

UNCLASSIFIED

been much more probable. Nevertheless, one may attribute the time dependency of the ratios to the different deformation experienced by rotating and fixed spheres.

It appears that sphere size is also a factor. The same conclusion may be drawn from the ratios obtained for gross losses in mass (Figure 48). Note that both methods, of presenting the results, mass and stagnation length loss, indicate a higher ratio for the smaller spheres for long exposure times, and both indicate a "cross-over" in the ratios for 1/4" and 1" spheres at about 250-300 seconds.

Either method can be used to help predict performance of a rotating sphere of a given size, if one has information on the performance of a stationary one. The former permits estimation of the net loss in mass and the latter, estimation of the equatorial dimensional change. Obviously, either should be deducible from the other, but the connective relationships are not easily evaluable.

### 3. Oxidation of Material "X"

After the individual test results had been paired and the mass loss rates determined (Tables 17-21), an Arrhenius plot of  $\dot{m}$  vs  $1/T$  was constructed (Figure 52) which exhibited a pattern whereby the data fell within a narrow, essentially linear band. There was no positive evidence that diffusion controlled oxidation had developed.

Assuming the data to be primarily in the reaction rate controlled regime, a slope was constructed through the data points and the reaction rate coefficient ( $k_0$ ) and the activation energy ( $E$ ) were

~~CONFIDENTIAL~~  
~~RESTRICTED DATA~~  
~~RESTRICTED DATA~~  
~~RESTRICTED DATA~~

UNCLASSIFIED

**UNCLASSIFIED**

determined. The reaction equation derived from the experimental data was

$$\dot{m} = 2090 \sqrt{\frac{R_B}{P_e}} e^{-19700/T}$$

An approximate analysis (Appendix D) provides conservative prediction of the plateau established when diffusion processes control the oxidation:

$$\dot{m} \sqrt{\frac{R_B}{P_e}} \approx 8.5 \times 10^{-3} \text{ lb/ft}^{3/2} \text{ sec-atm}^{1/2}$$

This and the empirical rate controlled equation were combined using the transition equation (Section II C, eq'n 30) to provide a means of calculating the theoretical oxidation curves for Material "X" (See Appendix B). These were overplotted on the experimental data points (Figure 52) where it may be seen that in general, the data did not depart markedly (beyond experimental scatter) from the "theory" curves.

However, since the data were acquired under conditions other than high Reynolds numbers, the values obtained required adjustment in order to be represented as equivalent high Reynolds number mass losses for proper comparison to the theory. The required modifications were made (Tables 17-21) and with the exception of the 1/4" models in the short nozzle, all data were corrected as predominantly rate controlled. Hence the appropriate effective pressure ratio corrections (Figure 23), as dictated by the corresponding shock Reynolds numbers,

**UNCLASSIFIED**

~~CONFIDENTIAL~~  
~~RESTRICTED DATA~~

UNCLASSIFIED

were applied. Since the 1/4" specimens in the short nozzle appeared to fall in a transition region, the weighting factors applied depended upon the extent to which each process, rate control and diffusion control, contributed during the transition. The factors were applied to the mass rate data and the resulting modified data were plotted on a second graph of mass rate vs. reciprocal surface temperature, (Figure 53). It may be seen that the corrections applied did not produce a major shift in the rate data with respect to the theory curves. Again it may be emphasized that when a higher degree of accuracy is justifiable, the reaction rate curve may be iterated and the individual data points adjusted by new correction factors consistent with the altered theoretical curves. As with the ATJ graphite, no iteration was applied to the Material "X" data.

The mass rate data were normalized with respect to pressure and model size and the corrective values were applied to the normalized data (Tables 17-21). The final comparison was a graph of the normalized mass rate data plotted against the corresponding temperatures (Figure 54). The empirical-theory curves are shown on the same graph. It may be seen that the data correspond reasonably well with the "theory" curves through the reaction rate regime. There is some disagreement between the two with regard to transition to the diffusion controlled regime. A number of data points appear to project the reaction rate to values greater than the  $8.5 \times 10^{-3} \text{ lb/ft}^{3/2} \text{ sec-atm}^{1/2}$

~~CONFIDENTIAL~~  
~~RESTRICTED DATA~~  
~~UNCLASSIFIED~~

UNCLASSIFIED

~~CONFIDENTIAL~~  
~~RESTRICTED DATA~~  
~~RESTRICTED DATA~~ UNCLASSIFIED

conservatively predicted for diffusion controlled activity (Appendix D). Indeed, the experimental data does not appear to indicate the incipience of diffusion controlled activity up to the limit of recorded values.

#### 4. Integrated Mass Loss - Material "X"

Spherical specimens of Material "X" analogous to those of ATJ graphite were tested under corresponding conditions. In addition, several short cylindrical specimens were exposed to the simulated re-entry environment. Fixed cylinders were oriented both coaxial to and perpendicular to the flow. As with the spheres, the tumbling cylinders were tested at two rates of rotation (end over end). The axis of rotation was perpendicular to the flow. Figure 55 shows the full variety of "X" specimens, one of each type (including the mass rate specimens) employed during the experimental program.

From profiles obtained using the optical comparator (Figure 56), the length losses of the one inch fixed spheres at two enthalpies were determined and plotted as a function of central angle (Figure 57). Both sets of curves exhibit the double inflections, indicating that the length changes are dependent upon the distribution of heat transfer across the surface of a specimen. With only two increments of time, an accurate representation of the time dependent variation of length loss is not assured; however, for illustrative purposes, curves are drawn (Figure 58) showing trends analogous to those determined for the ATJ graphite with respect to the stagnation point length changes. There is no reason to believe that the general shape of the time dependent

~~CONFIDENTIAL~~  
~~RESTRICTED DATA~~  
~~RESTRICTED DATA~~ UNCLASSIFIED  
1051



~~CONFIDENTIAL~~  
~~RESTRICTED DATA~~ UNCLASSIFIED

behavior of Material "X" differs drastically from that of the ATJ.

Since so little change in radial length was observed for the one inch rotating spheres of Material "X", even after nearly 800 seconds of exposure, the enlarged profiles illustrated on Figure 59 show only the maximum change as compared to the original contour. The actual incremental radial length losses for the rotating spheres, based on profile measurements are plotted in Figure 60. A comparison with the stationary sphere (run at the corresponding flow conditions) is made on Figure 61 for the stagnation point location. The large difference in radial length loss which shows up in this comparison does not also apply to the integrated mass loss since a great deal more surface is affected on the rotating spheres (Figure 67).

The 1/4" diameter spheres, both fixed and rotating, were also measured and profiles were prepared (Figures 62 and 63). Based on the profiles, graphs were constructed depicting radial length loss as a function of central angle (Figures 64 and 65). When the time dependency of stagnation point length change for fixed and rotating 1/4" spheres was plotted (Figure 66), it was necessary to construct approximations of the curve shapes through the limited number of data points. Again, it is evident that stagnation point length change comparisons do not represent those for integrated mass loss (Figure 67), although certain correlations can be made.

To summarize, the radial length measurements are subject to some error because of the irregularities of the ablated surfaces of Material "X"

~~CONFIDENTIAL~~  
~~RESTRICTED DATA~~ UNCLASSIFIED  
Atomic Energy Act of 1954

~~CONFIDENTIAL~~  
~~RESTRICTED DATA~~ UNCLASSIFIED

(Figure 68). In addition, the time resolved length change curves, constructed through two or at most, three data points are not necessarily representative -- they are contoured in a form analogous to those which were obtained with the ATJ specimens. Thus the question of whether the integrated mass loss data obtained on the spherical specimens tend to confirm any of the observations with regard to the radial length changes is one which must be considered within the limitations of the relatively small number of data points obtained. Total (integrated) mass loss, plotted as a function of time (Figure 67) for both size spheres -- fixed and rotating, depicts the actual mass losses of the 1/4" spheres multiplied by the ratio  $A'/A$  (surface area of a 1" sphere divided by that of a 1/4" sphere) to allow presentation of both sets of data to a comparable scale. Note that the normalized mass losses are approximately two to one, which are proportional to the heat transfer rates applicable to the two different sizes of spheres (Table 10). They also correlate well when compared on the plot of  $\dot{m}\sqrt{R_B/P_e}$  vs  $T_w$  (Figure 54), the steady state surface temperatures averaging about 200°K higher for the 1/4" spheres ( $R_B = .125/12$  ft.) in the region which is clearly reaction rate controlled.

In similar manner to the comparison plot of  $\dot{q}_r/\dot{q}_f$  vs time (Figure 48), constructed for ATJ graphite spheres where  $q^* = \dot{q}/\dot{m}$  is considered to be constant, the ratios of  $\Delta m_r/\Delta m_f$  for Material "X" spheres, taken directly, are plotted against time to show that the trends are

~~CONFIDENTIAL~~  
~~RESTRICTED DATA~~ UNCLASSIFIED  
Atomic Energy Act of 1954

~~CONFIDENTIAL~~  
~~RESTRICTED DATA~~

UNCLASSIFIED

significantly different and that the  $q^*$  for "X" is probably not a constant for these conditions (Figure 69).

Finally the results of the short cylinders ( $l/d=2$ ) were plotted in terms of mass loss versus time (Figure 70). In terms of the maximum time of test, they may be ranked according to the mass loss which each incurred. The cylinders placed in a fixed position with axis perpendicular to the flow lost the most mass. The next greatest mass loss was sustained by the cylinder tumbling at  $\omega = 1$  rad/sec. followed by that having an  $\omega=2$  rad/sec., entirely consistent with all previous comparisons. Least total mass was lost from a cylinder mounted coaxial to the flow ("cigarette"). Again, based on the ATJ spheres for illustrative purposes, the cylinders were assumed to have doubly inflected slopes. The graph suggests that mass losses from the tumbling cylinders may be compared to those of stationary cylinders with axis perpendicular to the flow in a manner completely analogous to the spheres, as discussed previously.

It is interesting to observe that the coaxially mounted cylinder lost the least mass. Clearly, in spite of the relatively high heat rate one may associate with the one quarter inch diameter exposed face, the net mass loss was diminished because only a relatively small surface area was exposed to the higher heat rate.

To assess the mass loss contributed by the side walls of the coaxial cylinder, the net change along the axis was measured and converted to an equivalent mass for the volume lost assuming no

~~CONFIDENTIAL~~  
~~RESTRICTED DATA~~  
~~RESTRICTED DATA~~

UNCLASSIFIED

~~CONFIDENTIAL~~  
~~RESTRICTED DATA~~

UNCLASSIFIED

diameter shrinkage. It is perhaps surprising to note that about 64% of the mass lost comes from the side wall. This evidence is sufficient to confirm that an idealized one dimensional heat conduction solution predicting material performance for the "cigarette" case would be entirely inadequate.

5. Comparison of Material "X" and ATJ Graphite

The density of ATJ graphite is  $108 \text{ lb/ft}^3$ ; that of Material "X" was determined to be  $134 \text{ lb/ft}^3$ . The evaluation was based on the average of fifteen measurements of weights and volumes of the  $1/4$ " diameter inserts supplied for the test program. These values were used in the reduction of all data.

An obvious inquiry might be whether the rates of mass lost from test specimens of the two materials was proportional to their densities. Inspection of the graph (Figure 71), prepared to illustrate the normalized mass rates of both materials, indicates that such was not the case. The lower density ATJ lost more mass per unit time than did Material "X" below about  $1800^\circ\text{K}$ . The empirical rate equation derived for ATJ graphite,  $\dot{m} = 4.42 \times 10^{-5} e^{-44000/RT}$ , can be compared to the representative "slow" and "fast" reaction graphites referred to by Scala. (Ref. 9). The reaction rate obtained for ATJ falls between them, although it is nearer in value to the "slow" graphite. The activation energy of a material determines the characteristics of the exponential portion of the rate expression. Note that the activation energies of the two materials are similar. Their slopes on an Arrhenius plot would

~~CONFIDENTIAL~~  
~~RESTRICTED DATA~~  
~~RESTRICTED DATA~~  
~~RESTRICTED DATA~~

UNCLASSIFIED

be nearly parallel. Hence the reaction rate coefficients are predominant in determining whether they are relatively "fast" or "slow" in reacting. Clearly, the Material "X" is very slow. Indeed, it has a rate approaching that of pyrolytic graphite. For similar activation energies, the rate is slower as the reaction rate coefficient decreases.

The ATJ graphite develops a well defined region of diffusion controlled oxidation. As temperature increases above approximately 1500°K, a value of mass rate is established which is independent of temperature. The experimental values obtained for Material "X" do not give positive evidence of leveling off within the range of data obtained. Consequently the exponential rise in mass rate of Material "X" crosses the constant, diffusion controlled value for ATJ. Thereafter, as the temperature increases, mass is lost from Material "X" at a rate greater than from ATJ. It is expected that Material "X" might conservatively exhibit a diffusion controlled region, as shown by the curves constructed for  $\dot{m} \sqrt{R_B/P_e} = 8.5 \times 10^{-3} \text{ lb/ft}^{3/2} \text{ sec. - atm}^{1/2}$  (Appendix D). Due to an unforeseen shortage of the smaller mass rate specimens of "X" which developed as a result of the significant difference in oxidation performance experienced between "X" and ATJ, the experiments with "X" were not extended far enough to establish a defined value for diffusion control. Perhaps, in the future this should be done, along with a thorough analytical evaluation of the chemistry of reactions.

For both materials, a comparison of mass lost from the 1/4" diameter inserts of one inch mass rate specimens was made with their

~~CONFIDENTIAL~~  
~~RESTRICTED DATA~~

UNCLASSIFIED

measured changes in length. To put the length and weight losses on a common basis they were both converted to weight lost per unit of area. The results were tabulated (Table 4). It may be seen that the ratio of unit mass loss--based on length, divided by unit mass loss--based on weight, consistently resulted in values of less than one for the ATJ. This result suggests that there was a small amount of mass driven from below the surface of the graphite. In appearance, the texture of the graphite surface became coarsened as a result of exposure to the arc heated air tending to suggest development of a porous surface of decreased density.

The same effect, to a much more pronounced degree, was observed on the surface of Material "X". Indeed, on the comparator enlargements, the profiles of Material "X" specimens were so irregular that frequently the mean surface was poorly defined. Because of the gross porosity of the inserts employed in the one inch diameter Material "X" mass rate specimens, there was a greater scatter in the ratios. Nevertheless, the mean value of the ratios falls below that of ATJ graphite. The relative effect on Material "X" is about 1 - 1/2 times that on ATJ graphite. However, when one compares the general texture of the two surfaces (Figure 68), the severe irregularity of Material "X" suggests that penetration below the mean surface was effected at more localized sites, whereas the penetration of the ATJ graphite appeared to be completely uniform in distribution.

~~CONFIDENTIAL~~  
~~RESTRICTED DATA~~  
~~1054~~

UNCLASSIFIED

RESTRICTED DATA

RESTRICTED DATA

UNCLASSIFIED

With respect to the integrated mass loss specimens (1/4" and 1" diameter spheres) of each material, both stationary ( $\omega = 0$ ) and spinning ( $\omega = 1\&2$  rad/sec), comparisons were made of the losses in radial length and weight sustained by the ATJ graphite and by Material "X". First, the total mass loss equivalent to the volume removed from each specimen was estimated by assuming simple geometries to describe the volume changes. For the stationary sphere, the difference between the volume of a hemisphere and one half the volume of an ellipsoid of revolution was used. For the rotating sphere, a uniform spherical shell of one half the equatorial radius change in thickness was employed. Using the densities for the ATJ graphite and Material "X", the corresponding total mass losses were determined. They compared within a few percent of those actually measured by weighing the spheres before and after test.

The radial length changes sustained by the one inch diameter stationary "X" spheres were taken from the data on Figure 58 and ratioed to corresponding ATJ values from Figure 37. The ratios increase from 0.36 to 0.65 as a function of time to 900 seconds. Thus, the radial length changes of ATJ graphite are always greater than those of Material "X", but the relative loss becomes less with increasing time. On performing such an exercise, one can see that these values are consistent and check with the mass rate curves (Figure 71). The increase in ratio can be attributed to two factors:

- (1) The shape change (flattening) of ATJ spheres is more severe. Consequently a decrease in heat transfer to the surface

RESTRICTED DATA

RESTRICTED DATA

1054

UNCLASSIFIED

CONFIDENTIAL

RESTRICTED DATA

UNCLASSIFIED

is experienced sooner.

(2) As test time is increased the ATJ graphite performs longer in the diffusion controlled regime while "X" continues to perform along the rising rate controlled curve. The observed temperatures ( $\sim 1700^{\circ}\text{K}$  for ATJ;  $\sim 1820^{\circ}\text{K}$  for "X") are such that the mass rate curves do not cross. Therefore, consistent with the actual measurements, the ratios appear to approach unity.

A similar examination of the two materials can be conducted for the rotating spheres. For example, when considering the one inch diameter spheres, the ratio varies from 0.32 to 0.22 as time increases from 200 to 900 seconds, (Figures 61 and 40). Casual inspection might suggest that the results of the spinning spheres are inconsistent with those obtained for the stationary spheres. However, it should be recalled that Material "X" displays a surge of lost material during the very early part of each test. Thus, the ratio should be expected to decrease as the mass rate from Material "X" falls to a more uniform, "steady-state" value. Note that the initial surge of lost material is confirmed by the mass loss data vs. time curves for Material "X" (Figure 67).

Study of the results obtained from the one quarter inch diameter spheres, although based on a more limited number of test points, indicates that the trends observed with the larger spheres persist. On comparing the data for both the stationary and the rotating spheres (Figures 43, 46 and 66), one finds that for the longer exposure times, "X" loses more radial length than ATJ. This is consistent, since

CONFIDENTIAL

RESTRICTED DATA

UNCLASSIFIED



the smaller spheres experienced surface temperatures which are higher than the cross over temperature found on the comparison plot of the mass rate parameter (Figure 71).

Total mass losses were also compared. For the stationary spheres, an increase of ratio (mass loss of "X"/mass loss of ATJ) was again noted. The ratio ranges from 0.36 at 200 seconds to 0.74 at 900 seconds. Hence, the results are approximately the same as those based on the radial length change ratios.

However, in the case of the rotating spheres, the weight loss surge was relatively more predominant. Consequently (for the one inch diameter) the ratios gave a maximum at approximately 400 seconds and thereafter declined.

While the ATJ graphite and Material "X" did not ablate in identical modes, in general each material is self consistent when considered with respect to weight loss and dimension change. The peculiarity of Material "X" in exhibiting a large loss of material for a short period during the early portion of test exposure is interpreted to be the principal cause of the differences in performance between the two materials, exclusive of those variations which are associated with their oxidation mass rate behavior as illustrated in Figure 71.

#### IV. SYSTEMS STUDY

##### A. INTRODUCTION

Appropriate flight trajectory, heat transfer, heat conduction and mass transfer equations have been incorporated into an IBM 7090 computer program which enables the re-entry behavior for specific shapes and materials of interest in this study to be predicted. The effects of variable drag coefficient, fragment weight and shape change on the flight trajectory have been included. Two specific fragment shapes may be analyzed one-dimensionally:

- (1) a rotating sphere whose actual behavior is assumed to be simulated by a monotonically shrinking sphere experiencing an average heat and mass transfer which is some fraction of the stagnation value uniformly distributed over the spherical surface, and
- (2) a cylinder whose axis is aligned with the local velocity vector (zero angle of attack) experiencing a uniform heat and mass transfer on its front surface which is a spherical segment whose radius of curvature equals the diameter of the cylinder (or such other radius as may be more suited to a specific analysis) and remains constant while the length of the cylinder diminished during re-entry.

Data input required include the following:

- (1) re-entry velocity, path angle and altitude.
- (2) thermal conductivity, specific heat as a function of temperature and density.
- (3) activation energy and specific reactivity.
- (4) selection of spherical or rectangular coordinates (sphere or

cylinder shape).

- (5) initial dimensions of sphere and/or cylinder.
- (6) appropriate averaging coefficient,  $\Phi$ , which modifies stagnation heat and mass transfer.

Data output includes:

- (1) instantaneous temperature distribution through the material.
- (2) instantaneous mass loss rate, heat transfer rate, and weight of the body.
- (3) instantaneous radius of sphere and length of the cylinder.
- (4) atmospheric properties such as stagnation pressure and free stream Reynolds number.

In addition to the one-dimensional idealizations, a multi-dimensional heat conduction solution involving a moving boundary was programmed for IBM 7094 digital computation. This program enabled a better approximation to be made regarding the shape changes associated with a re-entering sphere and also provided a tool for analytically simulating laboratory shape-change experiments. The program was written in generalized coordinates to allow flexibility in selecting coordinate systems for analyses. The theoretical heat and mass transfer relationships developed in Section II are incorporated as boundary conditions.

#### B. TRAJECTORY CONSIDERATIONS

A Two degree of freedom trajectory was selected to represent the motion of fragments re-entering the atmosphere. The effects of lift forces, rotating earth and winds were neglected. Lagrange's equations of motion were used to determine the differential equations for a point mass in polar coordinates. Figure 72 is a schematic of the

motion of a re-entry fragment. Lagrange's equations state that the rate of change of the generalized momentum is not in general equal to the generalized force, but equal to the force plus the derivative of the kinetic energy with respect to the corresponding coordinates.

Thus, the Lagrange equations

$$\frac{d}{dt} \left( \frac{\partial \bar{T}}{\partial \dot{q}_k} \right) - \frac{\partial \bar{T}}{\partial q_k} = F_k \quad k = r, \theta \quad (1)$$

reduce to

$$m\ddot{r} - mr\dot{\theta}^2 = F_r \quad (2)$$

$$mr^2\ddot{\theta} + 2mr\dot{r}\dot{\theta} = F_\theta \quad (3)$$

in polar coordinates where

$$\bar{T} + 1/2 mV^2 = 1/2 m [\dot{r}^2 + (r\dot{\theta})^2] \quad (4)$$

$$\frac{\partial \bar{T}}{\partial \dot{r}} = m\dot{r} \quad \frac{\partial \bar{T}}{\partial r} = mr\dot{\theta}^2$$

$$\frac{\partial \bar{T}}{\partial \dot{\theta}} = mr^2\dot{\theta} \quad \frac{\partial \bar{T}}{\partial \theta} = 0$$

$F_r$  is the total force measured along the radius vector

$$F_r = D \sin \gamma - mg_o \left( \frac{R_e}{r} \right)^2 \quad (5)$$

$$F_r = \frac{\rho_\infty}{2} V^2 C_{DA} \sin \gamma - mg_o \left( \frac{R_e}{r} \right)^2$$

The negative sign fixes the convention as downward negative.

$$V = [\dot{r}^2 + (r\dot{\theta})^2]^{1/2} \quad (6)$$

$$\sin \gamma = -\frac{\dot{r}}{V}; \quad \cos \gamma = \frac{r\dot{\theta}}{V} \quad (7)$$

Combining equations (2), (5), (6) and (7) yields

$$\ddot{r} - r\dot{\theta}^2 = -\frac{1}{2} \rho_\infty [\dot{r}^2 + (r\dot{\theta})^2]^{1/2} \left( \frac{C_{DA}}{W} \right) g_o \dot{r} - g_o \left( \frac{R_e}{r} \right)^2 \quad (8)$$

$F_{\theta}$  is the moment about the center of the earth.

$$F_{\theta} = - D \cos \gamma (r) = - \frac{1}{2} \rho_{\infty} V^2 C_D A \cos \gamma (r) \quad (9)$$

The negative sign in equation (9) fixes the convention as positive to the right. Substituting into equation (3) yields

$$r \ddot{\theta} + 2 \dot{r} \dot{\theta} = \frac{1}{2} \rho_{\infty} [\dot{r}^2 + (r \dot{\theta})^2]^{1/2} \left( \frac{C_D A}{W} \right) g_0 r \dot{\theta} \quad (10)$$

Equations (8) and (10) have been programmed with appropriate initial conditions as input to define the trajectories used in the systems study. The effects of decreased mass and frontal area as well as variable drag coefficient as described in Section IIC.1 are continuously determined throughout the trajectory.

### C. TRANSIENT HEAT CONDUCTION

#### 1. One Dimensional Idealization

The conduction of heat throughout an arbitrary volume may be written in vector notation as

$$\rho c_p \frac{\partial T}{\partial t} = \nabla \cdot (K \nabla T) \quad (11)$$

where  $K$  is the thermal conductivity coefficient which may be both position and temperature dependent. Figures 73 and 74 illustrate the monotonically shrinking sphere and one dimensional cylinder idealizations which were analyzed in the systems study.

For the monotonically shrinking sphere, equation (11) becomes in polar coordinates

$$\rho c_p \frac{\partial T}{\partial t} = \frac{1}{R^2} \frac{\partial}{\partial R} \left( K R^2 \frac{\partial T}{\partial R} \right) \quad (12)$$

and the following boundary and initial conditions applied:

$$T(R, 0) = T_E$$

$$\frac{\partial T}{\partial R} [s(R, t), t] = \frac{1}{K} \left[ Q_{W_{av}}(s, t) - \sigma \epsilon_W T_W^4 \right]$$

$$\frac{\partial T}{\partial R} (0, t) = 0 \quad (13)$$

It should be noted that the symbol  $s = s(R, t)$  denotes the instantaneous surface position which moves with a velocity

$$\dot{R} = \frac{\dot{m}_{W_{av}}}{\rho_W} \quad (14)$$

and the symbol  $Q_{W_{av}}(s, t)$  represents the suitably averaged heat transferred to the sphere surface and  $\dot{m}_{W_{av}}$  the suitably averaged rate of mass loss.

For the one dimensional cylinder, equation (11) becomes in rectilinear coordinates

$$\rho c_p \frac{\partial T}{\partial t} = \frac{\partial}{\partial x} \left( K \frac{\partial T}{\partial x} \right) \quad (15)$$

and the following boundary and initial conditions applied:

$$T(x, 0) = T_0$$

$$\frac{\partial T}{\partial x} [s(x, t), t] = - \frac{1}{K} \left[ Q_{W_{av}}(s, t) - \sigma \epsilon_W T_W^4 \right]$$

$$\frac{\partial T}{\partial x} [l, t] = 0 \quad (16)$$

In like manner, the symbol  $s = s(x, t)$  denotes the instantaneous position of the surface which moves with a velocity

$$\dot{x} = \frac{\dot{m}_{W_{av}}}{\rho_W} \quad (17)$$

and the symbol  $Q_{W_{av}}(s, t)$  represents the suitably averaged heat transferred to the stagnation region of the cylinder.

Equations (12) and (15) have been included in an IBM 7094 digital computer program together with trajectory equations developed

$$T(R, \theta) = T_o$$

$$\frac{\partial T}{\partial R} [s(R, \theta), t] = \frac{1}{K} [Q_w(\theta, t) - \sigma \epsilon_w T_w^4]$$

$$\lim_{R \rightarrow 0} T = 0 < T < \infty, 0 \leq \theta \leq \pi \quad (20)$$

where  $Q_w(\theta, t)$  is the local heat transferred to the sphere surface and the temperature at the center of the sphere is bounded.

Appendix E contains comparisons of exact and numerical solutions for both equations (12) and (18) utilizing boundary and initial conditions (13) and (20).

#### D. OXIDATION OF SPHERES

Table 22 summarizes the results of the systems study for the idealized monotonically shrinking sphere. Figures 77 through 91 present the results of the parametric study graphically. The material thermal properties which were used in the study are illustrated in Figures 92-94. It should be noted that two sets of chemical kinetic data were used in the parametric study, viz.,  $k_o = 2090$  and  $2.0 \text{ lbs/ft}^2 \text{-sec-atm}^{1/2}$ , and  $E = 31900$  and  $18000 \text{ cal/mole}$ . These represent the results of correlations from experimental data obtained during the final months of the study and the results of an earlier experimental correlation, respectively. The diffusion controlled regime constants of  $8.5 \times 10^{-3}$  and  $6.2 \times 10^{-3} \text{ lbs/ft}^{3/2} \text{-sec-atm}^{1/2}$  also represent final and earlier approximations for Material "X" (See Section II E). For ATJ graphite, the "slow" kinetics (Ref. 9) were

in Section IV. B. and heat, mass loss, and drag coefficient correlations developed in Section II. C.

## 2. Multi-dimensional Considerations

A more exact analysis of the mass loss associated with objects re-entering the earth's atmosphere requires a multi-dimensional formulation of the heat conduction within the object. A multi-dimensional heat conduction subroutine was developed in generalized coordinates to enable several geometric shapes to be analyzed with only minor modifications required in the program.

Figures 75 and 76 illustrate the rotational modes of the sphere analyzed multi-dimensionally. For an isotropic sphere, equation (11) becomes

$$\rho C_p \frac{\partial T}{\partial t} = \frac{1}{R^2} \frac{\partial}{\partial R} \left( K R^2 \frac{\partial T}{\partial R} \right) + \frac{1}{R^2 \sin \theta} \frac{\partial}{\partial \theta} \left( K \sin \theta \frac{\partial T}{\partial \theta} \right) + \frac{1}{R^2 \sin^2 \theta} \frac{\partial}{\partial \phi} \left( K \frac{\partial T}{\partial \phi} \right) \quad (18)$$

From symmetry one may set  $\frac{\partial T}{\partial \phi}$  equal to zero for both cases. The following boundary and initial conditions apply for the sphere rotating about an axis of  $90^\circ$  to the flow direction:

$$\begin{aligned} T(R, \theta) &= T_o \\ \frac{\partial T}{\partial R} [s(R, \theta), t] &= \frac{1}{K} [Q_{w_{av}}(\theta, t) - \sigma \epsilon_w T_w^4] \\ \frac{\partial T}{\partial R}(\theta, t) &= 0, \quad 0 \leq \theta \leq \frac{\pi}{2} \end{aligned} \quad (19)$$

where  $Q_{w_{av}}(\theta, t)$  is the suitably averaged heat transferred to the sphere surface. For the case where the axis of rotation is aligned to the flow direction (or stationary), the following boundary and initial conditions are applied:



used, <sup>2</sup> viz.,  $k_o = 4.47 \times 10^4 \text{ lbs/ft}^2\text{-sec-atm}^{1/2}$ ,  $E = 42,300 \text{ cal/mole}$ .

The average heat transfer and mass loss rate was assumed to be 37.5% of the stagnation value as discussed in Appendix F.

Figure 77 illustrates the percent mass loss for the monotonically shrinking sphere as a function of initial ballistic parameter (or size). It should be noted that the parameter,  $W/C_D A$ , is equal to  $4 \rho_w R/3C_D$  for a sphere and equal to  $\rho_w \ell / C_D$  for the cylinder, and is a more convenient parameter for describing the particle performance characteristics. The particle sizes investigated ranged from 1/16 to 1.0 inches in diameter. Figures 78 and 79 illustrate the instantaneous radii of the re-entering spheres for both the earlier and final experimental values of reaction-rate and diffusion controlled constants for Material "X". For the range of particle sizes investigated the presence of a critical boundary of particles having an acceptable initial size was not found; only slight mass loss was experienced by the Material "X" spheres. A maximum mass loss of approximately 14% was found for a sphere having an initial radius of 1/4 in. and a re-entry angle of  $2.5^\circ$ . Since the percent mass loss, defined as the ratio of the change in particle weight to the initial weight, is inversely proportional to the ballistic parameter and must be zero when the ballistic parameter is zero, the location of a maximum

2. The kinetics determined experimentally for ATJ (Section III E) a short time after the systems studies had been started, differ only slightly from the "slow" kinetic values assigned by Scala, thus an adjustment was deemed unwarranted.

~~CONFIDENTIAL~~  
~~RESTRICTED DATA~~

UNCLASSIFIED

percent mass loss is not surprising. A comparison of the instantaneous radii of a 1/4 in. ATJ and a Material "X" sphere re-entering is illustrated in Figure 80. Figures 81 and 82 illustrate the effect of varying the initial re-entry path angle, and also, the averaging factor which modifies the heat transfer and mass loss rate to the monotonically shrinking sphere utilizing the earlier Material "X" reaction-rate and assumed (graphite based) diffusion-controlled regime data. The percent mass loss increases with increasing angle of re-entry. Since the level of mass loss for this material is low, the fact that the actual averaging factor was unknown introduced no major uncertainty. Figures 83 thru 86 illustrate the trajectory parameters, surface temperatures and mass loss rates associated with the re-entry of a typical ATJ and Material "X" sphere compared in Figure 80. Figures 87 and 88 summarize the heat transfer data for the spherical re-entry objects. In Figure 87, the presence of a maximum in surface temperature illustrates a transition between very small and very large particles (corresponding to low and high values of the ballistic parameter) from a heat conduction point of view. For extreme values of the ballistic parameter, very small objects have negligible heat capacity while the very large particles act as heat sinks. Since the heat transfer rate increases with the ballistic parameter, the presence of a maximum surface temperature is anticipated. The results of a study conducted in Reference 24 found a similar maximum in surface temperature for re-entering stainless steel discs. From Figure 88 it may be concluded

~~CONFIDENTIAL~~  
~~RESTRICTED DATA~~  
~~RESTRICTED DATA~~  
~~RESTRICTED DATA~~

UNCLASSIFIED

that:

- (1) The maximum heat transfer rate increases with increasing re-entry path angle for a given value of the ballistic parameter,  $W/C_D A$ .
- (2) The integrated heat transfer rate decreases as the re-entry angle increases.
- (3) The maximum and integrated heat transfer rate increase with increasing value of the ballistic parameter.

Figure 89 illustrates the maximum temperature gradients experienced during the re-entry of the spherical and cylindrical objects. (Note: Cylinders are discussed in Section IV-E). The small temperature gradients experienced by the spheres suggest that a simpler approach, viz., assuming infinite thermal conductivity or equivalently an isothermal sphere, would have given reasonable values of mass loss for values of the ballistic parameter less than  $4 \text{ lbs/ft}^2$ . Figure 90 illustrates the effect of varying the ballistic parameter on a velocity-altitude-time plot. The effect of varying the initial re-entry path angle for a constant initial ballistic parameter is illustrated in Figure 91.

#### E. OXIDATION OF CYLINDERS

Figure 74 illustrates the idealized cylinder analyzed in the systems study. Table 23 summarizes the results of a parametric study on the behavior of re-entering cylinders. The average heat transfer and mass loss rate was assumed to be equal to the stagnation value associated with a radius of curvature equal to the cylinder diameter. (See

Appendix F). Figure 95 illustrates the percent mass loss as a function of the ballistic parameter. It should be noted that the percent mass loss is inversely proportional to the stagnation region radius of curvature. A maximum percent mass loss of 17% was found for a 1/4 in. dia. cylinder of Material "X" having a length equal to 1/2 in. using the final experimental values of the reaction-rate and diffusion-controlled regime constants. This value is 20% higher than the maximum value found for the monotonically shrinking sphere. Figures 96 and 97 illustrate the instantaneous length of the re-entering cylinders for both the earlier and final experimental values of the reaction-rate and diffusion-controlled regime constants for Material "X". Figures 98 and 99 illustrate the trajectory parameters, surface temperature and mass loss rate for the cylinder experiencing the maximum percent mass loss. Figures 100 and 101 summarize the heat transfer correlations for the earlier cylinders investigated. It should be noted that the surface temperature levels are considerably higher than those of the sphere for approximately the same value of ballistic parameter. For larger cylinders, the possibility of transition to the sublimation regime, although not investigated in this study, could possibly occur and result in considerably higher mass loss.

#### F. OXIDATION OF SPHERES (MULTIDIMENSIONAL APPROACH)

The development of the multidimensional, moving boundary computer program during the latter months of the study enabled an assessment to be made regarding the conservative or non-conservative

CONFIDENTIAL  
RESTRICTED DATA  
UNCLASSIFIED

nature of the monotonically shrinking sphere idealization used to conduct the systems study. Two rotational modes, illustrated in Figures 75 and 76 were investigated, viz., a sphere whose rotational axis is aligned with the flow (or equivalently a stationary axisymmetric sphere) and a sphere whose spin axis is aligned  $90^\circ$  to the direction of flow. These two orientations were assumed to represent the maximum and minimum mass loss situations associated with a re-entering sphere. A comparison of the three re-entry modes for an initial 1/2 in. radius, Material "X" sphere follows:

Mode	(A) Monotonically shrinking sphere (random move- ment of spin axis)	(B) Sphere, spin axis aligned with flow ( $\equiv$ stationary)	(C) Sphere, spin axis $90^\circ$ to flow
Percent Mass Loss	12.4	10.2	3.2
Maximum Surface Temp- erature (Stag. pt.)	$4100^\circ \text{ R}$	$4500^\circ \text{ R}$	$3580^\circ \text{ R}$
Averaging Factor for Heat & Mass Transfer	$\bar{\Phi}_M = \frac{\dot{m}_{w_{av}}}{\dot{m}_{w_o}} = .375$	$\bar{\Phi}_M = 1.0$	$\bar{\Phi}_M = \frac{\dot{m}_w(\theta)}{\dot{m}_w(\theta)_{aligned}} = .375$
Change in radius at stag. pt.	.022 in.	.056 in.	.008 in.

Figure 102 illustrates the surface temperature variation at the stagnation point for each of the above cases as a function of re-entry time. The average heat and mass transfer factor for case (C) of .375 was verified to some extent for the stagnation point during the analytical simulation of laboratory shape-change experiments (See Section V).

CONFIDENTIAL  
RESTRICTED DATA  
UNCLASSIFIED

It may be concluded from the above comparison that the integrated mass loss obtained for the monotonically shrinking sphere, also utilizing an averaging factor of .375, is non-conservative since it predicts a mass loss even greater than the maximum mass loss associated with the multidimensional analysis, (Case B). Thus, the percent mass losses obtained in the systems studies conducted in Section IV-D are non-conservative and should be adjusted downward by using a lower averaging factor in order to produce percent mass losses which are bounded by cases (B) and (C).

UNCLASSIFIED  
DECLASSIFIED

## V. COMPARISON: THEORY-ANALYSIS WITH EXPERIMENT

In the process of attempting to compare computer evaluated predictions of material performance in the facility environment with actual experimental results, evidence was acquired that theoretical expressions describing the flight environment were not directly applicable to the conditions of the test environment. In addition, it was demonstrated that the heat transfer relationships introduced into the computer program were not well suited to the prediction of actual shape change on spherical specimens exposed in an arc facility. Recognition of the differences between the test and flight environments led to a modified comparison of the loss in length of Material "X" cylinders as determined by computer calculation and by experiment in which the analytical expressions were altered to provide a heat transfer rate similar to that measured experimentally. Thereupon the results produced were found to compare quite favorably. While the findings of the comparison should not detract from the validity of the theory as applied to re-entry, it demonstrates the need for the use of actual measured stagnation heat transfer rates in the computations describing performance of materials in a facility test.

The first computer comparisons were made for stationary (or coaxially spinning) ATJ spheres since their behavior was more completely documented experimentally. For these calculations,

UNCLASSIFIED

only the experimentally measured gas enthalpy and model stagnation pressure were introduced into the computer program. All other conditions, such as heat transfer and pressure distributions, were evaluated from the programmed theoretical expressions. The predicted performance of the stationary spheres as obtained from the computer data is illustrated (Figs. 106-108). Performance data were obtained for 600 seconds of exposure. On comparison with the experimental data (Fig. 109) it was found that predicted radial length changes were significantly larger than those measured except for the region near the stagnation point. Refer to Figs. 38 and 107. In addition, surface temperatures were well above those recorded during test ( $T_{w_{\text{exper.}}} \approx 3100^{\circ}\text{R}$  at  $\theta = 0^{\circ}$ ).

A similar disparity existed between computation and experiment for the rotating ATJ spheres. These were programmed for calculation with the same data as was provided for the stationary spheres. One additional factor was introduced. Since the spinning of the sphere reduces the effectiveness of the heat transfer to the specimen, it was necessary to introduce into the computer program a reduced effective heat transfer rate. The choice of the reduced rate was dictated by consideration of both analytical evaluations (Ref. 26) and by evidence from the experiment. A factor of 0.375 based on stagnation point information was used. The predicted performance of the spinning sphere obtained by computer is illustrated



UNCLASSIFIED

(Figures 110-112). The run was evaluated for 600 seconds. As in the case of the stationary sphere, it was found that predicted mass losses were high compared to those actually measured as inferred by  $\Delta R$  measurements (Figure 113). Refer also to Figures 41 and 111. Similarly, surface temperature values exceeded those measured ( $T_{w_{\text{exper.}}} \approx 2900^{\circ}\text{R}$  at  $\theta = 0^{\circ}$ ). It is most significant however, that the relative mass loss curves for both fixed and rotating spheres are similar. This consistency of results suggests that the spin factor introduced for the rotating spheres was of approximately the correct magnitude to predict satisfactorily the effect of rotation.

When one attempts to analyze the differences between prediction and performance, the greater radial length losses obtained on the computer immediately recall a similar discrepancy between measured and predicted heat transfer rates, discussed in Section III D.8. There, it was found that Scala's correlation equation, described as showing good agreement with experimental flight data, predicted heat transfer rates significantly higher than those measured in the test facility. The distributed heat transfer to a sphere has been plotted (Figure 114) showing both the predicted and the measured values to illustrate the differences. It may be seen that, relatively, the heat transfer rates exhibit characteristics which would produce a ratio curve similar to the mass loss ratio curves as defined by radial

UNCLASSIFIED

UNCLASSIFIED

length loss. Note that if the measured values of heat transfer were introduced into the computer program to reduce the mass rates predicted, the prediction would be much more representative of the results actually obtained.

The variation in the relative magnitudes of the heat transfer rates as a function of angle with stagnation point suggests the only obvious area in which the flight theory may not be entirely satisfactory for application to the facility experiment. The forward hemispheric region of the specimens are, according to analytic representation, subject to a heat transfer distribution based on a modified Newtonian pressure distribution. Hence the variation in heat transfer rate is approximately proportional to the cosine of the angle made with the stagnation point. Experimental data suggests that a distribution related to the cosine square of the angle might be more appropriate for the test facility. This tendency seems to be confirmed by the increase through a maximum of the relative values of the heat transfer as one progresses around the sphere toward the  $90^{\circ}$  position (Figure 115). In summary, a better computer prediction of facility performance can be obtained by incorporating a representation of the measured heat transfer rates into a program.

UNCLASSIFIED

[REDACTED] UNCLASSIFIED

This approach was utilized in providing computer prediction of the performance of a cylinder of Material "X". The program evaluated the performance of a cylinder subject to a theoretical one dimensional heat transfer situation (Figure 116). This situation was closely approximated by the one inch mass rate specimens with 1/4" diameter inserts at their stagnation regions, recalling that when a fully exposed axially oriented cylinder was employed, 64% of mass lost was removed from surfaces other than the front face (Sect. III E. 4). The body of one inch diameter was the basic size considered. In the experiment, the body-cylinder acted as an oxidation guard ring, also providing thermal balance, for the 1/4" diameter cylindrical inserts, from which the measured length changes were obtained. Hence, the heat transfer through the insert approximated the one dimensional situation. Since heat transfer is a variable dependent on the nose radius of a specimen in the computer program, an effective radius was chosen for the calculation which led to a rate of heat transfer approximating that to which the experimental specimens were subjected. In turn, the measurements taken from the inserts were considered to be representative of results obtained from an actual specimen, the overall diametral dimension of which was one inch. This is, of course, realistic, since the incident flow distinguishes the specimen as a whole. The other computer input data, gas enthalpy and stagnation pressure, correspond to the conditions of test.

[REDACTED]  
[REDACTED]  
[REDACTED] UNCLASSIFIED

A graph (Figure 117) was prepared on which both computed and experimental length changes have been plotted. A mean curve was passed through the data points and extrapolated linearly to 600 seconds. It is immediately evident that the computed values show better correspondence with the experimental results, although the experimental data indicates a change in length early in time which the computer prediction does not.

Hence, as a result of the comparisons, it may be concluded that the analytical evaluation of the oxidation process presented here, coupled with material properties and trajectory information, may be incorporated into a computer program to yield reliable predictions of actual re-entry behavior. The differences existing between flight environment and the test facility environment require that inputs to the computer program be sufficiently modified to compensate for the discrepancies between flight and facility environments, particularly in the case of heat transfer.

Of particular interest is the apparent departure of the mass loss profile plots relating to rotating spheres of Material "X" from a correspondence to the heat transfer distribution such as occurred on similar rotating spheres of ATJ graphite. Refer to Figures 31, 39, 41, 45, 46, 59, 60, 63 and 65. Note that for "X" the radial length changes are relatively uniform over most of the spherical surface. This is not so for ATJ, and may well be attributable to the differences in

~~CONFIDENTIAL~~

~~RESTRICTED DATA~~

UNCLASSIFIED

thermal properties between the materials. By implication then, for bodies which do not constantly present the same face to stagnation heating, materials which behave thermo-chemically like Material "X" appear to lend themselves to re-entry degradation solution by the simpler one dimensional trajectory analysis--that of the monotonically shrinking sphere--provided, of course, that the proper heat transfer averaging factor ( $\bar{\Phi}_M$ ) is applied. ATJ graphite, for example, and perhaps many materials, require for analyses the more elaborate multidimensional solution. Stationary bodies (or equivalently those spinning about an axis coaxial to the flight direction) should be treated multidimensionally regardless of the constituent material.

~~CONFIDENTIAL~~  
~~RESTRICTED DATA~~  
~~RESTRICTED DATA~~

UNCLASSIFIED

~~CONFIDENTIAL~~  
~~RESTRICTED DATA~~

UNCLASSIFIED

## VI. CONCLUSIONS

Throughout the text of this report the various considerations have been discussed, and where possible, conclusions drawn in context with the discussions. The primary conclusions are, however, summarized as follows:

(1) Over the range of re-entry situations considered, and probably for any shallow re-entry trajectory where the velocity is orbital or less, small objects of Material "X" will not decrease via oxidation mass transfer to an acceptable impact size with respect to the potential radiological hazard. Thus for this material, a critical boundary of minimum initial particle size is not defined and the computation of residual activity inventories based upon integrating over a statistical distribution of re-entering particles would be currently academic.

(2) Upon experimental determination and/or verification of  $k_o$ ,  $E$  and  $C$  for a specific graphitic material, a mathematical expression describing the aerothermochemical mass transfer characteristics of that material can be derived and applied in the convenient form  $\dot{m} \sqrt{R_B/P_e}$  vs.  $T_w$ . Further, although Reynolds number and surface pressure have an appreciable effect on the oxidation behavior in the non-continuum flow regimes, the results can be expressed and compared in terms of continuum oxidation theory; conversely, the theory can be used to define the oxidation performance of graphitic materials in any flow regime.

~~CONFIDENTIAL~~  
~~RESTRICTED DATA~~  
~~RESTRICTED DATA~~  
~~RESTRICTED DATA~~

UNCLASSIFIED

**CONFIDENTIAL**

**RESTRICTED DATA**

**UNCLASSIFIED**

(3) Predictions with respect to integrated mass transfer and to shape change for basic geometric configurations, both in the stationary and in the spinning modes relative to the flow direction (flight path) can be obtained within the limits normally required for engineering accuracy. The multidimensional computer program (and with special care, the one dimensional monotonically shrinking sphere analysis) appear to be well suited for predicting the flight and mass transfer characteristics of re-entering objects using the theoretical-empirical expressions derived. However, specific flow environment and experimental heat transfer distribution data must be factored into any computer analysis in order to adequately predict ground facility test performance.

**CONFIDENTIAL**

**RESTRICTED DATA**

**Atomic Energy Act of 1954**

**UNCLASSIFIED**

## APPENDIX A

### LOW DENSITY EFFECTS ON SPECIFICATION OF CHEMICAL KINETICS

If one considers the oxidation reaction as first order one writes:

$$\dot{m}_{\text{ox}} = k_w (p_{\text{O}_2})_{\text{eff.}} \quad (1)$$

If one considers eq. (1) in the limit of high Reynolds number:

$$(p_{\text{O}_2})_{\text{eff.}} = .21 \rho_{\infty} V_{\infty}^2 \quad (2)$$

and:

$$k_w = \frac{2\gamma}{\pi \bar{C}_w} \quad \text{where } \gamma \text{ is a reaction probability.} \quad (3)$$

However, if one attempts the use of eq. (1) in free molecular flow some modification is necessary in the definition of  $p_{\text{O}_2}$ , in this limit it is necessary to write for  $(p_{\text{O}_2})_{\text{eff.}}$

$$(p_{\text{O}_2})_{\text{eff.}} = \left[ .21 \rho_{\infty} V_{\infty}^2 \right] \left[ \frac{\pi}{2} \frac{\bar{C}_w}{V_{\infty}} \right] \quad (4)$$

and in the near free molecular regime:

$$(p_{\text{O}_2})_{\text{eff.}} = \left[ p_{\text{O}_2} \right]_{\text{F.M.}} \left\{ 1 + .5 \text{Re}_{\infty} \right\} \quad (5)$$

Using the results of Levinsky Ref. 19 for  $p_{\text{O}_2}$  in the low Reynolds number regime and interpolating between these results and eqs. (4) and (5) one obtains the results shown in Fig. 23 .

The result for  $(p_{\text{O}_2})_{\text{eff.}}$  shown in Fig. 23 , can then be utilized in eq. (1) to obtain the mass transfer for reaction controlled oxidation.



## APPENDIX B

### DERIVATION OF COMBINED THEORETICAL-EMPIRICAL EQUATIONS

In order to graphically represent the combined theoretical-empirical mass loss performance of the materials studied in this program, the following expressions were employed:

$$\text{Let } \dot{m}_R = k_o \sqrt{P_e} e^{-E/RT} \quad \begin{array}{l} \text{represent rate controlled} \\ \text{mass loss} \end{array} \quad (1)$$

$$\text{Let } \dot{m}_D = C \sqrt{P_e/R_B} \quad \begin{array}{l} \text{represent diffusion con-} \\ \text{trolled mass loss} \end{array} \quad (2)$$

$$\text{Let } \dot{m} = \frac{1}{\left[ \frac{1}{(\dot{m}_R)^2} + \frac{1}{(\dot{m}_D)^2} \right]^{1/2}} \quad \begin{array}{l} \text{represent transition (3)} \\ \text{from rate controlled} \\ \text{to diffusion controlled} \\ \text{mass loss} \end{array}$$

Substitution of (1) and (2) into (3) yields, after some algebraic re-arrangement,

$$\dot{m} = \left[ \frac{k_o \sqrt{P_e}}{e^{2E/RT} + \left( \frac{k_o}{C} \right)^2 R_B} \right]^{1/2} \quad (4)$$

from which the curves on Figures 32, 33, 52 and 53 were calculated.

Further, if one lets

$f_1$  = fractional ratio of Stanton No.

$f_2$  = fractional ratio of effective pressure ratio

replacing  $\dot{m}_D$  by  $f_1 \dot{m}_D$  and  $\dot{m}_R$  by  $f_2 \dot{m}_R$  in eq. (3) one may derive

$$\dot{m}' = \left[ \frac{f_2 k_o \sqrt{P_e}}{e^{2E/RT} + \left( \frac{f_2 k_o}{f_1 C} \right)^2 R_B} \right]^{1/2} \quad (5)$$

For the normalized mass loss rates a similar series of substitutions gave

$$\dot{m} \sqrt{\frac{R_B}{P_e}} = \frac{k_o e^{-E/RT}}{\left[ \frac{1}{R_B} + \left( \frac{k_o}{C} \right)^2 e^{-2E/RT} \right]^{1/2}} \quad (6)$$

for curves expressed in terms of the theory (Figures 35 and 54).

The theory curves modified to correspond to data points acquired in their actual environments were determined from

$$\dot{m}' \sqrt{\frac{R_B}{P_e}} = \frac{f_2 k_o e^{-E/RT}}{\left[ \frac{1}{R_B} + \left( \frac{f_2 k_o}{f_1 C} \right)^2 e^{-2E/RT} \right]^{1/2}} \quad (7)$$

This arrangement was used to relate the ATJ data more clearly with respect to the theory (Figure 34).

In order to correlate data points with the theory curves (as represented by eq'ns. (4) and (6)), a slightly different approach was used in which it was necessary to determine a weighting factor for each test point. To establish this factor a tabulation of  $\dot{m}$  was made for conditions under which the ratio of  $\dot{m}_R/\dot{m}_D$  assumed particular values. For each material, the ratio

$$\frac{\dot{m}_R}{\dot{m}_D} = \frac{k_o \sqrt{R_B} e^{-E/RT}}{C}$$

was evaluated and the appropriate range of temperatures was determined for each size specimen. The extent to which each mass rate ( $\dot{m}_D, \dot{m}_R$ )

CONFIDENTIAL

RESTRICTED DATA

UNCLASSIFIED

contributed to the combined mass rate ( $\dot{m}$ ) for the corresponding condition was evaluated as the weighting factor for the datum point. See Appendix C.

For a given set of nominal operating conditions, the factors  $f_1$  and  $f_2$  were dependent upon the shock Reynolds number and hence were treated as constants to which the weighting factors were applied.

In the preceding equations:

	ATJ Graphite	Material "X"
$k_o$ (lb. /sec. -ft <sup>2</sup> -atm <sup>1/2</sup> )	$4.42 \times 10^5$	$2.09 \times 10^3$
E (cal/mole)	$44.0 \times 10^3$	$39.1 \times 10^3$
C (lb. /sec. -ft <sup>3/2</sup> atm <sup>1/2</sup> )	$6.2 \times 10^{-3}$	$8.5 \times 10^{-3}$

CONFIDENTIAL

RESTRICTED DATA

UNCLASSIFIED

## APPENDIX C

DISCUSSION AND PRESENTATION OF SAMPLE CALCULATIONS  
REGARDING DATA REDUCTION

To illustrate the process of reducing mass rate data in the experimental program, the results of two test runs are presented and carried through each of the calculations used. Where necessary, details of the specific procedures are expanded.

Consider the results of runs 521 and 560 on 1/16" diameter ATJ graphite mass rate specimens (Table 15):

Run No.	Time sec.	Length Chg. inches	Mass Loss lb/ft. <sup>2</sup>	Mass Rate lb/sec.ft.	Ave. Surf. Temp. °K
560	250	.0750	.6751	---	---
521	60	.0166	.1494	---	---
	190	.0584	.5257	$2.77 \times 10^{-3}$	1515

Difference in time and mass loss between the two runs at the same test conditions result in one mass rate data point at an average surface temperature ( $T_w$ ) of 1515°K.

$$\dot{m}' = \frac{\Delta m}{\Delta t} = \frac{\rho \Delta l}{12 \Delta t} = \frac{108 \times .0584}{12 \times \Delta t} = \frac{.5257}{\Delta t}$$

$$\dot{m}' = 2.77 \times 10^{-3} \text{ lb/sec.ft.}^2 \text{ (data pt. Figure 32, sym. } \bullet \text{)}$$

Other data, useful later in the computations are:

$$\text{Reynolds number per foot} = 520 \text{ ft.}^{-1}$$

$$\text{Reynolds number, } Re_s = 520 \times \frac{1}{16} \times \frac{1}{12} = 2.7$$

$$\text{Effective radius, } R_B = 2.46 \times \frac{1}{32} \times \frac{1}{12} = 6.41 \times 10^{-3} \text{ ft.}$$

$$\text{Model stagnation pressure, } P_e = 7.70 \times 10^{-3} \text{ atmos.}$$

The individual data points ( $\dot{m}'$ ) were located on an Arrhenius plot ( $\dot{m}'$  vs  $1/T$ , Figure 32). Collectively, they were used to establish a reaction rate slope from which the specific reactivity ( $k_o$ ) and activation energy ( $E$ ) of the ATJ graphite were evaluated. The values obtained were expressed in a reaction rate equation, which when coupled with the theoretical expression for diffusion controlled activity by the transition equation, provided a single equation (Appendix B) from which "theoretical" performance curves were evaluated. These were overplotted on the Arrhenius graph (Figure 32).

The computed mass rates are for data acquired in regimes other than those of high Reynolds number, for which the original theory was derived. Hence experimental data have to be modified to correspond to the theory. The value of the modification factor ( $F_m$ ) depends on the degree to which oxidation is rate controlled or diffusion controlled. The plotted theory curves depict graphically a qualitative sense of the contribution of each process and indicate that the modifying factor required by either process must be weighted against that of the other process depending on their relative predominance for a given test point. The following discussion constitutes the basis for obtaining a "weight" applicable to a given data point. Every point was individually weighted.

$$\dot{m} = \left[ \frac{1}{\dot{m}_D^2} + \frac{1}{\dot{m}_R^2} \right]^{1/2} \quad \text{(Transition equation, Sec. IIC, eq'n 30)}$$

Let  $N = \dot{m}_R / \dot{m}_D$  ( $0 \leq N \leq \infty$ ). Then

$$\dot{m} = \left[ \frac{1}{\dot{m}_D^2} + \frac{1}{N^2 \dot{m}_D^2} \right]^{1/2} = \frac{\dot{m}_D}{\left[ 1 + \frac{1}{N^2} \right]^{1/2}}$$

Divide both sides by  $\dot{m}_D$

$$\frac{\dot{m}}{\dot{m}_D} = \left[ 1 + \frac{1}{N^2} \right]^{1/2} = \left[ \frac{N^2 + 1}{N^2} \right]^{1/2}$$

The ratio gives  $0 \leq \frac{\dot{m}}{\dot{m}_D} \leq 1$ , which has the virtue of excluding explicit use of mass rates in the right hand member. For any given value of  $N$ , the contributing mass rates are  $\dot{m}_D$  and  $\dot{m}_R = N\dot{m}_D$ .

The relative contribution of either process can be seen in the expression:

$$\frac{\dot{m}}{\dot{m}_D} = \left[ 1 + \frac{1}{N^2} \right]^{1/2}$$

If  $\dot{m}_R$  is  $N$  times  $\dot{m}_D$  (as postulated), it contributes  $\frac{1}{N^2}$  toward the value of  $\dot{m}$  when  $\dot{m}_D$  contributes unity, relative to it. Their total contribution is  $1 + \frac{1}{N^2}$  and their fractional contributions are

$$\text{for } \dot{m}_R; \quad \frac{1/N^2}{1 + 1/N^2} = \frac{1}{1 + N^2}$$

$$\text{for } \dot{m}_D; \quad \frac{1}{1 + 1/N^2} = \frac{N^2}{1 + N^2}$$

Note that for  $N \rightarrow \infty$ , ratio  $\dot{m}/\dot{m}_D \rightarrow 1$ . (diff. control)

$N \rightarrow 0$ , ratio  $\dot{m}/\dot{m}_D \rightarrow N$  (rate control)

$N = 1$ , ratio  $\dot{m}/\dot{m}_D \rightarrow \frac{1}{2}\sqrt{2}$  (equal control)

Numerical solutions follow:

$$\frac{\dot{m}_R}{\dot{m}_D} = N = \frac{k_o \sqrt{P_e} e^{-E/RT}}{\sqrt{C \frac{P_e}{R_B}}} = \frac{k_o \sqrt{R_B} e^{-E/RT}}{C}$$

where  $C$  is the diffusion control level in  $\text{lb/ft.}^{3/2}\text{-sec-atm}^{1/2}$

$$\text{Then } N = \frac{4.42 \times 10^5 (e^{-22150/1515})}{6.2 \times 10^{-3} (384)^{1/2}}$$

$$N = \frac{7.15 \times 10^7}{19.6 (2.705 \times 10^6)}$$

$$N = 1.35$$

Thus, the contributed fractions are

$$\text{for } \dot{m}_R; \quad \frac{1}{1 + N^2} = .335$$

$$\text{for } \dot{m}_D; \quad \frac{N^2}{1 + N^2} = .645; \text{ where } .645 + .335 = 1.00$$

For the 1/16" diameter mass rate models,  $Re_s = 2.7$ ; using this value one obtains a Stanton Number ratio ( $f_1$ ) of 0.60 (Figure 22) for the diffusion controlled oxidation and an effective pressure ratio ( $f_2$ ) of 0.44 (Figure 23) for rate controlled oxidation.

Then

$$\frac{f_1 N^2}{1 + N^2} + \frac{f_2}{1 + N^2} = F_m; \text{ Weighted Modifying Factor}$$

$$0.60 (0.645) + 0.44(0.355) = 0.543$$

The originally calculated data point can now be modified,  $\dot{m}/F_m = \dot{m}'$ ,

$$\text{thus, } \dot{m}' = \frac{2.77 \times 10^{-3}}{0.543} = 5.22 \times 10^{-3} \text{ lb/sec.ft.}^2 (\text{data pt., Figure 33})$$

giving the value of the mass rate corresponding to that predicted by the original theory. The value of  $\dot{m}'$  or of  $\dot{m}$  may be normalized with respect to body radius and pressure and plotted against surface temperature (for this pt.,  $T_w = 1515^\circ \text{K}$ ).

Therefore,

$$\begin{aligned} \dot{m}' \sqrt{\frac{R_B}{P_e}} &= 2.77 \times 10^{-3} \left( \frac{6.41 \times 10^{-3}}{7.70 \times 10^{-3}} \right)^{1/2} \\ &= 2.54 \times 10^{-3} \text{ lb/ft}^{3/2} \text{-sec-atm}^{1/2} (\text{data pt. Figure 34}) \end{aligned}$$

Similarly,

$$\begin{aligned} \dot{m} \sqrt{\frac{R_B}{P_e}} &= 5.22 \times 10^{-3} \left( \frac{6.41 \times 10^{-3}}{7.70 \times 10^{-3}} \right)^{1/2} \\ &= 4.78 \times 10^{-3} \text{ lb/ft}^{3/2} \text{-sec-atm}^{1/2} (\text{data pt. Figure 35}) \end{aligned}$$

Thus, each datum point for comparison with the theory is established, calculated in the form pertinent to the type presentation for which it is to be used.



CONFIDENTIAL  
UNCLASSIFIED

## APPENDIX D

### DIFFUSION CONTROL LEVEL FOR MATERIAL "X"

In the absence of available information regarding the chemical reactions likely to exist on the ablating surface of Material "X", a sound theoretical evaluation of the mass rate representative of diffusion controlled reactions cannot be obtained. The problem is probably further complicated by the presence of at least two reacting substances which may be combined with the available air to form various species. In view of the difficulties of attacking the problem in a strictly analytical manner, a method is presented in order to establish some criterion with which to compare the experimental data and to provide a conservative value for application to the systems analyses.

Assuming the constituents to be uniformly and homogeneously distributed within the specimens, and postulating no preferential reactivity of oxygen with the constituents of Material "X", the mass fraction and number density relationships predict a normalized diffusion controlled mass rate of  $\dot{m} \sqrt{R_B/P_e} = C_X = 7.67 \times 10^{-3}$ . Given  $n_X = n_C + n_U = 1.0$ ; where  $n_C = .9875$  and  $n_U = .0125$  (Ref. 22), and  $n_{ATJ} = n_C = 1.0$ , one can weigh the contributions of each constituent to the normalized mass rate.

$$C_X = \frac{n_C m_C + n_U m_U}{n_C m_C} \left( C_{ATJ} \right)$$

CONFIDENTIAL  
UNCLASSIFIED

CONFIDENTIAL

RESTRICTED DATA

UNCLASSIFIED

where  $C_{ATJ} = 6.2 \times 10^{-3}$  in units of  $\text{lb/ft}^{3/2}\text{-sec-atm}^{1/2}$

$$\begin{aligned} \text{then } C_X &= \frac{.9875 (12) + .0125 (238)}{1.00 (12)} (6.2 \times 10^{-3}) \\ &= 7.67 \times 10^{-3} \end{aligned}$$

However, there is considerable evidence available from the experimental results which suggest that the uranium did indeed exhibit a greater affinity for the available oxygen. It was observed that when initially exposed to the hot air flow, there was a sizeable shower of brilliant particles shed by the specimens, which gradually diminished with time. In addition, the motion pictures show local minute areas on the surface which become much more intensely bright than the overall surface, last for a short time and then disappear. These phenomena recall the well-known behavior of uranium and uranium carbides having small specific areas to ignite spontaneously in air at very moderate temperatures with a very significant generation of heat (Ref. 23). Close examination of the specimen surfaces of Material "X" tends to confirm that such a process does occur. The fissured and porous appearance of the specimen surfaces after exposure suggest that indeed, the oxygen combines preferentially with the uranium.

Without well defined data to establish the degree to which a selectivity phenomenon might operate, it was postulated from an analysis of the data in Table 4 that a conservative value might be a rate  $1-1/2$

CONFIDENTIAL

RESTRICTED DATA

UNCLASSIFIED

CONFIDENTIAL

RESTRICTED DATA

UNCLASSIFIED

times the parity loss value of uranium (see Section III E. 5). Calculated on this basis,

$$C_X \approx \frac{n_C m_C + 1.5 n_U m_U}{n_C m_C} (C_{ATJ})$$

one finds the diffusion controlled mass rate parameter  $C_X \approx 8.5 \times 10^{-3}$ .

This value was then combined with the empirically evaluated reaction rate expression using the transition equation (Section II C, equation 30), and empirical-theory curves were calculated and plotted with the mass rate experimental data (Figure 54). Examination of the graph clearly indicates that the experimental data define no trend toward a leveling off of mass loss over the range explored. Rather, the data points suggest a continuance of the exponential rise of mass rate parameter up to  $10.5 \times 10^{-3}$ .

The results of the experiment indicate that selective reactions do occur and, indeed that oxygen has, perhaps, an even greater affinity for the uranium constituent of Material "X" than is postulated.

CONFIDENTIAL

RESTRICTED DATA

UNCLASSIFIED

## APPENDIX E

COMPARISON OF EXACT AND NUMERICAL  
HEAT CONDUCTION SOLUTIONS FOR SPHERES

The transient heat conduction equation for a sphere heated by a constant rate is

$$\rho c_p \frac{\partial T}{\partial t} = \frac{1}{R^2} \frac{\partial}{\partial R} \left( KR^2 \frac{\partial T}{\partial R} \right) \quad (1)$$

and the following boundary and initial conditions applied:

$$\begin{aligned} T(R, 0) &= T_E \\ \frac{\partial T}{\partial R}(a, t) &= \frac{Q_w}{K} \\ \frac{\partial T}{\partial R}(0, t) &= 0 \end{aligned} \quad (2)$$

The exact solution to this problem is given in Reference 25 as:

$$\begin{aligned} T - T_E &= \frac{3Q_w t}{\rho c_p a} + \frac{Q_w (5R^2 - 3a^2)}{10Ka} \\ &\quad - \frac{2Q_w a^2}{KR} \sum_{n=1}^{\infty} \frac{\sin\left(\frac{R\zeta_n}{a}\right) \frac{\alpha \zeta_n^2 t}{R^2}}{\zeta_n^2 \sin \zeta_n} \end{aligned} \quad (3)$$

where  $Q_w$  is the uniform heating rate

$a$  is the radius of the sphere

$\zeta_n$  ( $n = 1, 2, 3, \dots$ ) are the positive real roots of the transcendental equation,  $\tan \zeta = \zeta$

$\alpha$  is the thermal diffusivity  $= \left(\frac{K}{\rho c_p}\right)$

For  $R = a$ , equation (3) reduces to

$$T - T_o = \frac{3Q_w t}{\rho c_p a} + \frac{Q_w a}{5K} - \frac{2Q_w a}{K} \sum_{n=1}^{\infty} \frac{\sin \zeta_n \ell}{\zeta_n^2 \sin \zeta_n} - \frac{\zeta_n^2 \alpha t}{a^2} \quad (4)$$

Figure 103 illustrated the comparison of the surface temperature as a function of time obtained from the IBM 7094 computer solution and the exact solution of equation (4). At  $3000^\circ\text{R}$ , the percent error of the numerical technique is less than 2% for the case considered. Further improvement in accuracy is possible for this comparison by decreasing the time interval between computations.

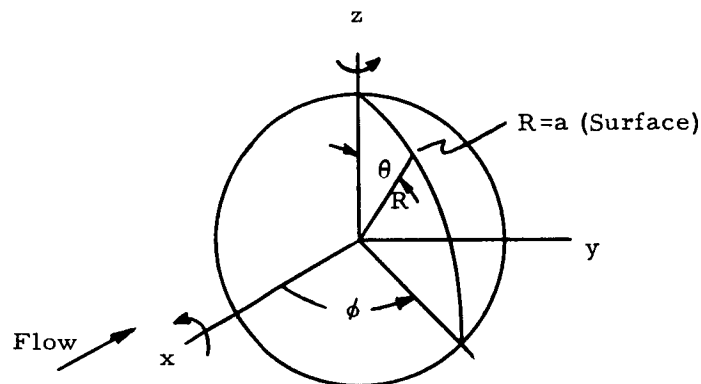
The transient heat conduction equation for a sphere analyzed multi-dimensionally is

$$\begin{aligned} \rho c_p \frac{\partial T}{\partial t} = & \frac{1}{R^2} \frac{\partial}{\partial R} \left( KR^2 \frac{\partial T}{\partial R} \right) + \frac{1}{R^2 \sin \theta} \frac{\partial}{\partial \theta} \left( K \sin \theta \frac{\partial T}{\partial \theta} \right) \\ & + \frac{1}{R^2 \sin^2 \theta} \frac{\partial}{\partial \theta} \left( K \frac{\partial T}{\partial \theta} \right) \end{aligned} \quad (5)$$

In Reference 26, a three dimensional solution was obtained for the case of a sphere rotating about an axis  $90^\circ$  to the flow direction. If the spin rate is set to zero, the solution may be applied to a sphere whose axis of rotation is aligned to the flow direction and the following boundary applied

$$K \frac{\partial T}{\partial R} (a, \theta, \varphi) = \frac{Q_{wo}}{2} (1 + \sin \theta \cos \varphi) \quad (6)$$

where the product,  $\sin \theta \cos \phi = \text{constant}$ , locates a plane perpendicular to the flow direction (x - direction) as illustrated in the following sketch.



Since the flow is axisymmetric, the solution is obtained for a specific heat flux distribution in the x-y plane, Figure 104, where

$$K \frac{\partial T}{\partial R} \left( a, \frac{\pi}{2}, \phi \right) = \frac{Q_{w0}}{2} (1 + \cos \phi) \quad (7)$$

The surface temperature  $T$  is given as the sum of four parts:

$$T = T_E + T_1 + T_2 + T_3 \text{ where}$$

$T_E$  is the initial temperature,  $T_1$  is the solution obtained for a constant heat flux,  $\frac{Q_{w0}}{2}$  as listed in Equation (3) and

$$T_2 + T_3 = \frac{Q_{w0} R}{2K} \sin \theta \cos \phi \left[ \frac{R}{a} + \frac{2a^2}{R^2} \sum_{n=1}^{\infty} \frac{\zeta_n^4 \cos \zeta_n}{\zeta_n^4 \cos \zeta_n} \left( \sin \zeta_n \frac{R}{a} - \zeta_n \frac{R}{a} \cos \zeta_n \frac{R}{a} \right) \right]$$

UNCLASSIFIED

Figure 104 illustrates the specific surface heat flux distribution for which an exact analytic solution exists. Figure 105 compares this exact solution with the numerical solution obtained from the IBM 7094 computer program at three surface locations ( $R = a$ ) in order to check the accuracy of the numerical solution. The numerical solution deviates by less than  $3/4$  of 1% at  $4000^{\circ}\text{R}$ . Note that this chosen heat flux distribution does not pertain to the systems analyses per se.

UNCLASSIFIED

## APPENDIX F

DETERMINATION OF AVERAGE HEAT AND MASS  
TRANSFER FOR SPHERES AND CYLINDERS

In order to analyze the sphere one-dimensionally, a suitably averaged heat and mass transfer rate must be determined. Assuming a Newtonian pressure distribution on a hemisphere, the heat and mass transfer at a given body angle, becomes

$$Q_{w_{\text{local}}} = Q_{w_o} \cos \theta \quad (1)$$

$$\dot{m}_{w_{\text{local}}} = \dot{m}_{w_o} \cos \theta$$

As a first approximation, one may base the average heat and mass transfer on a surface-area basis:

$$\bar{Q}_{w_{\text{hemisphere}}} = \frac{\int_A Q_{w_{\text{local}}} dA}{\int_A dA} \quad (2)$$

or in spherical coordinates

$$\bar{Q}_{w_{\text{hemisphere}}} = \frac{\int_0^{2\pi} \int_0^{\pi/2} Q_{w_o} \cos \theta R^2 \sin \theta d\theta d\varphi}{\int_0^{2\pi} \int_0^{\pi/2} R^2 \sin \theta d\theta d\varphi} \quad (3)$$

$$\bar{Q}_{w_{\text{hemisphere}}} = .5 Q_{w_o} \quad (4)$$



If one assumes the aft heating (and mass transfer) to be zero, then for the entire sphere, the average heat transfer would be

$$\overline{Q}_{w_{\text{sphere}}} = .25 Q_{w_o} \quad (5)$$

For the systems study an average value between .5 and .25 of the stagnation heating rate (and mass transfer), viz., .375 was assumed. It should be noted that a more exact calculation for the average heat transfer to a non-ablating hemisphere was found in Reference 27 to be  $0.436 Q_{w_o}$ . The effects of varying the averaging factor between .5 and .2 were investigated in the systems study (Figure 82). For the cylindrical rod an average value equal to the stagnation value was imposed over the entire front ~~face~~<sup>FACE.</sup>

## REFERENCES

1. Enoch, J., "Kinetic Model for High Velocity Ratio Near Free Molecular Flow", Physics of Fluids, Vol. 5, No. 8, p. 918, 1962.
2. Bonnetain, L., "Combustion de Graphites Artificiels Sous Basses Pressions D'Oxygene", Jour. Chim. Phys., 1959, Part I, pp. 266-276, Part II, pp. 486-494.
3. Blyholder, E.A., "Mechanism of the Oxidation of Graphite at Temperatures of 425° C to 575° C", Ind. Eng. Chem., Vol. 44 No. 5, 1952, pp. 1045-1051.
4. Rott and Whittenbury, "A Flow Model for Hypersonic Rarefied Gas Dynamics", Douglas Report SM-38524, 1961.
5. Masson, D., et al., "Measurements of Sphere Drag from Hypersonic Continuum to Free-Molecule Flow", Second Symposium on Rarefied Gas Dynamics, L. Talbot-Editor, Academic Press, 1961.
6. Geiger, R., "Summary of GE-MSD Tunnel Experimental Investigations of Low Density Drag", GE TIS 63SD4671, 1963.
7. Willis, D.R., "Methods of Analysis of Nearly Free Molecular Flow for a Satellite or Other Space Vehicle", GE MSD TIS R60SD399.
8. Schamberg, R., "Analytical Representation of Surface Interaction for Free-Molecule Flow with Application to Drag of Various Bodies" Rand Symposium Aerodynamics of the Upper Atmosphere", June 1959.
9. Scala, S.M., "The Ablation of Graphite in Dissociated Air. Part I-Theory", GE TIS R62SD72, 1962.
10. Cheng, H., "Hypersonic Shock Layer Theory of the Stagnation Region at Low Reynolds", Cornell Aero. Lab., Report AF-1285-A-7, 1961.
11. Goldberg, L. and Scala, S.M., "Mass Transfer in the Hypersonic Low Reynolds Number Viscous Layer", GE MSD TIS R62SD7, 1962.
12. Diaconis, N.S., et al., "The Ablation of Graphite in Dissociated Air. Part II - Experimental Investigation", GE TIS R62SD86, 1962.
13. Bellinger, B.A., "Operation and Maintenance of the Two Color Pyrometer", Manual No. 1, GE-SSL-64-4, May 1962.

14. Sutton, G.W. and Miksch, G.E., "Heat Transfer from Malta 3 1/2 Inch Alcohol Oxygen Motor Exhaust to a One Inch Diameter Hemisphere Cylinder", GE-Aerophysics T.M. #32, Dec. 1956.
15. Warren, W.R. and Diaconis, N.S., "Air Arc Simulation of Hypersonic Environments", GE TIS R62SD25, April 1962.
16. Eschenroeder, A.Q. et al., "Exact Solutions for Nonequilibrium Expansions of Air with Coupled Chemical Reactions", Cornell Aero. Lab. Rpt. No. AF-1413-A-1, AFO SR 622, May 1961.
17. Tsien, H.S., "Superaerodynamics, Mechanics of Rarefied Gases", Journ. Aero. Sci., V13, No. 12, pp. 653-654, Dec. 1946.
18. Boison, J.C. and Curtiss, H.A., "An Experimental Investigation of Blunt Body Stagnation Point Velocity Gradient", ARS Journal, Vol. 29, No. 2, pp. 130-135, Feb. 1959.
19. Levinsky, E.S. and Yoshihara, H., "Rarefied Hypersonic Flow Over a Sphere", pp. 81-106, Hypersonic Flow Research, Edited by F.R. Riddell, Academic Press, 1961.
20. Scala, S.M., "The Hypersonic Environment-Heat Transfer in Multicomponent Gases", Aerospace Engineering, Jan. 1963.
21. Hickmass, R.S. and Giedt, W.H., "Heat Transfer to a Hemisphere Cylinder at Low Reynolds Numbers", AIAA Journ. Vol. I, No. 3, Mar. 1963.
22. Nichols, L.R., Letter to S.M. Scala dated Aug. 7, 1963, Re: Data on Material "X"; Confidential, AEC Restricted Data.
23. Wilkinson, W.D., "Uranium Metallurgy, Vol. II: Uranium Corrosion and Alloys", pp. 809-814 and 959, Interscience Publishers, John Wiley and Sons, 1962.
24. Gallaher, W.H., Sibulkin, M., "Successful Re-Entry of Space Fragments from a Decaying Earth Orbit", AIAA Journal, Vol. I, No. 6, June 1963, pp. 1444-1445.
25. Carslaw, H.S., Jaeger, J.C., "Conduction of Heat in Solids", Oxford: University Press, 2nd Edition, 1959, p. 242.
26. Reissman, H., "Temperature Distribution in a Spinning Sphere During Atmospheric Entry", Journal of Aerospace Sciences, Feb. 1962, pp. 151-159.
27. Myer, H.G., Ambrosio, A., "Area-Integrated Heat Rates for Several Axisymmetric Vehicles", AIAA Journal, Vol. I, No. 8, Aug. 1963, pp. 1904-1906.

TABLE 1

## SUMMARY OF PRESSURE PROBE MEASUREMENTS

Position *	Stagnation Pressure, Atmospheres x 10 <sup>3</sup>		
	High Enthalpy		Low Enthalpy
	5.0" Station	1.2" Station	5.0" Station
0.563	8.25	56.0	7.00
1.000	7.98	-----	-----
1.500	7.70	-----	-----

\* Distance from Nozzle Exit

Note: Each tabulated value represents the average of the several test exposures made at that position. Maximum variation in results was  $\pm 3.5\%$

TABLE 2  
MASS LOSS DATA  
1/4" Dia. Cylinders

Specimen Material ATJ Graphite  
Orientation Coaxial to  
C. L. of Nozzle

Air Mass Flow, Lb/sec. .0015  
Nozzle Exit Dia., In. 5.0

Run No.	Delivered Power, KW	Flenum Press., psia	$h_{s/ro}$	Test Time Sec.	Length Loss, Ins.	Mass Loss Lb/ft <sup>2</sup>	Remarks (4)
458	238	22.2	350	128	.0199	.1791	(1) (2)
459	235	22.2	348	100	.0121	.1089	(1) (2)
460	245	22.7	364	60	.0104	.0936	(1) (2)
461	238	22.2	350	100	.0153	.1377	(1) (2)
462	242	22.2	354	127	.0243	.2187	(1) (2)
463	238	23.2	366	39	.0051	.0459	(1) (2)
465	234	21.5	337	141	.0173	.1557	(1) (2)
472	241	22.7	361	80	.0133	.1197	(2) (3)
473	227	22.9	354	120	.0220	.1980	(2) (3)
474	234	22.7	356	160	.0322	.2898	(2) (3)

- (1) See Fig. 12, Item 17  
(2) Position: 0.5625" from nozzle exit  
(3) See Fig. 13, (c)  
(4) For two color surface temperature data, see Table 11

TABLE 2  
MASS LOSS DATA  
1/4" Dia. Cylinders

Specimen  
Material ATJ Graphite  
Orientation Coaxial to  
C. L. of Nozzle

Air Mass Flow, Lb/sec. .0015  
Nozzle Exit Dia., In. 1.2

Run No.	Delivered Power, KW	Flenum Press., psia	$h_s/RT_o$	Test Time Sec.	Length Loss, Ins.	Mass Loss Lb/ft <sup>2</sup>	Remarks (5)
488	260	20.7	342	165	.2160	1.9440	(1) (2)
489	245	20.7	332	100	.1177	1.0593	(1) (2)
490	234	20.7	324	130	.1567	1.4103	(1) (2)
493	242	20.2	324	---	Burn thru	-----	(2) (3)
494	234	20.2	316	45	.0488	.4392	(2) (3)
495	241	20.7	330	100	.1156	1.0404	(2) (3)
496	241	20.7	330	80	.0935	.8415	(2) (3)
497	241	19.8	315	160	.1940	1.7460	(2) (4)
498	238	20.4	322	130	.1610	1.4490	(2) (4)
500	238	20.7	327	100	.1178	1.0602	(2) (4)
501	240	20.7	328	87.5	.1078	.9702	(2) (4)

(1) See Fig. 12, Item 21

(2) Position: 0.5625" from nozzle exit

(3) See Fig. 13, (b)

(4) See Fig. 13, (a)

(5) For two color surface temperature data, see Table 12

TABLE 2  
MASS LOSS DATA  
1/16" Dia. Cylinders

Specimen Material ATJ Graphite  
Orientation Coaxial to  
C. L. of Nozzle

Air Mass Flow, Lb/sec. .0015  
Nozzle Exit Dia., In. 5.0

Run No.	Delivered Power, KW	Plenum Press., psia	$h_s$ , RT	Test Time Sec.	Length Loss, Ins.	Mass Loss Lb/ft <sup>2</sup>	Remarks (5)
513	245	20.7	332	40	.0123	.1107	(1) (2)
514	247	20.7	333	60	.0180	.1620	(1) (3)
515	241	20.7	329	80	.0223	.2007	(1) (3)
516	259	20.2	333	80	.0207	.1863	(1) (3)
517	238	21.7	342	100	.0280	.2520	(1) (3)
518	248	20.6	335	100	.0284	.2556	(1) (3)
519	252	20.2	329	120	.0332	.2988	(1) (3)
520	245	20.5	329	120	.0352	.3168	(1) (3)
521	255	20.6	337	60	.0166	.1494	(1) (3)
557	276	23.2	395	100	.0245	.2205	(3) (4)
558	266	21.8	364	200	.0606	.5454	(3) (4)
559	254	21.9	358	150	.0439	.3954	(3) (4)
560	266	21.1	352	250	.0750	.6751	(3) (4)

(1) See Fig.12, Item 21

(2) Position: 0.5625" from nozzle exit

(3) Position: 1.50" from nozzle exit

(4) See Fig.13, (d)

(5) For two color surface temperature data, see Table 15

TABLE 2  
MASS LOSS DATA  
1" Dia. Cylinders

Specimen Material Orientation ATJ Graphite Coaxial to C.L. of nozzle Air Mass Flow, Lt/sec. .0014 Nozzle Exit Dia., In. 5.0

Run No.	Delivered Power, KW	Plenum Press., psia	$h_s$ / °	Test Time Sec.	Length Loss, Ins.	Mass Loss Lb/ft <sup>2</sup>	Remarks (3)
631	84	16.0	165	1200	.1355	1.2195	(1) (2)
632	72	15.8	150	960	.0770	.6930	(1) (2)
633	85	16.3	169	463	.0514	.4626	(1) (2)
634	88	16.5	163	240	.0248	.2232	(1) (2)
635	76	16.5	141	360	.0331	.2979	(1) (2)
638	77	16.2	160	720	.0682	.6138	(1) (2)
639	80	16.6	167	600	.0523	.4707	(1) (2)
641	84	16.7	172	480	.0456	.4104	(1) (2)
642	80	16.7	168	310	.0255	.2305	(1) (2)
643	82	16.7	170	772	.0718	.6462	(1) (2)
644	80	16.9	170	801	.0793	.7137	(1) (2)

- (1) See Fig.12, Items 18, 19  
(2) Position: 0.800" from nozzle exit  
(3) For two color surface temperature data, see Table 16



TABLE 3  
MASS LOSS DATA  
1" Dia. Cylinders

Specimen Material Mat'l. "X"  
Orientation Coaxial to  
C.L. of Nozzle

Air Mass Flow, lb/sec. .0014  
Nozzle Exit Dia., In. 5.0

Run No.	Delivered Power, KW	Plenum Press., psia	$h_s$ , RT °	Test Time Sec.	Length Loss, Ins.	Mass Loss Lb/ft. <sup>2</sup>	Remarks (3)
649	80	16.6	167	840	.0145	.1618	(1) (2) $T_g = 1460^\circ K$ (*)
650	82	16.5	168	480	.0102	.1138	(1) (2) $T_g = 1470^\circ K$ (*)
651	80	16.5	166	720	.0134	.1493	(1) (2) $T_g = 1445^\circ K$ (*)
652	77	16.7	165	360	.0104	.1160	(1) (2) $T_g = 1440^\circ K$ (*)
653	72	16.9	161	500	.0104	.1160	(1) (2) $T_g = 1450^\circ K$ (*)
654	72	17.1	163	577	.0115	.1282	(1) (2) $T_g = 1440^\circ K$ (*)
655	89	17.1	181	240	.0066	.0737	(1) (2) $T_g = 1450^\circ K$ (*)
656	83	16.8	172	120	.0029	.0323	(1) (2)

- (1) See Fig. 12, Items 18, 19  
(2) Position: 0.800" from nozzle exit  
(\*) Optical pyrometer  
(3) For two color surface temperature data, see Table 21

UNCLASSIFIED

UNCLASSIFIED

TABLE 3  
MASS LOSS DATA  
1" Dia. Cylinders

Specimen Material Mat'l. "X"  
Orientation Coaxial to  
C.L. of Nozzle

Air Mass Flow, Lb/sec. .0015  
Nozzle Exit Dia., In. 5.0

Run No.	Delivered Power, KW	Plenum Press., psia	$h_s/RT_o$	Test Time Sec.	Length Loss, Ins.	Mass Loss Lb/ft. <sup>2</sup>	Remarks (3)
667	225	23.1	354	180	.0074	.0817	(1) (2)
669	239	21.1	334	300	.0169	.1868	(1) (2)
678	239	21.3	336	240	.0108	.1193	(1) (2)
679	221	21.5	327	180	.0069	.0763	(1) (2)
680	221	21.1	321	360	.0176	.1964	(1) (2)
681	218	21.0	317	120	.0040	.0454	(1) (2)
682	218	21.1	319	300	.0140	.1562	(1) (2)
683	224	21.4	328	60	.0025	.0279	(1) (2)

- (1) See Fig. 12, Items 18, 19  
(2) Position: 0.800" from nozzle exit  
(3) For surface temperature data, see Table 19

UNCLASSIFIED

UNCLASSIFIED

TABLE 3  
MASS LOSS DATA  
1/16" Dia. Cylinders

Specimen Material Orientation Mat'l. "X" Coaxial to C.I. of Nozzle Air Mass Flow, Lb/sec. .0015  
Nozzle Exit Dia., In. 5.0

Run No.	Delivered Power, KW	Flenum Press., psia	$h_s$ , RT	Test Time Sec.	Length Loss, Ins.	Mass Loss Lb/ft	Remarks (3)
670	238	21.1	333	300	.0316	.3520	(1) (2)
671	226	20.0	308	180	.0149	.1661	(1) (2)
672	226	21.9	337	60	.0039	.0435	(1) (2)
673	226	20.7	319	240	.0212	.2365	(1) (2)
674	214	20.9	313	120	.0143	.1594	(1) (2)
675	227	22.0	339	60	.0068	.0758	(1) (2)
676	221	21.7	330	42	-----	.0310	(1) (2)
677	239	21.0	332	120	.0103	.1150	(1) (2)

- (1) See Fig. 12, Item 21  
(2) Position: .800" from nozzle exit  
(3) For two color surface temperature data, see Table 20

UNCLASSIFIED

UNCLASSIFIED

TABLE 3  
MASS LOSS DATA  
1/4" Dia. Cylinders

Specimen	Material	Mat'l, "X"	Air Mass Flow, Lb/sec.	.0015
	Orientation	Coaxial to	Nozzle Exit Dia., In.	5.0
		C.L. of Nozzle		

Run No.	Delivered Power, KW	Plenum Press., psia	$h_s/RT_o$	Test Time Sec.	Length Loss, Ins.	Mass Loss Lb/ft <sup>2</sup>	Remarks (3)
684	218	21.2	320	300	.0232	.2590	(1) (2)
685	236	20.8	327	180	.0166	.1853	(1) (2)
686	242	21.7	346	60	.0045	.0502	(1) (2)
687	233	21.7	339	175	.0150	.1676	(1) (2)
688	216	20.6	310	240	.0224	.2500	(1) (2)
689	216	20.7	312	120	.0109	.1218	(1) (2)
690	216	20.8	313	300	.0332	.3705	(1) (2)
695	218	21.0	318	360	.0357	.3970	(1) (2)
696	218	21.0	318	300	.0269	.3000	(1) (2)

- (1) See Fig. 12, Item 17  
 (2) Position: .800" from nozzle exit  
 (3) For two color surface temperature data, see Table 17

UNCLASSIFIED

UNCLASSIFIED

TABLE 3  
MASS LOSS DATA  
1/4" Dia. Cylinders

Specimen Material Mat'l. "X"  
Orientation Coaxial to  
C.L. of Nozzle

Air Mass Flow, Lb/sec. .0014  
Nozzle Exit Dia., In. 1.2

Run No.	Delivered Power, KW	Plenum Press., psia	h RT s / °	Test Time Sec.	Length Loss, Ins.	Mass Loss Lb/ft. <sup>2</sup>	Remarks (3)
720	219	21.8	330	281	.3244	3.618	(1) (2)
721	231	21.8	340	40	.0393	0.438	(1) (2)
722	230	21.3	330	90	.0672	0.749	(1) (2)
723	230	21.3	330	121	.0909	1.013	(1) (2)
724	230	20.7	321	160	.1468	1.637	(1) (2)
725	227	21.3	329	280	.2384	3.216	(1) (2)
726	224	21.7	322	240	.2428	2.707	(1) (2)
727	230	21.3	330	200	.2220	2.472	(1) (2)
728	230	20.9	324	40	.0462	0.515	(1) (2)

- (1) See Fig. 12, Item 17  
(2) Position: 0.5625" from nozzle exit  
(3) For two color surface temperature data, see Table 18

UNCLASSIFIED

TABLE 4  
COMPARISON: MASS LOSS DATA  
ONE INCH CYLINDERS WITH 1/4" INSERTS

Run	Mat'l.	Length Loss Basis		Insert Mass Loss Basis		Ratio*
		length loss inches	mass loss lb/ft. <sup>2</sup>	mass loss grams	mass loss lb/ft. <sup>2</sup>	
631	ATJ	.1355	1.2195	.1902	1.230	.992
632	"	.0770	.6930	.1128	.728	.953
633	"	.0540	.4626	.0756	.489	.947
634	"	.0248	.2232	.0370	.239	.934
635	"	.0331	.2979	.0497	.321	.928
638	"	.0682	.6138	.1037	.671	.905
639	"	.0523	.4707	.0798	.516	.912
641	"	.0456	.4104	.0670	.433	.947
642	"	.0255	.2305	.0397	.257	.898
643	"	.0718	.6462	.1003	.649	.996
644	"	.0793	.7137	.1104	.714	.999
649	X	.0145	.1618	.0277	.1790	.905
650	"	.0102	.1138	.0209	.1351	.843
651	"	.0134	.1493	.0231	.1388	1.077
652	"	.0104	.1160	.0201	.1298	.895
653	"	.0104	.1160	.0188	.1215	.955
654	"	.0115	.1282	.0250	.1617	.794
655	"	.0066	.0737	.0135	.0873	.845
656	"	.0029	.0323	.0042	.0271	1.192
667	"	.0074	.0817	.0148	.0956	.847
669	"	.0169	.1868	.0318	.2566	.728
678	"	.0108	.1193	.0180	.1162	1.027
679	"	.0069	.0763	.0142	.0918	.832
680	"	.0176	.1964	.0334	.2160	.909
681	"	.0040	.0454	.0107	.0692	.657
682	"	.0140	.1562	.0274	.1770	.884
683	"	.0025	.0279	.0053	.0343	.814

\* Mass Loss, length basis  $\div$  Mass Loss, mass basis

UNCLASSIFIED

TABLE 5  
INTEGRATED MASS LOSS DATA  
SPHERES

Specimen

Material ATJ Graphite

Air Mass Flow, Lb/sec. .0015  
Nozzle Exit Dia., In. 5.0

Run No.	Delivered Power, KW	Plenum Press., psia	$h_s/RT_0$	Test Time Sec.	Mass Loss, gms.	Avg. Surf. Temp. °K	Remarks
523	245	20.7	332	303	1.1406	1720	(1) (3)
524	252	20.7	340	504	1.9916	1730	(1) (3)
525	248	20.6	332	471	1.9024	1720	(1) (3)
527	245	23.4	374	97	0.3291	1640	(1) (3)
529	259	20.2	332	900	3.0236	1690	(1) (3)
530	248	20.0	323	120	0.0612	1830	(2) (3)
531	269	19.4	326	241	0.1252	1800	(2) (3)
532	270	19.8	333	180	0.0972	1800	(2) (3)
533	270	19.7	331	398	0.1952	1850	(2) (3)
535	261	19.8	328	500	1.5904	1570	1 rad/sec. (1) (4)
536	266	20.2	337	500	1.6540	1550	1 rad/sec. (1) (4)
537	259	20.1	331	300	.1247	1750	1 rad/sec. (2) (5)
538	262	20.3	337	150	.0553	1710	1 rad/sec. (2) (5)
539	263	20.7	344	300	.1154	1740	2 rad/sec. (2) (5)
540	266	20.7	346	150	.0468	1740	2 rad/sec. (2) (5)
541	258	20.5	337	500	1.4413	1600	2 rad/sec. (1) (4)
542	---	---	---	171	0.5823	----	2 rad/sec. (1) (4)
543	---	22.7	3--	449	1.7120	----	2 rad/sec. (1) (4)
545	259	24.7	407	500	1.9656	1660	2 rad/sec. (1) (4)
546	261	20.3	336	1035	2.7382	1380	2 rad/sec. (1) (4)
547	258	20.8	342	500	1.3260	1610	2 rad/sec. (1) (4)
646	82	16.7	170	600	1.6018	1470	$T_g=1420^{\circ}\text{K} (*) (1)$ (6) (7)
648	81	16.4	166	999	2.5812	1470	$T_g=1420^{\circ}\text{K} (*) (1)$ (6) (7)

(1) See Fig. 12 Item 13

(2) See Fig. 12 Item 14

(3) Position: L. 500" from nozzle exit

(4) Position: 1.850" from nozzle exit

(5) Position: 2.225" from nozzle exit

(6) Position: 0.800" from nozzle exit

(7) Air Mass Flow .0014 lb/sec.

(\*) Optical pyrometer

TABLE 6  
INTEGRATED MASS LOSS DATA  
SPHERES

Specimen

Material

Mat'l. "X"

Air Mass Flow, Lb/sec. .0015  
Nozzle Exit Dia., In. 5.0

Run No.	Delivered Power, KW	Plenum Press., psia	$h_s/R T_o$	Test Time Sec.	Mass Loss, gms.	Avg. Surf. Temp. °K	Remarks
691	227	21.0	324	1000	2.2514	1850	(1) (3)
692	225	21.0	323	500	1.2724	1800	(1) (3)
697	225	21.4	328	300	.1322	2020	(2) (4)
698	220	21.5	325	150	.0500	1930	(2) (4)
699	220	20.8	316	798	1.3845	1660	(1) (4)
700	221	21.5	327	500	1.1998	1620	(1) (4)
701	218	21.2	321	300	.0992	1930	(2) (5)
702	220	21.1	320	150	.0638	1850	(2) (5)
703	218	20.7	313	283	.1058	1910	(2) (5)
706	220	20.9	318	177	.5625	1670	(1) (4)
707	243	20.7	334	303	.9796	1720	(1) (4)
710	220	21.2	322	400	.1499	1900	(2) (5)
711	217	21.4	323	200	.0862	1930	(2) (5)
712	222	21.6	329	310	.8215	1750	(1) (4)
719	210	20.8	309	677	1.4656	1740	(1) (4)
657	75	16.6	162	1000	1.5979	1490	$T_s = 1550^\circ K$ (*) (1)
658	77	16.8	166	600	0.6840	1480	$T_s = 1550^\circ K$ (*) (1)

(1) See Fig. 12, Item 13

(2) See Fig. 12, Item 14

(3) Position: 1.500" from nozzle exit

(4) Position: 1.850" from nozzle exit

(5) Position: 2.225" from nozzle exit

(6) Position: 0.800" from nozzle exit

(7) Air Mass Flow .0014 lb/sec.

(\*) Optical pyrometer

UNCLASSIFIED



TABLE 7  
INTEGRATED MASS LOSS DATA  
CYLINDERS

Run No.	Delivered Power, KW	Plenum Press., psia	$h_{s/RT}$	Test Time Sec.	Mass Loss, gms.	Avg. Surf. Temp. °K	Remarks
693	225	21.0	323	500	.4405	2150	↓ to flow, $T_s = 2180^\circ K(*)$ (1)
694	218	20.7	313	250	.2027	2140	↓ to flow, $T_s = 2150^\circ K(*)$ (1)
704	222	20.9	319	480	.2618	1730	2 rad/sec. (2)
705	222	21.9	334	240	.1766	1790	2 rad/sec. (2)
708	215	21.0	315	465	.2655	1820	1 rad/sec. (2)
709	222	21.4	318	240	.1951	1820	1 rad/sec. (2)
716	214	21.2	317	250	.1153	----	↑ to flow, $T_s = 1920^\circ K(*)$ (3)
717	212	21.8	325	500	.1849	----	↑ to flow, $T_s = 1920^\circ K(*)$ (3)

Specimen Material Mat'l. "X" Air Mass Flow, Lb/sec. .0015  
Nozzle Exit Dia., In. 5.0

Cylinders 1/4" dia. x 1/2" long  
(1) Position: 2.225" from nozzle exit  
(2) Position: 0.800" from nozzle exit  
(\*) Optical pyrometer

UNCLASSIFIED

UNCLASSIFIED

TABLE 8  
SUMMARY OF TOTAL CALORIMETER  
ENTHALPY MEASUREMENTS

$E_k, \text{KW}$	$\dot{m}, \text{lb/sec.}$	$P_s, \text{psia}$	$h_s/RT_o$	$h_s, \text{Btu/lb.}$
238	.0015	22.2	351	11880
238	↓	20.8	327	11070
230		20.6	316	10700
283	↓	19.5	332	11230
76.7	.0014	16.0	157	5310
76.7	↓	15.9	166	5610
76.7		16.0	162	5480
87.5	↓	16.3	162	5480

TABLE 9  
SUMMARY OF COLD WALL HEAT TRANSFER MEASUREMENTS  
FLAT FACE SPECIMENS

Configuration (1)	Nozzle	Position (2)	Nominal $h_g/RT_o$	Heat Transfer Rates
1" D-1/4" d	5.0"	0.563"	350	75.0 Btu/ft <sup>2</sup> -sec
		1.500"		76.0
		"		68.5
		1.850"		76.0
		"		63.5
		"		58.5
		2.225"		71.5
		"		69.5
1/4" D-1/8" d		0.563"		144.5
		"		139.0
1/4" d (3)		1.500"		141.0
1/4" D-1/8" d	1.2	0.563"		130.0
		0.563"		482
		"		497
1/4" d (3)		"		505
1/16" d (3)	5.0	1.500"		269
		"		283
		"		288
1" D-1/4" d	5.0	0.800"	160	49.0
		"		48.6

- (1) Configuration: Gives model dia. followed by copper insert dia.  
 (2) Station: Distance to stagnation point, from nozzle exit  
 (3) Copper cylinder with .003" RTV coating

TABLE 10  
SUMMARY OF COLD WALL HEAT TRANSFER MEASUREMENTS  
SPHERICAL SPECIMENS

Configuration (1)	Nozzle	Station (2)	Nominal $h_s / RT_o$	Heat Transfer Rates Btu/ft <sup>2</sup> -sec.	Remarks
1" D-1/4" d	5.0"	0.563"	350	111.0	(Stag = 0°)
		1.500		104.5	( 50°)
		-----		102.0	( 60°)
		-----		26.3	( 120°)
		1.500		1.0	(Stag = 0°)
		-----		101.0	( 50°)
		-----		27.0	( 60°)
		-----		1.5	( 120°)
		1.500		70.0	( 30°)
		-----		41.6	( 45°)
		-----		5.3	( 90°)
		1.500		70.1	( 30°)
		-----		26.4	( 60°)
		-----		4.1	( 90°)
		1.500		96.5	
1/4" D-1/8" d	5.0"	1.350		92.5	
		"		91.0	
		"		88.0	
		2.225		97.5	
		"		94.0	
		"		83.0	
		1.500		75.0	
		"		74.0	
		"		78.0	
		"		80.5 (4)	
		1.500		226.0 (4)	
		"		229.0 (4)	
		2.225		193.0 (4)	
				195.0	
					Decay form of specimen, Run 529
					" " " " " "
					" " " " " "
					" " " " " "
					119.0 Actual measure
					121.0 " "
					104.0 " "
					103.0 " "

(1) Configuration: Gives model dia. followed by copper insert dia. (2) Station: Distance to stag. point, from nozzle exit  
 (3) Decayed model position increased by amount ablated @ stag. point  
 (4) These values corrected for relatively oversize insert-see text

UNCLASSIFIED

**TABLE 11**  
SUMMARY OF MASS RATE DATA

Specimen Dia.	1/4"	Notes -
Specimen Mat'l	ATJ	(1) Unmodified data
Nozzle Exit Dia.	5"	(2) Data modified for
Stag'n Press., atm	$8.25 \times 10^{-3}$	Reynolds No. Effects
Enthalpy Ratio	350	☐ Symbol on graphs
Reynolds No., $Re_s$	11	

Run Nos.	Time Sec.	Mass Loss Lb/ft. <sup>2</sup>	Avg. °K Temp.	Mass Rate $\times 10^3$ lb/ft <sup>2</sup> - sec		$\dot{m} \sqrt{\frac{Rb}{Pe}} \times 10^3$ lb/ft <sup>3/2</sup> - sec - Atm <sup>1/2</sup>	
				(1)	(2)	(1)	(2)
472	80	.1197					
463	39	.0459					
	41	.0738	1425	1.93	2.185	3.42	3.875
473	120	.1980					
472	80	.1197					
	40	.0783	1485	1.995	2.065	3.53	3.83
462	127	.2187					
472	80	.1197					
	47	.0990	1480	2.155	2.35	3.56	3.88
474	160	.2898					
462	127	.2187					
	33	.0711	1405	2.195	2.52	3.57	4.13
474	160	.2898					
473	120	.1980					
	40	.0918	1435	2.34	2.64	3.60	4.06
473	120	.1980					
463	39	.0459					
	81	.1521	1400	1.915	2.225	3.39	3.93
458	128	.1791					
461	100	.1377					
	28	.0414	1385	1.54	1.82	2.72	3.21
458	128	.1791					
459	100	.1089					
	28	.0702	1370	2.56	3.06	4.53	5.42
474	160	.2898					
461	100	.1377					
	60	.1521	1410	2.585	2.965	4.58	5.26
474	160	.2898					
459	100	.1089					
	60	.1809	1400	3.075	3.57	5.44	6.30

UNCLASSIFIED

TABLE 11  
SUMMARY OF MASS RATE DATA

Specimen Dia.	1/4"	Notes -
Specimen Mat'l	ATJ	(1) Unmodified data
Nozzle Exit Dia.	5"	(2) Data modified for
Stag'n Press., atm	$8.25 \times 10^{-3}$	Reynolds No. Effects
Enthalpy Ratio	350	<input checked="" type="checkbox"/> Symbol on graphs
Reynolds No., $Re_s$	11	

Run Nos.	Time Sec.	Mass Loss Lb/ft. <sup>2</sup>	Avg. °K Temp.	Mass Rate $\times 10^3$ lb/ft <sup>2</sup> - sec		$\dot{m} \sqrt{\frac{Rb}{Pe}} \times 10^3$ lb/ft <sup>3/2</sup> - sec - Atm <sup>1/2</sup>	
				(1)	(2)	(1)	(2)
473	120	.1980					
461	100	.1377					
	20	.0603	1410	3.07	3.53	5.43	6.24
462	127	.2187					
461	100	.1377					
	27	.0810	1405	3.06	3.55	5.42	6.28
462	127	.2187					
473	120	.1980					
	7	.0207	1425	3.015	3.415	5.34	6.05
474	160	.2898					
472	80	.1197					
	80	.1701	1440	2.175	2.44	3.87	4.34
463	39	.0459	1300	1.20	1.655	2.12	2.92
461	100	.1377	1320	1.40	1.825	2.48	4.05
473	120	.1980	1300	1.68	2.035	2.97	3.61
462	127	.2187	1340	1.79	2.25	3.16	3.97
474	160	.2898	1300	1.85	2.25	3.28	3.99

UNCLASSIFIED

TABLE 12  
SUMMARY OF MASS RATE DATA

Specimen Dia. 1/4"	Notes -
Specimen Mat'l ATJ	(1) Unmodified data
Nozzle Exit Dia. 1.2"	(2) Data modified for
Stag'n Press., atm $5.60 \times 10^{-2}$	Reynolds No. Effects
Enthalpy Ratio 350	⊙ Symbol on graphs
Reynolds No., $Re_s$ 85	

Run Nos.	Time Sec.	Mass Loss Lb/ft. <sup>2</sup>	Avg. °K Temp.	Mass Rate $\times 10^3$ lb/ft <sup>2</sup> - sec		$\dot{m} \sqrt{\frac{Rb}{Pe}} \times 10^3$ lb/ft <sup>3/2</sup> - sec - Atm <sup>1/2</sup>	
				(1)	(2)	(1)	(2)
496	80	.8415					
494	45	.4392					
	35	.4023	2150	11.50	8.86	7.80	6.07
501	87.5	.9702					
494	45	.4392					
	42.5	.5310	2125	12.48	9.71	8.46	6.58
495	100	1.0404					
494	45	.4392					
	55	.6012	2175	11.14	8.68	7.56	5.88
489	100	1.0593					
494	45	.4392					
	55	.6201	2230	11.29	8.77	7.65	5.95
490	130	1.4103					
494	45	.4392					
	85	.9711	2660	11.42	8.84	7.75	6.00
498	130	1.4490					
494	45	.4392					
	85	1.0108	2160	11.83	9.19	8.02	6.24
497	160	1.7460					
494	45	.4392					
	115	1.3068	2160	11.34	8.81	7.69	5.98
488	165	1.9440					
494	45	.4392					
	120	1.4048	2320	11.70	9.08	7.94	6.16
501	100	1.0602					
494	45	.4392					
	55	.6210	2180	11.28	8.77	7.65	5.95

UNCLASSIFIED

UNCLASSIFIED

TABLE 12  
SUMMARY OF MASS RATE DATA

Specimen Dia. 1/4" Notes -  
Specimen Mat'l ATJ (1) Unmodified data  
Nozzle Exit Dia. 1.2" (2) Data modified for  
Stag'n Press., atm  $5.60 \times 10^{-2}$  Reynolds No. Effects  
Enthalpy Ratio 350  $\odot$  Symbol on graphs  
Reynolds No.,  $Re_s$  85

Run Nos.	Time Sec.	Mass Loss Lb/ft. <sup>2</sup>	Avg. °K Temp.	Mass Rate $\times 10^3$ lb/ft <sup>2</sup> - sec		$\dot{m} \sqrt{\frac{Rb}{Pe}} \times 10^3$ lb/ft <sup>3/2</sup> - sec - Atm <sup>1/2</sup>	
				(1)	(2)	(1)	(2)
489	100	1.0593	2230	11.88	9.24	8.05	6.25
496	80	.8415					
	20	.2178					
501	100	1.0602	2180	11.90	9.25	8.07	6.28
496	80	.8415					
	20	.2187					
498	130	1.4490	2160	12.14	9.44	8.23	6.39
496	80	.8415					
	50	.6075					
490	130	1.4103	2660	11.37	8.80	7.71	5.97
496	80	.8415					
	50	.5688					
497	160	1.7460	2160	11.30	8.79	7.66	5.95
496	80	.8415					
	80	.9045					
488	165	1.9440	2320	12.95	10.08	8.78	6.72
496	80	.8415					
	85	1.1025					
498	130	1.4490	2135	11.28	8.77	7.65	5.95
501	87.5	.9702					
	42.5	.4788					
488	165	1.9440	2290	12.57	9.76	8.52	6.62
501	87.5	.9702					
	77.5	.9738					
490	130	1.4103	2685	12.32	9.55	8.35	6.45
495	100	1.0404					
	30	.3699					

UNCLASSIFIED



TABLE 12  
SUMMARY OF MASS RATE DATA

Specimen Dia.	1/4"	Notes -
Specimen Mat'l	ATJ	(1) Unmodified data
Nozzle Exit Dia.	1.2"	(2) Data modified for
Stag'n Press., atm	$5.60 \times 10^{-2}$	Reynolds No. Effects
Enthalpy Ratio	350	⊙ Symbol on graphs
Reynolds No., $Re_s$	85	

Run Nos.	Time Sec.	Mass Loss $\frac{Lb}{ft.}^2$	Avg. °K Temp.	Mass Rate $\times 10^3$ lb/ft <sup>2</sup> - sec		$\dot{m} \sqrt{\frac{Rb}{Pe}} \times 10^3$ lb/ft <sup>3/2</sup> - sec - Atm <sup>1/2</sup>	
				(1)	(2)	(1)	(2)
497	160	1.7460					
495	100	1.0404					
	60	.7056	2185	11.77	9.14	7.98	6.20
488	165	1.9440	2350	11.77	9.11	7.98	6.11
498	130	1.4490	2170	11.13	8.66	7.55	5.87
501	87.5	.9702	2100	11.08	8.62	7.51	5.85
490	130	1.4103					
489	100	1.0593					
	30	.3510	2740	11.70	9.06	7.94	6.17
497	160	1.7640					
489	100	1.0593					
	60	.7047	2280	11.77	9.15	7.98	6.20
490	130	1.4103					
501	100	1.0602					
	30	.3501	2690	11.69	9.05	7.92	6.06
497	160	1.7640					
501	100	1.0602					
	60	.7038	2190	11.72	9.13	7.95	6.11
497	160	1.7640					
490	130	1.4103					
	30	.3537	2670	11.76	9.10	7.98	6.18

UNCLASSIFIED

TABLE 13  
SUMMARY OF MASS RATE DATA

Specimen Dia. 1" Notes -  
Specimen Mat'l ATJ (1) Unmodified data  
Nozzle Exit Dia. 5" (2) Data modified for  
Stag'n Press., atm  $9.7 \times 10^{-3}$  Reynolds No. Effects  
Enthalpy Ratio 400  $\Delta$  Symbol on graphs  
Reynolds No.,  $Re_s$  44

Run Nos.	Time Sec.	Mass Loss Lb/ft. <sup>2</sup>	Avg. °K Temp.	Mass Rate $\times 10^3$ lb/ft <sup>2</sup> - sec		$\dot{m} \sqrt{\frac{Rb}{Pe}} \times 10^3$ lb/ft <sup>3/2</sup> - sec - Atm <sup>1/2</sup>	
				(1)	(2)	(1)	(2)
303	120	.0936					
305	60	.0324					
	60	.0612	1235	1.019	1.112	3.31	3.61
308	150	.1224					
305	60	.0324					
	90	.0900	1245	1.00	1.080	3.25	3.51
311	180	.1467					
305	60	.0324					
	120	.1143	1245	.939	1.013	3.05	3.19
316	240	.2007					
305	60	.0324					
	180	.1683	1245	.897	.969	2.92	3.15
307	110	.0828					
306	100	.0711					
	10	.0117	1280	1.171	1.211	3.81	3.94
303	120	.0936					
306	100	.0711					
	20	.0225	1290	1.127	1.139	3.68	3.72
308	150	.1224					
306	100	.0711					
	50	.0513	1300	1.023	1.021	3.33	3.32
311	180	.1467					
306	100	.0711					
	80	.0756	1300	.947	.945	3.08	3.07
316	240	.2007					
306	100	.0711					
	140	.1296	1300	.926	.925	3.01	3.00
303	120	.0936					
307	110	.0828					
	10	.0108	1300	1.082	1.080	3.52	3.51

UNCLASSIFIED

TABLE 13  
SUMMARY OF MASS RATE DATA

Specimen Dia.	1"	Notes -
Specimen Mat'l	ATJ	(1) Unmodified data
Nozzle Exit Dia.	5"	(2) Data modified for
Stag'n Press., atm	$9.7 \times 10^{-3}$	Reynolds No. Effects
Enthalpy Ratio	400	$\Delta$ Symbol on graphs
Reynolds No., $Re_s$	44	

Run Nos.	Time Sec.	Mass Loss Lb/ft. <sup>2</sup>	Avg. °K Temp.	Mass Rate $\times 10^3$ lb/ft <sup>2</sup> - sec		$\dot{m} \sqrt{\frac{R_b}{P_e}} \times 10^3$ lb/ft <sup>3/2</sup> - sec - Atm <sup>1/2</sup>	
				(1)	(2)	(1)	(2)
308	150	.1224					
307	110	.0828					
	40	.0396	1310	.988	.968	3.21	3.16
311	180	.1467					
307	110	.0828					
	70	.0639	1310	.909	.892	2.96	2.91
316	240	.2007					
307	110	.0828					
	130	.1179	1310	.906	.890	2.94	2.89
308	150	.1224					
303	120	.0936					
	30	.0288	1320	.964	.930	3.13	3.02
311	180	.1467					
303	120	.0936					
	60	.0531	1320	.885	.854	2.88	2.78
316	240	.2007					
303	120	.0936					
	120	.1071	1320	.890	.859	2.90	2.80
311	180	.1467					
308	150	.1224					
	30	.0243	1330	.811	.770	2.64	2.505
316	240	.2007					
308	150	.1224					
	90	.0783	1330	.868	.823	2.82	2.68
316	240	.2007					
311	180	.1467					
	60	.0540	1330	.902	.856	2.93	2.78

TABLE 13  
SUMMARY OF MASS RATE DATA

Specimen Dia.	1"	Notes -
Specimen Mat'l	ATJ	(1) Unmodified data
Nozzle Exit Dia.	5"	(2) Data modified for
Stag'n Press., atm	$9.7 \times 10^{-3}$	Reynolds No. Effects
Enthalpy Ratio	400	Δ Symbol on graphs
Reynolds No., $Re_s$	44	

Run Nos.	Time Sec.	Mass Loss Lb/ft. <sup>2</sup>	Avg. °K Temp.	Mass Rate $\times 10^3$ lb/ft <sup>2</sup> - sec		$\dot{m} \sqrt{\frac{R_b}{P_s}} \times 10^3$ lb/ft <sup>3/2</sup> - sec - Atm <sup>1/2</sup>	
				(1)	(2)	(1)	(2)
327	300	.720					
323	63	.126					
	237	.594	1670	2.50	2.075	8.12	6.23
326	240	.567					
323	63	.126					
	177	.441	1685	2.49	2.065	8.10	6.21
322	213	.495					
323	63	.126					
	150	.369	1745	2.46	2.03	8.00	6.10
325	139	.297					
323	63	.126					
	76	.171	1685	2.31	1.908	7.52	5.74
327	300	.720					
324	77	.153					
	223	.567	1680	2.54	2.108	8.25	6.32
326	240	.567					
324	77	.153					
	163	.414	1695	2.54	2.108	8.25	6.32
322	213	.495					
324	77	.153					
	136	.342	1755	2.52	2.075	8.19	6.24
325	139	.297					
324	77	.153					
	62	.144	1695	2.33	1.934	7.58	5.82
327	300	.720					
325	139	.297					
	161	.423	1690	2.63	2.18	8.55	6.55

**TABLE 13**  
SUMMARY OF MASS RATE DATA

Specimen Dia.	1"	Notes -
Specimen Mat'l	ATJ	(1) Unmodified data
Nozzle Exit Dia.	5"	(2) Data modified for
Stag'n Press., atm	$9.7 \times 10^{-3}$	Reynolds No. Effects
Enthalpy Ratio	400	$\Delta$ Symbol on graphs
Reynolds No., $Re_s$	44	

Run Nos.	Time Sec.	Mass Loss Lb/ft. <sup>2</sup>	Avg. °K Temp.	Mass Rate $\times 10^3$ lb/ft <sup>2</sup> - sec		$\dot{m} \sqrt{\frac{R_b}{P_e}} \times 10^3$ lb/ft <sup>3/2</sup> - sec - Atm <sup>1/2</sup>	
				(1)	(2)	(1)	(2)
326	240	.567					
325	139	.297					
	101	.270	1710	2.67	2.21	8.68	6.63
322	213	.495					
325	139	.297					
	74	.198	1770	2.68	2.21	8.71	6.64
327	300	.720					
322	213	.495					
	87	.225	1750	2.59	2.138	8.42	6.43
326	240	.567					
322	213	.495					
	27	.072	1770	2.67	2.20	8.68	6.61
327	300	.720					
326	240	.567					
	60	.153	1690	2.55	2.115	8.29	6.35
323	63	.126	1350	2.00	1.833	6.50	6.02
324	77	.153	1450	1.99	1.73	6.47	5.63
325	139	.297	1450	2.14	1.86	6.95	6.04
322	213	.495	1750	2.32	1.915	7.54	5.75
326	240	.567	1630	2.37	1.975	7.70	5.93
327	300	.720	1600	2.40	2.008	7.80	6.03

TABLE 14  
SUMMARY OF MASS RATE DATA

Specimen Dia. 1" Notes -  
 Specimen Mat'l ATJ (1) Unmodified data  
 Nozzle Exit Dia. 1.2" (2) Data modified for  
 Stag'n Press., atm  $4.43 \times 10^{-2}$  Reynolds No. Effects  
 Enthalpy Ratio 400  $\diamond$  Symbol on graphs  
 Reynolds No.,  $Re_s$  342

Run Nos.	Time Sec.	Mass Loss Lb/ft.	Avg. °K Temp.	Mass Rate $\times 10^3$ lb/ft <sup>2</sup> - sec		$\dot{m} \sqrt{\frac{Rb}{Pe}} \times 10^3$ lb/ft <sup>3/2</sup> - sec - Atm <sup>1/2</sup>	
				(1)	(2)	(1)	(2)
342	200	1.0017					
330	39	.216					
	161	0.7857	2050	4.88	3.71	7.46	5.68
331	100	.513					
330	39	.216					
	61	.297	1825	4.88	3.74	7.46	5.73
342	200	1.0017					
336	60	.2970					
	140	.7047	1790	5.05	3.88	7.71	5.92
331	100	.513					
336	60	.297					
	40	.216	1960	5.39	4.10	8.24	6.28
342	200	1.0017					
331	100	.513					
	100	.4887	2115	4.86	3.69	7.42	5.65
342	200	1.0017					
332	150	.729					
	50	.2727	2135	5.45	4.14	8.33	6.30
342	200	1.0017	1600	5.01	3.93	7.66	6.00
331	100	.513	2050	5.12	3.89	7.83	5.95
330	39	.216	1600	5.53	4.32	8.45	6.13

**TABLE 15**  
**SUMMARY OF MASS RATE DATA**

<b>Specimen Dia.</b>	1/16"	<b>Notes -</b>
<b>Specimen Mat'l</b>	ATJ	(1) Unmodified data
<b>Nozzle Exit Dia.</b>	5"	(2) Data modified for
<b>Stag'n Press., atm</b>	$7.70 \times 10^{-3}$	Reynolds No. Effects
<b>Enthalpy Ratio</b>	350	● Symbol on graphs
<b>Reynolds No., <math>Re_s</math></b>	2.7	

Run Nos.	Time Sec.	Mass Loss Lb/ft. <sup>2</sup>	Avg. °K Temp.	Mass Rate $\times 10^3$ lb/ft <sup>2</sup> - sec		$\dot{m} \sqrt{\frac{Rb}{Pe}} \times 10^3$ lb/ft <sup>3/2</sup> - sec - Atm <sup>1/2</sup>	
				(1)	(2)	(1)	(2)
560	250	.6751					
521	60	.1494					
	190	.5257	1515	2.77	5.21	2.54	4.78
560	250	.6751					
520	120	.3168					
	130	.3583	1520	2.75	5.15	2.52	4.73
560	250	.6751					
519	120	.2988					
	130	.3763	1540	2.90	5.38	2.66	4.94
560	250	.6751					
518	100	.2556					
	150	.4195	1545	2.80	5.17	2.56	4.73
560	250	.6751					
517	100	.2520					
	150	.4231	1560	2.82	5.15	2.58	4.72
560	250	.6751					
516	80	.1863					
	170	.4888	1545	2.87	5.30	2.62	4.84
560	250	.6751					
515	80	.2007					
	170	.4744	1520	2.79	5.23	2.55	4.79
560	250	.6751					
514	60	.1620					
	190	.5131	1500	2.70	5.13	2.47	4.70
560	250	.6751					
513	40	.1107					
	210	.5644	1485	2.69	5.17	2.46	4.72

TABLE 15  
SUMMARY OF MASS RATE DATA

Specimen Dia. 1/16" Notes -  
Specimen Mat'l ATJ (1) Unmodified data  
Nozzle Exit Dia. 5" (2) Data modified for  
Stag'n Press., atm  $7.70 \times 10^{-3}$  Reynolds No. Effects  
Enthalpy Ratio 350 ● Symbol on graphs  
Reynolds No.,  $Re_s$  2.7

Run Nos.	Time Sec.	Mass Loss Lb/ft.. <sup>2</sup>	Avg. °K Temp.	Mass Rate $\times 10^3$ lb/ft <sup>2</sup> - sec		$\dot{m} \sqrt{\frac{Rb}{Pe}} \times 10^3$ lb/ft <sup>3/2</sup> - sec - Atm <sup>1/2</sup>	
				(1)	(2)	(1)	(2)
558	200	.5454	1615	2.35	5.75	2.97	4.79
557	100	.2205					
	100	.3249					
558	200	.5454	1525	2.83	5.29	2.59	4.85
521	60	.1494					
	140	.3960					
558	200	.5454	1530	2.86	5.33	2.62	4.89
520	120	.3168					
	80	.2286					
558	200	.5454	1550	3.08	5.65	2.82	4.99
519	120	.2988					
	80	.2466					
558	200	.5454	1555	2.90	5.31	2.65	4.85
518	100	.2556					
	100	.2898					
558	200	.5454	1570	2.93	6.31	2.68	4.86
517	100	.2520					
	100	.2934					
558	200	.5454	1555	2.99	5.47	2.74	5.02
516	80	.1863					
	120	.3591					
558	200	.5454	1530	2.87	5.34	2.63	4.90
515	80	.2007					
	120	.3447					
558	200	.5454	1510	2.74	5.17	2.51	4.74
514	60	.1620					
	140	.3834					



**TABLE 15**  
**SUMMARY OF MASS RATE DATA**

Specimen Dia.	1/16"	Notes -
Specimen Mat'l	ATJ	(1) Unmodified data
Nozzle Exit Dia.	5"	(2) Data modified for
Stag'n Press., atm	7.70 x 10 <sup>-3</sup>	Reynolds No. Effects
Enthalpy Ratio	350	● Symbolion graphs
Reynolds No., Re <sub>s</sub>	2.7	

Run Nos.	Time Sec.	Mass Loss Lb./ft. <sup>2</sup>	Avg. °K Temp.	Mass Rate x 10 <sup>3</sup> lb/ft <sup>2</sup> - sec		$\dot{m} \sqrt{\frac{Rb}{Pe}} \times 10^3$ lb/ft <sup>3/2</sup> - sec - Atm <sup>1/2</sup>	
				(1)	(2)	(1)	(2)
558	200	.5454					
513	40	.1107					
	160	.4347	1495	2.72	5.20	2.49	4.75
559	150	.3954					
557	100	.2205					
	50	.1749	1640	3.49	6.22	3.19	5.69
559	150	.3954					
521	60	.1494					
	90	.2460	1550	2.73	5.02	2.50	4.60
559	150	.3954					
520	120	.3168					
	30	.0786	1555	2.62	4.79	2.40	4.40
559	150	.3954					
519	120	.2988					
	30	.0966	1575	3.22	5.85	2.95	5.35
559	150	.3954					
518	100	.2556					
	50	.1398	1580	2.79	5.05	2.55	4.62
559	150	.3954					
517	100	.2520					
	50	.1434	1595	2.87	5.15	2.63	4.72
559	150	.3954					
516	80	.1863					
	70	.2091	1580	2.98	5.40	2.72	4.92
559	150	.3954					
515	80	.2007					
	70	.1947	1555	2.78	5.09	2.54	4.65
559	150	.3754					
514	60	.1620					
	90	.2334	1535	2.54	4.65	2.32	4.25

TABLE 15  
SUMMARY OF MASS RATE DATA

Specimen Dia. 1/16" Notes -  
 Specimen Mat'l ATJ (1) Unmodified data  
 Nozzle Exit Dia. 5" (2) Data modified for  
 Stag'n Press., atm  $7.70 \times 10^{-3}$  Reynolds No. Effects  
 Enthalpy Ratio 350 ● Symbol on graphs  
 Reynolds No.,  $Re_s$  2.7

Run Nos.	Time Sec.	Mass Loss Lb./ft. <sup>2</sup>	Avg. °K Temp.	Mass Rate $\times 10^3$ lb/ft <sup>2</sup> - sec		$\dot{m} \sqrt{\frac{Rb}{Pe}} \times 10^3$ lb/ft <sup>3/2</sup> - sec - Atm <sup>1/2</sup>	
				(1)	(2)	(1)	(2)
559	150	.3954	1520	2.59	4.85	2.37	4.44
513	40	.1107					
	110	.2847					
557	100	.2205	1480	1.83	3.53	1.68	3.24
513	40	.1107					
	60	.1098					
521	60	.1495	1445	2.99	5.90	2.74	5.41
513	40	.1107					
	20	.0588					
520	120	.3168	1465	2.78	5.43	2.54	4.95
521	60	.1494					
	60	.1674					
520	120	.3168	1495	3.06	5.83	2.80	5.33
518	100	.2556					
	20	.0612					
520	120	.3168	1510	3.24	6.12	2.96	5.59
517	100	.2520					
	20	.0648					
520	120	.3168	1495	3.26	6.22	2.98	5.69
516	80	.1863					
	40	.1305					
520	120	.3168	1470	2.91	5.65	2.66	5.17
515	80	.2007					
	40	.1161					
520	120	.3168	1450	2.58	5.08	2.36	4.65
514	60	.1620					
	60	.1548					

TABLE 15

## SUMMARY OF MASS RATE DATA

Specimen Dia. 1/16"  
 Specimen Mat'l ATJ  
 Nozzle Exit Dia. 5"  
 Stag'n Press., atm  $7.70 \times 10^{-3}$   
 Enthalpy Ratio 350  
 Reynolds No.,  $Re_s$  2.7

Notes -  
 (1) Unmodified data  
 (2) Data modified for Reynolds No. Effects  
 ● Symbol on graphs

Run Nos.	Time Sec.	Mass Loss Lb/ft. <sup>2</sup>	Avg. °K Temp.	Mass Rate $\times 10^3$ lb/ft <sup>2</sup> - sec		$\dot{m} \sqrt{\frac{Rb}{Pe}} \times 10^3$ lb/ft <sup>3/2</sup> - sec - Atm <sup>1/2</sup>	
				(1)	(2)	(1)	(2)
520	120	.3168					
513	40	.1107					
	80	.2061	1435	2.57	5.11	2.35	4.64
519	120	.2988					
521	60	.1494					
	60	.1494	1480	2.49	4.80	2.28	4.40
519	120	.2988					
518	100	.2556					
	20	.0432	1510	2.15	4.00	1.97	3.67
519	120	.2988					
517	100	.2520					
	20	.0468	1475	2.34	4.54	2.14	4.15
519	120	.2988					
516	80	.1863					
	40	.1125	1510	2.81	5.23	2.57	4.79
519	120	.2988					
515	80	.2007					
	40	.0979	1485	2.45	4.70	2.24	4.30
519	120	.2988					
514	60	.1620					
	60	.1368	1465	2.28	4.45	2.08	4.06
519	120	.2988					
513	40	.1107					
	80	.1881	1450	2.35	4.61	2.15	4.22
518	100	.2556					
521	60	.1494					
	40	.1062	1475	2.66	5.15	2.43	4.70

**TABLE 15**  
SUMMARY OF MASS RATE DATA

Specimen Dia.	1/16"	Notes - (1) Unmodified data (2) Data modified for Reynolds No. Effects ● Symbol on graphs
Specimen Mat'l	ATJ	
Nozzle Exit Dia.	5"	
Stag'n Press., atm	$7.70 \times 10^{-3}$	
Enthalpy Ratio	350	
Reynolds No., $Re_s$	2.7	

Run Nos.	Time Sec.	Mass Loss Lb./ft. <sup>2</sup>	Avg. °K Temp.	Mass Rate $\times 10^3$ lb/ft <sup>2</sup> - sec		$\dot{m} \sqrt{\frac{R_b}{P_e}} \times 10^3$ lb/ft <sup>3/2</sup> - sec - Atm <sup>1/2</sup>	
				(1)	(2)	(1)	(2)
518	100	.2556					
516	80	.1863					
	20	.0693	1505	3.46	6.55	3.16	5.99
518	100	.2556					
515	80	.2007					
	20	.0549	1480	2.74	5.20	2.51	4.84
518	100	.2556					
514	60	.1620					
	40	.0936	1460	2.34	4.58	2.14	4.17
518	100	.2556					
513	40	.1107					
	60	.1449	1445	2.41	4.75	2.21	4.36
517	100	.2520					
521	60	.1494					
	40	.1026	1495	2.56	4.89	2.34	4.47
517	100	.2520					
516	80	.1494					
	20	.0657	1525	3.29	6.15	3.01	5.63
517	100	.2520					
515	80	.2007					
	20	.0513	1500	2.56	4.85	2.34	4.45
517	100	.2520					
514	60	.1620					
	40	.0900	1480	2.24	4.26	2.05	3.95
517	100	.2520					
513	40	.1107					
	60	.1413	1465	2.35	4.59	2.15	4.19

TABLE 15  
SUMMARY OF MASS RATE DATA

Specimen Dia. 1/16" Notes -  
 Specimen Mat'l ATJ (1) Unmodified data  
 Nozzle Exit Dia. 5" (2) Data modified for  
 Stag'n Press., atm  $7.70 \times 10^{-3}$  Reynolds No. Effects  
 Enthalpy Ratio 350 ● Symbol on graphs  
 Reynolds No.,  $Re_s$  2:7

Run Nos.	Time Sec.	Mass Loss Lb/ft. <sup>2</sup>	Avg. °K Temp.	Mass Rate $\times 10^3$ lb/ft <sup>2</sup> - sec		$\dot{m} \sqrt{\frac{Rb}{Pe}} \times 10^3$ lb/ft <sup>3/2</sup> - sec - Atm <sup>1/2</sup>	
				(1)	(2)	(1)	(2)
516	80	.1863					
521	60	.1494					
	20	.0369	1470	1.85	3.60	1.69	3.28
516	80	.1863					
513	40	.1107					
	40	.0756	1440	1.89	3.74	1.73	3.43
515	80	.2007					
521	60	.1494					
	20	.0513	1475	2.56	5.00	2.34	4.53
515	80	.2007					
514	60	.1620					
	20	.0387	1460	1.93	3.77	1.77	3.46
515	80	.2007					
513	40	.1107					
	40	.0900	1445	2.24	4.42	2.05	4.04
521	60	.1494					
513	40	.1107					
	20	.0387	1445	1.94	3.82	1.78	3.51
514	60	.1620					
513	40	.1107					
	20	.0513	1445	2.56	5.05	2.34	4.62
521	60	.1494	1400	2.49	5.09	2.28	4.65
516	80	.1863	1460	2.33	4.55	2.13	4.17
520	120	.3168	1410	2.64	5.35	2.42	4.90

TABLE 16  
SUMMARY OF MASS RATE DATA

Specimen Dia. 1" Notes -  
 Specimen Mat'l ATJ (1) Unmodified data  
 Nozzle Exit Dia. 5" (2) Data modified for  
 Stag'n Press., atm  $7.00 \times 10^{-3}$  Reynolds No. Effects  
 Enthalpy Ratio 160  $\nabla$  Symbol on graphs  
 Reynolds No.,  $Re_s$  51

Run Nos.	Time Sec.	Mass Loss Lb/ft. <sup>2</sup>	Avg. °K Temp.	Mass Rate $\times 10^3$ lb/ft <sup>2</sup> - sec		$\dot{m} \sqrt{\frac{Rb}{Pe}} \times 10^3$ lb/ft <sup>3/2</sup> - sec - Atm <sup>1/2</sup>	
				(1)	(2)	(1)	(2)
631	1200	1.2195	1280	1.02	1.042	3.90	3.98
631	1200	1.2195					
634	240	.2232					
	960	.9963	1270	1.04	1.09	3.975	4.165
631	1200	1.2195					
642	310	.2305					
	890	.9890	1280	1.11	1.134	4.24	4.34
631	1200	1.2195					
635	360	.2979					
	840	.9216	1285	1.10	1.123	4.21	4.29
631	1200	1.2195					
633	463	.4626					
	737	.7569	1260	1.03	1.090	3.94	4.165
631	1200	1.2195					
639	600	.4707					
	600	.7488	1285	1.25	1.278	4.77	4.89
631	1200	1.2195					
638	720	.6138					
	480	.6057	1275	1.26	1.307	4.82	5.00
631	1200	1.2195					
643	772	.6462					
	428	.5733	1300	1.34	1.348	5.12	5.15
631	1200	1.2195					
644	801	.7137					
	399	.5058	1295	1.265	1.287	4.84	4.92
632	960	.6930	1260	0.722	.765	2.76	2.92

**TABLE 16**  
SUMMARY OF MASS RATE DATA

Specimen Dia.	1"	Notes -
Specimen Mat'l	ATJ	(1) Unmodified data
Nozzle Exit Dia.	5"	(2) Data modified for
Stag'n Press., atm	$7.00 \times 10^{-3}$	Reynolds No. Effects
Enthalpy Ratio	160	▽ Symbol on graphs
Reynolds No., $Re_s$	51	

Run Nos.	Time Sec.	Mass Loss Lb/ft. <sup>2</sup>	Avg. °K Temp.	Mass Rate $\times 10^3$ lb/ft <sup>2</sup> - sec		$\dot{m} \sqrt{\frac{Rb}{Pe}} \times 10^3$ lb/ft <sup>3/2</sup> - sec - Atm <sup>1/2</sup>	
				(1)	(2)	(1)	(2)
632	960	.6930					
634	240	.2232					
	720	.4698	1255	0.653	.695	2.66	3.045
632	960	.6930					
642	310	.2305					
	650	.4625	1260	0.713	.765	2.725	2.925
632	960	.6930					
635	360	.2979					
	600	.3951	1270	0.658	.690	2.515	2.64
632	960	.6930					
633	463	.4626					
	497	.2304	1245	0.464	.481	1.773	1.84
632	960	.6930					
641	480	.4104					
	480	.2826	1275	0.589	.610	2.25	2.33
632	960	.6930					
639	600	.4707					
	360	.2223	1270	0.618	.648	2.36	2.48
632	960	.6930					
638	720	.6138					
	240	.0792	1260	0.330	.350	1.262	1.339
632	960	.6930					
643	772	.6462					
	188	.0468	1210	0.249	.278	.947	1.062
644	801	.7137	1265	0.890	.938	3.405	3.585
644	801	.7137					
634	240	.2232					
	561	.4905	1325	0.885	.860	3.38	3.285

TABLE 16  
SUMMARY OF MASS RATE DATA

Specimen Dia. 1" Notes -  
Specimen Mat'l ATJ (1) Unmodified data  
Nozzle Exit Dia. 5" (2) Data modified for  
Stag'n Press., atm  $7.00 \times 10^{-3}$  Reynolds No. Effects  
Enthalpy Ratio 160  $\nabla$  Symbol on graphs  
Reynolds No.,  $Re_s$  51

Run Nos.	Time Sec.	Mass Loss Lb/ft. <sup>2</sup>	Avg. °K Temp.	Mass Rate $\times 10^3$ lb/ft <sup>2</sup> - sec		$\dot{m} \sqrt{\frac{Rb}{Pe}} \times 10^3$ lb/ft <sup>3/2</sup> - sec - Atm <sup>1/2</sup>	
				(1)	(2)	(1)	(2)
644	801	.7137					
642	310	.2305					
	491	.4832	1255	0.985	1.048	3.76	4.00
644	801	.7137					
635	360	.2979					
	441	.4158	1340	0.944	.895	3.61	3.42
644	801	.7137					
633	463	.4626					
	338	.2511	1315	0.744	.733	2.85	2.91
644	801	.7137					
641	480	.4104					
	321	.3033	1270	0.942	.988	3.60	3.775
644	801	.7137					
639	600	.4707					
	201	.2430	1340	1.210	1.147	4.62	4.38
644	801	.7137					
638	720	.6138					
	81	.0999	1330	1.233	1.193	4.71	4.56
643	772	.6462					
634	240	.2232					
	532	.4230	1280	.795	.820	3.04	3.135
643	772	.6462					
642	310	.2305					
	462	.4157	1285	.900	.919	3.44	3.51
643	772	.6462					
635	360	.2979					
	412	.3483	1295	.845	.854	3.23	3.265



TABLE 16  
SUMMARY OF MASS RATE DATA

Specimen Dia. 1" Notes -  
 Specimen Mat'l ATJ (1) Unmodified data  
 Nozzle Exit Dia. 5" (2) Data modified for  
 Stag'n Press., atm  $7.00 \times 10^{-3}$  Reynolds No. Effects  
 Enthalpy Ratio 160 ▽ Symbol on graphs  
 Reynolds No.,  $Re_s$  51

Run Nos.	Time Sec.	Mass Loss Lb./ft. <sup>2</sup>	Avg. °K Temp.	Mass Rate $\times 10^3$ lb/ft <sup>2</sup> - sec		$\dot{m} \sqrt{\frac{Rb}{Pe}} \times 10^3$ lb/ft <sup>3/2</sup> - sec - Atm <sup>1/2</sup>	
				(1)	(2)	(1)	(2)
643	772	.6462	1270	.593	.622	2.265	2.38
633	463	.4626					
	309	.1836					
643	772	.6462	1225	.807	.893	3.085	3.42
641	480	.4104					
	292	.2358					
643	772	.6462	1295	1.021	1.031	3.90	3.94
639	600	.4707					
	172	.1755					
643	772	.6462	1285	0.623	.637	2.38	2.44
638	720	.6138					
	52	.0324					
638	720	.6138	1225	0.853	.943	3.26	3.60
638	720	.6138	1285	0.815	.832	3.12	3.18
634	240	.2232					
	480	.3906					
638	720	.6138	1290	0.935	.949	3.575	3.63
642	310	.2305					
	410	.3833					
638	720	.6138	1300	0.878	.883	3.36	3.38
635	360	.2979					
	360	.3159					
638	720	.6138	1275	0.588	.609	2.25	2.325
633	463	.4626					
	257	.1512					
638	720	.6138	1230	0.432	.494	1.65	1.89
641	480	.4104					
	240	.1034					

TABLE 16  
SUMMARY OF MASS RATE DATA

Specimen Dia.	1"	Notes -
Specimen Mat'l	ATJ	(1) Unmodified data
Nozzle Exit Dia.	5"	(2) Data modified for
Stag'n Press., atm	$7.00 \times 10^{-3}$	Reynolds No. Effects
Enthalpy Ratio	160	▽ Symbol on graphs
Reynolds No., $Re_s$	51	

Run Nos.	Time Sec.	Mass Loss Lb/ft. <sup>2</sup>	Avg. °K Temp.	Mass Rate $\times 10^3$ lb/ft <sup>2</sup> - sec		$\dot{m} \sqrt{\frac{Rb}{Pe}} \times 10^3$ lb/ft <sup>3/2</sup> - sec - Atm <sup>1/2</sup>	
				(1)	(2)	(1)	(2)
638	720	.6138					
639	600	.4707					
	120	.1431	1300	1.190	1.197	4.55	4.57
642	310	.2305	1250	0.745	.798	2.85	3.05
639	600	.4707	1245	0.785	.849	3.00	3.24
639	600	.4707					
634	240	.2232					
	360	.2475	1295	0.688	.695	2.63	2.66
639	600	.4707					
642	310	.2305					
	290	.2402	1225	0.829	.917	3.17	3.51
639	600	.4707					
635	360	.2979					
	240	.1728	1320	0.720	.703	2.75	2.69
639	600	.4707					
641	480	.4104					
	120	.0603	1240	0.504	.549	1.927	2.10
641	480	.4104	1255	0.855	.911	3.27	3.48
641	480	.4104					
634	240	.2232					
	240	.1872	1270	0.780	.817	2.98	3.125
641	480	.4104					
642	310	.2305					
	170	.1799	1275	1.068	1.108	4.08	4.23
641	480	.4104					
635	360	.2979					
	120	.1125	1285	0.938	.958	3.585	3.66

TABLE 16  
SUMMARY OF MASS RATE DATA

Specimen Dia.	1"	Notes -
Specimen Mat'l	ATJ	(1) Unmodified data
Nozzle Exit Dia.	5"	(2) Data modified for
Stag'n Press., atm	$7.00 \times 10^{-3}$	Reynolds No. Effects
Enthalpy Ratio	160	▽ Symbol on graphs
Reynolds No., $Re_s$	51	

Run Nos.	Time Sec.	Mass Loss Lb/ft. <sup>2</sup>	Avg. °K Temp.	Mass Rate $\times 10^3$ lb/ft <sup>2</sup> - sec		$\dot{m} \sqrt{\frac{R_b}{P_e}} \times 10^3$ lb/ft <sup>3/2</sup> - sec - Atm <sup>1/2</sup>	
				(1)	(2)	(1)	(2)
635	360	.2979	1245	0.829	.899	3.17	3.44
635	360	.2979					
642	240	.2232					
	120	.0747	1290	0.623	.569	2.38	2.175
635	360	.2979					
634	310	.2305					
	50	.0674	1285	1.347	1.374	5.14	5.25

CONFIDENTIAL

RESTRICTED DATA

UNCLASSIFIED

TABLE 17  
SUMMARY OF MASS RATE DATA

Specimen Dia. 1/4" Notes -  
Specimen Mat'l Mat'l. X (1) Unmodified data  
Nozzle Exit Dia. 5" (2) Data modified for  
Stag'n Press., atm 8.25 x 10<sup>-3</sup> Reynolds No. Effects  
Enthalpy Ratio 350 ☒ Symbol on graphs  
Reynolds No., Re<sub>s</sub> 11

Run Nos.	Time Sec.	Mass Loss Lb/ft. <sup>2</sup>	Avg. °K Temp.	Mass Rate x 10 <sup>3</sup> lb/ft <sup>2</sup> - sec		$\dot{m} \sqrt{\frac{Rb}{Pe}} \times 10^3$ lb/ft <sup>3/2</sup> - sec - Atm <sup>1/2</sup>	
				(1)	(2)	(1)	(2)
690	300	.3705	1650	1.235	1.995	2.19	3.54
690	300	.3705					
688	240	.2500					
	60	.1205	1765	2.008	3.24	3.56	5.74
690	300	.3705					
685	180	.1853					
	120	.1852	1700	1.54	2.485	2.73	4.40
690	300	.3705					
687	175	.1676					
	125	.2029	1705	1.63	2.63	2.88	4.65
690	300	.3705					
689	120	.1218					
	180	.2487	1775	1.38	2.23	2.44	3.94
690	300	.3705					
686	60	.0502					
	240	.3203	1725	1.34	2.16	2.37	3.82
688	240	.2500	1710	1.04	1.688	1.84	2.97
688	240	.2500					
685	180	.1853					
	60	.0647	1690	1.08	1.74	1.91	3.08
688	240	.2500					
687	175	.1676					
	65	.0824	1695	1.29	2.08	2.28	3.68
688	240	.2500					
689	120	.1218					
	120	.1282	1765	1.07	1.726	1.89	3.05

CONFIDENTIAL  
RESTRICTED DATA  
UNCLASSIFIED

UNCLASSIFIED

UNCLASSIFIED

TABLE 17  
SUMMARY OF MASS RATE DATA

Specimen Dia. 1/4" Notes -  
 Specimen Mat'l Mat'l. X (1) Unmodified data  
 Nozzle Exit Dia. 5" (2) Data modified for  
 Stag'n Press., atm  $8.25 \times 10^{-3}$  Reynolds No. Effects  
 Enthalpy Ratio 350 ☐ Symbol on graphs  
 Reynolds No.,  $Re_s$  11

Run Nos.	Time Sec.	Mass Loss Lb/ft. <sup>2</sup>	Avg. °K Temp.	Mass Rate $\times 10^3$ lb/ft <sup>2</sup> - sec		$\dot{m} \sqrt{\frac{Rb}{Pe}} \times 10^3$ lb/ft <sup>3/2</sup> - sec - Atm <sup>1/2</sup>	
				(1)	(2)	(1)	(2)
688	240	.2500					
686	60	.0502					
	180	.1998	1715	1.11	1.79	1.97	3.18
685	180	.1853					
689	120	.1218					
	60	.0635	1765	1.06	1.71	1.87	3.02
685	180	.1853					
686	60	.0502					
	120	.1351	1715	1.125	1.815	1.99	3.21
687	175	.1676	1590	.96	1.55	1.70	2.74
687	175	.1676					
689	120	.1218					
	55	.0458	1715	.83	1.34	1.47	2.37
687	175	.1676					
686	60	.0502					
	115	.1174	1665	1.02	1.647	1.81	2.92
689	120	.1218	1730	1.015	1.64	1.80	2.90
689	120	.1218					
686	60	.0502					
	60	.0716	1735	1.19	1.92	2.11	3.41
686	60	.0502	1630	.837	1.35	1.48	2.39
695	360	.3970	1750	1.10	1.775	1.95	3.15
695	360	.3970					
696	300	.3000					
	60	.0970	1755	1.62	2.61	2.87	4.63

UNCLASSIFIED

~~CONFIDENTIAL~~  
~~RESTRICTED DATA~~

UNCLASSIFIED

TABLE 17  
SUMMARY OF MASS RATE DATA

Specimen Dia.	1/4"	Notes -
Specimen Mat'l	Mat'l. X	(1) Unmodified data
Nozzle Exit Dia.	5"	(2) Data modified for
Stag'n Press., atm	$8.25 \times 10^{-3}$	Reynolds No. Effects
Enthalpy Ratio	350	<input type="checkbox"/> Symbol on graphs
Reynolds No., $Re_s$	11	

Run Nos.	Time Sec.	Mass Loss Lb/ft. <sup>2</sup>	Avg. °K Temp.	Mass Rate $\times 10^3$ lb/ft <sup>2</sup> - sec		$\dot{m} \sqrt{\frac{Rb}{Pe}} \times 10^3$ lb/ft <sup>3/2</sup> - sec - Atm <sup>1/2</sup>	
				(1)	(2)	(1)	(2)
695	360	.3970					
688	240	.2500					
	120	.1470	1790	1.23	1.985	2.18	3.52
695	360	.3970					
685	180	.1853					
	180	.2117	1725	1.175	1.90	2.08	3.36
695	360	.3970					
687	175	.1676					
	185	.2294	1730	1.24	2.00	2.20	3.55
695	360	.3970					
689	120	.1218					
	240	.2752	1800	1.145	1.85	2.03	3.28
695	360	.3970					
686	60	.0502					
	300	.3468	1750	1.156	1.867	2.05	3.31
696	300	.3000	1640	1.00	1.617	1.77	2.86
696	300	.3000					
688	240	.2500					
	60	.0500	1755	.83	1.34	1.47	2.37
696	300	.3000					
685	180	.1853					
	120	.1147	1700	.875	1.412	1.55	2.50
696	300	.3000					
687	175	.1676					
	125	.1324	1705	1.06	1.71	1.87	3.02

~~CONFIDENTIAL~~  
~~RESTRICTED DATA~~  
~~RESTRICTED DATA~~

UNCLASSIFIED

~~CONFIDENTIAL~~  
~~RESTRICTED DATA~~

UNCLASSIFIED

TABLE 17  
SUMMARY OF MASS RATE DATA

Specimen Dia.	1/4"	Notes -
Specimen Mat'l	Mat'l. X	(1) Unmodified data
Nozzle Exit Dia.	5"	(2) Data modified for
Stag'n Press., atm	$8.25 \times 10^{-3}$	Reynolds No. Effects
Enthalpy Ratio	350	<input type="checkbox"/> Symbol on graphs
Reynolds No., $Re_s$	11	

Run Nos.	Time Sec.	Mass Loss Lb/ft. <sup>2</sup>	Avg. °K Temp.	Mass Rate $\times 10^3$ lb/ft <sup>2</sup> - sec		$\dot{m} \sqrt{\frac{Rb}{Pe}} \times 10^3$ lb/ft <sup>3/2</sup> - sec - Atm <sup>1/2</sup>	
				(1)	(2)	(1)	(2)
696	300	.3000					
689	120	.1218					
	180	.1782	1775	.99	1.60	1.75	2.83
696	300	.3000					
686	60	.0502					
	240	.2498	1725	.96	1.518	1.66	2.68

~~CONFIDENTIAL~~  
~~RESTRICTED DATA~~  
~~Atomic Energy Act of 1954~~

UNCLASSIFIED

~~CONFIDENTIAL~~  
~~RESTRICTED DATA~~

UNCLASSIFIED

TABLE 18  
SUMMARY OF MASS RATE DATA

Specimen Dia.	1/4"	Notes -
Specimen Mat'l	Mat'l. X	(1) Unmodified data
Nozzle Exit Dia.	1.2"	(2) Data modified for
Stag'n Press., atm	$5.60 \times 10^{-2}$	Reynolds No. Effects
Enthalpy Ratio	350	⊙ Symbol on graphs
Reynolds No., $Re_s$	85	

Run Nos.	Time Sec.	Mass Loss Lb/ft. <sup>2</sup>	Avg. °K Temp.	Mass Rate $\times 10^3$ lb/ft <sup>2</sup> - sec		$\dot{m} \sqrt{\frac{Rb}{Pe}} \times 10^3$ lb/ft <sup>3/2</sup> - sec - Atm <sup>1/2</sup>	
				(1)	(2)	(1)	(2)
720	281	3.618	2030	12.87	12.31	8.72	8.35
720	281	3.618					
727	200	2.472					
	81	1.146	1990	14.16	13.80	9.59	9.35
720	281	3.618					
724	160	1.637					
	121	1.981	2070	16.38	15.38	11.15	10.47
720	281	3.618					
723	121	1.013					
	160	2.605	2070	16.30	15.31	11.00	10.32
720	281	3.618					
722	90	0.749					
	191	2.869	2085	15.03	14.08	10.20	9.54
720	281	3.618					
721	40	0.438					
	241	3.180	2085	13.20	12.35	8.84	8.27
720	281	3.618					
728	40	0.515					
	241	3.103	2025	12.87	12.37	8.71	8.37
725	280	.3216	2060	11.48	10.81	7.77	7.33
725	280	.3216					
726	240	.2707					
	40	.0509	2060	12.70	11.96	8.61	8.12
725	280	.3216					
727	200	.2472					
	80	.0744	2000	9.30	9.02	6.30	6.11

~~CONFIDENTIAL~~  
~~RESTRICTED DATA~~

UNCLASSIFIED



~~CONFIDENTIAL~~  
~~RESTRICTED DATA~~

UNCLASSIFIED

TABLE 18  
SUMMARY OF MASS RATE DATA

Specimen Dia.	1/4"	Notes -
Specimen Mat'l	Mat'l. X	(1) Unmodified data
Nozzle Exit Dia.	1.2"	(2) Data modified for
Stag'n Press., atm	$5.60 \times 10^{-2}$	Reynolds No. Effects
Enthalpy Ratio	350	⊙ Symbol on graphs
Reynolds No. $Re_s$	85	

Run Nos.	Time Sec.	Mass Loss Lb/ft. <sup>2</sup>	Avg. °K Temp.	Mass Rate $\times 10^3$ lb/ft <sup>2</sup> - sec		$\dot{m} \sqrt{\frac{Rb}{Pe}} \times 10^3$ lb/ft <sup>3/2</sup> - sec - Atm <sup>1/2</sup>	
				(1)	(2)	(1)	(2)
725	280	.3216					
724	160	.1637					
	120	.1579	2075	13.17	12.33	8.92	8.37
725	280	.3216					
723	121	.1013					
	159	.2203	2080	13.87	12.98	9.30	8.70
725	280	.3216					
722	90	.0749					
	190	.2467	2095	13.00	12.08	8.71	8.09
725	280	.3216					
721	40	.0438					
	240	.2778	2090	11.58	10.76	7.84	7.30
725	280	.3216					
728	40	.0515					
	240	.2701	2035	11.26	10.77	7.62	7.29
726	240	.2707	1990	11.28	10.98	7.64	7.45
726	240	.2707					
724	160	.1637					
	80	.1070	2010	13.38	12.92	9.06	8.76
726	240	.2707					
723	121	.1013					
	119	.1694	2010	14.26	13.78	9.65	9.33
726	240	.2707					
722	90	.0749					
	150	.1958	2025	13.04	12.53	8.84	8.50
726	240	.2707					
721	40	.0438					
	200	.2269	2025	11.45	11.00	7.75	7.45

~~CONFIDENTIAL~~  
~~RESTRICTED DATA~~

UNCLASSIFIED

~~CONFIDENTIAL~~  
~~RESTRICTED DATA~~

UNCLASSIFIED

TABLE 18  
SUMMARY OF MASS RATE DATA

Specimen Dia. 1/4" Notes -  
Specimen Mat'l Mat'l. X (1) Unmodified data  
Nozzle Exit Dia. 1.2" (2) Data modified for  
Stag'n Press., atm  $5.60 \times 10^{-2}$  Reynolds No. Effects  
Enthalpy Ratio 350 ☉ Symbol on graphs  
Reynolds No.,  $Re$  85

Run Nos.	Time Sec.	Mass Loss Lb/ft. <sup>2</sup>	Avg. °K Temp.	Mass Rate $\times 10^3$ lb/ft <sup>2</sup> - sec		$\dot{m} \sqrt{\frac{Rb}{Pe}} \times 10^3$ lb/ft <sup>3/2</sup> - sec - Atm <sup>1/2</sup>	
				(1)	(2)	(1)	(2)
726	240	.2707					
728	40	.0515					
	200	.2192	1965	10.96	10.80	7.42	7.31
727	200	.2472	1870	12.36	12.62	8.37	8.55
727	200	.2472					
722	90	.0749					
	110	.1723	1990	15.67	15.28	10.7	10.43
727	200	.2472					
721	40	.0438					
	160	.2034	1990	12.71	12.40	8.61	8.39
727	200	.2472					
728	40	.0515					
	160	.1957	1930	12.24	12.23	8.36	8.35
724	160	.1637	2030	10.23	9.80	6.94	6.65
724	160	.1637					
723	121	.1013					
	39	.0624	2035	16.00	15.31	10.85	10.38
724	160	.1637					
722	90	.0749					
	70	.0888	2050	12.69	12.02	8.69	8.24
724	160	.1637					
721	40	.0438					
	120	.1199	2050	9.99	9.47	6.76	6.41
724	160	.1637					
728	40	.0515					
	120	.1122	1990	9.35	9.12	6.33	6.17

~~CONFIDENTIAL~~  
~~RESTRICTED DATA~~

UNCLASSIFIED

RESTRICTED DATA

UNCLASSIFIED

TABLE 18  
SUMMARY OF MASS RATE DATA

Specimen Dia. 1/4" Notes -  
Specimen Mat'l Mat'l. X (1) Unmodified data  
Nozzle Exit Dia. 1.2" (2) Data modified for  
Stag'n Press., atm  $5.60 \times 10^{-2}$  Reynolds No. Effects  
Enthalpy Ratio 350 © Symbol on graphs  
Reynolds No.  $Re_s$  85

Run Nos.	Time Sec.	Mass Loss Lb/ft. <sup>2</sup>	Avg. °K Temp.	Mass Rate $\times 10^3$ lb/ft. <sup>2</sup> - sec		$\dot{m} \sqrt{\frac{R_b}{P_e}} \times 10^3$ lb/ft. <sup>3/2</sup> - sec - Atm <sup>1/2</sup>	
				(1)	(2)	(1)	(2)
723	121	.1013	2030	8.37	8.10	5.67	5.49
723	121	.1013					
722	90	.0749					
	31	.0264	2045	8.52	8.10	5.77	5.48
722	90	.0749	2060	8.33	7.85	5.64	5.31
721	40	.0438	1870	10.95	11.20	7.42	7.59
728	40	.0515	1940	12.88	12.80	8.71	8.66

RESTRICTED DATA

UNCLASSIFIED

~~CONFIDENTIAL~~  
~~RESTRICTED DATA~~

UNCLASSIFIED

TABLE 19  
SUMMARY OF MASS RATE DATA

Specimen Dia.	1"	Notes -	
Specimen Mat'l	Mat'l. X	(1)	Unmodified data
Nozzle Exit Dia.	5"	(2)	Data modified for
Stag'n Press., atm	$8.25 \times 10^{-3}$		Reynolds No. Effects
Enthalpy Ratio	350	$\Delta$	Symbol on graphs
Reynolds No., $Re_s$	44		

Run Nos.	Time Sec.	Mass Loss Lb/ft. <sup>2</sup>	Avg. °K Temp.	Mass Rate $\times 10^3$ lb/ft <sup>2</sup> - sec		$\dot{m} \sqrt{\frac{Rb}{Pe}} \times 10^3$ lb/ft <sup>3/2</sup> - sec - Atm <sup>1/2</sup>	
				(1)	(2)	(1)	(2)
682	300	.1562					
678	240	.1193					
	60	.0369	1610	.615	.733	2.17	2.48
678	240	.1193	1580	.499	.594	1.76	2.095
678	240	.1193					
681	120	.0454					
	120	.0739	1560	.615	.731	2.17	2.58
678	240	.1193					
667	180	.0817					
	60	.0376	1565	.627	.746	2.21	2.63
678	240	.1193					
679	180	.0763					
	60	.0430	1640	.717	.853	2.52	3.00
679	180	.0763	1500	.425	.506	1.50	1.785
679	180	.0763					
681	120	.0454					
	60	.309	1555	.602	.717	2.12	2.52
680	360	.1964	1490	.546	.650	1.92	2.29
680	360	.1964					
679	180	.0763					
	180	.1199	1555	.665	.791	2.34	2.79
680	360	.1964					
678	240	.1193					
	120	.0771	1595	.642	.765	2.26	2.69
680	360	.1964					
683	60	.0279					
	300	.1685	1555	.562	.670	1.97	2.34

~~CONFIDENTIAL~~  
~~RESTRICTED DATA~~  
~~RESTRICTED DATA~~

UNCLASSIFIED

~~CONFIDENTIAL~~  
~~RESTRICTED DATA~~

UNCLASSIFIED

TABLE 19  
SUMMARY OF MASS RATE DATA

Specimen Dia. 1"  
Specimen Mat'l Mat'l. X  
Nozzle Exit Dia. 5"  
Stag'n Press., atm  $8.25 \times 10^{-3}$   
Enthalpy Ratio 350  
Reynolds No.,  $Re_g$  44

Notes -  
(1) Unmodified data  
(2) Data modified for Reynolds No. Effects  
 $\triangle$  Symbol on graphs

Run Nos.	Time Sec.	Mass Loss Lb/ft. <sup>2</sup>	Avg. °K Temp.	Mass Rate $\times 10^3$ lb/ft <sup>2</sup> - sec		$m \sqrt{\frac{Rb}{Pe}} \times 10^3$ lb/ft <sup>3/2</sup> - sec - Atm <sup>1/2</sup>	
				(1)	(2)	(1)	(2)
680	360	.1964					
682	300	.1562					
	60	.0406	1570	.678	.807	2.39	2.85
669	300	.1868					
683	60	.0279					
	240	.1589	1565	.663	.790	2.33	2.78
682	300	.1562	1500	.521	.620	1.83	2.18
682	300	.1562					
681	120	.0454					
	180	.1108	1590	.615	.732	2.17	2.685
682	300	.1562					
667	180	.0817					
	120	.0745	1495	.620	.738	2.18	2.60
682	300	.1562					
679	180	.0763					
	120	.0799	1570	.665	.791	2.34	2.79
683	60	.0279	1530	0.465	.554	1.64	1.95

~~CONFIDENTIAL~~  
~~RESTRICTED DATA~~

UNCLASSIFIED

~~RESTRICTED DATA~~

UNCLASSIFIED

TABLE 20  
SUMMARY OF MASS RATE DATA

Specimen Dia. 1/16" Notes -  
Specimen Mat'l Mat'l. X (1) Unmodified data  
Nozzle Exit Dia. 5" (2) Data modified for  
Stag'n Press., atm  $7.70 \times 10^{-3}$  Reynolds No. Effects  
Enthalpy Ratio 350 • Symbol on graphs  
Reynolds No.,  $Re_s$  2.7

Run Nos.	Time Sec.	Mass Loss Lb./ft. <sup>2</sup>	Avg. °K Temp.	Mass Rate $\times 10^3$ lb/ft <sup>2</sup> - sec		$\dot{m} \sqrt{\frac{R_b}{P_e}} \times 10^3$ lb/ft <sup>3/2</sup> - sec - Atm <sup>1/2</sup>	
				(1)	(2)	(1)	(2)
676	42	.0310	1580	0.720	1.635	.619	1.405
674	120	.1594					
675	60	.0758					
	60	.0836	1715	1.39	3.06	1.27	2.88
670	300	.3520					
672	60	.0435					
	240	.3085	1690	1.29	2.93	1.18	2.68
673	240	.2365					
677	120	.1260					
	120	.1105	1670	0.920	2.09	.842	1.92
673	240	.2365					
671	60	.1661					
	60	.0704	1705	1.17	2.66	1.06	2.41
671	180	.1661	1750	0.92	2.09	.842	1.915
671	180	.1661					
676	42	.0310					
	138	.1351	1750	0.98	2.22	.896	2.035
671	180	.1661					
672	60	.0435					
	120	.1226	1675	1.02	2.315	.933	2.12
671	180	.1661					
677	120	.1260					
	60	.0401	1715	670	1.52	.613	1.39
677	120	.1260					
676	42	.0310					
	78	.0950	1630	1.22	2.77	1.12	2.54

~~RESTRICTED DATA~~

UNCLASSIFIED

UNCLASSIFIED

TABLE 20  
SUMMARY OF MASS RATE DATA

Specimen Dia. 1/16" Notes -  
 Specimen Mat'l Mat'l. X (1) Unmodified data  
 Nozzle Exit Dia. 5" (2) Data modified for  
 Stag'n Press., atm  $7.70 \times 10^{-3}$  Reynolds No. Effects  
 Enthalpy Ratio 350 • Symbol on graphs  
 Reynolds No.,  $Re_s$  2.7

Run Nos.	Time Sec.	Mass Loss Lb/ft. <sup>2</sup>	Avg. °K Temp.	Mass Rate $\times 10^3$ lb/ft <sup>2</sup> - sec		$\dot{m} \sqrt{\frac{R_b}{P_e}} \times 10^3$ lb/ft <sup>3/2</sup> - sec - Atm <sup>1/2</sup>	
				(1)	(2)	(1)	(2)
672	60	.0435	1550	0.730	1.66	.669	1.52
672	60	.0435					
676	42	.0310					
	18	.0125	1615	0.700	1.59	.641	1.455
670	300	.3520	1780	1.17	2.66	1.07	2.43
670	300	.3520					
676	42	.0310					
	258	.3210	1730	1.25	2.84	1.145	2.60
670	300	.3520					
677	120	.1260					
	180	.2260	1730	1.26	2.86	1.155	2.63
670	300	.3520					
671	180	.1661					
	120	.1859	1765	1.55	3.52	1.42	3.22
670	300	.3520					
673	240	.2365					
	60	.1155	1900	1.93	4.39	1.77	4.02
673	240	.2365	1660	0.99	2.25	.907	2.06
673	240	.2365					
676	42	.0310					
	198	.2055	1670	1.04	2.36	.952	2.16
673	240	.2365					
672	60	.0435					
	180	.1930	1630	1.07	2.43	.979	2.22

UNCLASSIFIED

~~CONFIDENTIAL~~  
~~RESTRICTED DATA~~

UNCLASSIFIED

TABLE 21  
SUMMARY OF MASS RATE DATA

Specimen Dia.	1"	Notes -
Specimen Mat'l	Mat'l. X	(1) Unmodified data
Nozzle Exit Dia.	5"	(2) Data modified for
Stag'n Press., atm	$7.00 \times 10^{-3}$	Reynolds No. Effects
Enthalpy Ratio	160	▽ Symbol on graphs
Reynolds No., $Re_s$	51	

Run Nos.	Time Sec.	Mass Loss Lb/ft. <sup>2</sup>	Avg. °K Temp.	Mass Rate $\times 10^3$ lb/ft <sup>2</sup> - sec		$\dot{m} \sqrt{\frac{Rb}{Pe}} \times 10^3$ lb/ft <sup>3/2</sup> - sec - Atm <sup>1/2</sup>	
				(1)	(2)	(1)	(2)
649	840	.1618					
651	720	.1493					
	120	.0125	1420	.104	.124	.398	.474
649	840	.1618					
654	577	.1282					
	263	.0336	1440	.128	.152	.489	.582
649	840	.1618					
653	500	.1160					
	340	.0458	1370	.135	.161	.517	.615
649	840	.1618					
650	480	.1138					
	360	.0480	1390	.133	.159	.508	.605
649	840	.1618					
652	360	.1160					
	480	.0458	1420	.0955	.1137	.365	.435
649	840	.1618					
655	240	.0737					
	600	.0881	1400	.147	.175	.561	.669
649	840	.1618					
656	120	.0323					
	720	.1295	1425	.180	.214	.688	.820
649	840	.1618	1380	.192	.229	.734	.874
651	720	.1493	1400	.208	.248	.795	.948
651	720	.1493					
654	577	.1282					
	143	.0211	1420	.147	.175	.562	.670

~~CONFIDENTIAL~~  
~~RESTRICTED DATA~~  
1054

UNCLASSIFIED



~~CONFIDENTIAL~~  
~~RESTRICTED DATA~~

UNCLASSIFIED

TABLE 21  
SUMMARY OF MASS RATE DATA

Specimen Dia. 1" Notes -  
Specimen Mat'l Mat'l. X (1) Unmodified data  
Nozzle Exit Dia. 5" (2) Data modified for  
Stag'n Press., atm  $7.00 \times 10^{-3}$  Reynolds No. Effects  
Enthalpy Ratio 160  $\nabla$  Symbol on graphs  
Reynolds No.,  $Re_s$  51

Run Nos.	Time Sec.	Mass Loss Lb/ft. <sup>2</sup>	Avg. °K Temp.	Mass Rate $\times 10^3$ lb/ft <sup>2</sup> - sec		$\dot{m} \sqrt{\frac{Rb}{Pe}} \times 10^3$ lb/ft <sup>3/2</sup> - sec - Atm <sup>1/2</sup>	
				(1)	(2)	(1)	(2)
651	720	.1493					
653	500	.1160					
	220	.0333	1370	.151	.180	.577	.688
651	720	.1493					
650	480	.1138					
	240	.0355	1390	.148	.176	.565	.674
651	720	.1493					
652	360	.1160					
	360	.0333	1420	.0925	.110	.354	.421
651	720	.1493					
655	240	.0737					
	480	.0756	1400	.157	.187	.600	.715
651	720	.1493					
656	120	.0323					
	600	.1170	1425	.195	.232	.745	.888
654	577	.1282	1460	.222	.264	.810	.964
654	577	.1282					
653	500	.1160					
	77	.0122	1390	.159	.189	.608	.723
654	577	.1282					
650	480	.1138					
	97	.0144	1410	.149	.1773	.570	.679
654	577	.1282					
655	240	.0737					
	337	.0545	1420	.162	.193	.619	.736

~~CONFIDENTIAL~~  
~~RESTRICTED DATA~~  
Atomic Energy Act of 1954

UNCLASSIFIED

~~CONFIDENTIAL~~  
~~RESTRICTED DATA~~

UNCLASSIFIED

TABLE 21  
SUMMARY OF MASS RATE DATA

Specimen Dia. 1" Notes -  
Specimen Mat'l Mat'l. X (1) Unmodified data  
Nozzle Exit Dia. 5" (2) Data modified for  
Stag'n Press., atm  $7.00 \times 10^{-3}$  Reynolds No. Effects  
Enthalpy Ratio 160  $\nabla$  Symbol on graphs  
Reynolds No.,  $Re_s$  51

Run Nos.	Time Sec.	Mass Loss Lb/ft. <sup>2</sup>	Avg. °K Temp.	Mass Rate $\times 10^3$ lb/ft <sup>2</sup> - sec		$\sqrt{\frac{R_b}{P_e}} \times 10^3$ lb/ft <sup>3/2</sup> - sec - Atm <sup>1/2</sup>	
				(1)	(2)	(1)	(2)
654	577	.1282					
656	120	.0323					
	457	.0959	1445	.129	.1537	.493	.587
653	500	.1160					
650	480	.1138					
	20	.0022	1415	.110	.131	.421	.501
653	500	.1160					
655	240	.0737					
	260	.0423	1425	.163	.1942	.623	.742
653	500	.1160					
656	180	.0323					
	320	.0837	1450	.261	.311	.998	1.188
650	480	.1138					
655	240	.0737					
	240	.0401	1410	.167	.199	.639	.761
650	480	.1138					
656	120	.0323					
	360	.0815	1435	.226	.269	.864	1.03
655	240	.0737					
656	120	.0323					
	120	.0414	1475	.345	.411	1.32	1.57
656	120	.0323	1430	.269	.320	1.03	1.227

~~CONFIDENTIAL~~  
~~RESTRICTED DATA~~  
~~GROUP 1, EXC 1054~~

UNCLASSIFIED

CONFIDENTIAL

CONFIDENTIAL

CONFIDENTIAL

TABLE 22 MONOTONICALLY SHRINKING SPHERES

UNCLASSIFIED

$\left(\frac{W}{C_D A}\right)_E$ (lb/ft <sup>2</sup> )	R <sub>E</sub> (inches)	W <sub>E</sub> (lb)	W <sub>f</sub> (lb)	Δ W (lb)	Mass Loss (%)	Δ R (inches)	Φ	Q <sub>w max</sub> (Btu/ft <sup>2</sup> -sec)	∫ Q <sub>T</sub> (Btu/ft <sup>2</sup> )	T <sub>w max</sub> (° R)	(T <sub>w</sub> -T <sub>b</sub> ) (° R)	γ <sub>E</sub> (deg)	Mat'l.	E (cal/mole)	k <sub>o</sub> $\left(\frac{2}{\text{ft-sec-atm}}\right)\left(\frac{\text{lb.}}{\text{ft-sec-atm}}\right)^{1/2}$	β <sub>Diff.</sub> $\left(\frac{3/2}{\text{ft-sec-atm}}\right)\left(\frac{\text{lb.}}{\text{ft-sec-atm}}\right)^{1/2}$
.231	.03125	1.01(-5) <sub>1</sub>	.995(-5)	1.1(-7)	1.10	1.2(-4)	.375	18.	1045	2790	0	2.5	X <sub>i</sub>	18000 <sub>2</sub>	2.0 <sub>2</sub>	6.2 (-3) <sub>2</sub>
.465	.0625	8.05(-5)	7.9(-5)	1.5(-6)	1.86	3.6(-4)	.375	31.6	1847	3033	0	2.5	X <sub>i</sub>	18000	2.0	6.2 (-3)
.928	.125	6.441(-4)	6.25(-4)	1.9(-5)	2.91	1.2(-3)	.375	52.9	3356	3433	8	2.5	X <sub>i</sub>	18000	2.0	6.2 (-3)
1.864	.250	5.153(-3)	4.994(-3)	1.59(-4)	3.08	2.64(-3)	.375	63.4	6151	3563	15	1.0	X <sub>i</sub>	18000	2.0	6.2 (-3)
1.864	.250	5.153(-3)	4.956(-3)	2.03(-4)	3.93	3.20(-3)	.375	90.9	5837	3897	45	2.5	X <sub>i</sub>	18000	2.0	6.2 (-3)
1.864	.250	5.153(-3)	4.399(-3)	7.539(-4)	14.60	1.28(-2)	.375	138.5	5037	4195	113	5.0	X <sub>i</sub>	18000	2.0	6.2 (-3)
1.864	.250	5.153(-3)	5.103(-3)	5.01(-5)	0.97	8.0(-4)	.200	49.7	3230	3304	31	2.5	X <sub>i</sub>	18000	2.0	6.2 (-3)
1.864	.250	5.153(-3)	4.805(-3)	3.477(-4)	6.75	5.7(-3)	.500	119.9	7649	4190	49	2.5	X <sub>i</sub>	18000	2.0	6.2 (-3)
2.808	.375	1.756(-2)	1.688(-2)	6.79(-4)	3.87	4.8(-3)	.375	107.9	7508	4045	115	2.5	X <sub>i</sub>	18000	2.0	6.2 (-3)
3.748	.500	4.152(-2)	4.009(-2)	1.43(-3)	3.44	5.76(-3)	.375	117.9	8622	4097	188	2.5	X <sub>i</sub>	18000	2.0	6.2 (-3)
7.520	1.000	3.309(-1)	3.213(-1)	9.67(-3)	2.92	9.78(-3)	.375	134.3	11204	4007	509	2.5	X <sub>i</sub>	18000	2.0	6.2 (-3)
1.470	.250	4.071(-3)	3.357(-3)	7.138(-4)	17.53	1.552(-2)	.375	76.8	4755	3744	25	2.5	ATJ	42300 <sub>3</sub>	4.47(4) <sub>3</sub>	6.35 (-3) <sub>3</sub>
.231	.03125	1.01(-5)	.9986(-5)	.7(-7)	0.7	7.97(-5)	.375	18.1	1075	2790	0	2.5	"X"	39100 <sub>4</sub>	2090 <sub>4</sub>	8.5 (-3) <sub>4</sub>
.928	.125	6.441(-4)	5.945(-4)	4.96(-5)	7.7	3.28(-3)	.375	52.9	3338	3432	8	2.5	"X"	39100	2090	8.5 (-3)
1.864	.250	5.153(-3)	4.454(-3)	6.99(-4)	13.56	1.18(-2)	.375	90.9	5801	3898	45	2.5	"X"	39100	2090	8.5 (-3)
3.748	.500	4.152(-2)	3.637(-2)	5.15(-3)	12.40	2.16(-2)	.375	118.1	8672	4098	188	2.5	"X"	39100	2090	8.5 (-3)

- Notes: 1. Exponent of base ten multiplier.  
2. Values for E and k<sub>o</sub> are early estimates based upon preliminary experimental data from lower enthalpy experiments; value for β<sub>Diff</sub> based upon graphite.  
3. Values for E and k<sub>o</sub> taken from slow kinetics (Ref. 9); β<sub>Diff</sub> represents a further theoretical adjustment to the β<sub>Diff</sub> for graphite.  
4. Values for E and k<sub>o</sub> obtained from completed experiment; value for β<sub>Diff</sub> obtained from experiment and Appendix D.

CONFIDENTIAL  
RESTRICTED DATA  
UNCLASSIFIED

CONFIDENTIAL

33000000

CONFIDENTIAL

UNCLASSIFIED

TABLE 23 ONE DIMENSIONAL CYLINDERS

$\left(\frac{W}{C_{DA}}\right)_E$ (lb/ft <sup>2</sup> )	R <sub>c</sub> =d (inches)	ℓ (inches)	W <sub>E</sub> (lb)	W <sub>f</sub> (lb)	Δ W (lb)	Mass Loss (%)	Δ ℓ (inches)	Φ	Q <sub>w</sub> <sup>max</sup> (Btu/ft <sup>2</sup> -sec)	∫ Q <sub>T</sub> <sup>max</sup> (Btu/ft <sup>2</sup> )	T <sub>w</sub> <sup>max</sup> (°R)	(T <sub>w</sub> -T <sub>b</sub> ) <sup>max</sup> (°R)	γ <sub>E</sub> (deg)	Mat'l.	E (cal/mole)	k <sub>o</sub> $\left(\frac{\text{lb.}}{\text{ft}^2\text{-sec-atm}}\right)^{1/2}$	β $\left(\frac{\text{lb.}}{\text{ft}^2\text{-sec-atm}}\right)^{1/2}$ Diff.
1.38	.250	.250	9.662(-4) <sub>1</sub>	9.161(-4)	5.013(-5)	5.19	1.29(-2)	1.0	191.5	11431	4500	188	2.5	X <sub>i</sub>	18000 <sub>2</sub>	2.0 <sub>2</sub>	6.2(-3) <sub>2</sub>
2.77	.250	.500	1.937(-3)	1.831(-3)	1.06 (-4)	5.47	2.74(-2)	1.0	311.4	20474	4832	739	2.5	X <sub>i</sub>	18000	2.0	6.2(-3)
5.55	.250	1.000	3.865(-3)	3.672(-3)	1.93(-4)	4.99	4.98(-2)	1.0	478.6	35290	5173	1967	2.5	X <sub>i</sub>	18000	2.0	6.2(-3)
11.11	.250	2.000	7.747(-3)	7.433(-3)	3.14(-4)	4.05	8.13(-2)	1.0	710.1	58180	5777	3656	2.5	X <sub>i</sub>	18000	2.0	6.2(-3)
5.55	.500	1.000	1.549(-2)	1.487(-2)	6.2(-4)	4.00	4.03(-2)	1.0	388.5	29900	4802	1692	2.5	X <sub>i</sub>	18000	2.0	6.2(-3)
11.11	.500	2.000	3.10(-2)	3.0(-2)	1.0(-3)	3.22	6.28(-2)	1.0	558.7	47550	5312	3226	2.5	X <sub>i</sub>	18000	2.0	6.2(-3)
1.38	.250	.250	9.662(-4)	8.122(-4)	1.54(-4)	15.94	3.98(-2)	1.0	190.7	11209	4494	187	2.5	"X"	39100 <sub>4</sub>	2090 <sub>4</sub>	8.5(-3) <sub>4</sub>
2.77	.250	.500	1.937(-3)	1.615(-3)	3.22(-4)	16.62	6.32(-2)	1.0	310.5	20129	4820	734	2.5	"X"	39100	2090	8.5(-3)
5.55	.250	1.000	3.865(-3)	3.286(-3)	5.79(-4)	14.98	14.94(-2)	1.0	477.1	34780	5145	1950	2.5	"X"	39100	2090	8.5(-3)
11.11	.250	2.000	7.747(-3)	6.931(-3)	8.16(-4)	10.53	21.08(-2)	1.0	707.5	57590	5740	3628	2.5	"X"	39100	2090	8.5(-3)

Notes: 1, 2, & 4. See Table 22.

CONFIDENTIAL  
UNCLASSIFIED

UNCLASSIFIED

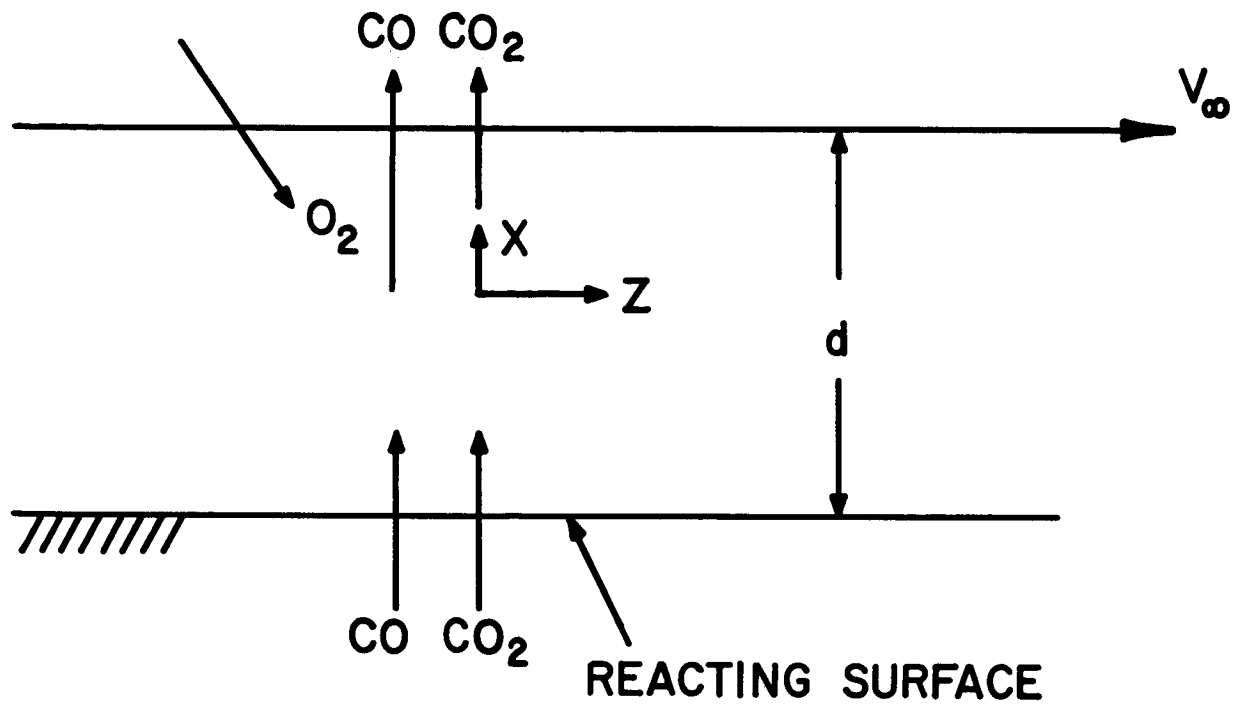


FIGURE 1. OXIDATION OF GRAPHITE IN NEAR FREE MOLECULE  
HYPERSONIC COUETTE FLOW

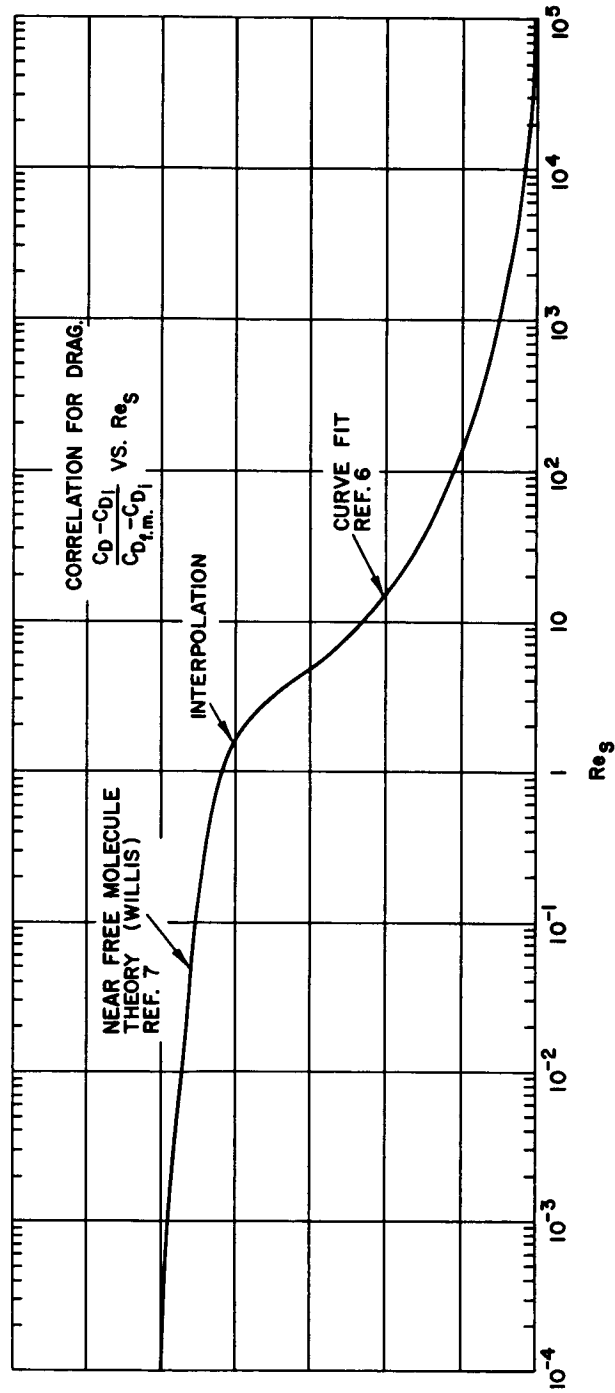


FIGURE 2.

$$\frac{C_D - C_{D_l}}{C_{D_{t.m.}} - C_{D_l}}$$

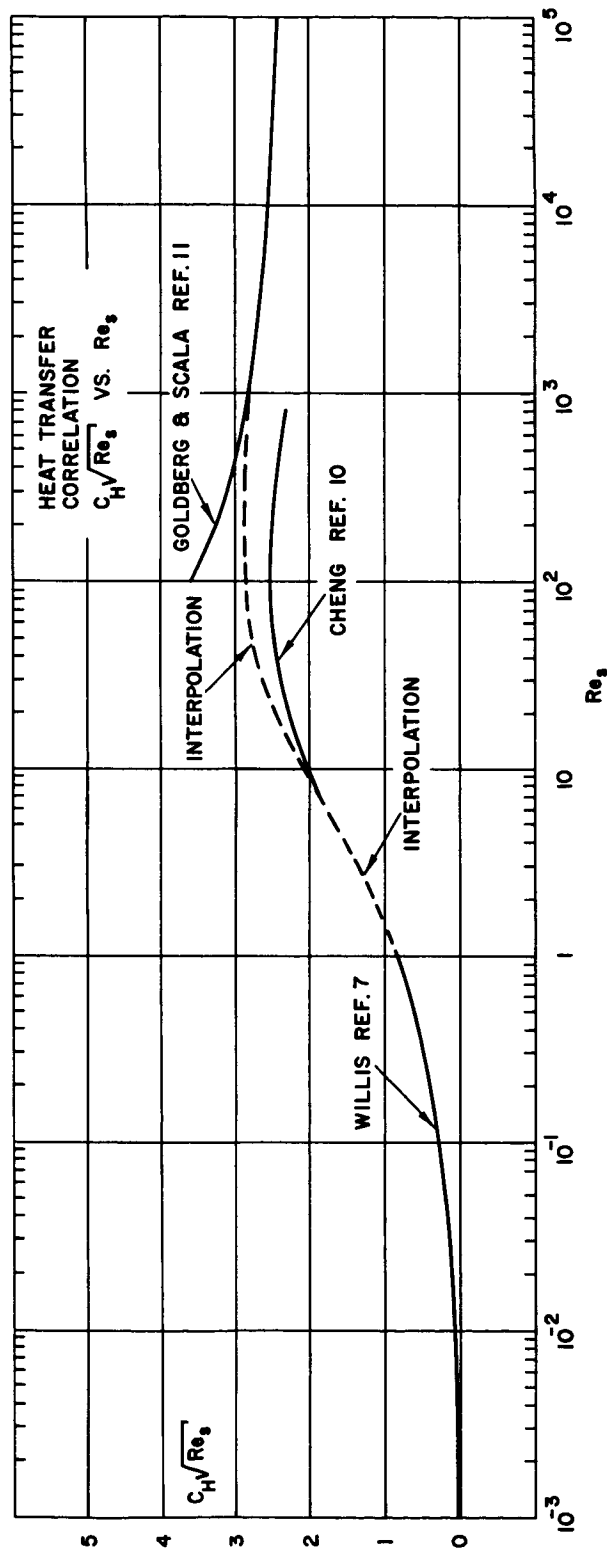


FIGURE 3.

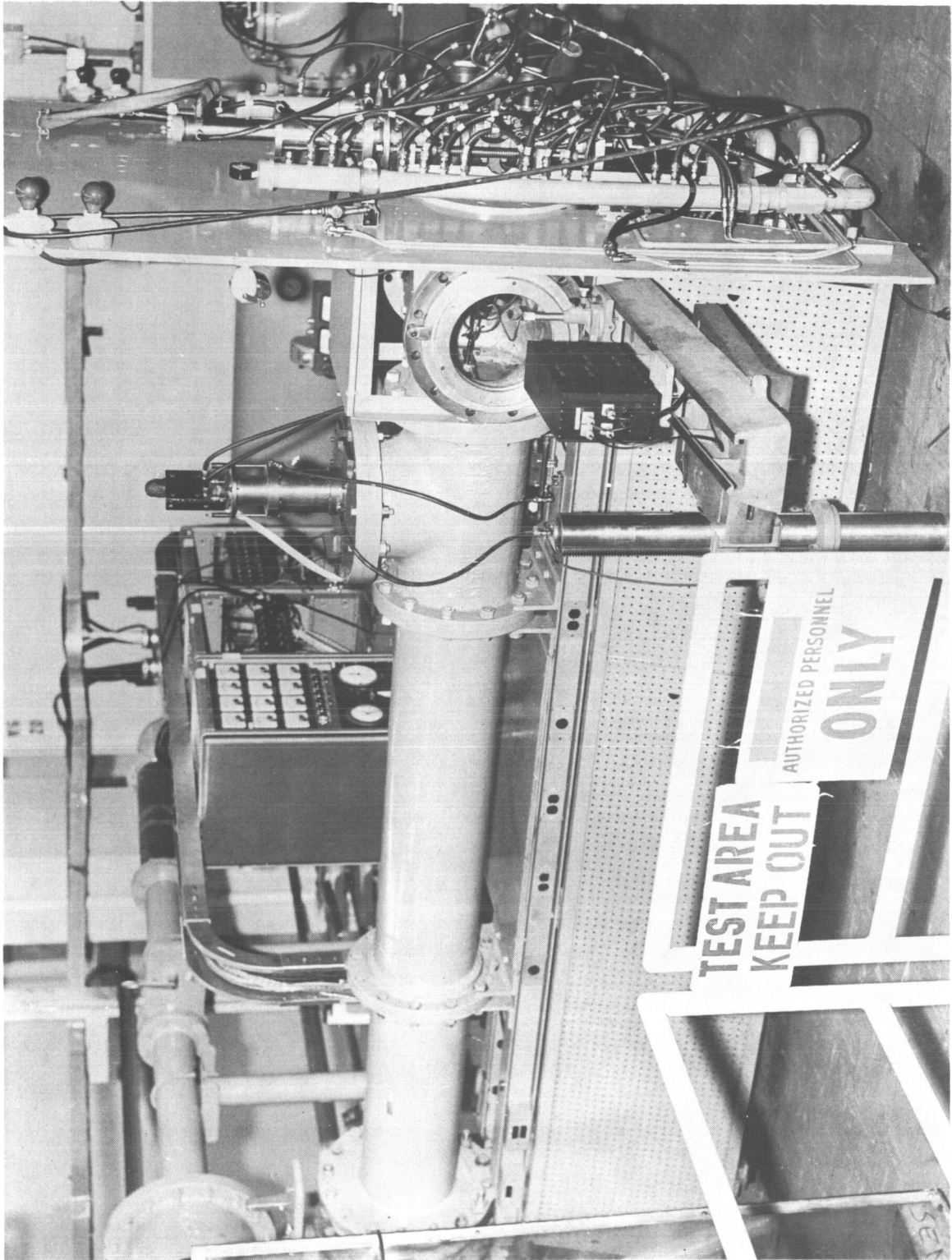
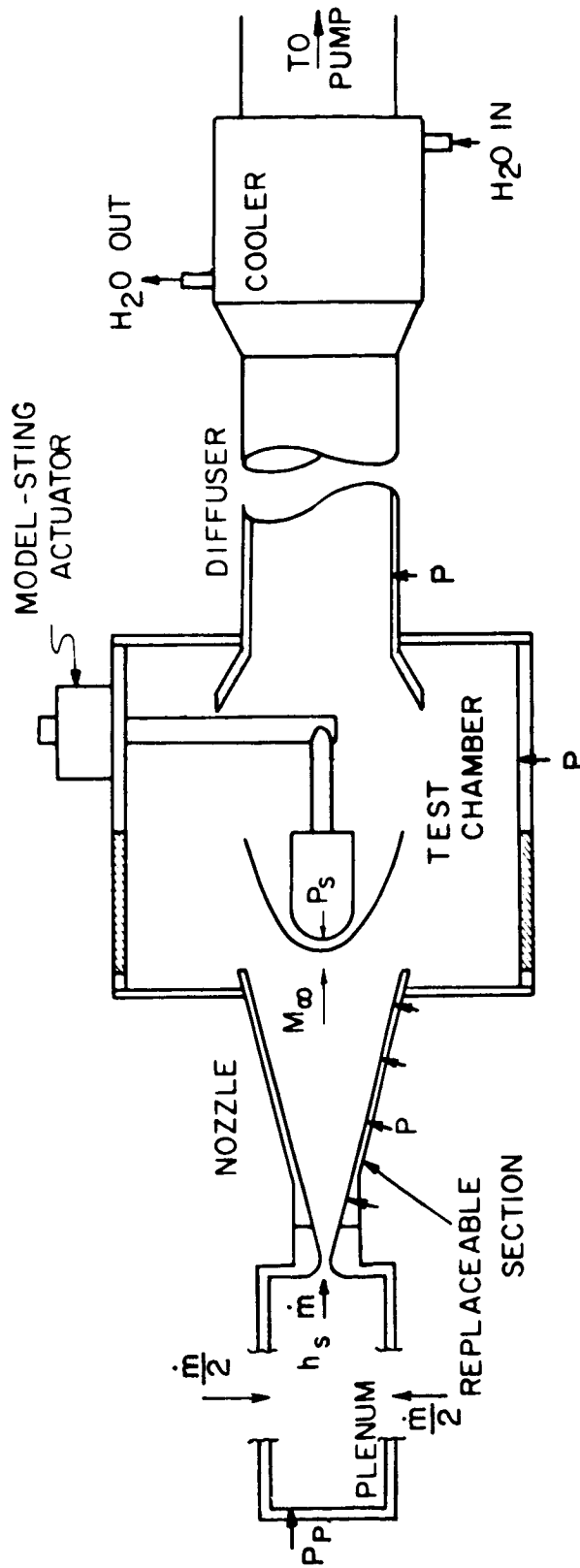


FIGURE 4. HYPERSONIC ARC HEATED WIND TUNNEL



A101A/51

# CHARACTERISTICS OF HYPERSONIC ARC WIND TUNNEL



202

## TYPICAL TEST MEASUREMENTS

- | MODEL                                    | FACILITY AND CALIBRATION                   |
|--|--|
| 1. SURFACE TEMPERATURE (T)               | 1. VOLTAGE AND CURRENT TO HEATER           |
| 2. SUB-SURFACE AND BACKWALL T            | 2. MASS FLOW RATE ( $\dot{m}$ ) - TEST GAS |
| 3. SURFACE PRESSURE                      | 3. ( $P_p$ ) PLENUM PRESSURE               |
| 4. SURFACE HEAT TRANSFER ( $\dot{q}_o$ ) | 4. GAS T - THROAT, PLENUM, TEST SECTION    |
| 5. ABLATION RATE-LOCAL AND TOTAL         | 5. ( $h_s$ ) ENTHALPY - TEST GAS           |
| 6. FORCES-3 COMPONENT                    | 6. STATIC PRESSURE - P                     |
| 7. FLOW FIELD PROPERTIES                 | 7. $q_o$ PROFILES - TEST SECTION           |
| 8. PHOTOGRAPHY                           | 8. $P_s$ PROFILES - TEST SECTION           |
|  | 9. TEST GAS SPECIES                        |

FIGURE 5.

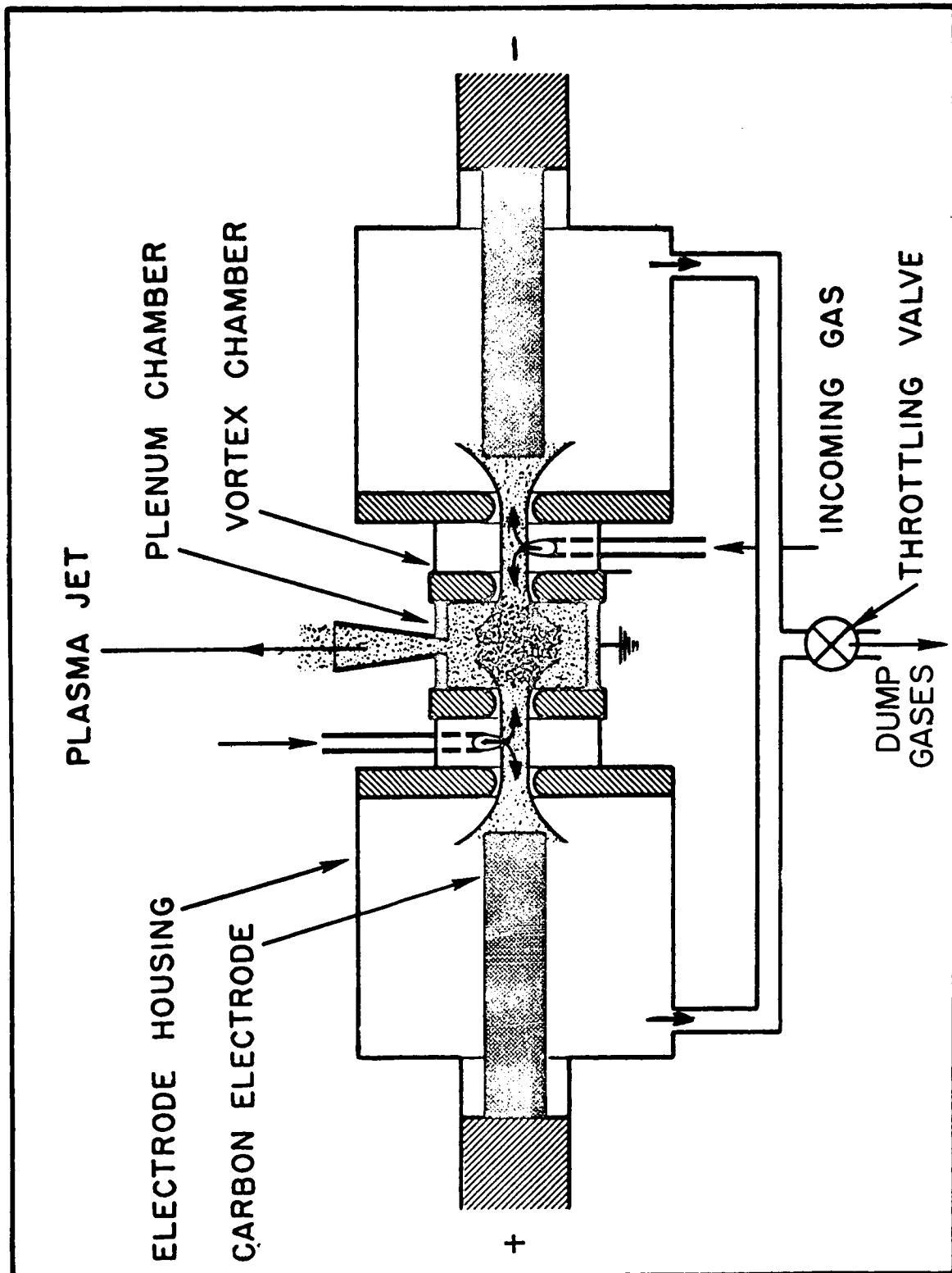


FIGURE 6. GENERAL ARRANGEMENT OF THE TANDEM GERDIEN PLASMA JET APPARATUS

UNCLASSIFIED : O P I E D

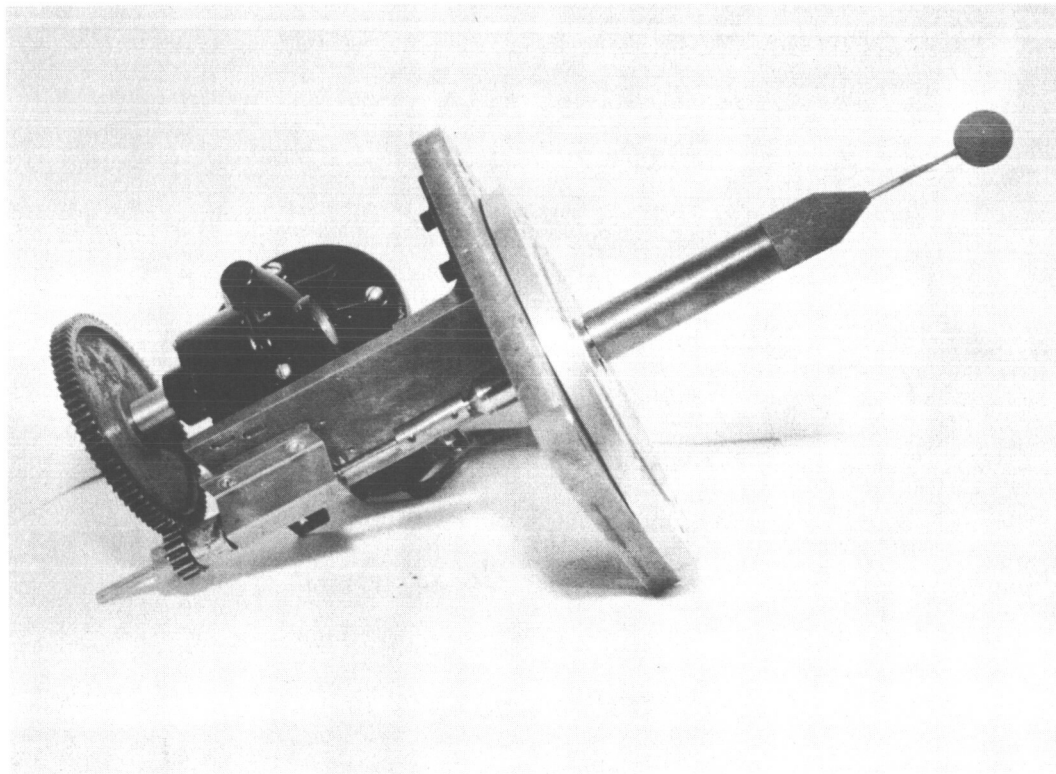


FIGURE 7. MODEL ROTATING STING APPARATUS

UNCLASSIFIED

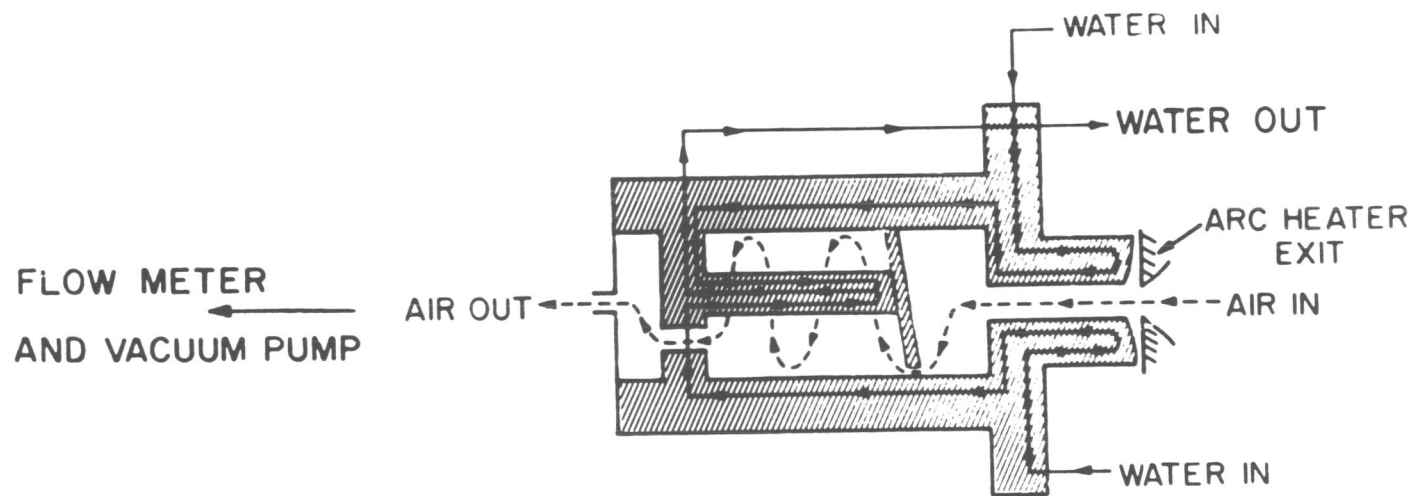
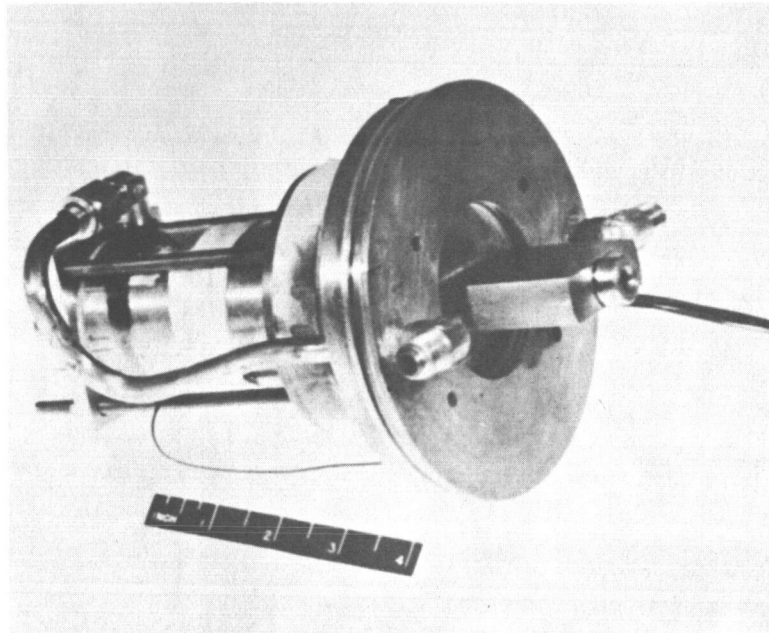


FIGURE 8. TOTAL ENTHALPY CALORIMETER

UNCLASSIFIED: C I F I O

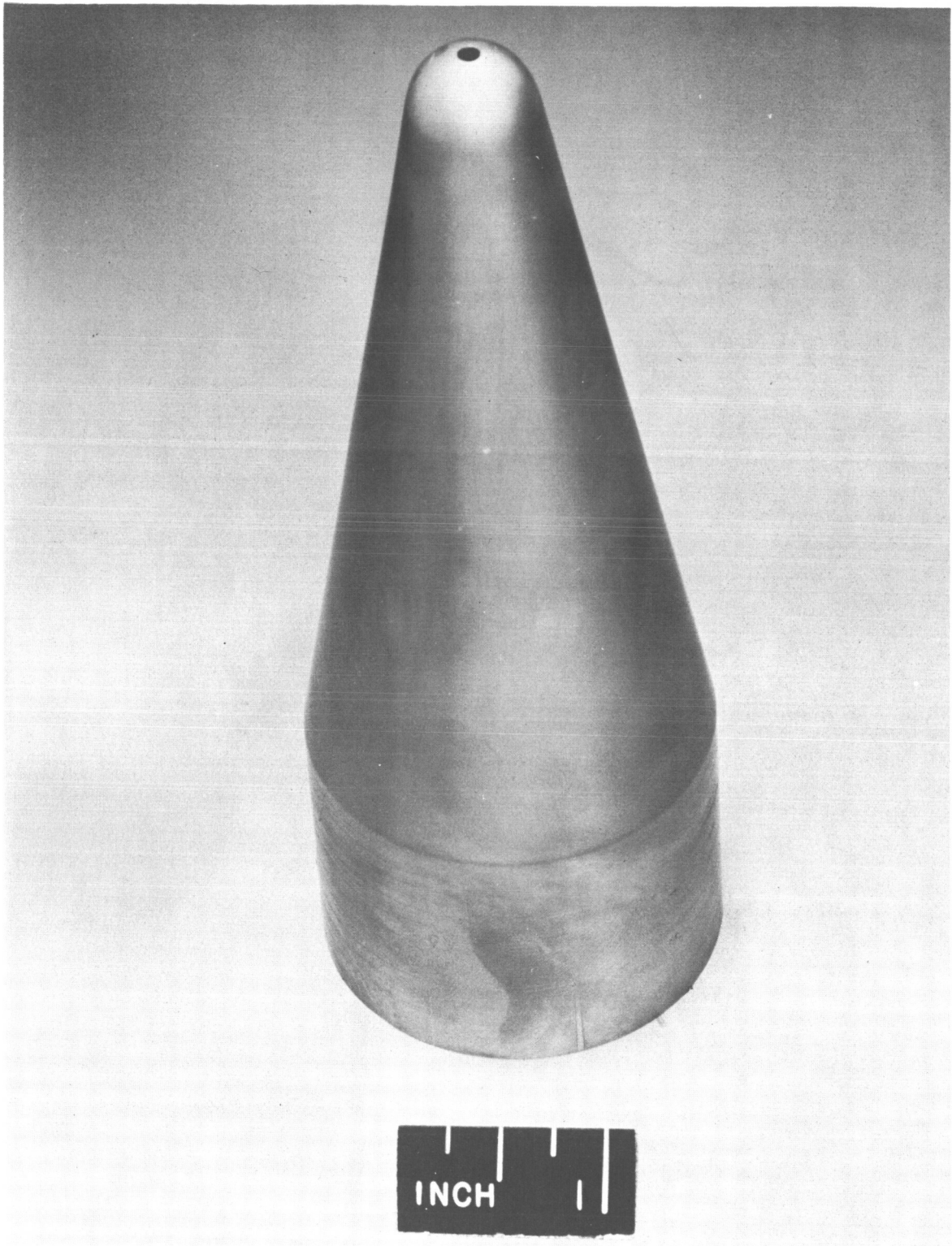


FIGURE 9. MODEL STAGNATION PRESSURE PROBE  
206

UNCLASSIFIED

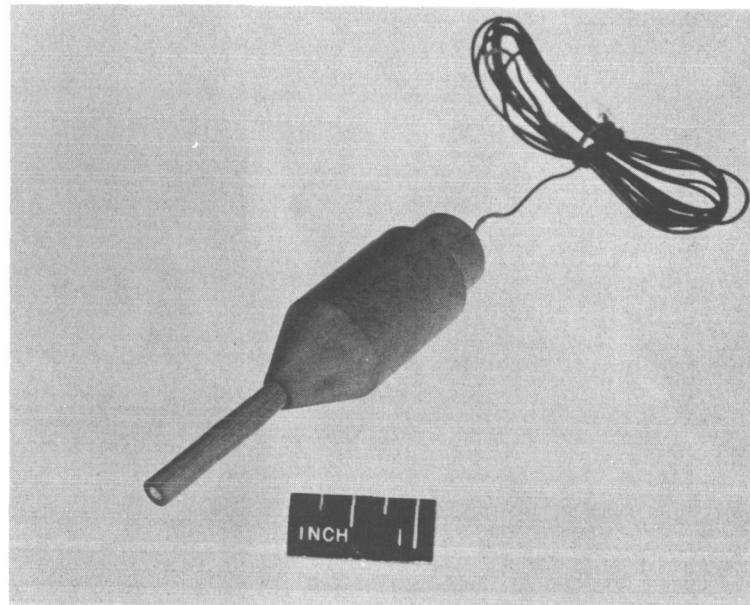


FIGURE 10. TYPICAL MASS TRANSFER MODEL CALORIMETER

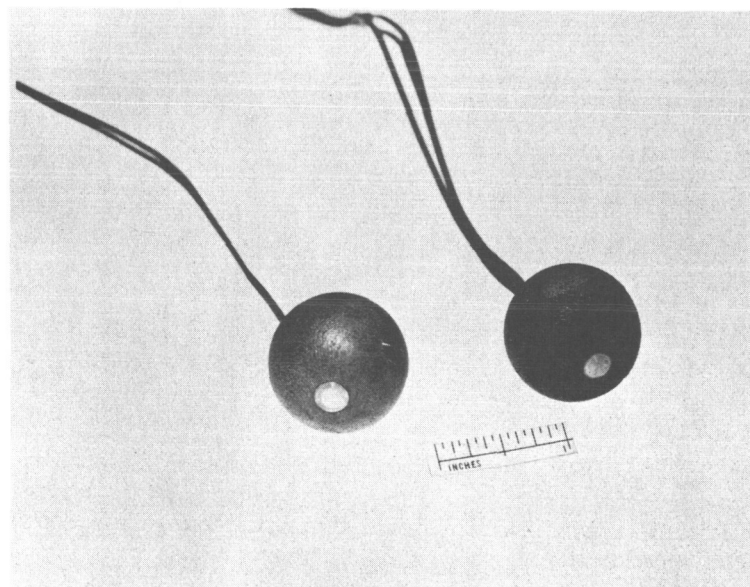
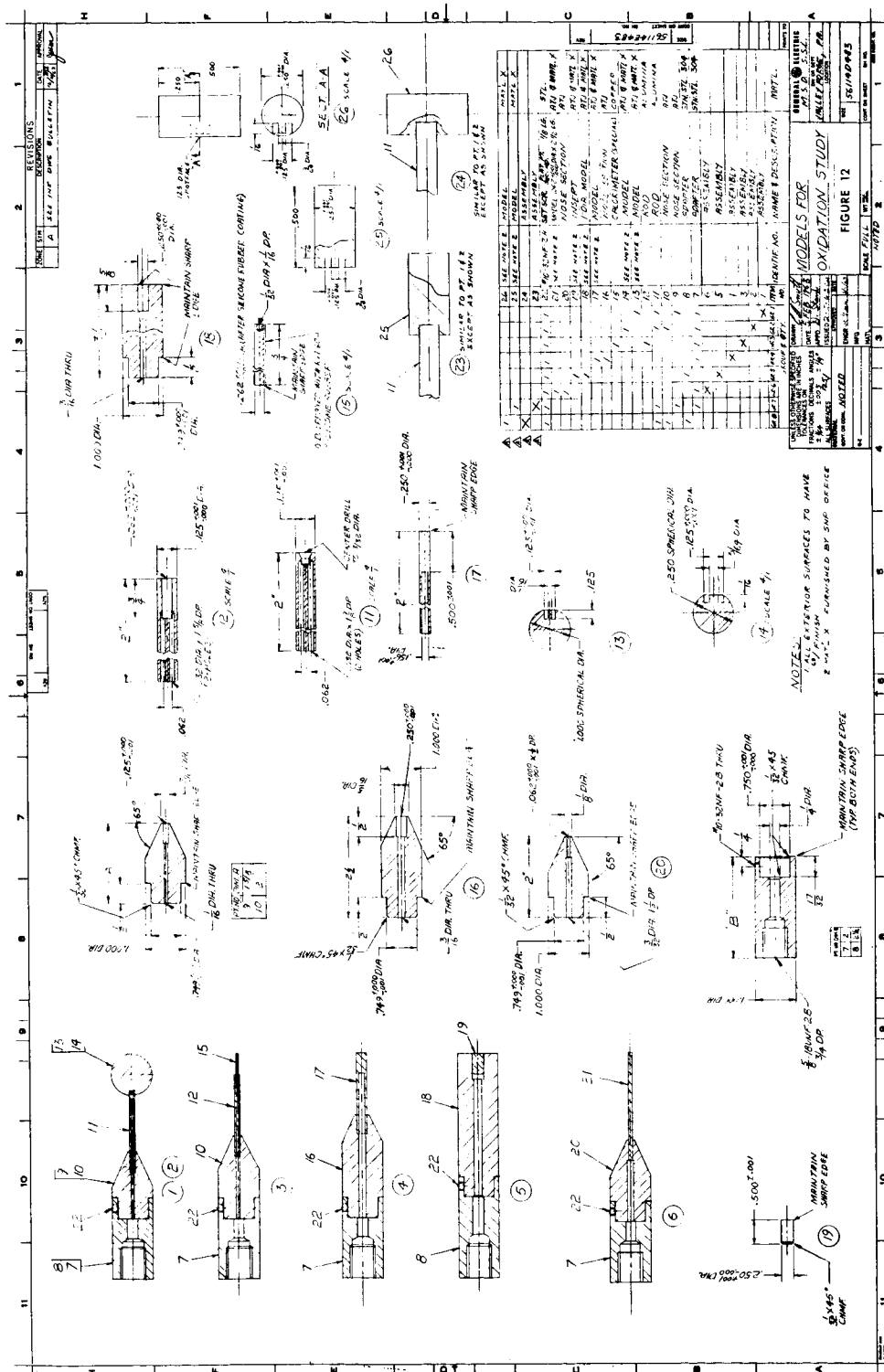


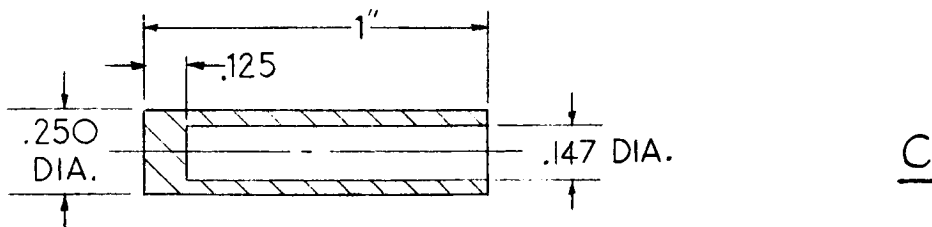
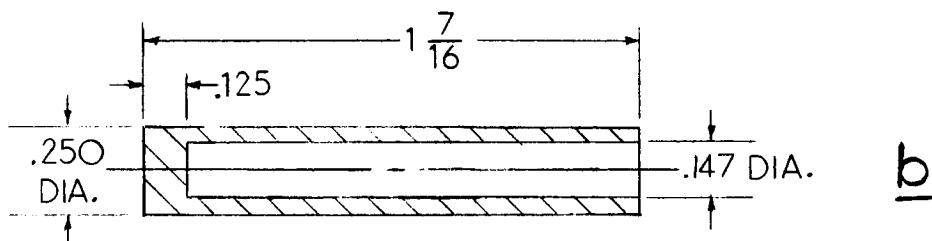
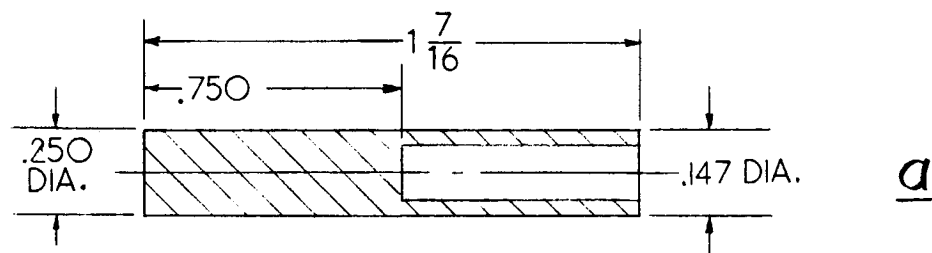
FIGURE 11. TYPICAL SPHERICAL MODEL CALORIMETERS  
(BEFORE AND AFTER EXPOSURE)



# MODIFICATIONS OF ATJ GRAPHITE SPECIMENS

## $\frac{1}{4}$ IN. DIA. MODELS

ITEM 17 FIG.12



## $\frac{1}{16}$ IN. DIA. MODEL

ITEM 21 FIG.12

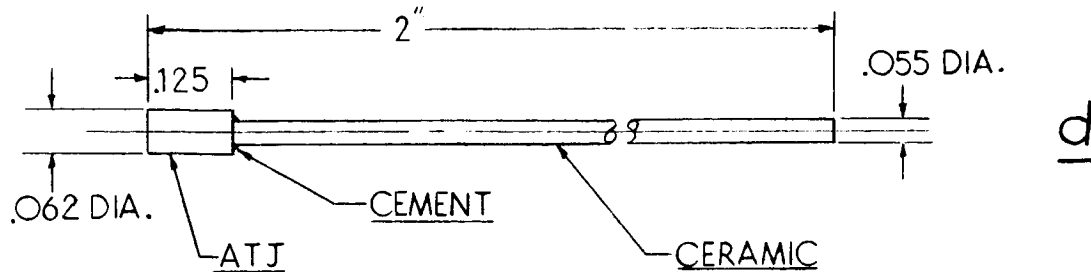


FIGURE 13



UNCLASSIFIED

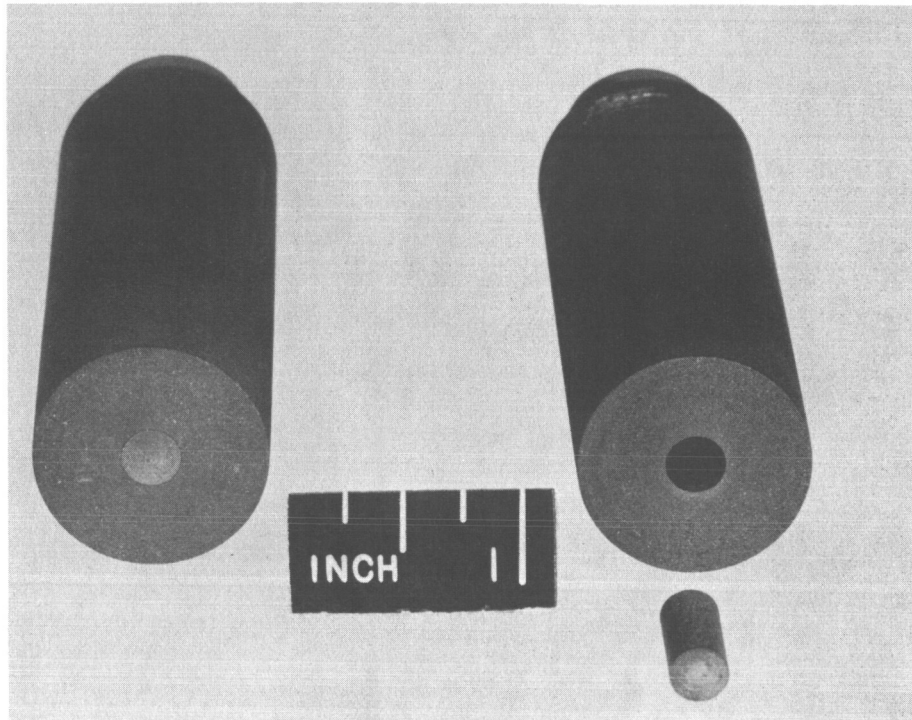


FIGURE 14. MASS RATE SPECIMEN, 1.0" DIAMETER

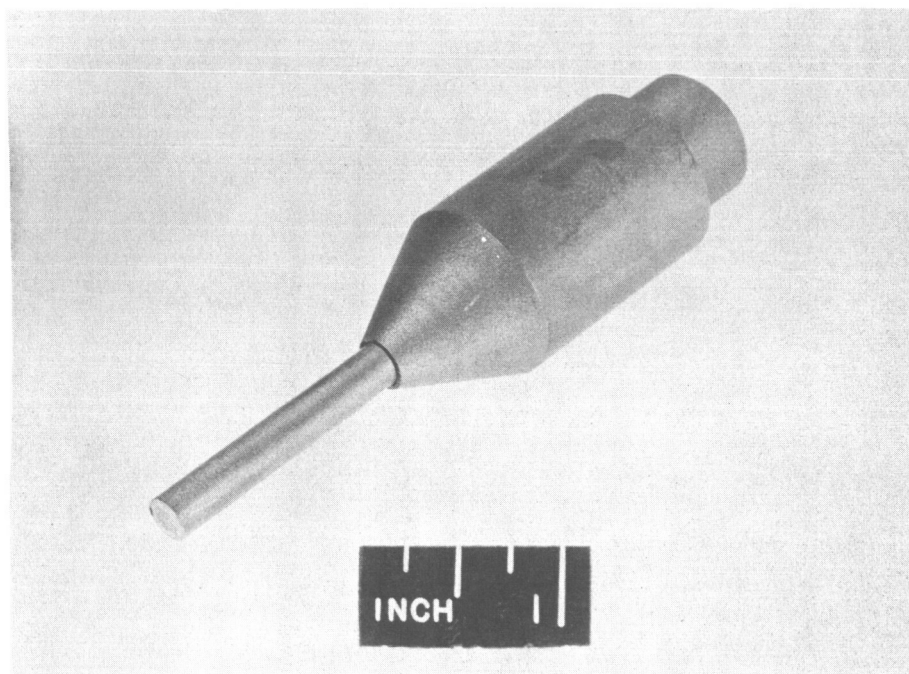


FIGURE 15. MASS RATE SPECIMEN, 1/4" DIAMETER  
210

UNCLASSIFIED

UNCLASSIFIED

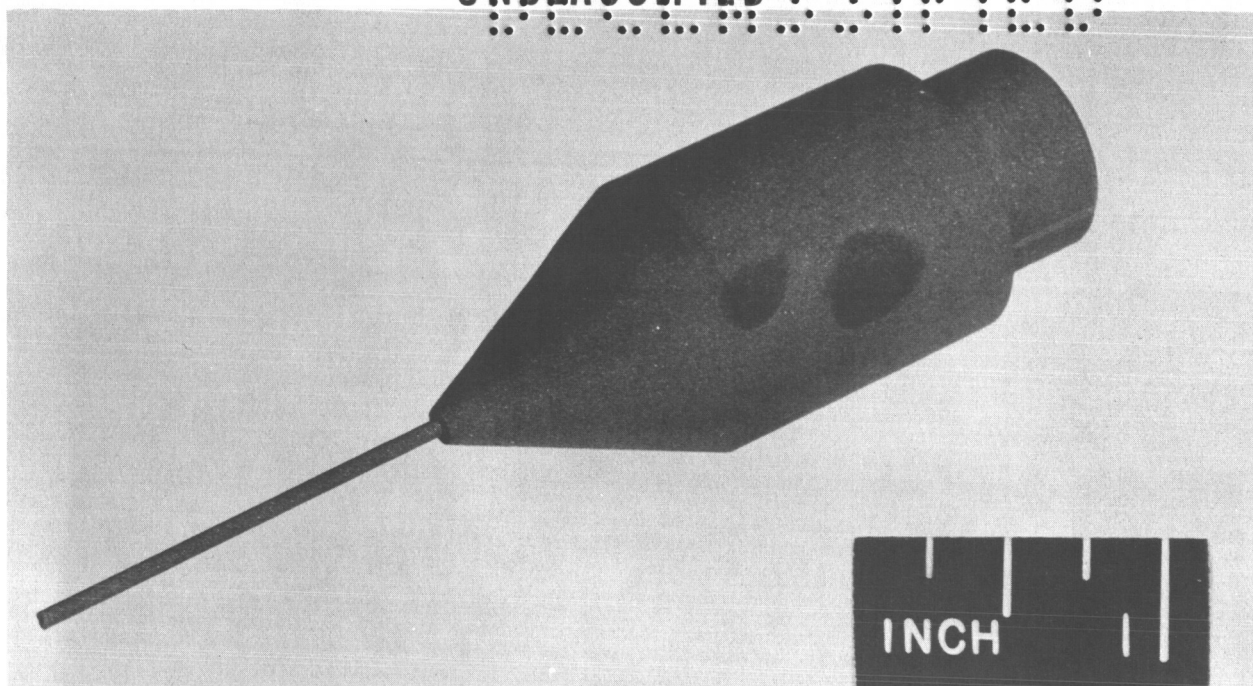


FIGURE 16. MASS RATE SPECIMEN, 1/16" DIAMETER

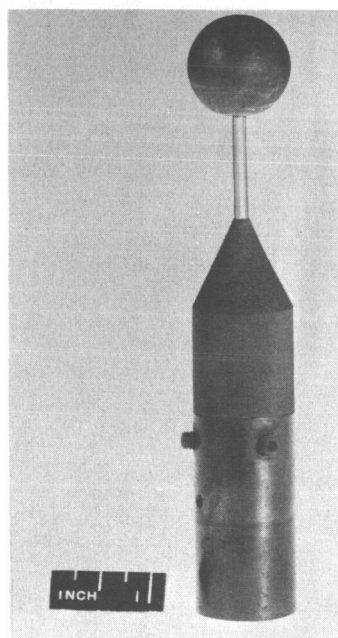


FIGURE 17. INTEGRATED MASS  
TRANSFER MODEL,  
1.0" DIAMETER SPHERE

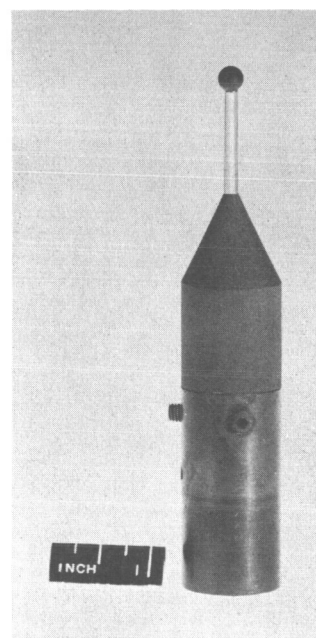


FIGURE 18. INTEGRATED MASS  
TRANSFER MODEL,  
1/4" DIAMETER SPHERE

UNCLASSIFIED

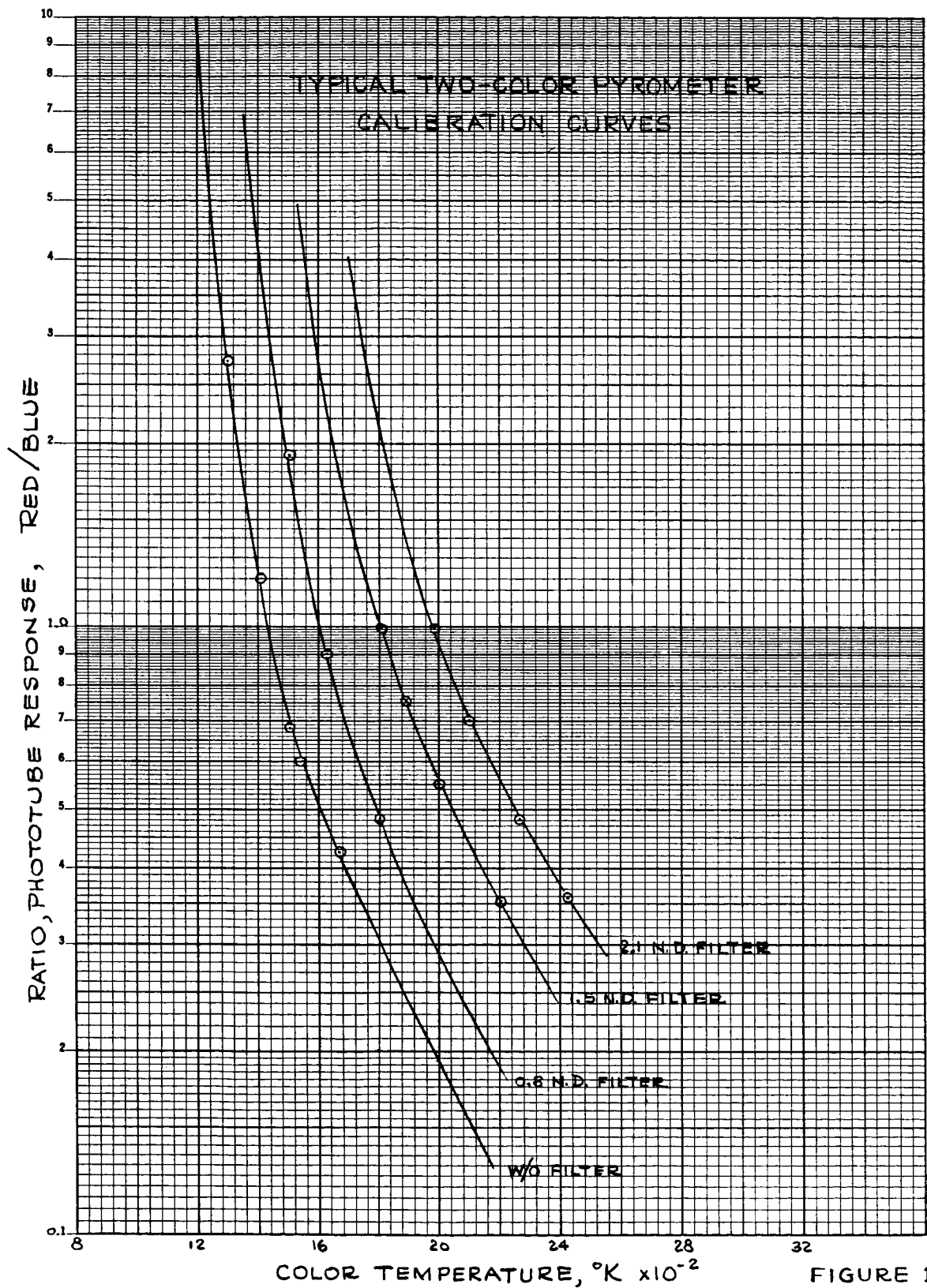


FIGURE 19

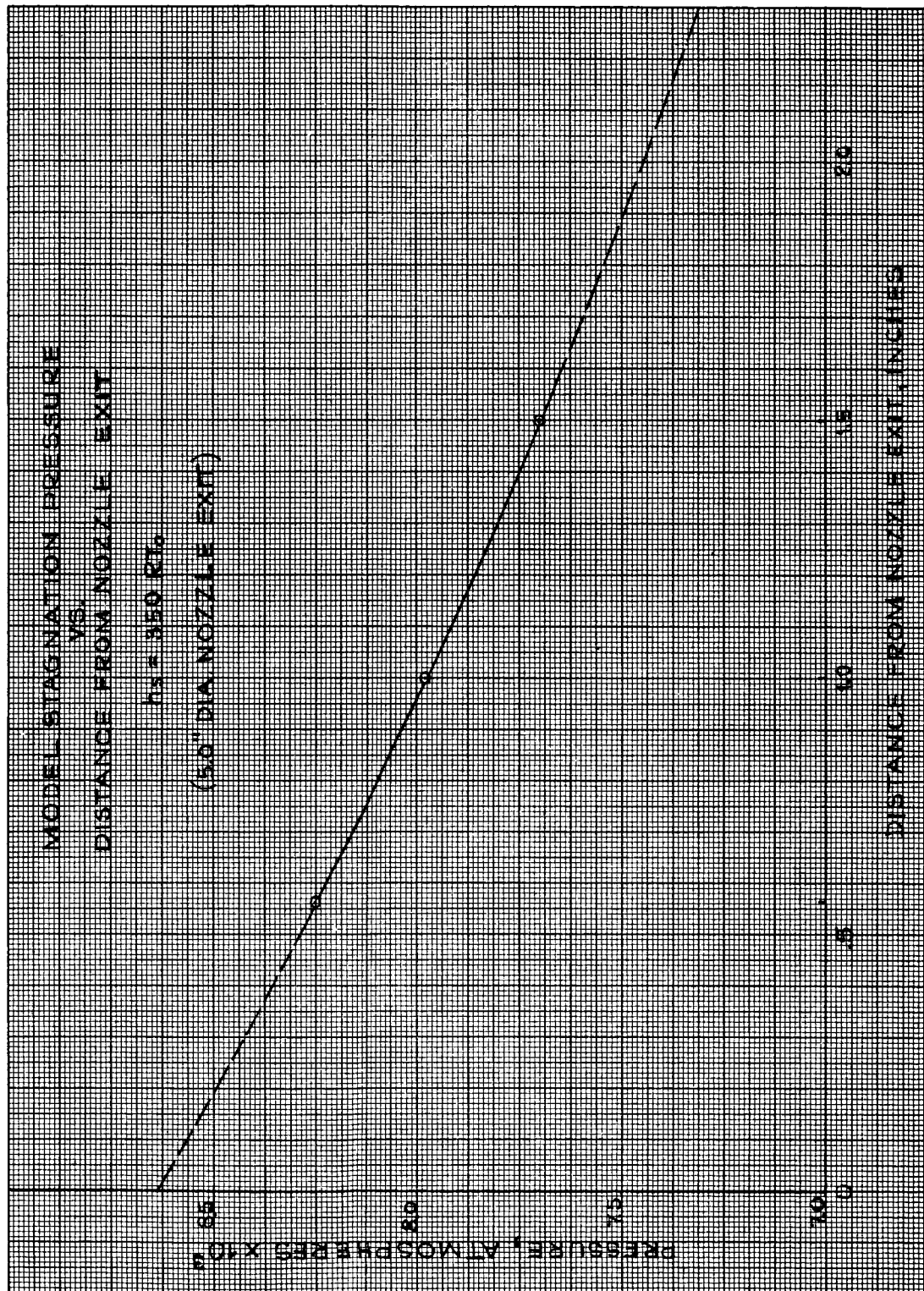


FIGURE 20

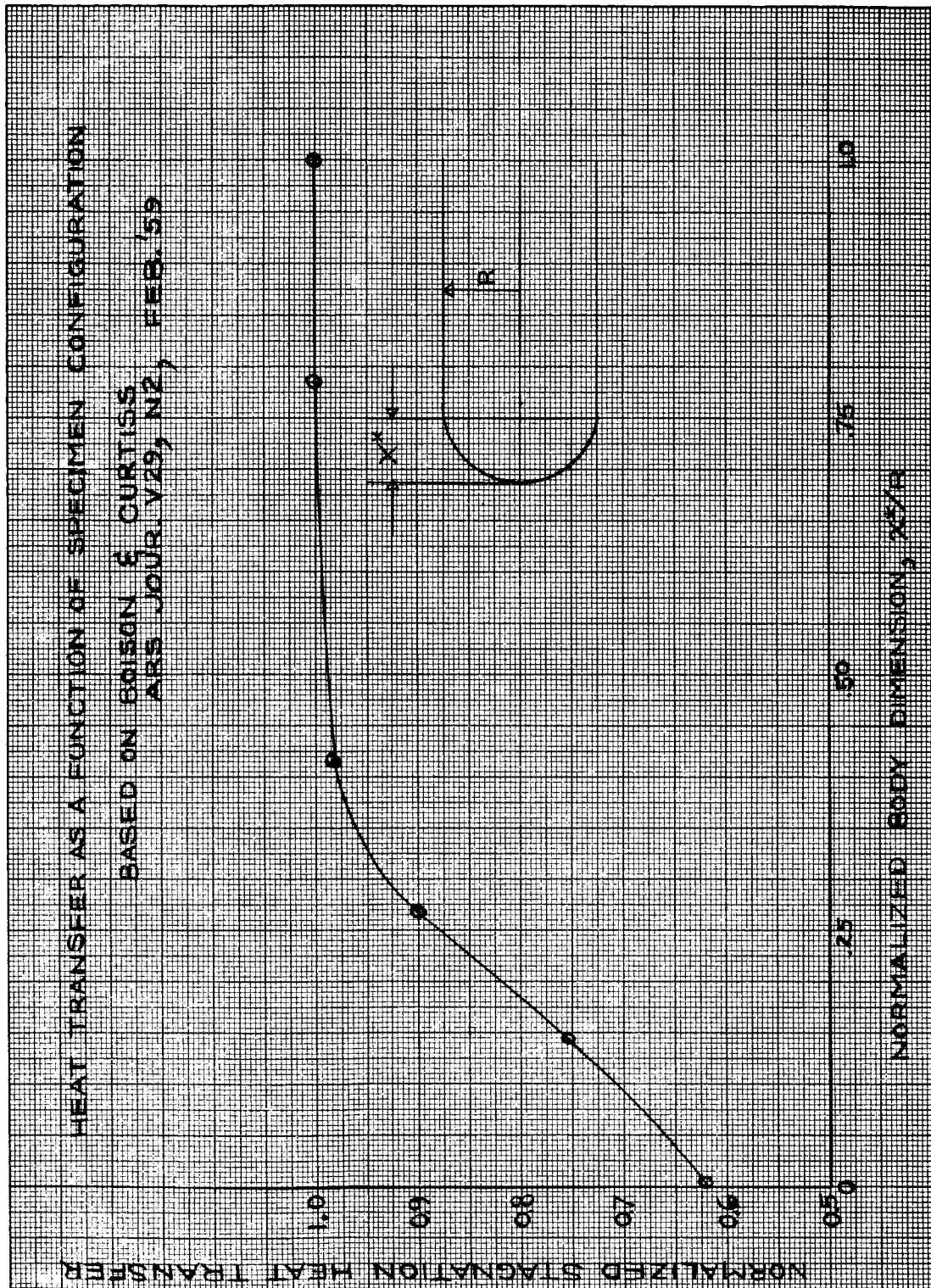


FIGURE 21



# FLOW REGIME CORRELATION FUNCTION

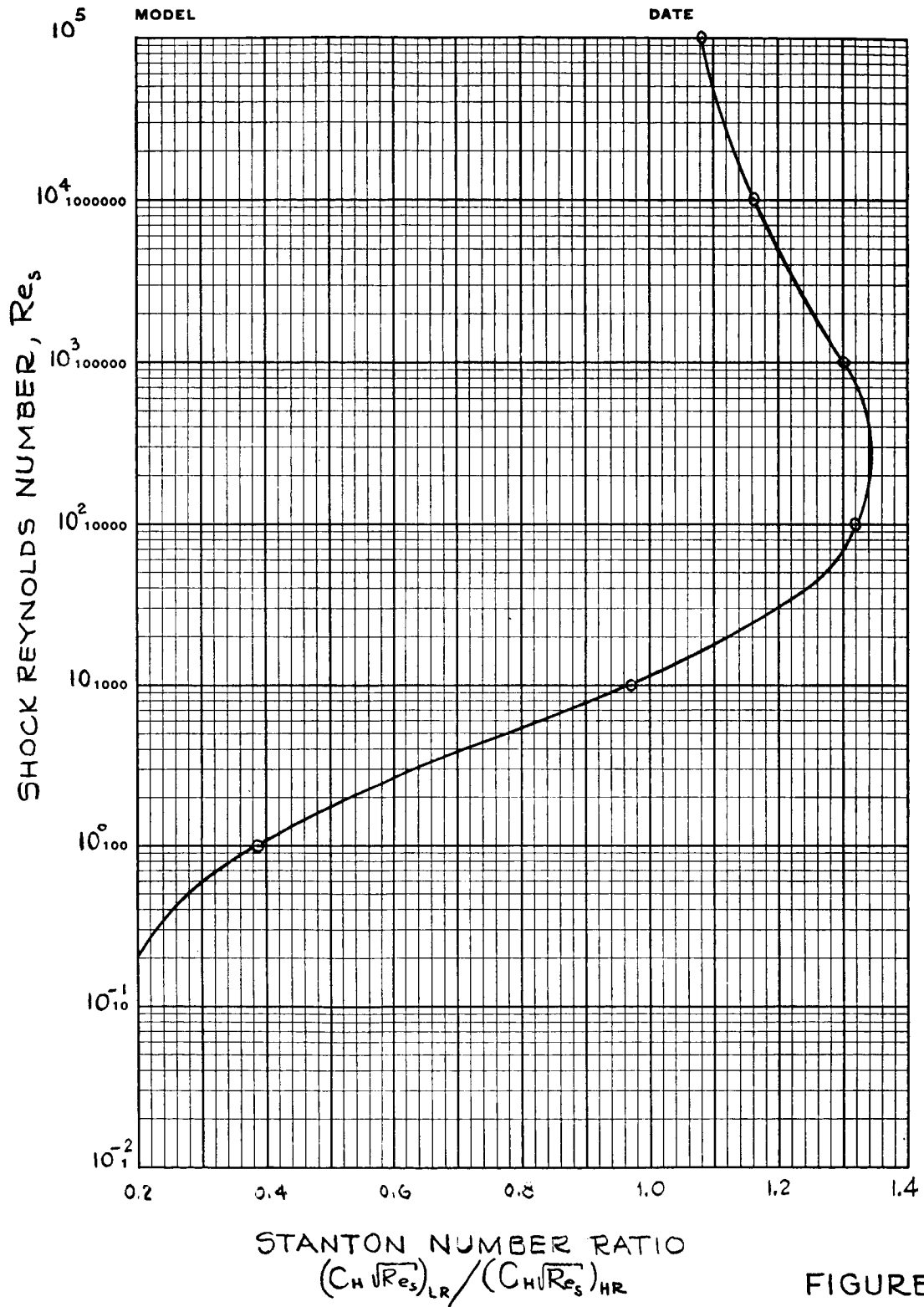


FIGURE 22

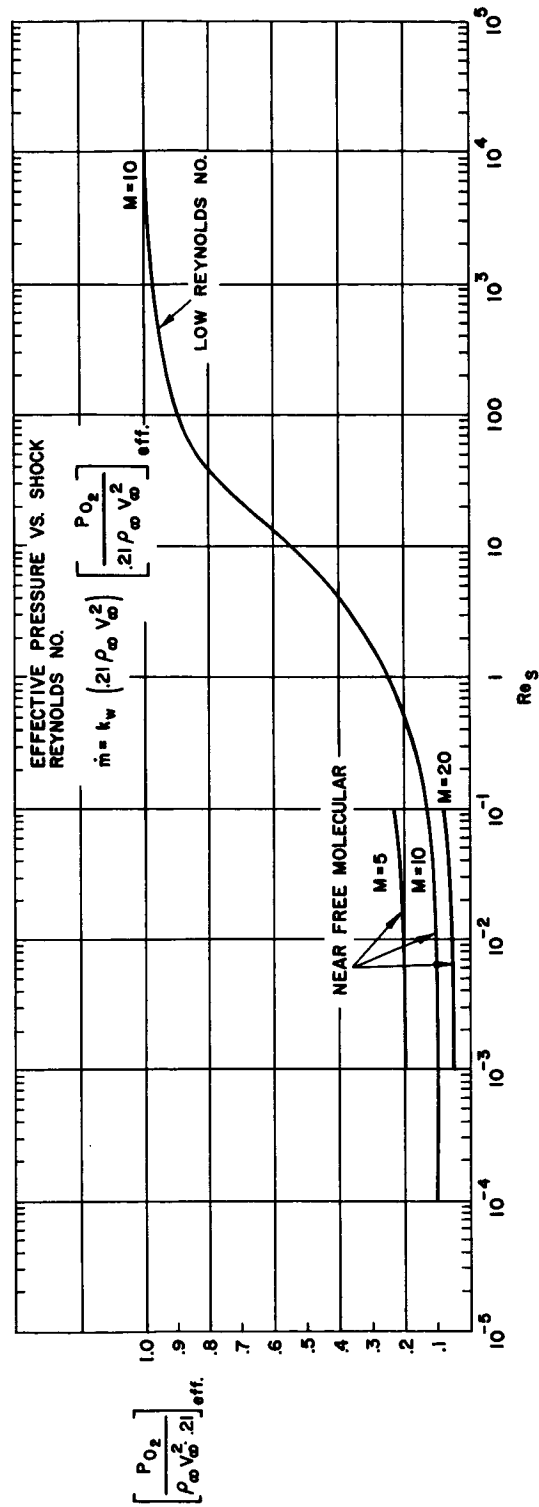


FIGURE 23.

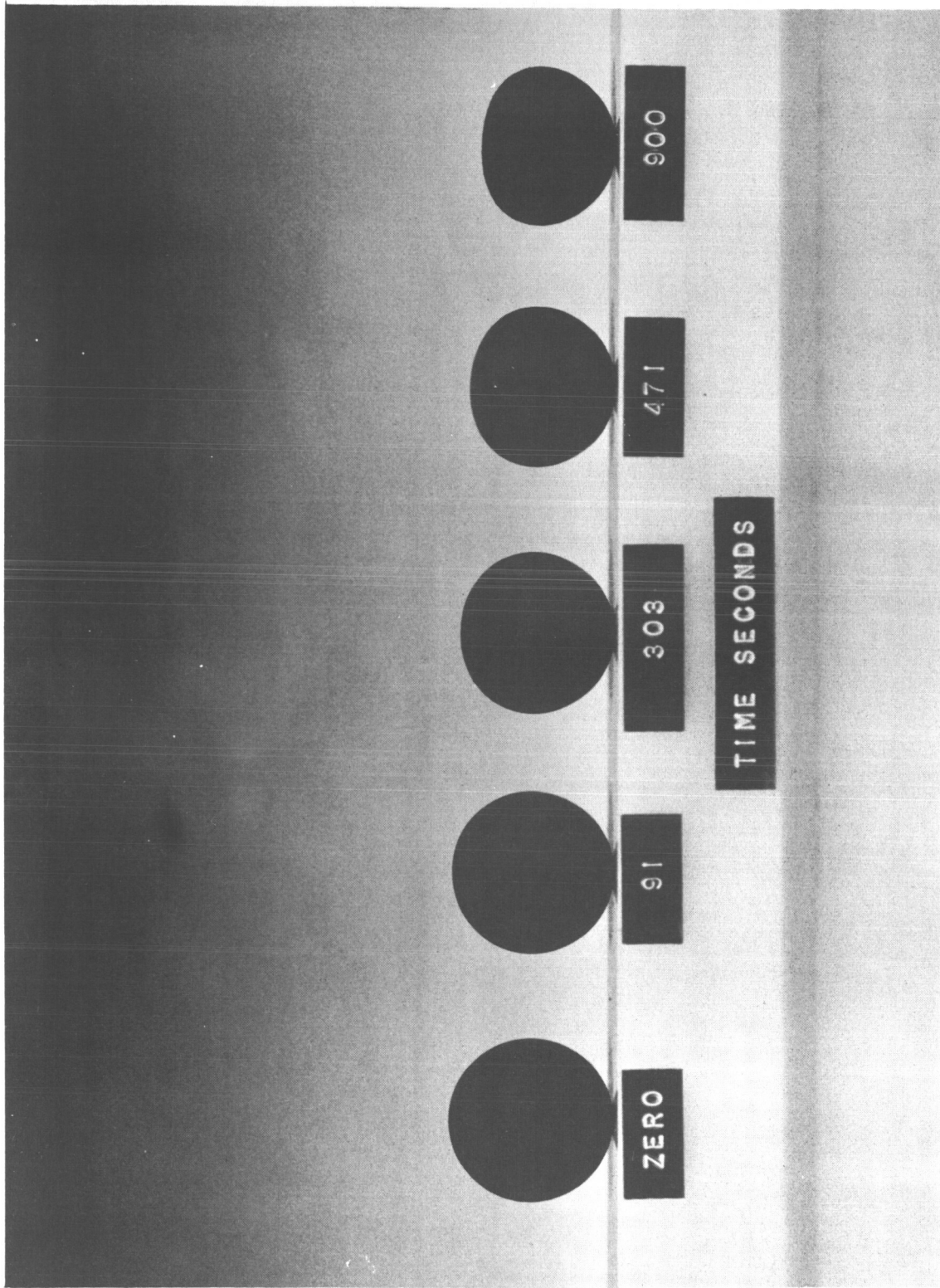


FIGURE 24. FIXED SPHERES, 1.0" DIAMETER - ATJ ABLATED SPECIMENS  
(Support Axis Co-Axial with Flow Direction During Test: Downward)



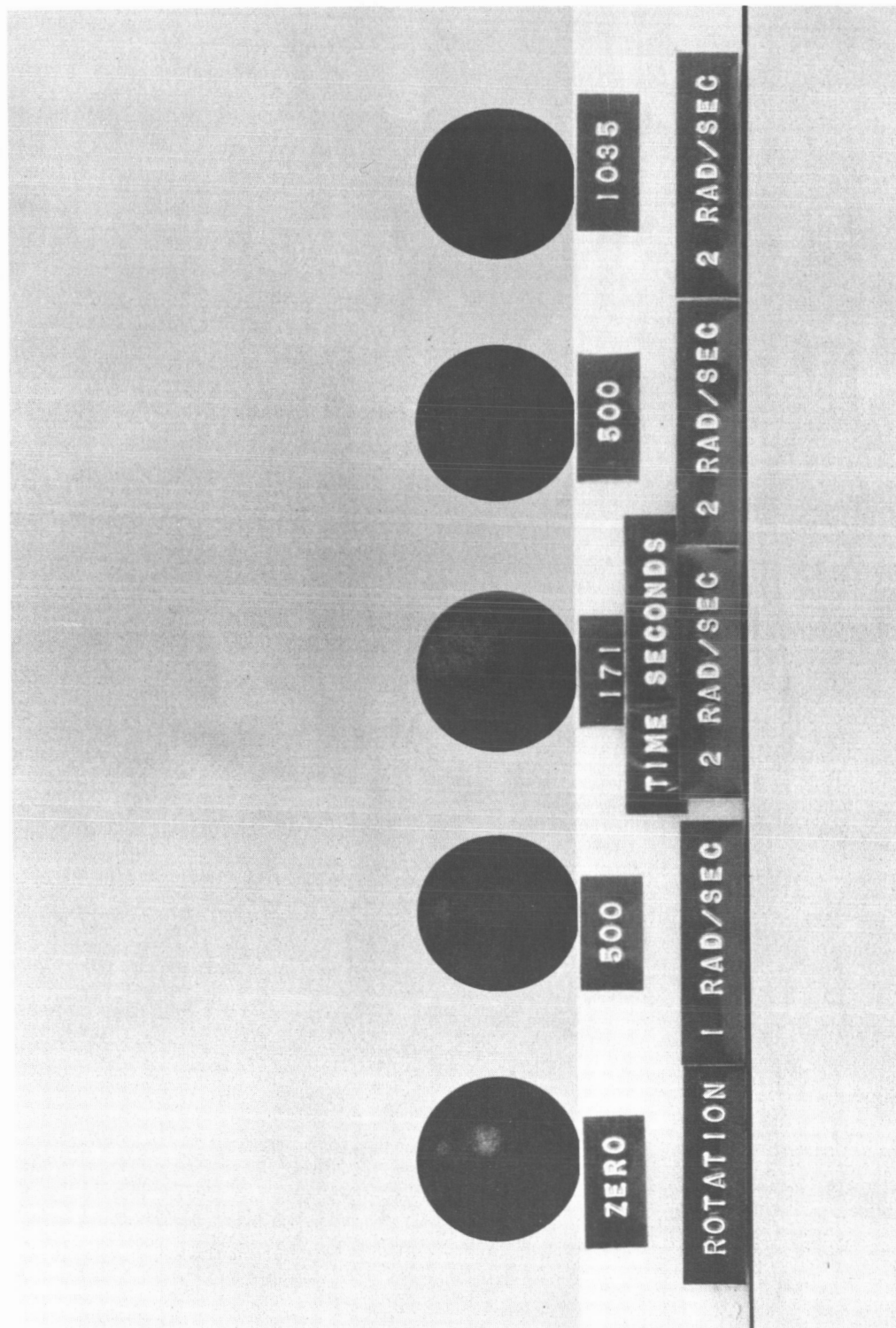


FIGURE 25. ROTATED SPHERES, 1.0" DIAMETER - ATJ SHOWN  
(Axis of Rotation Perpendicular to the Flow Direction During Test: Horizontal)

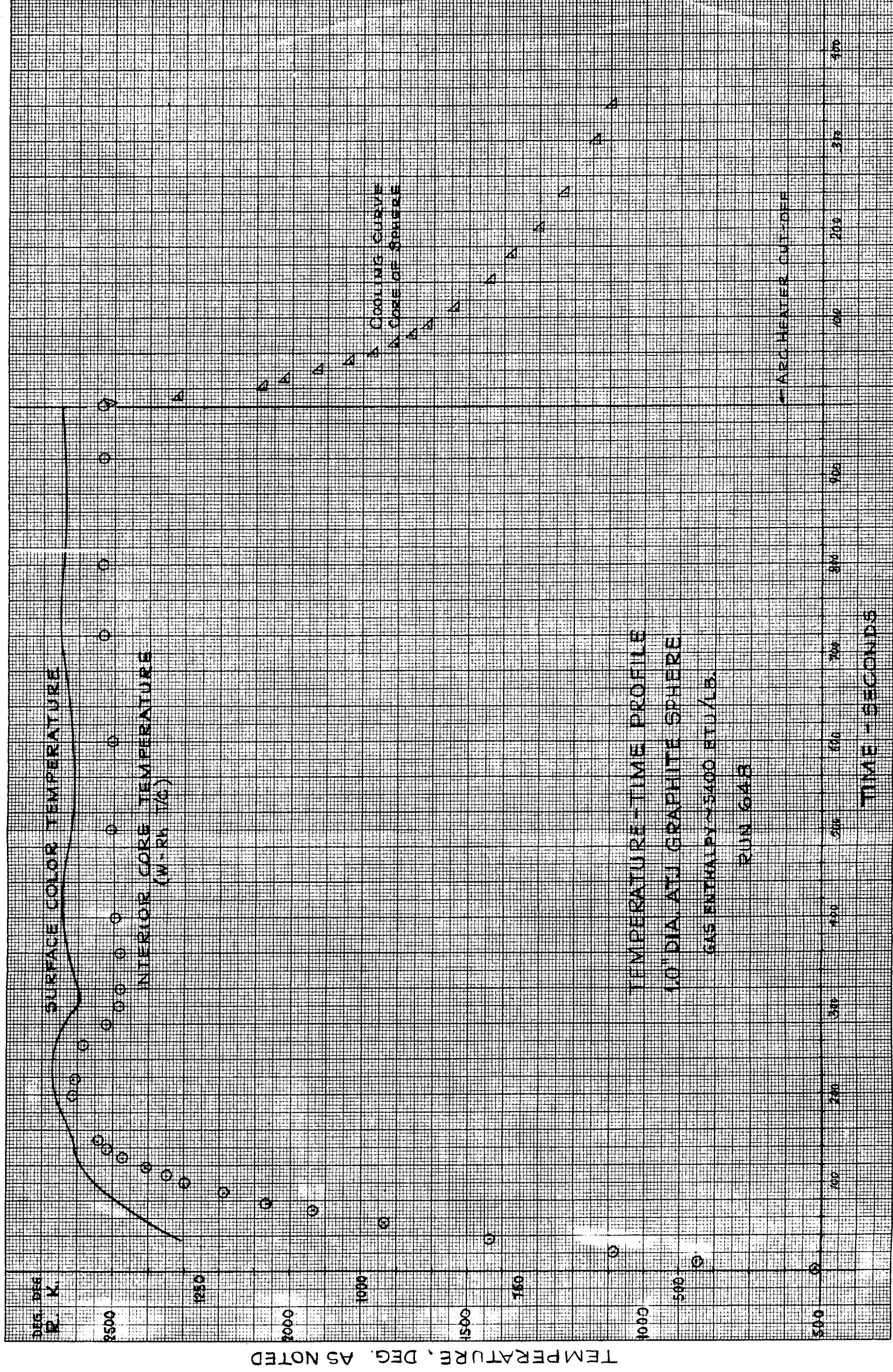


FIGURE 26

~~CONFIDENTIAL~~  
~~RESTRICTED DATA~~

UNCLASSIFIED

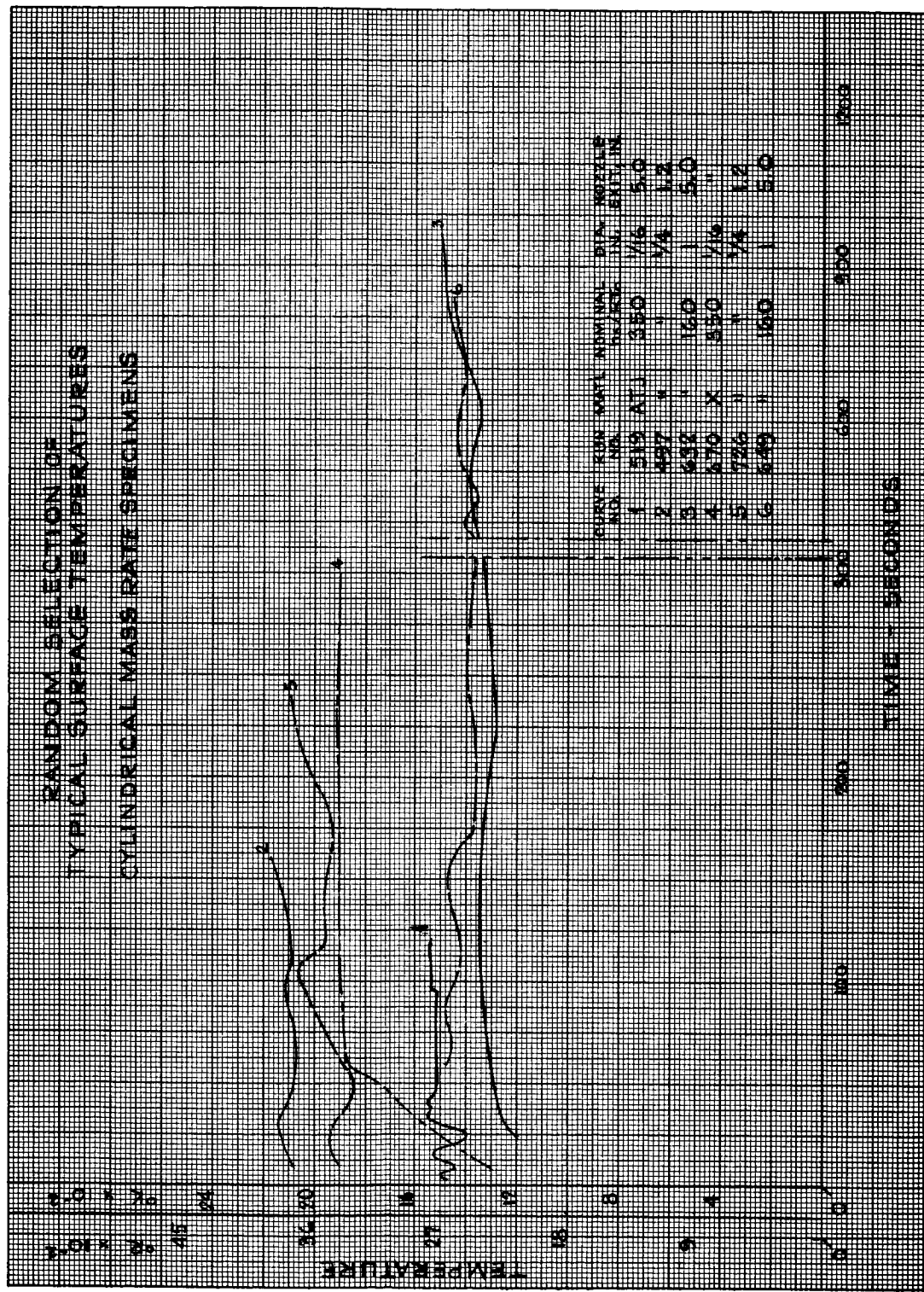


FIGURE 27

~~CONFIDENTIAL~~  
~~RESTRICTED DATA~~  
~~Atomic Energy Act of 1954~~

UNCLASSIFIED



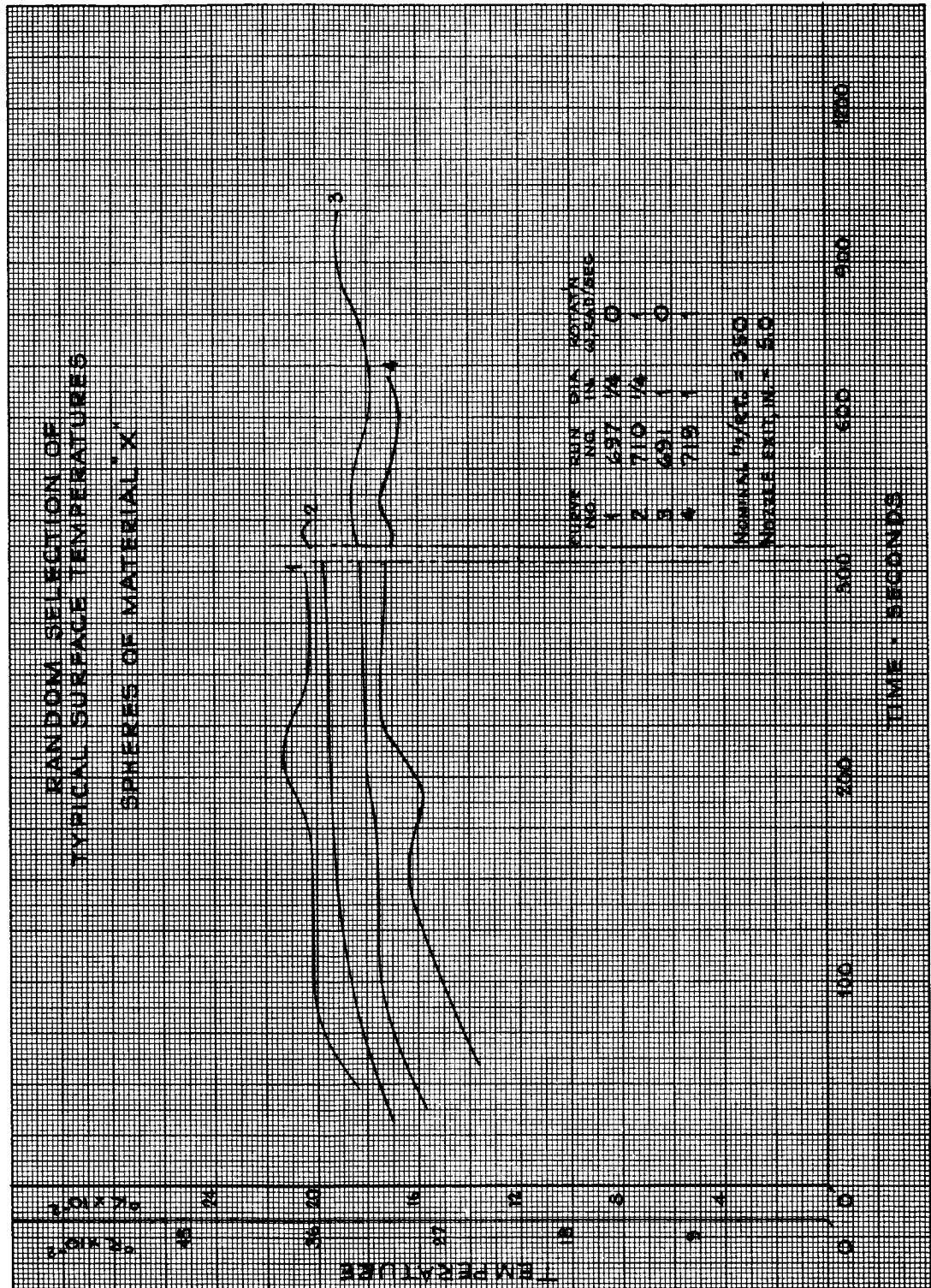


FIGURE 28

RESTRICTED DATA

UNCLASSIFIED

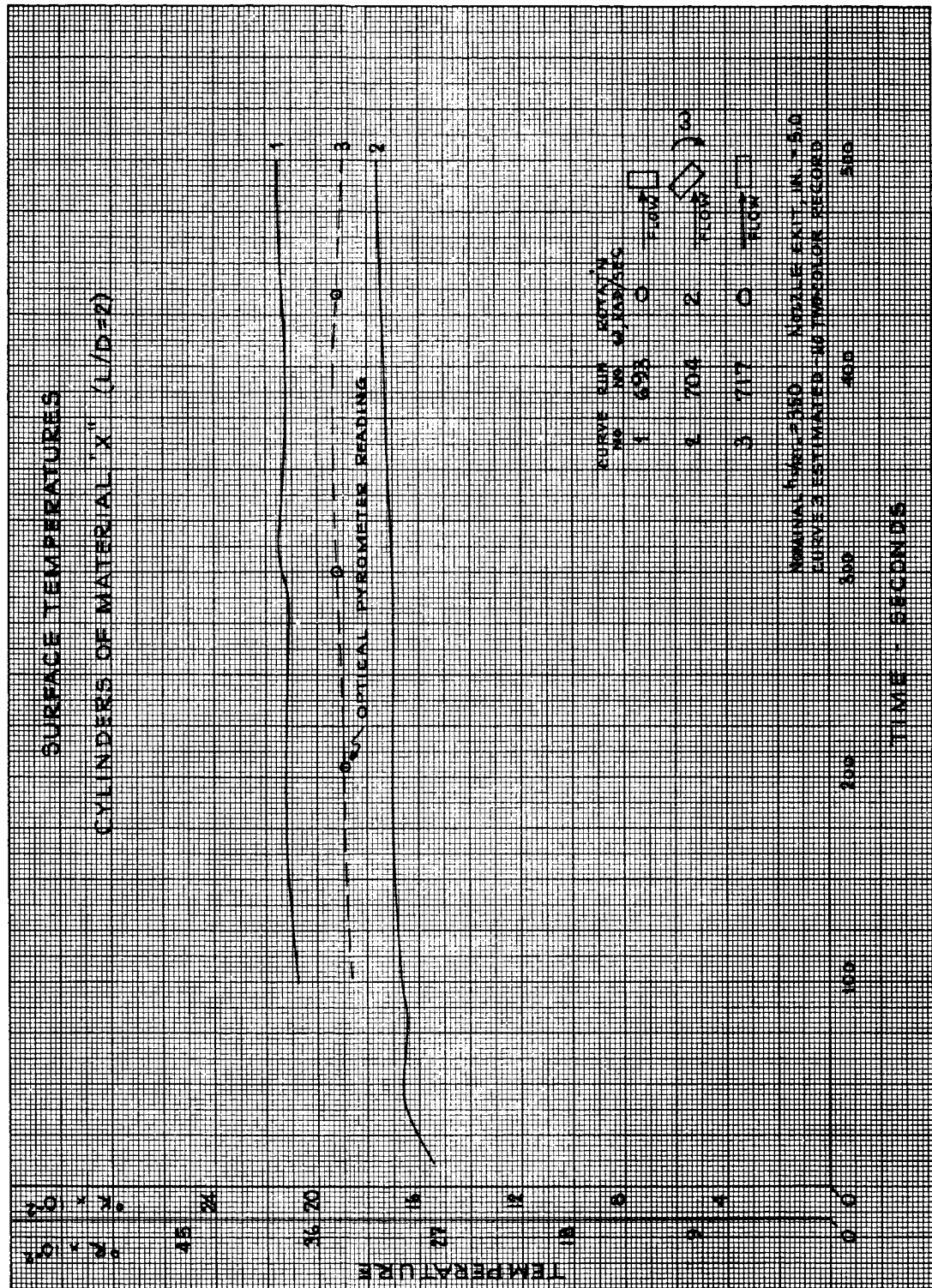


FIGURE 29

CONFIDENTIAL

RESTRICTED DATA

UNCLASSIFIED

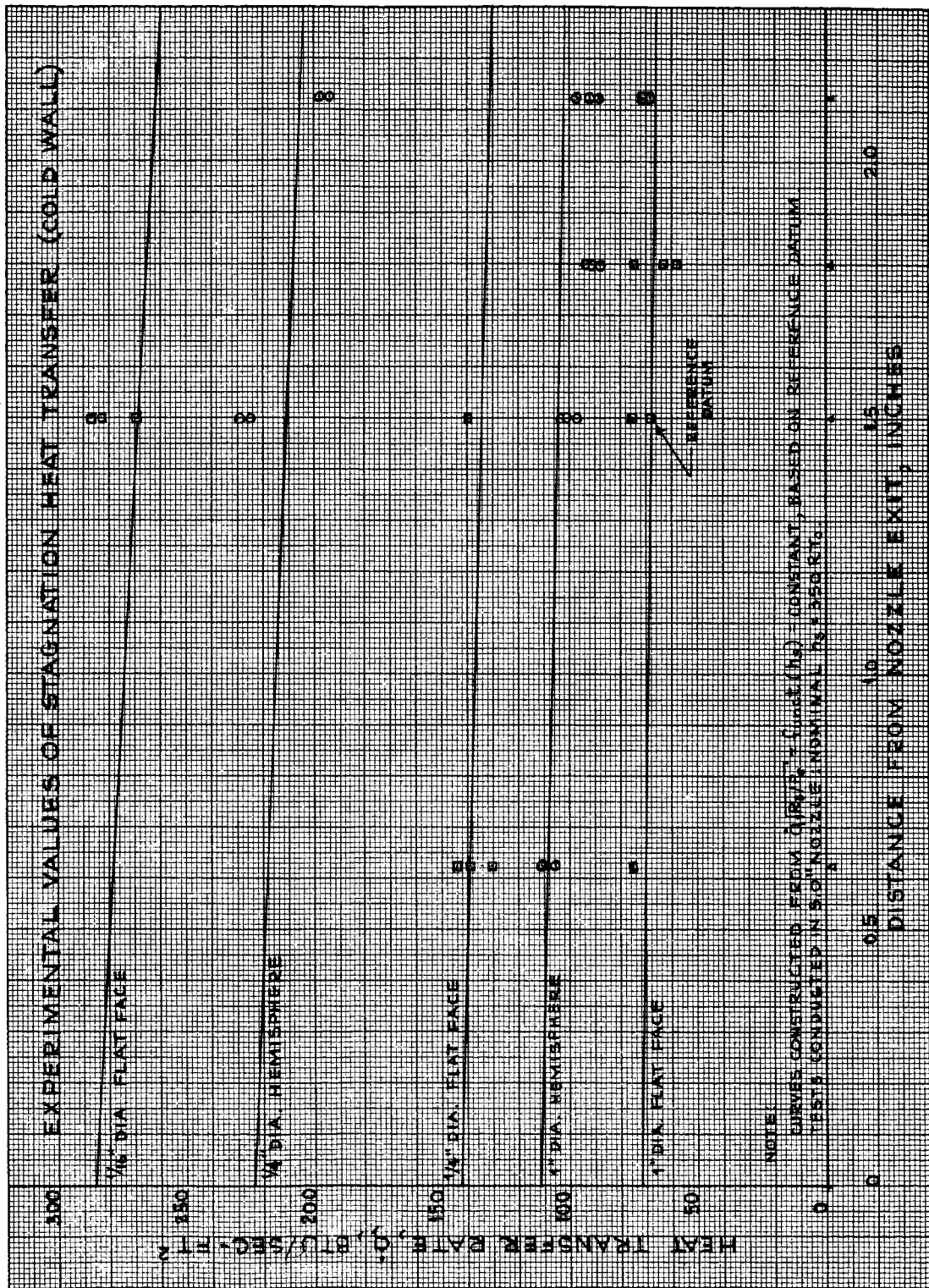


FIGURE 30

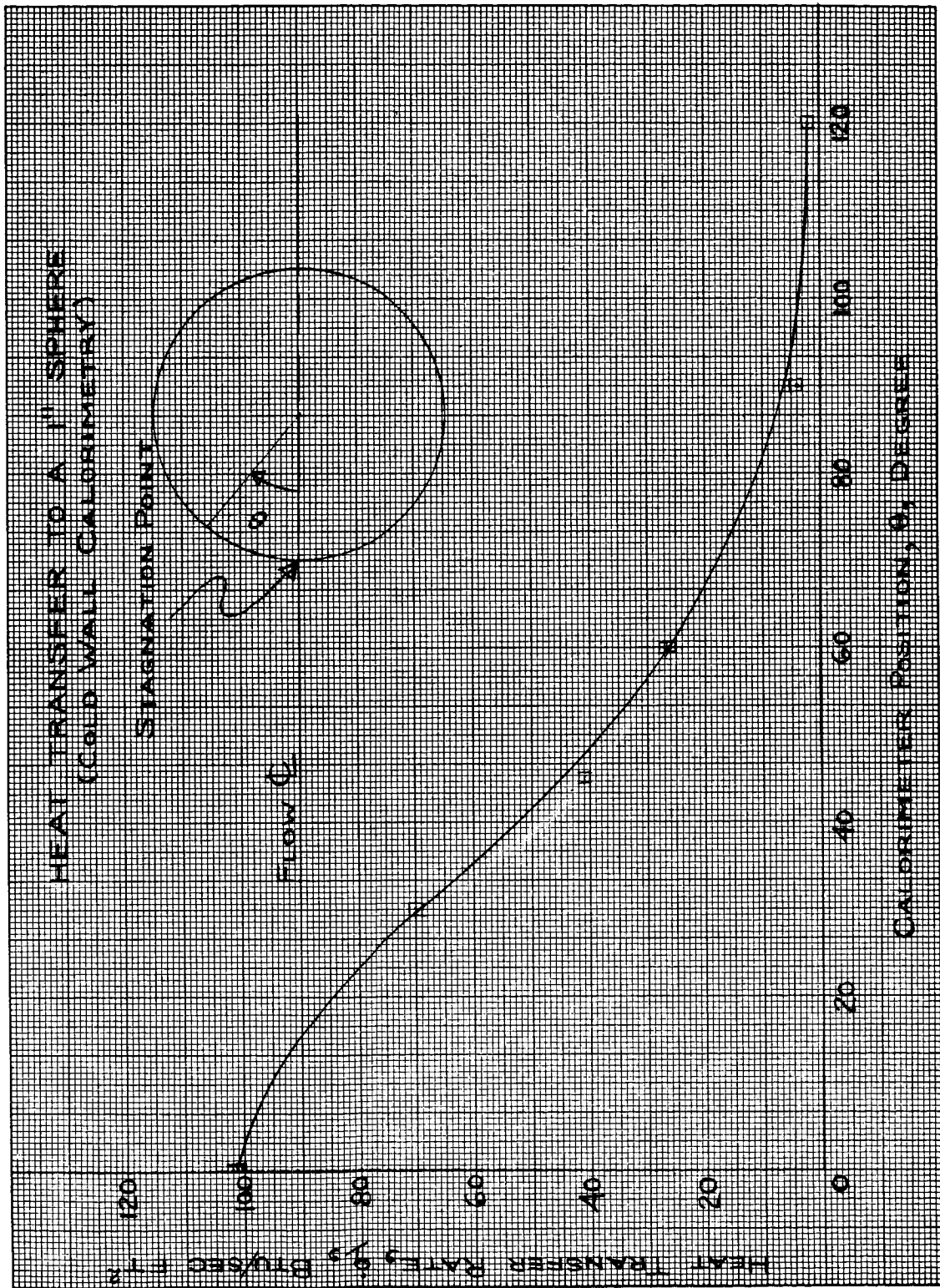


FIGURE 31



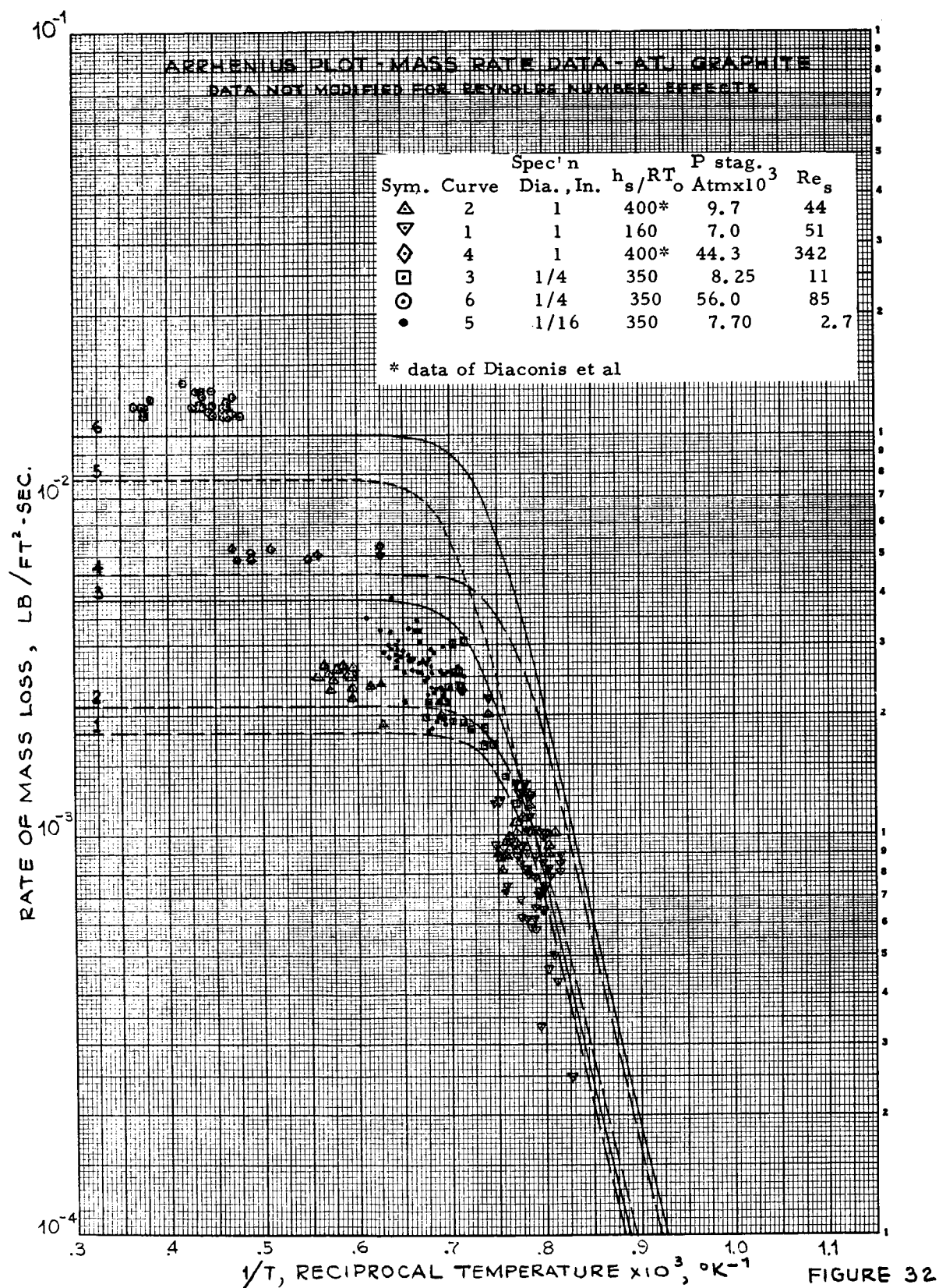
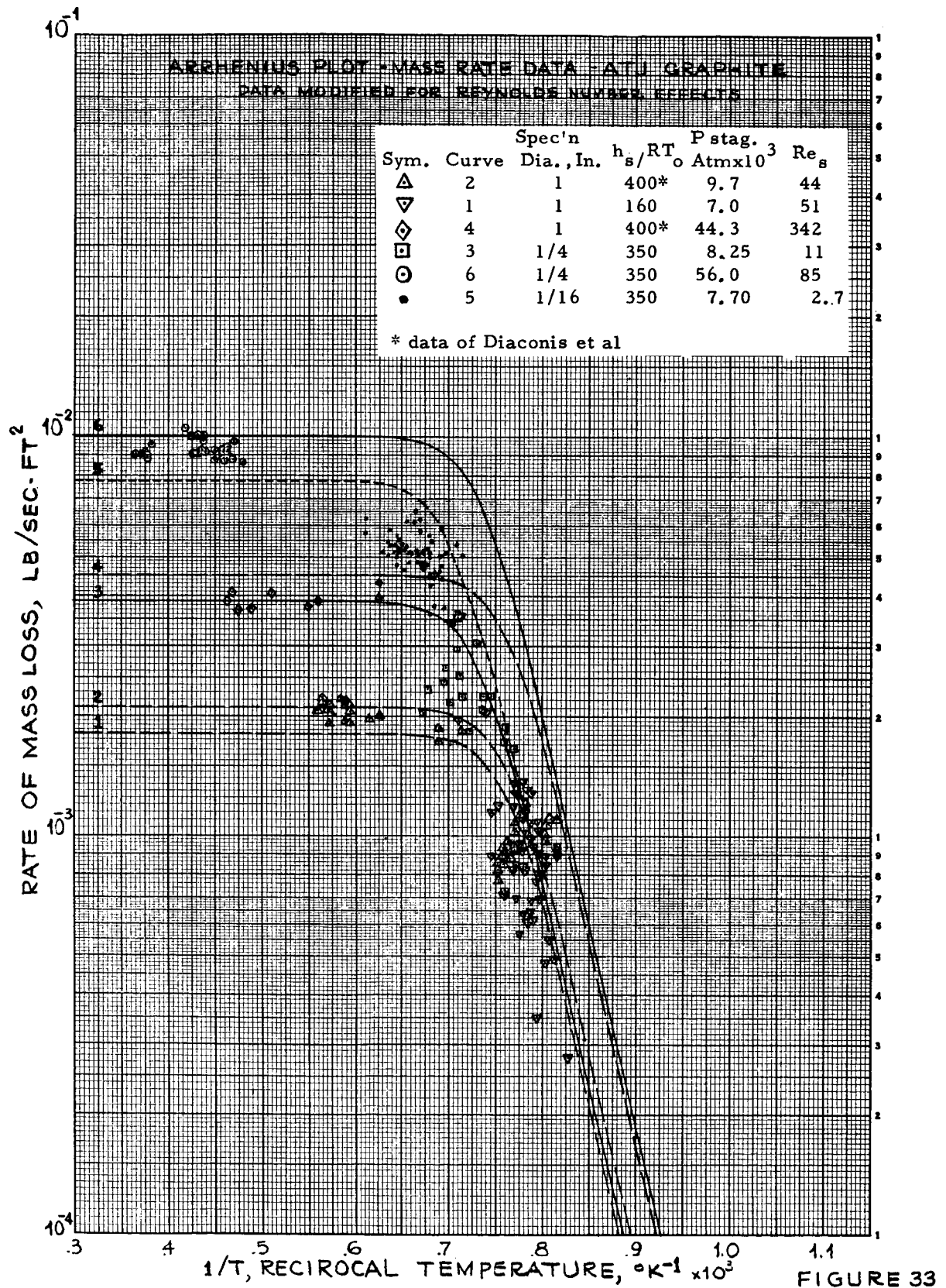


FIGURE 32





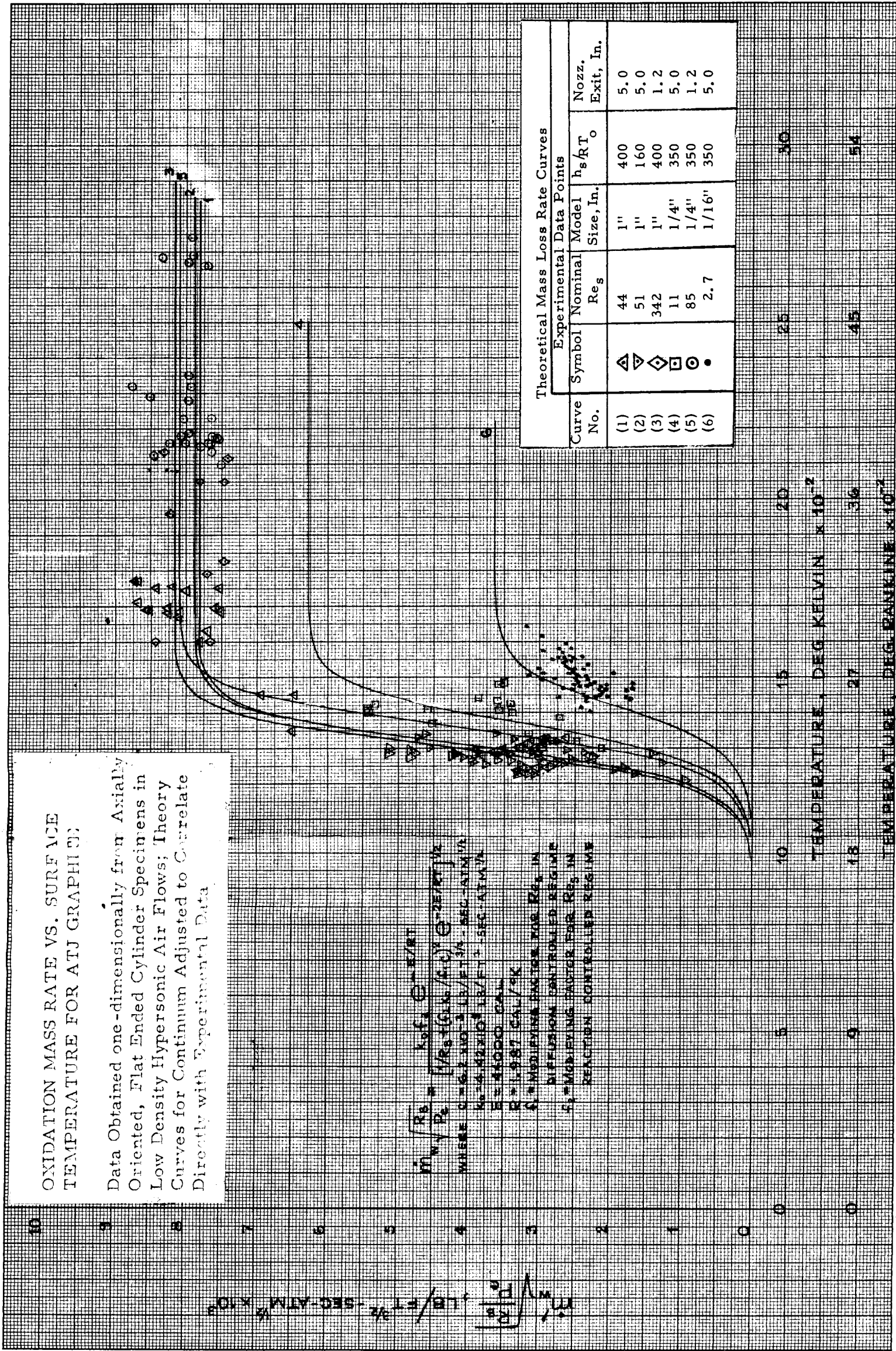


FIGURE 34<sup>227</sup>





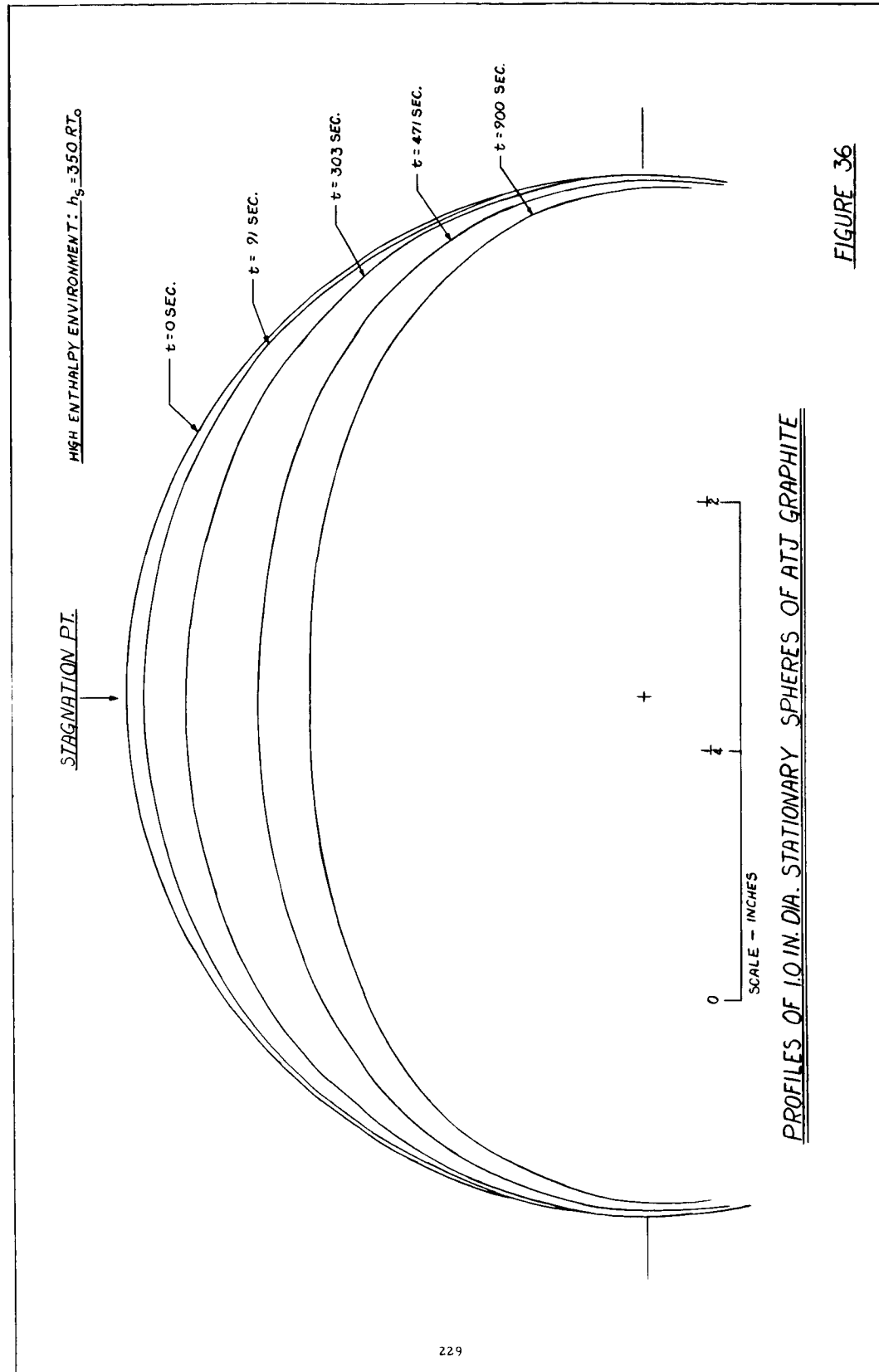


FIGURE 36

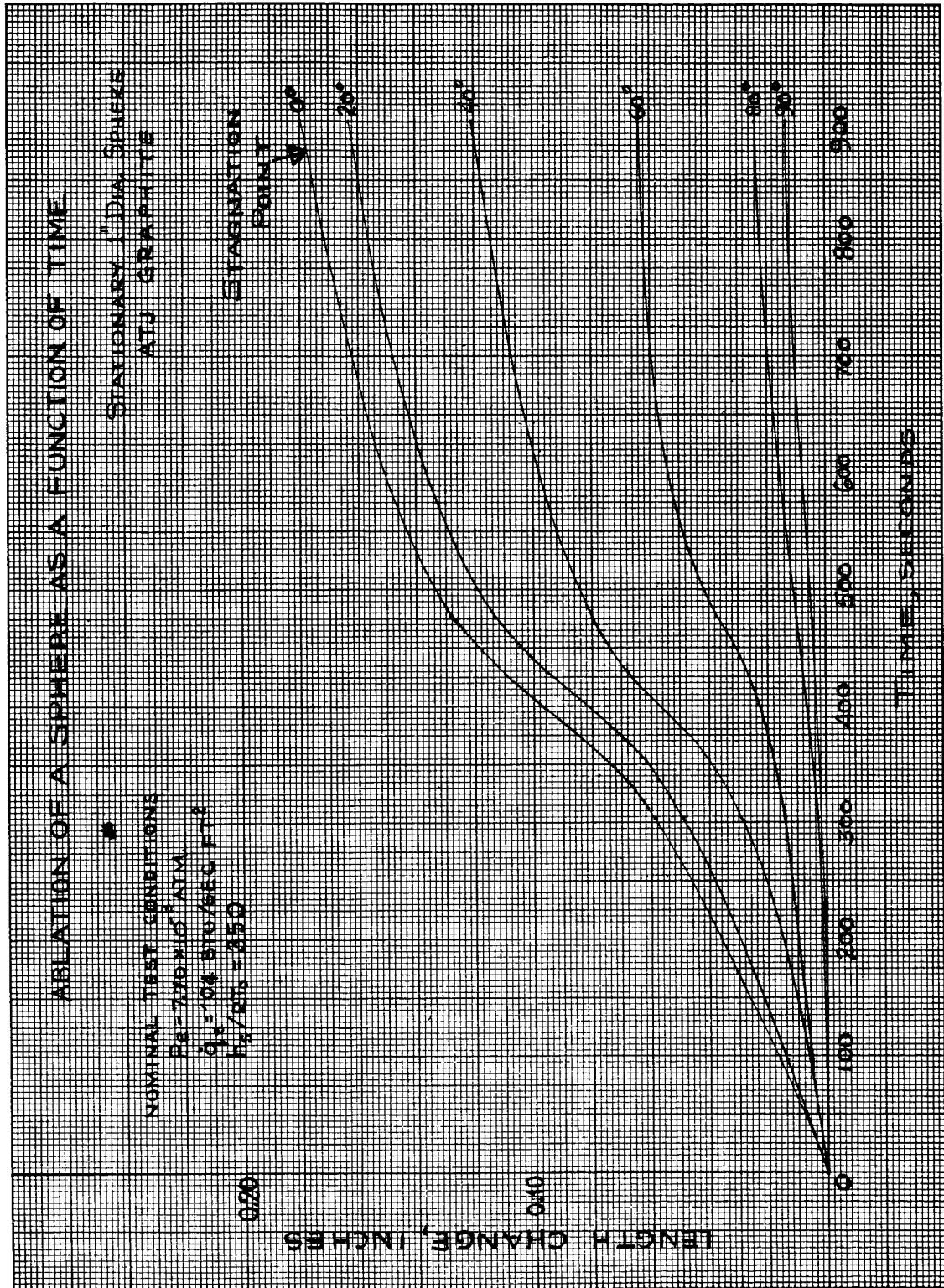
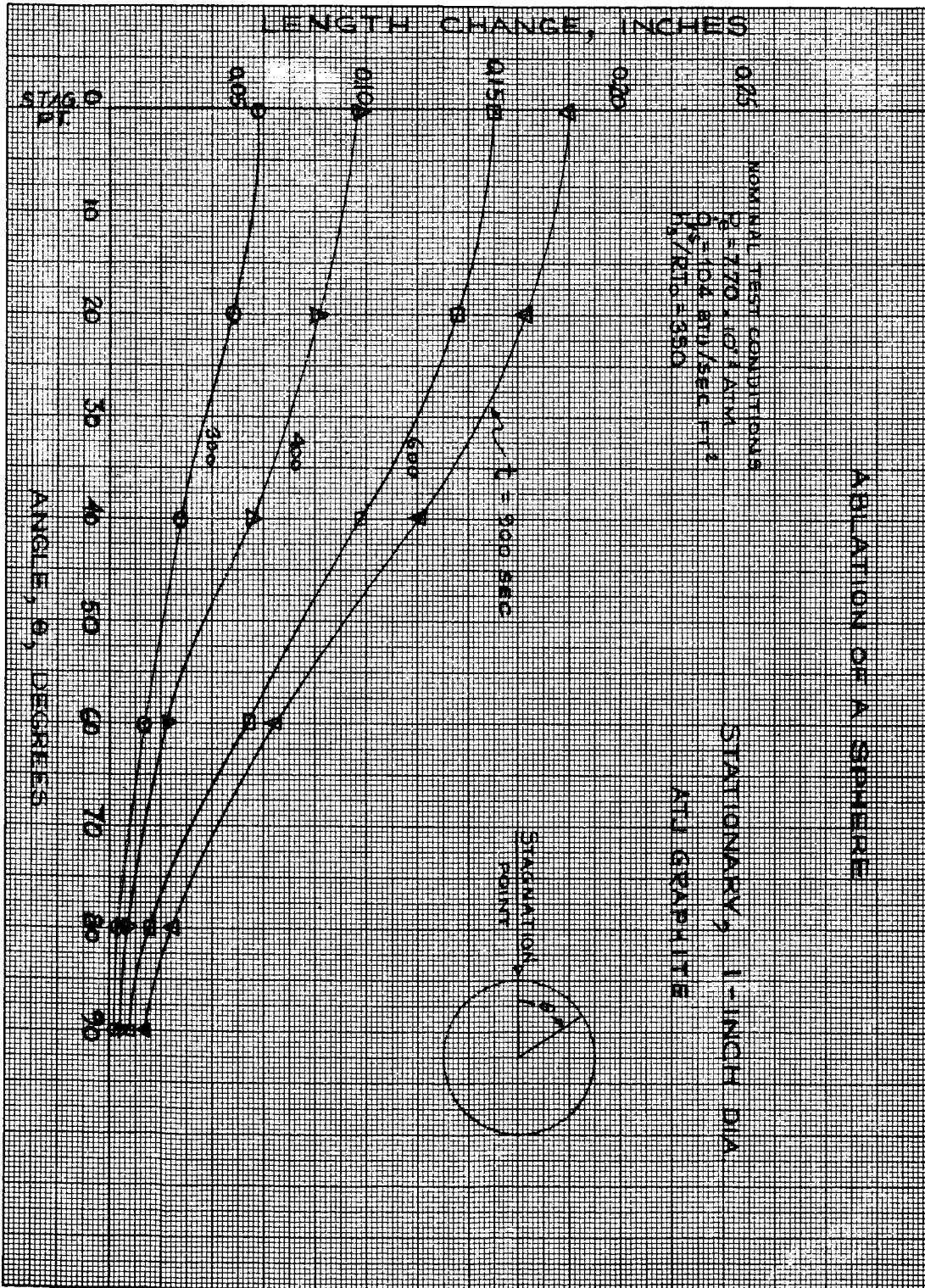
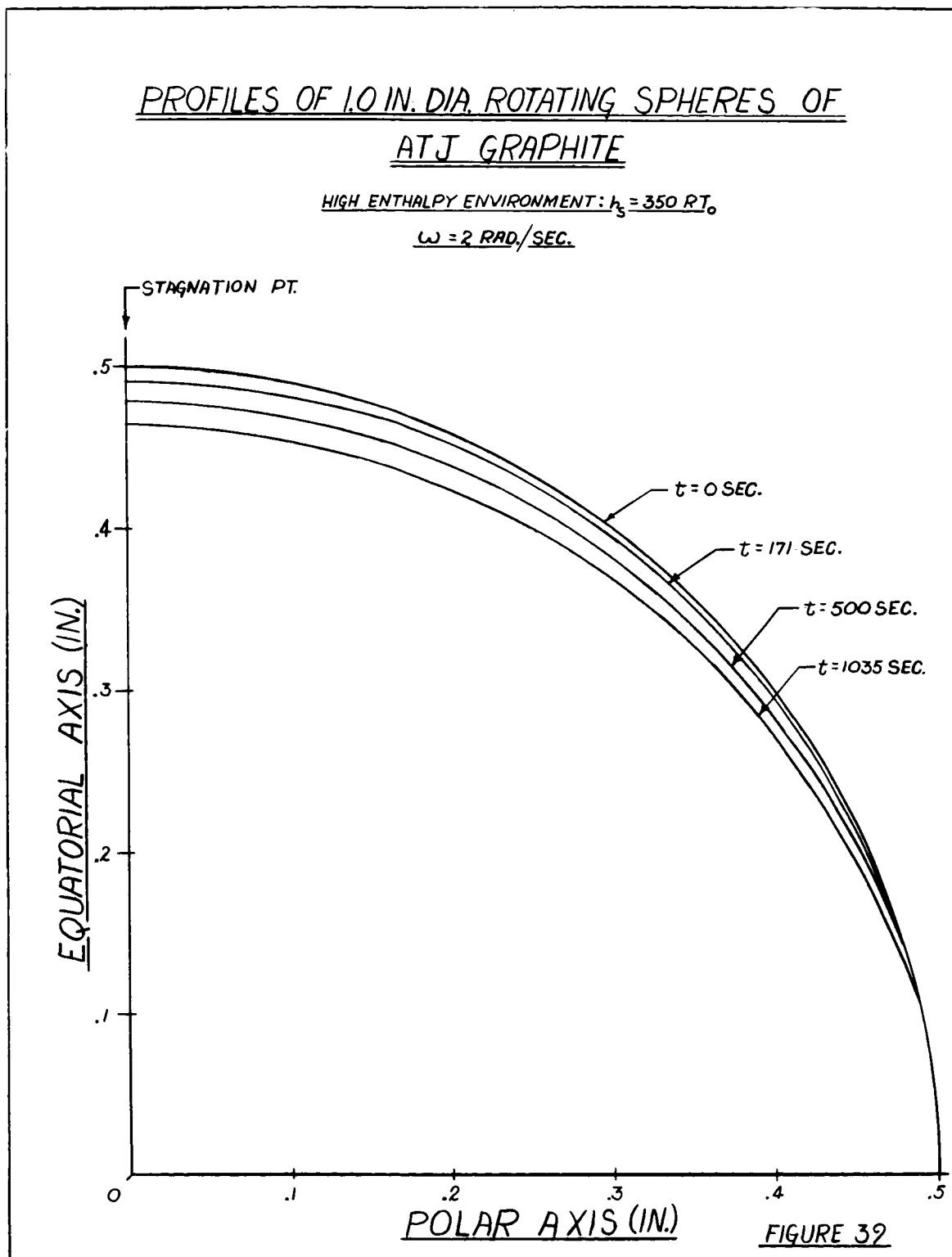


FIGURE 37

FIGURE 38







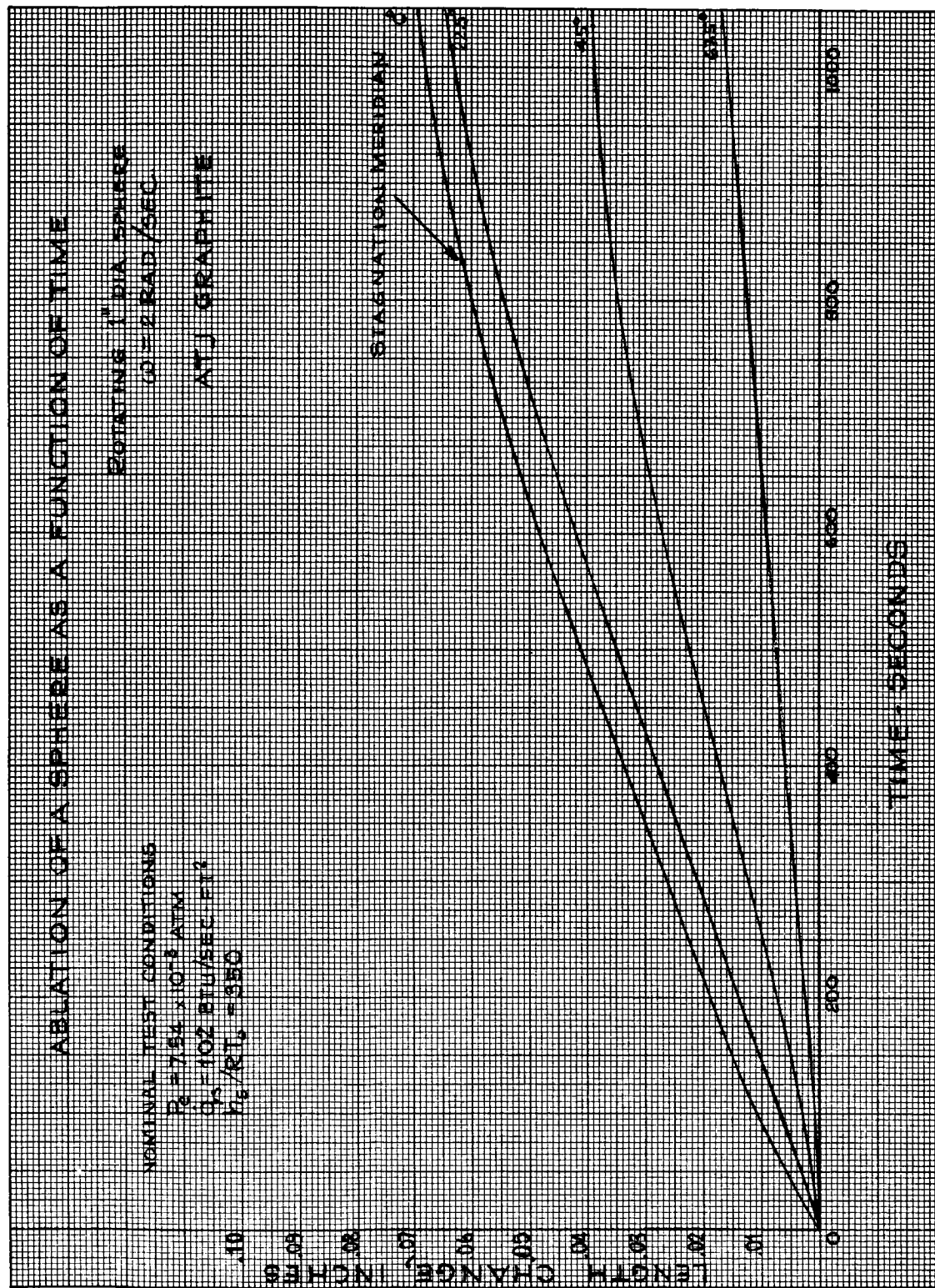
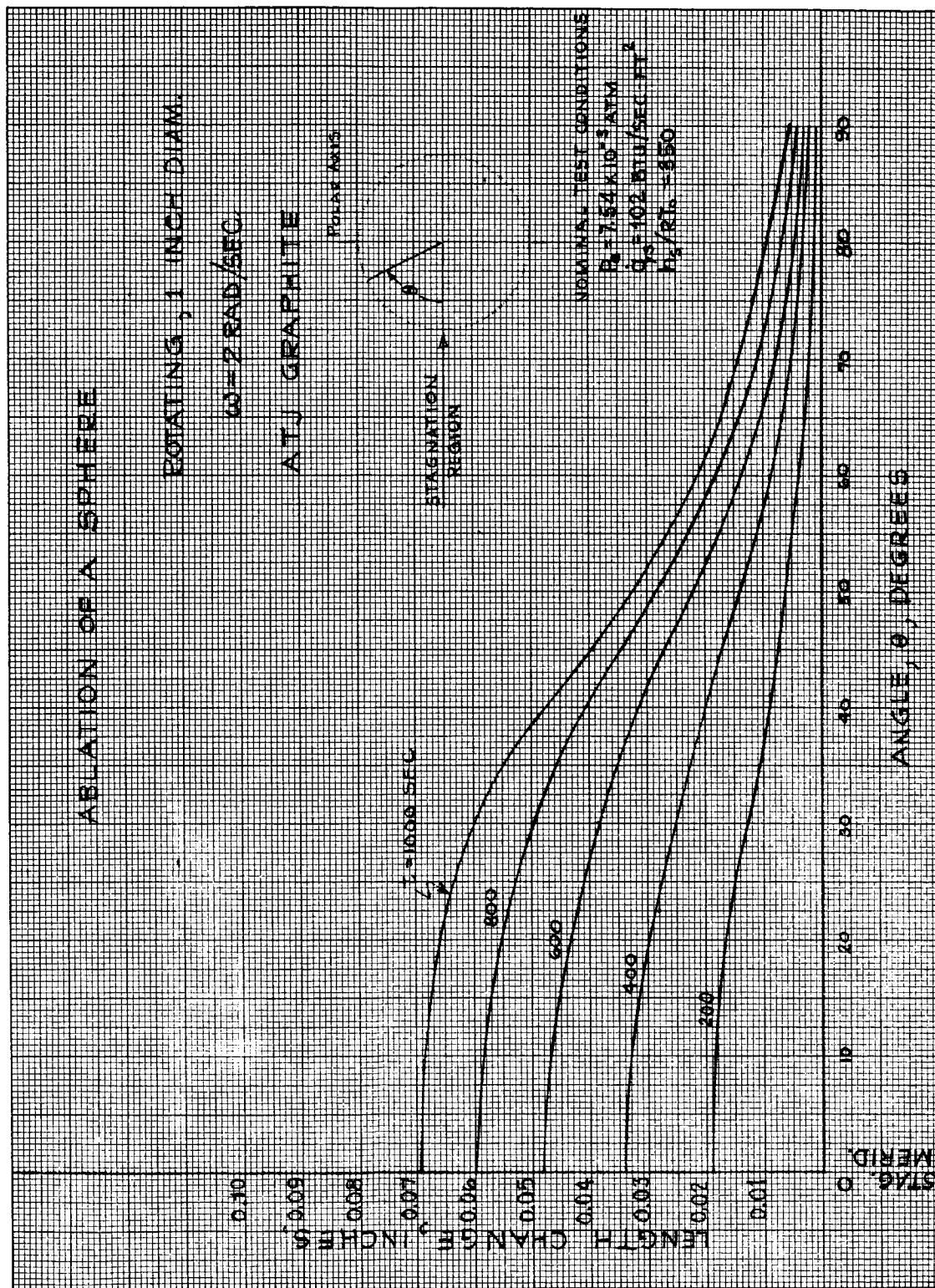


FIGURE 40





PROFILES OF .250 IN. DIA. STATIONARY SPHERES OF  
ATJ GRAPHITE

HIGH ENTHALPY ENVIRONMENT:  $h_3 = 350 T_0$

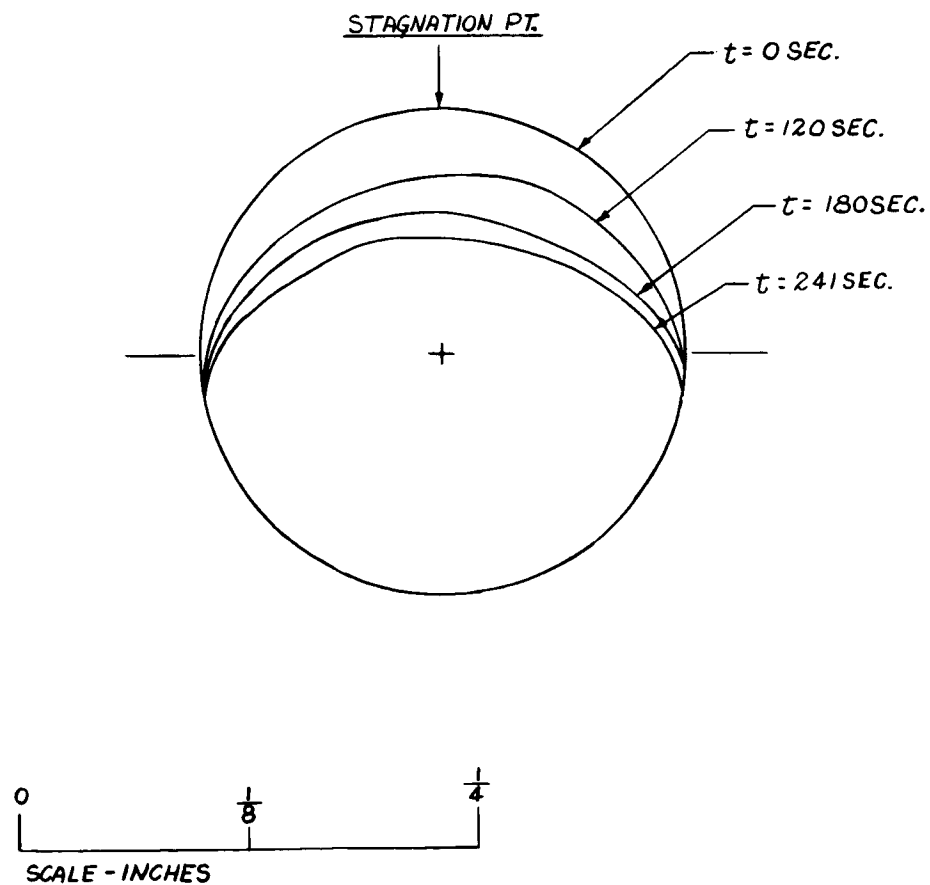
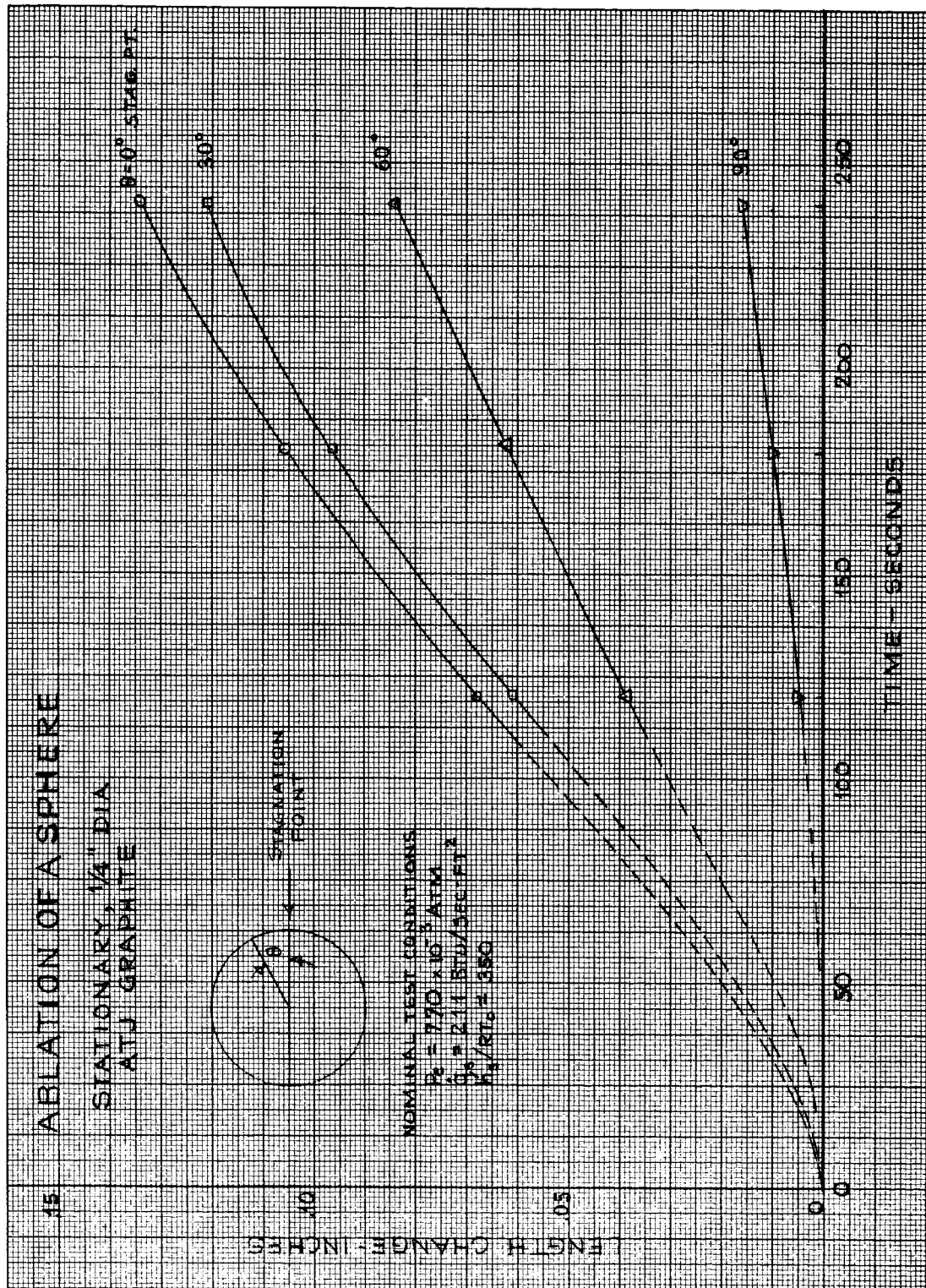
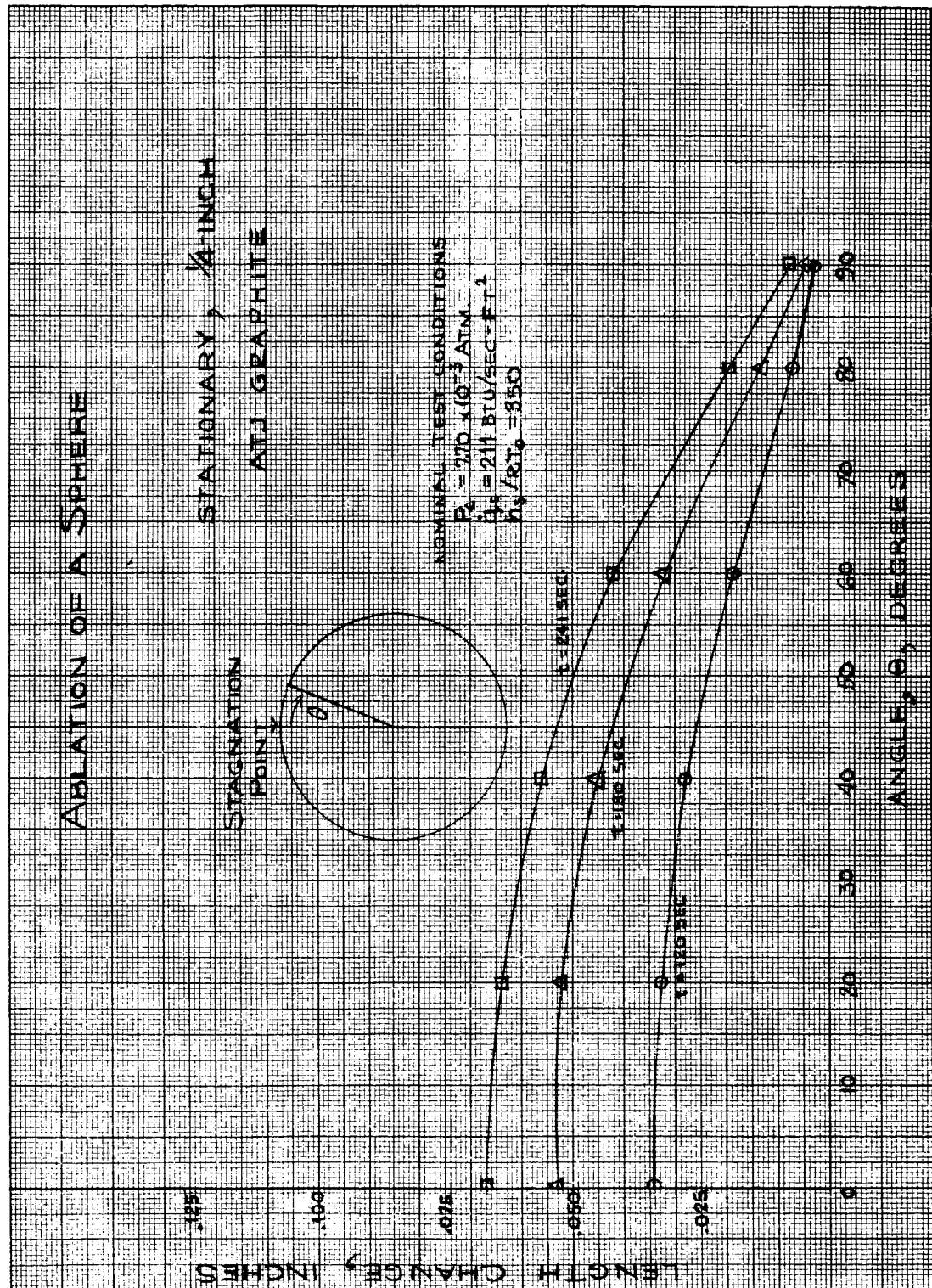


FIGURE 42





PROFILES OF .250 IN. DIA. ROTATING SPHERES OF  
ATJ GRAPHITE

HIGH ENTHALPY ENVIRONMENT:  $h_s = 350 R T_0$

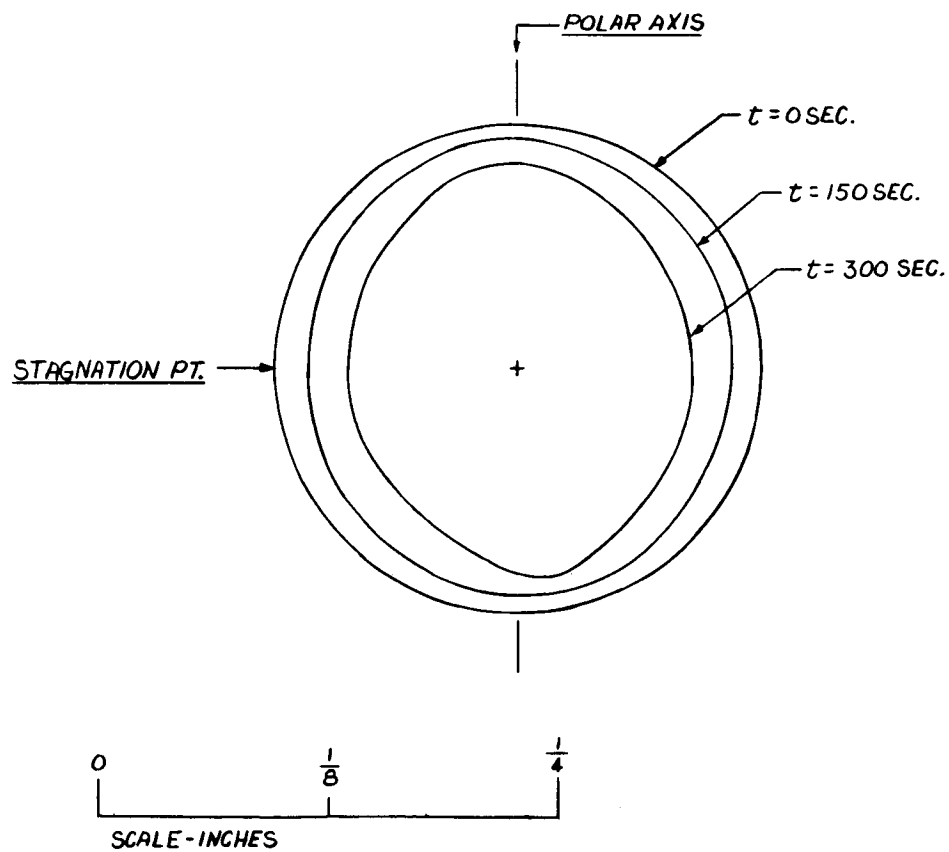


FIGURE 45

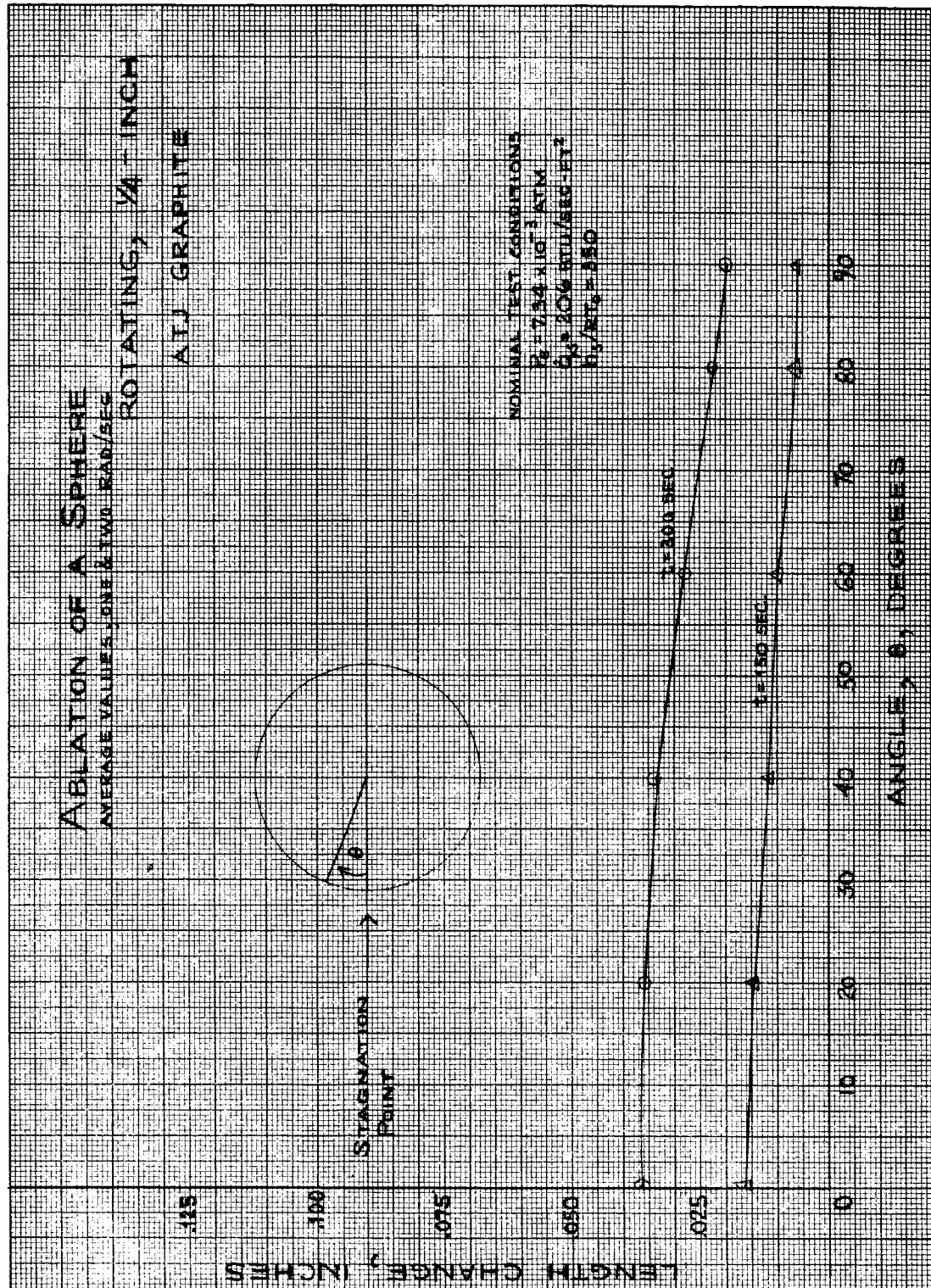
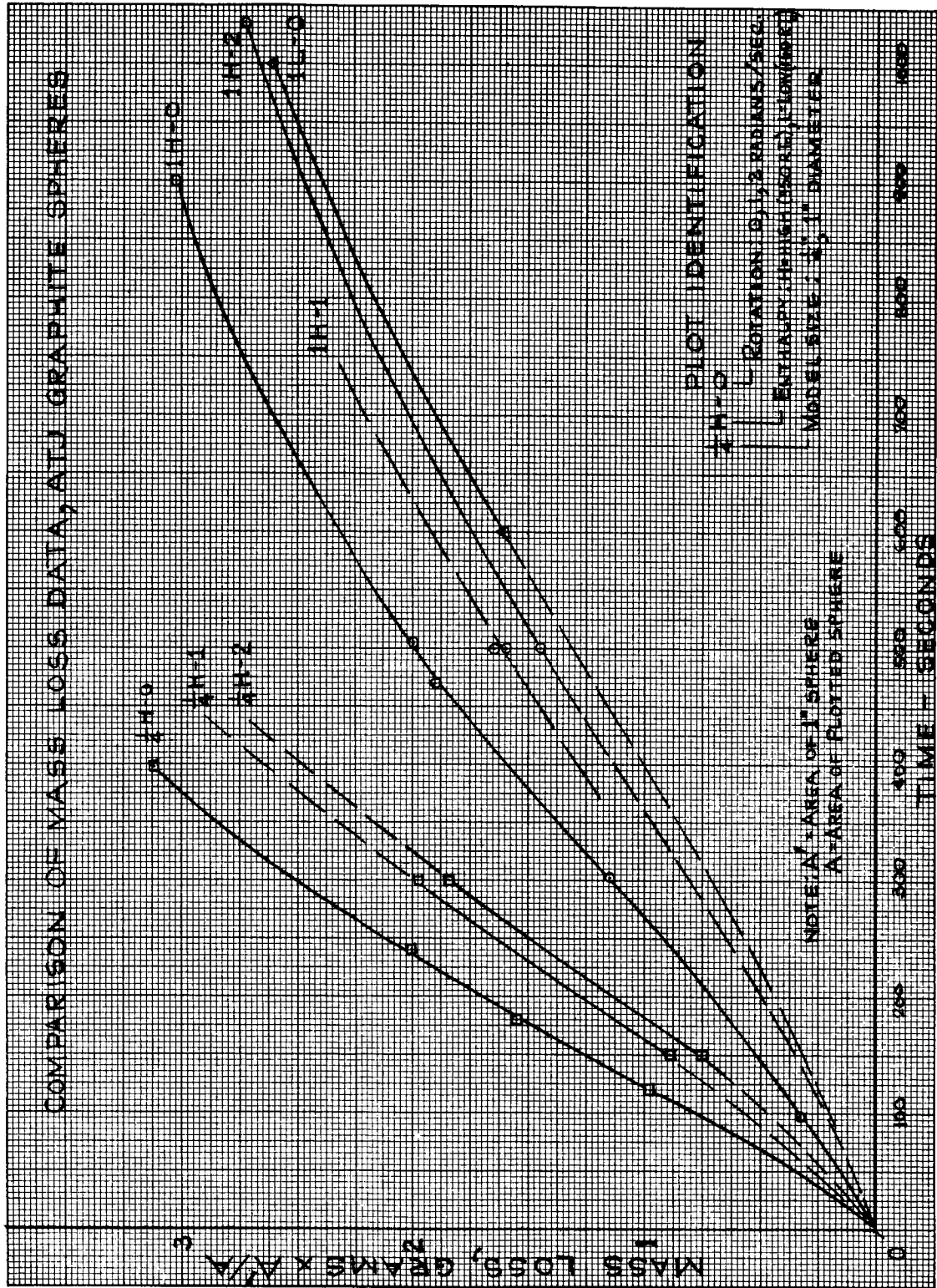
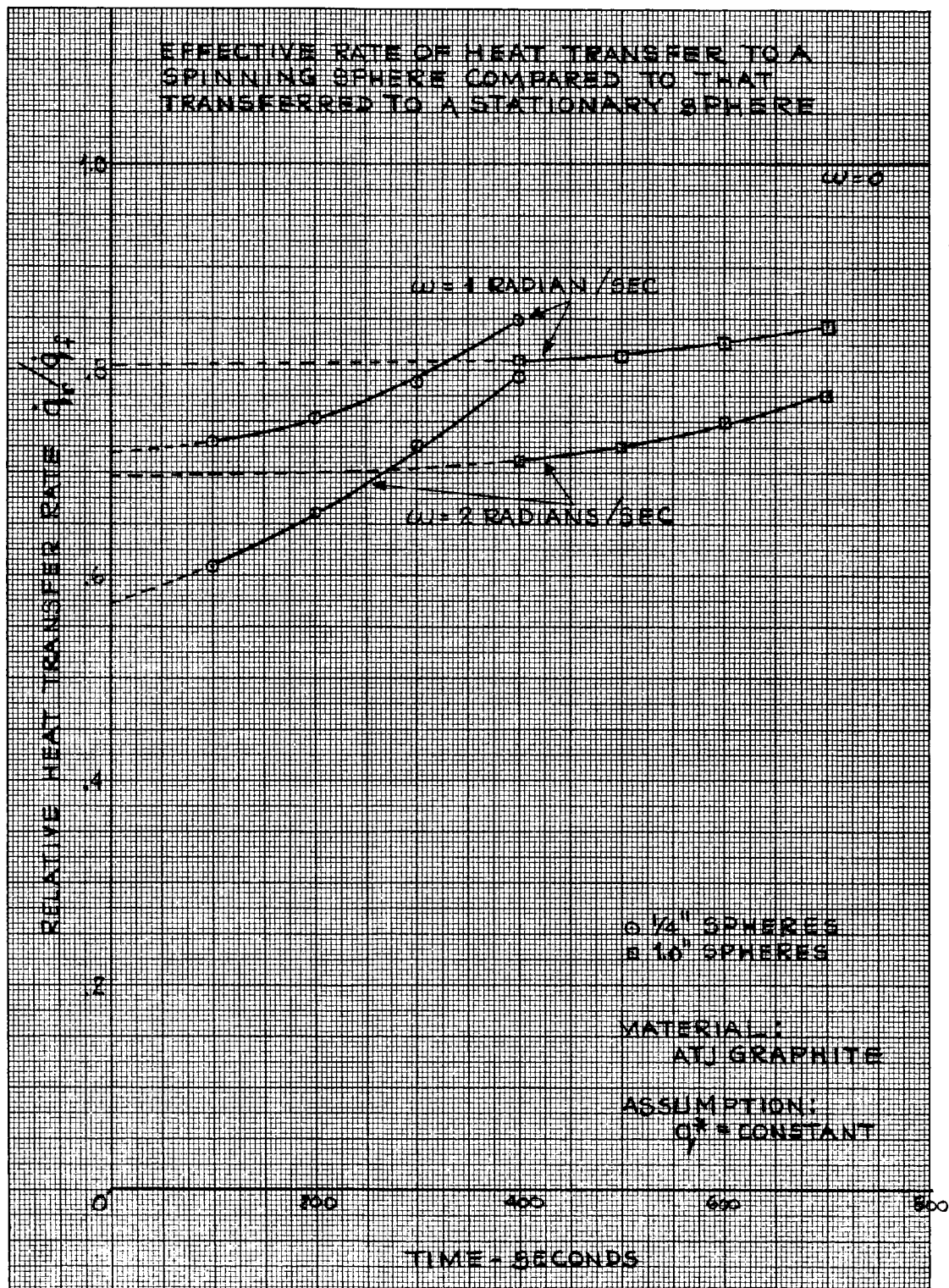


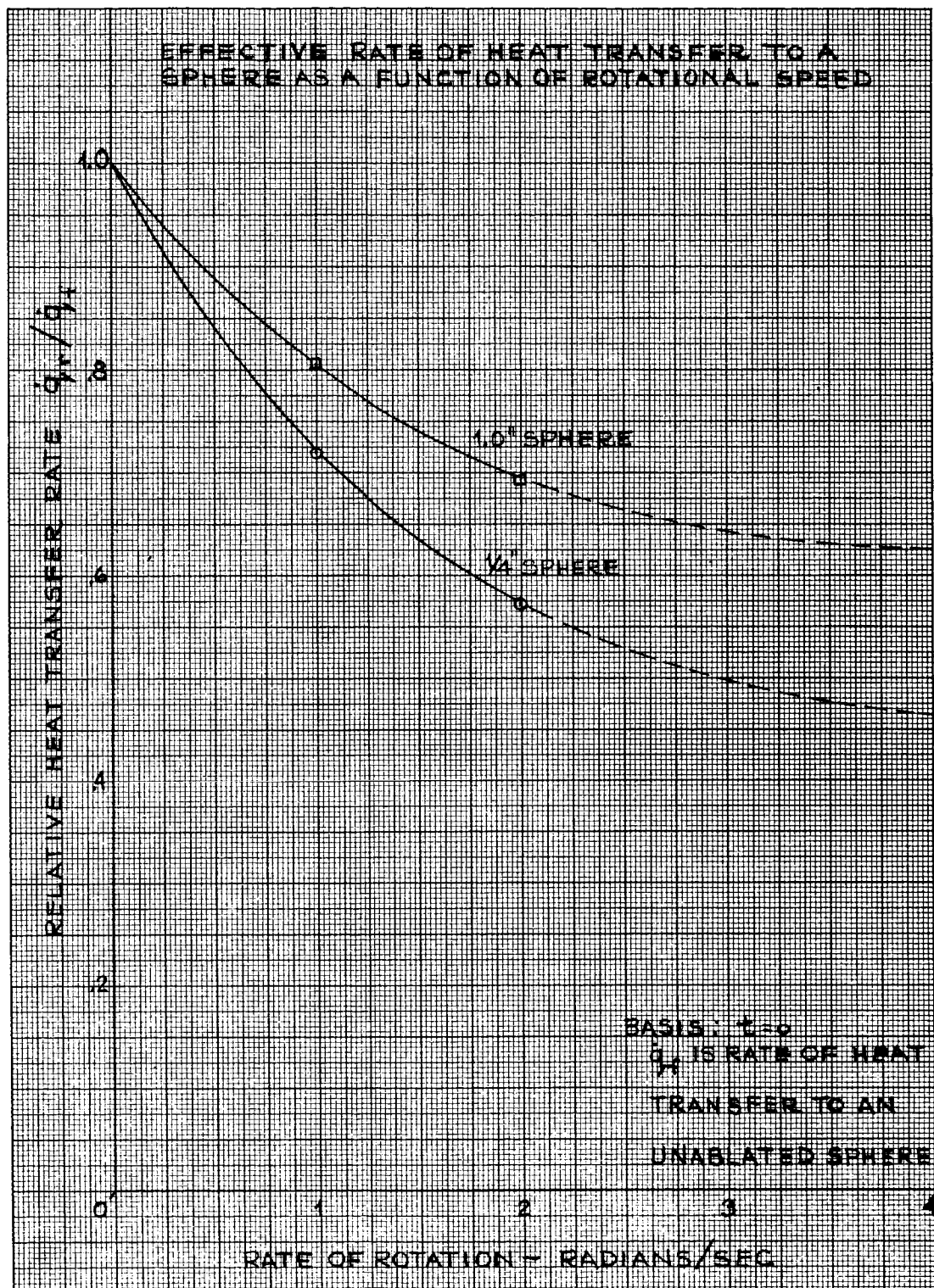
FIGURE 46

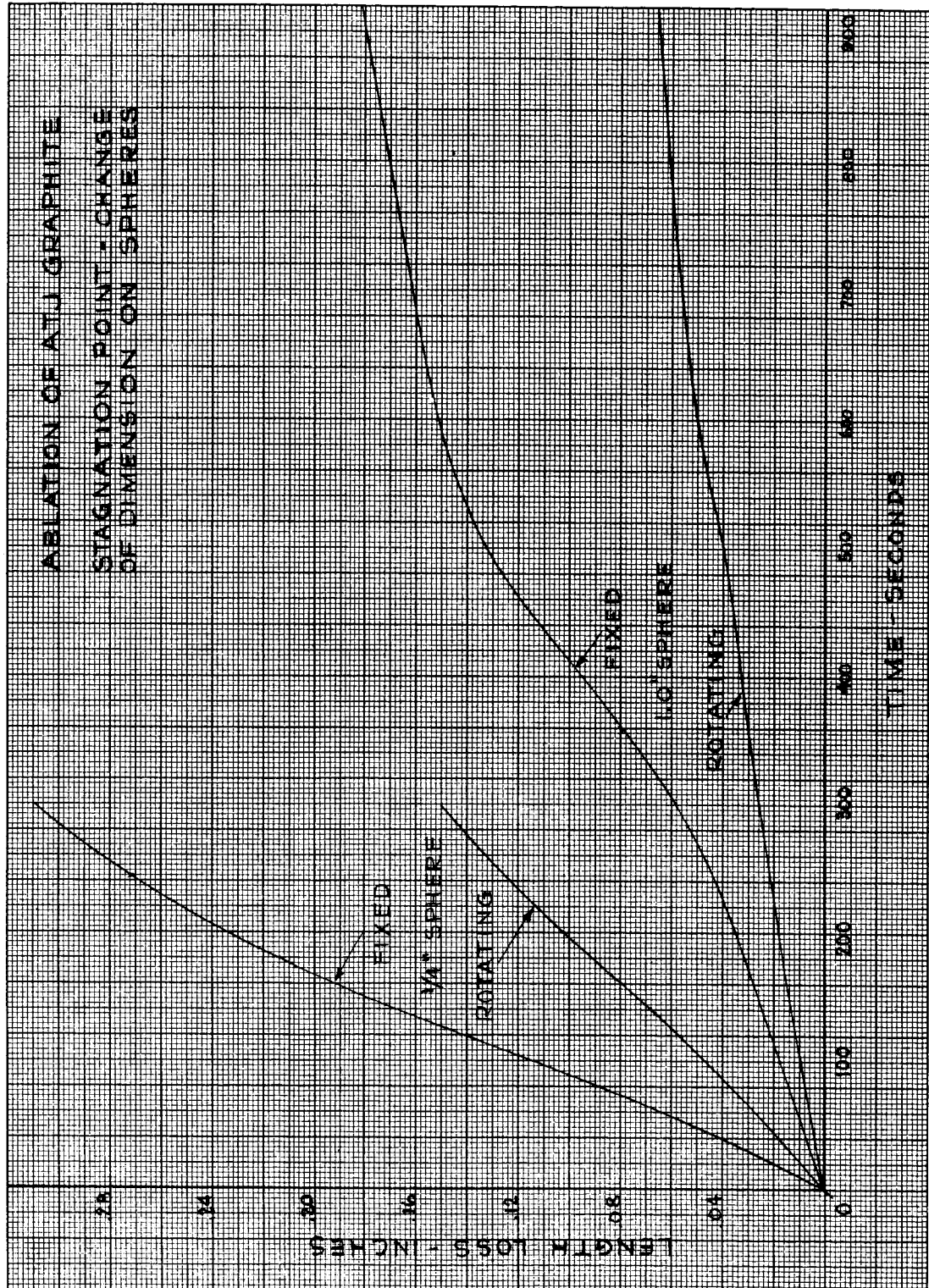


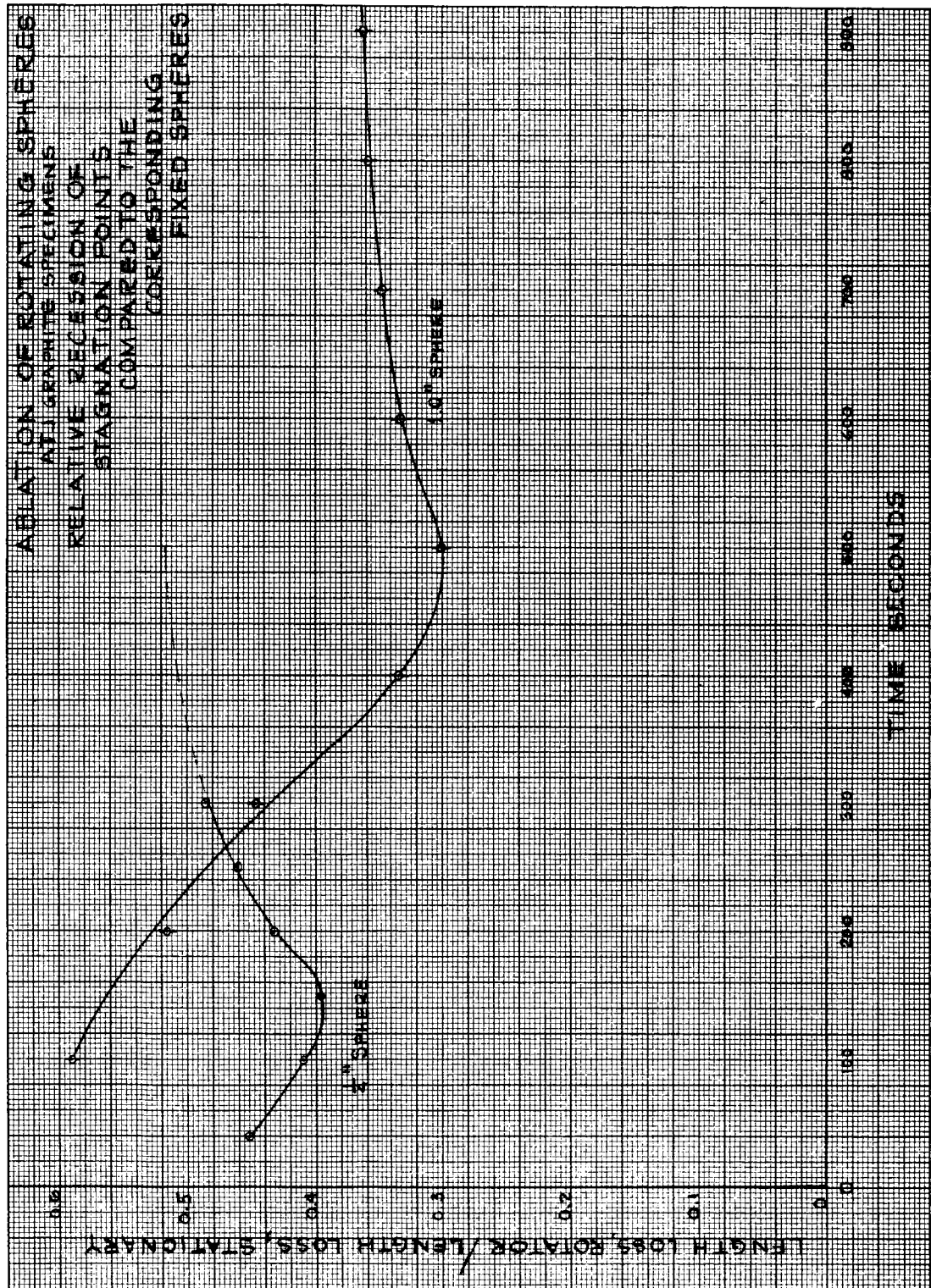






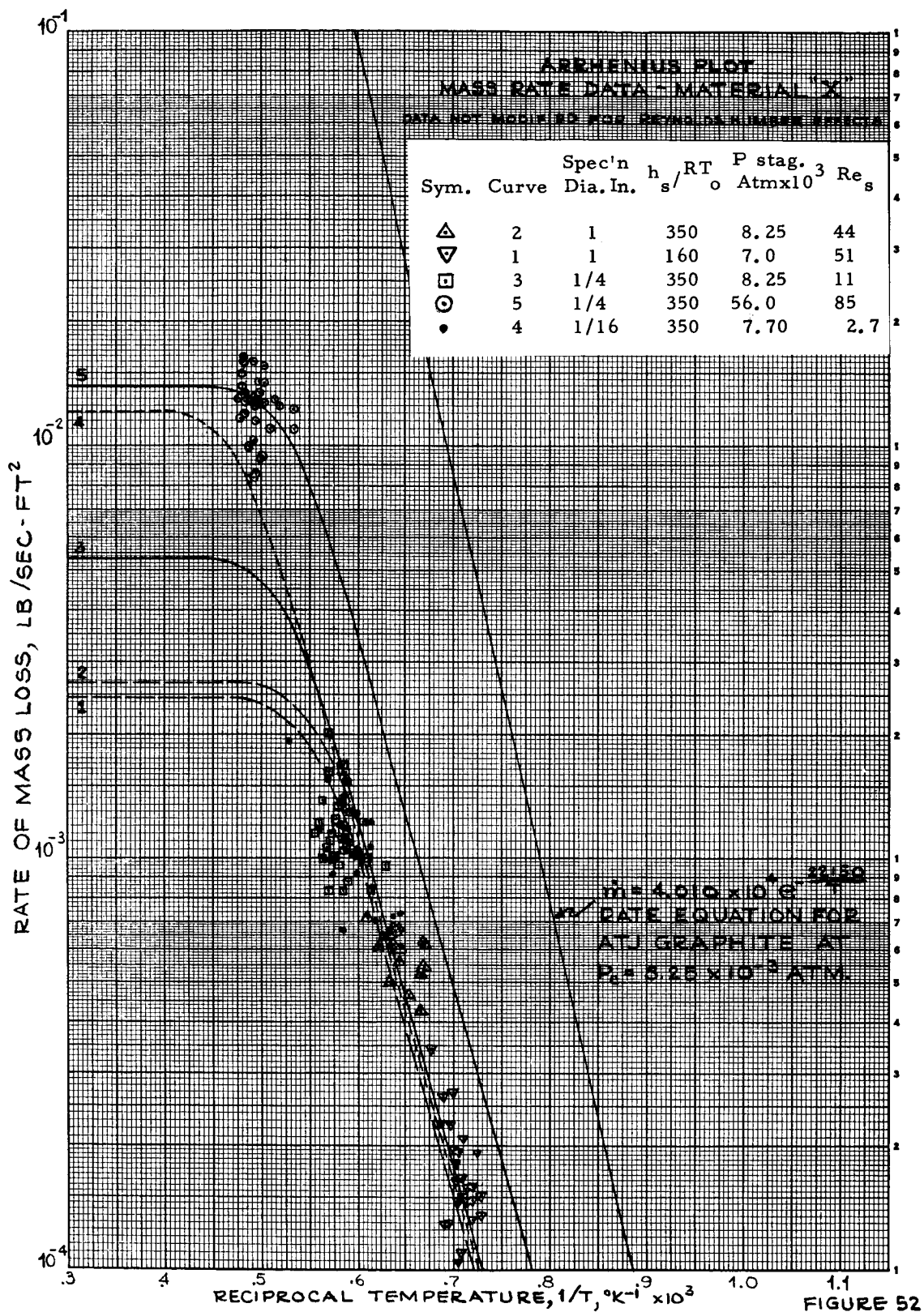






~~CONFIDENTIAL~~  
~~RESTRICTED DATA~~

UNCLASSIFIED





CONFIDENTIAL  
RESTRICTED DATA

UNCLASSIFIED

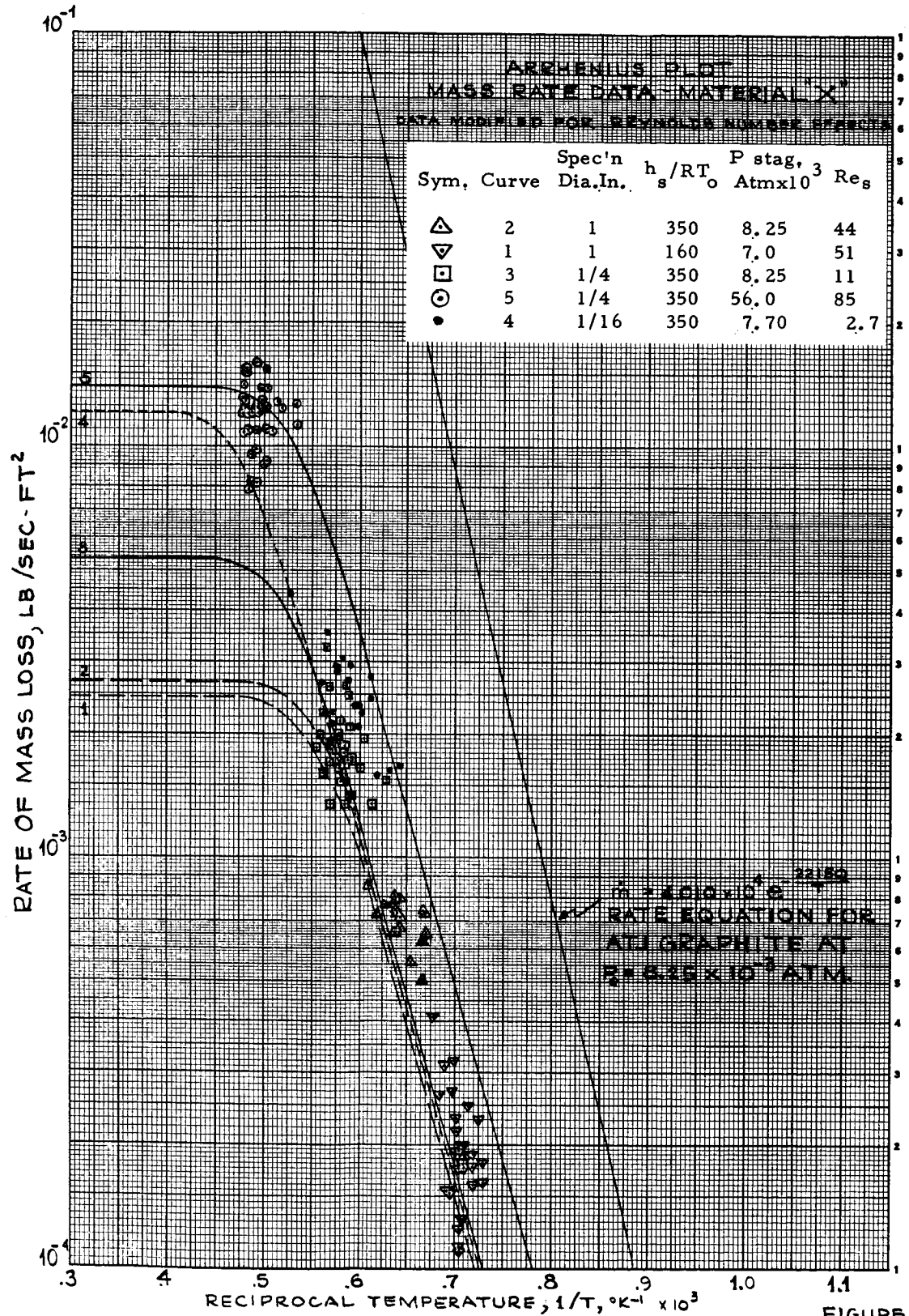


FIGURE 53

CONFIDENTIAL  
RESTRICTED DATA

UNCLASSIFIED

CONFIDENTIAL

CONFIDENTIAL

CONFIDENTIAL

UNCLASSIFIED

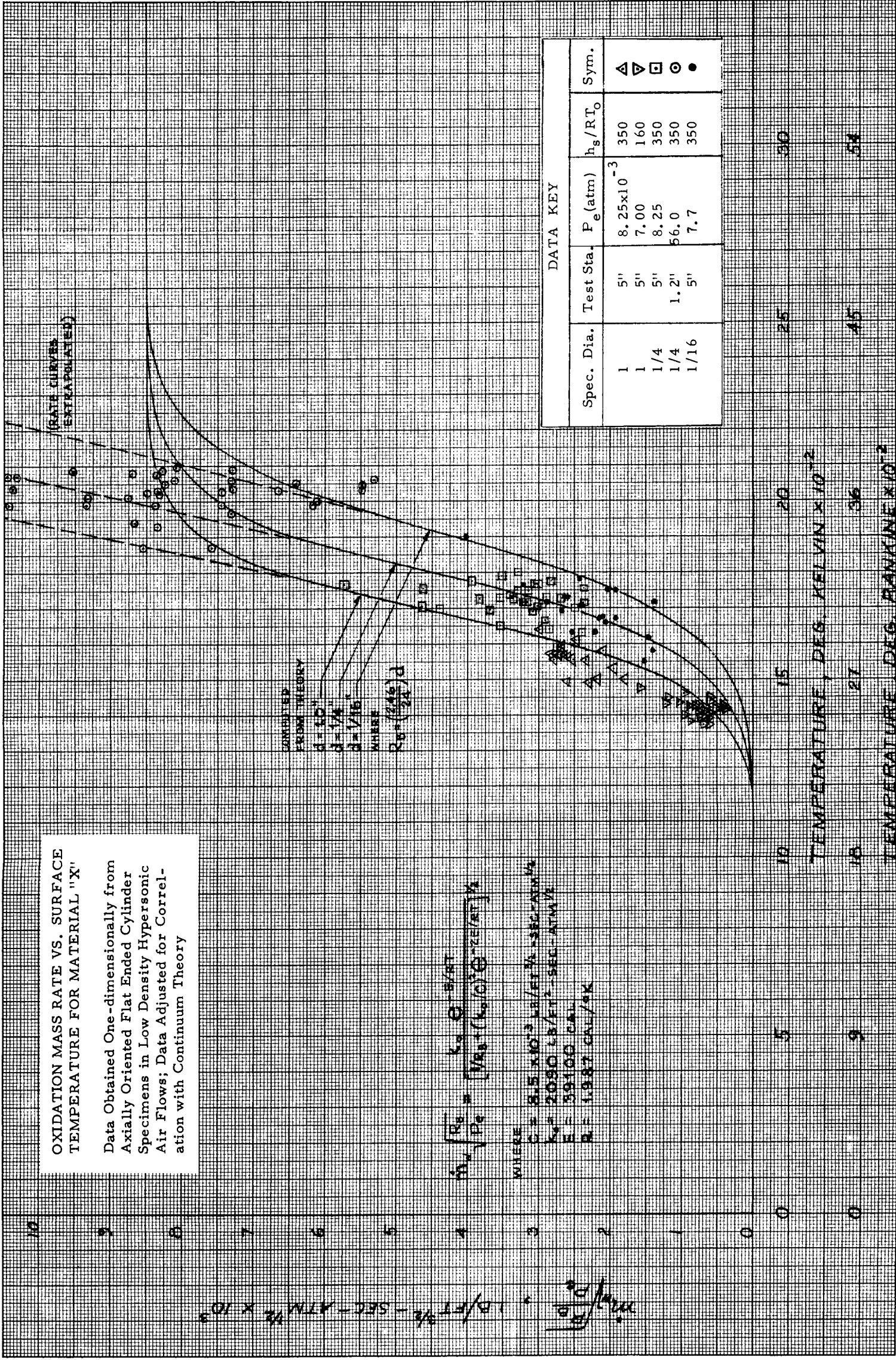


FIGURE 54

CONFIDENTIAL

UNCLASSIFIED

UNCLASSIFIED

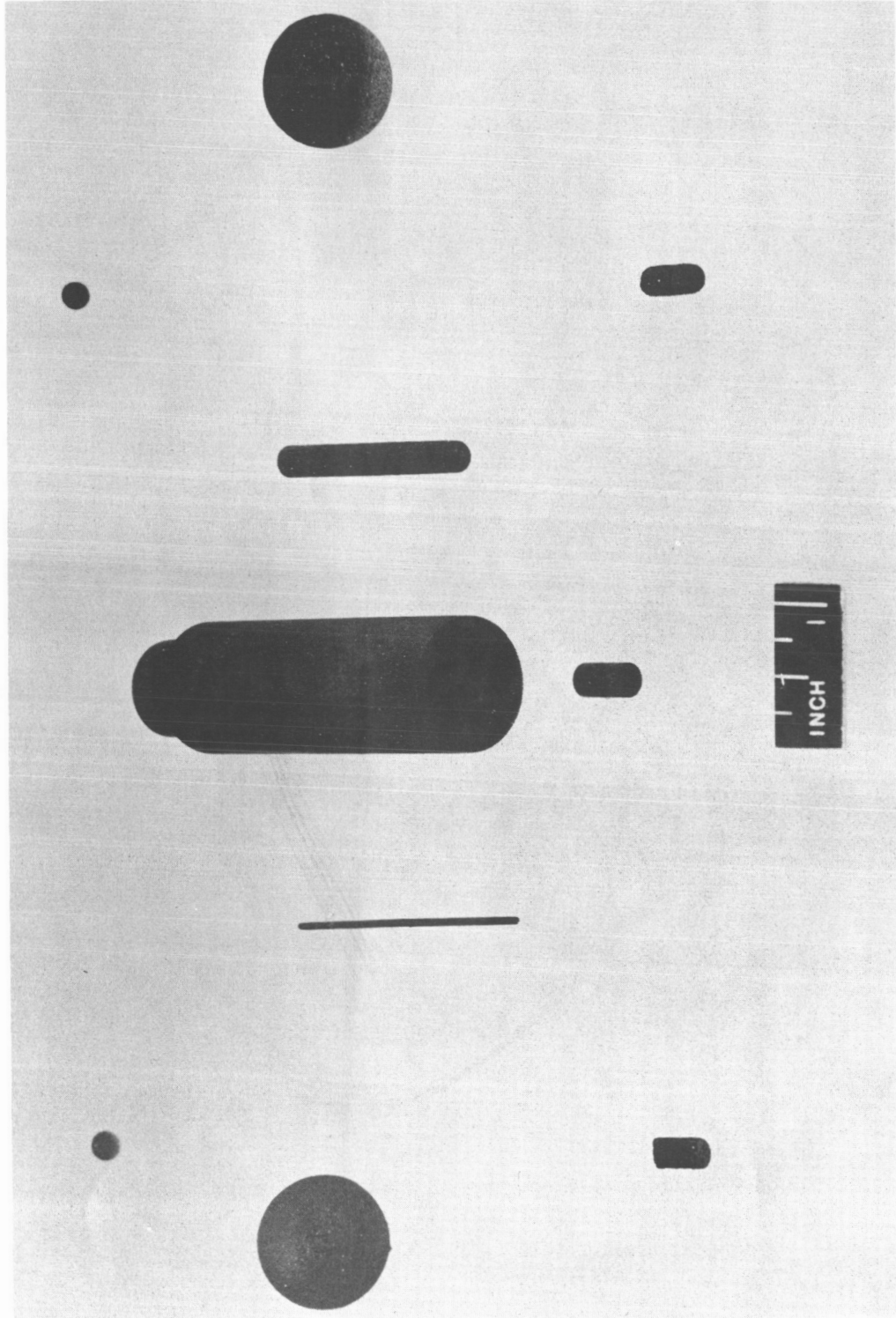
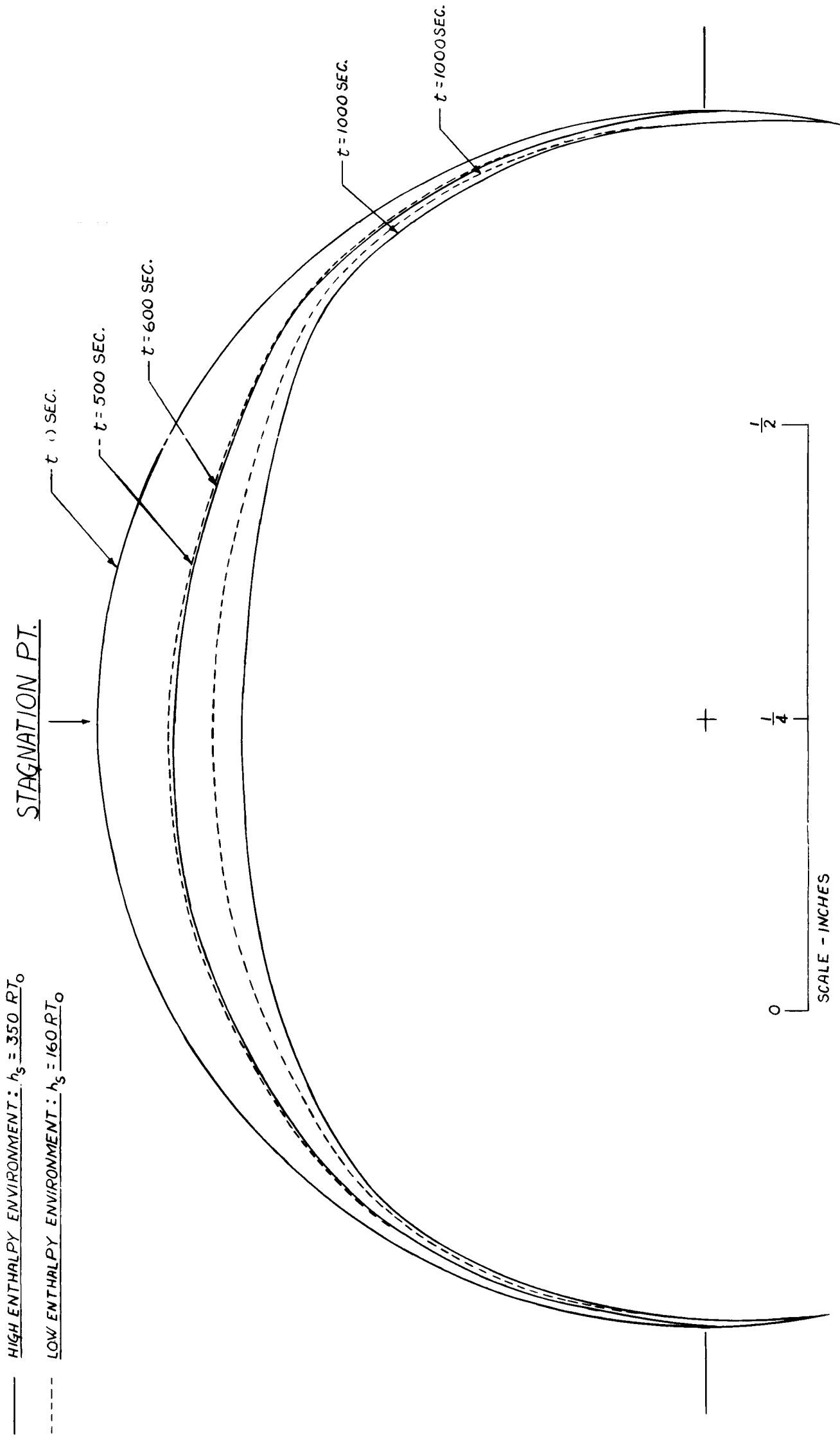


FIGURE 55. TYPICAL SPECIMENS OF MATERIAL "X" (After Exposure)

UNCLASSIFIED

CONFIDENTIAL  
COMPUTER DATA  
UNCLASSIFIED

UNCLASSIFIED



PROFILES OF 1.0 IN. DIA. STATIONARY SPHERES OF MATERIAL "X"

FIGURE 56

CONFIDENTIAL  
COMPUTER DATA  
UNCLASSIFIED



~~CONFIDENTIAL~~  
~~RESTRICTED DATA~~

UNCLASSIFIED

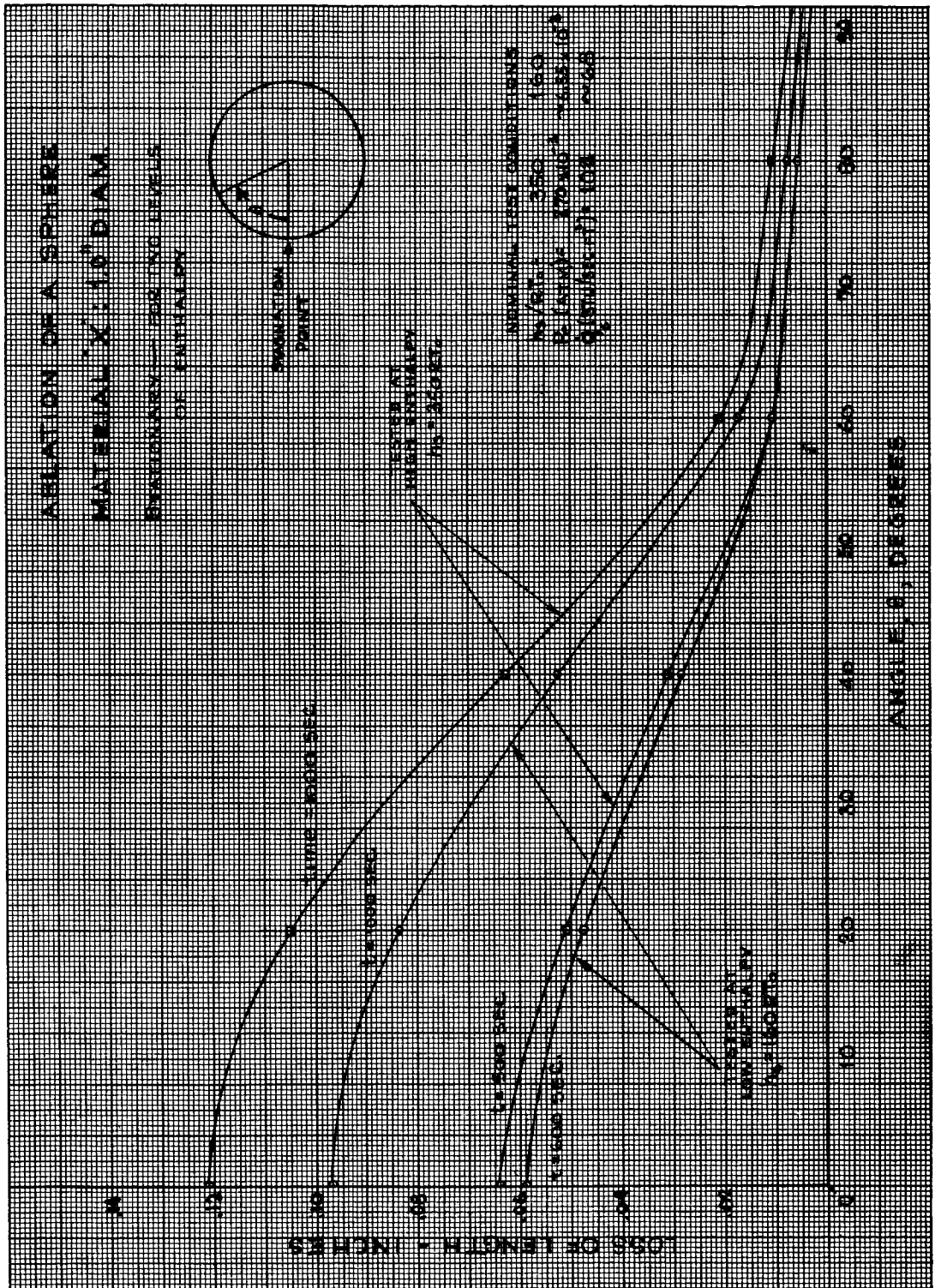


FIGURE 57

~~CONFIDENTIAL~~  
~~RESTRICTED DATA~~  
~~RESTRICTED DATA~~

UNCLASSIFIED

~~CONFIDENTIAL~~  
~~RESTRICTED DATA~~

UNCLASSIFIED

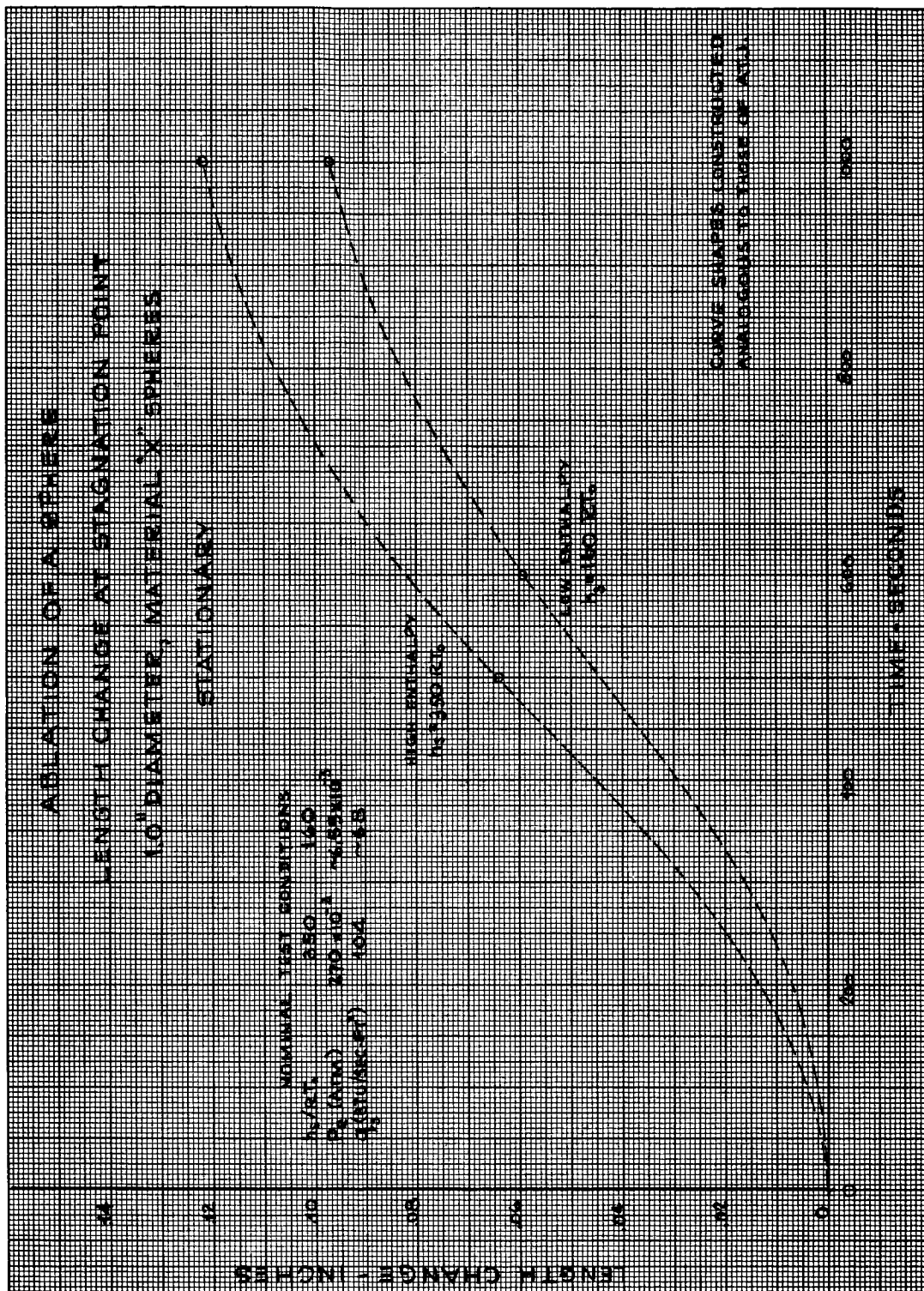


FIGURE 58

~~CONFIDENTIAL~~  
~~RESTRICTED DATA~~  
~~RESTRICTED DATA~~

UNCLASSIFIED

PROFILE OF 1.0 IN. DIA. ROTATING SPHERE OF  
MATERIAL "X"

HIGH ENTHALPY ENVIRONMENT:  $h_s = 350 \text{ RT}_0$

$\omega = 2 \text{ RAD./SEC.}$

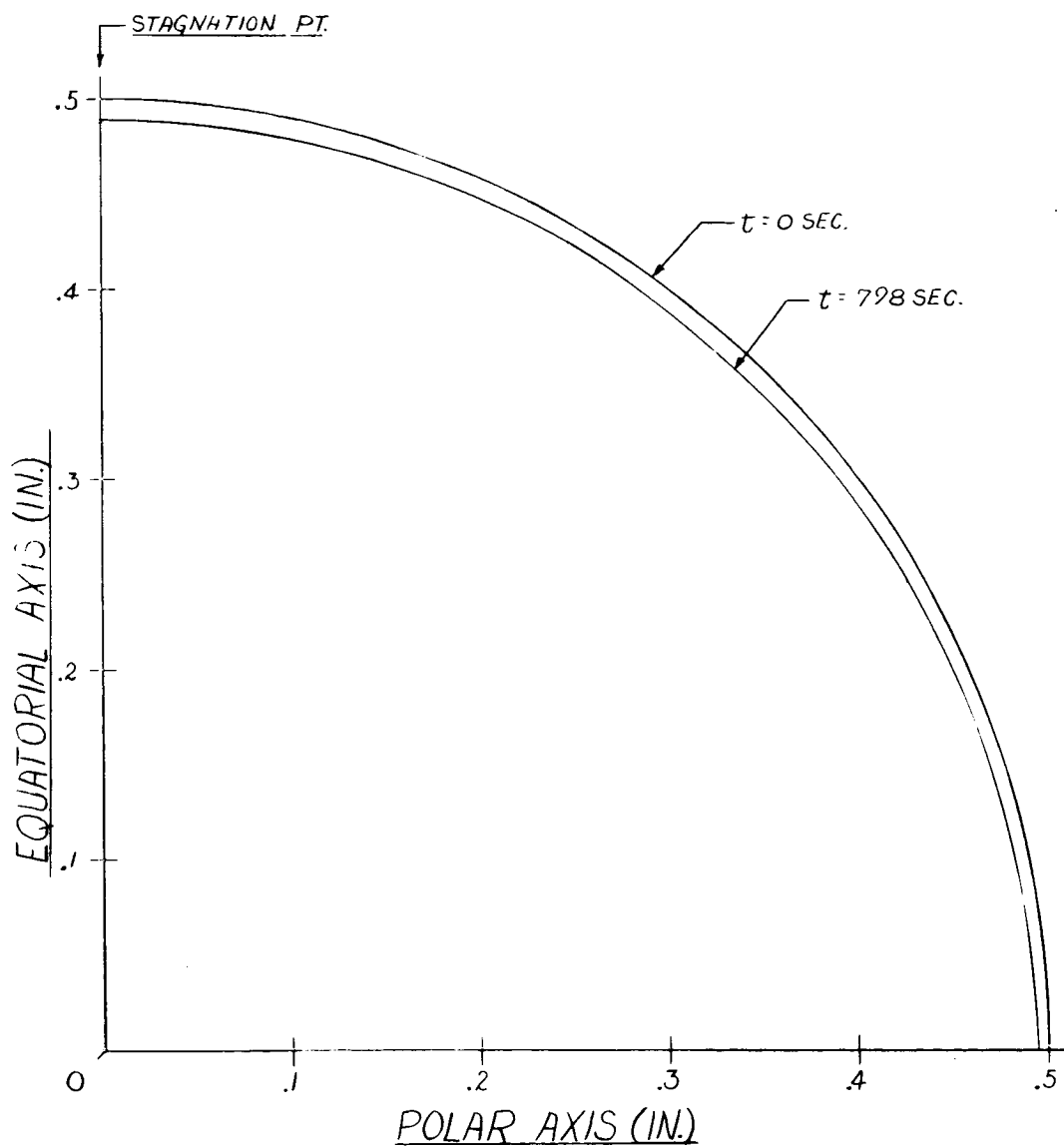


FIGURE 59

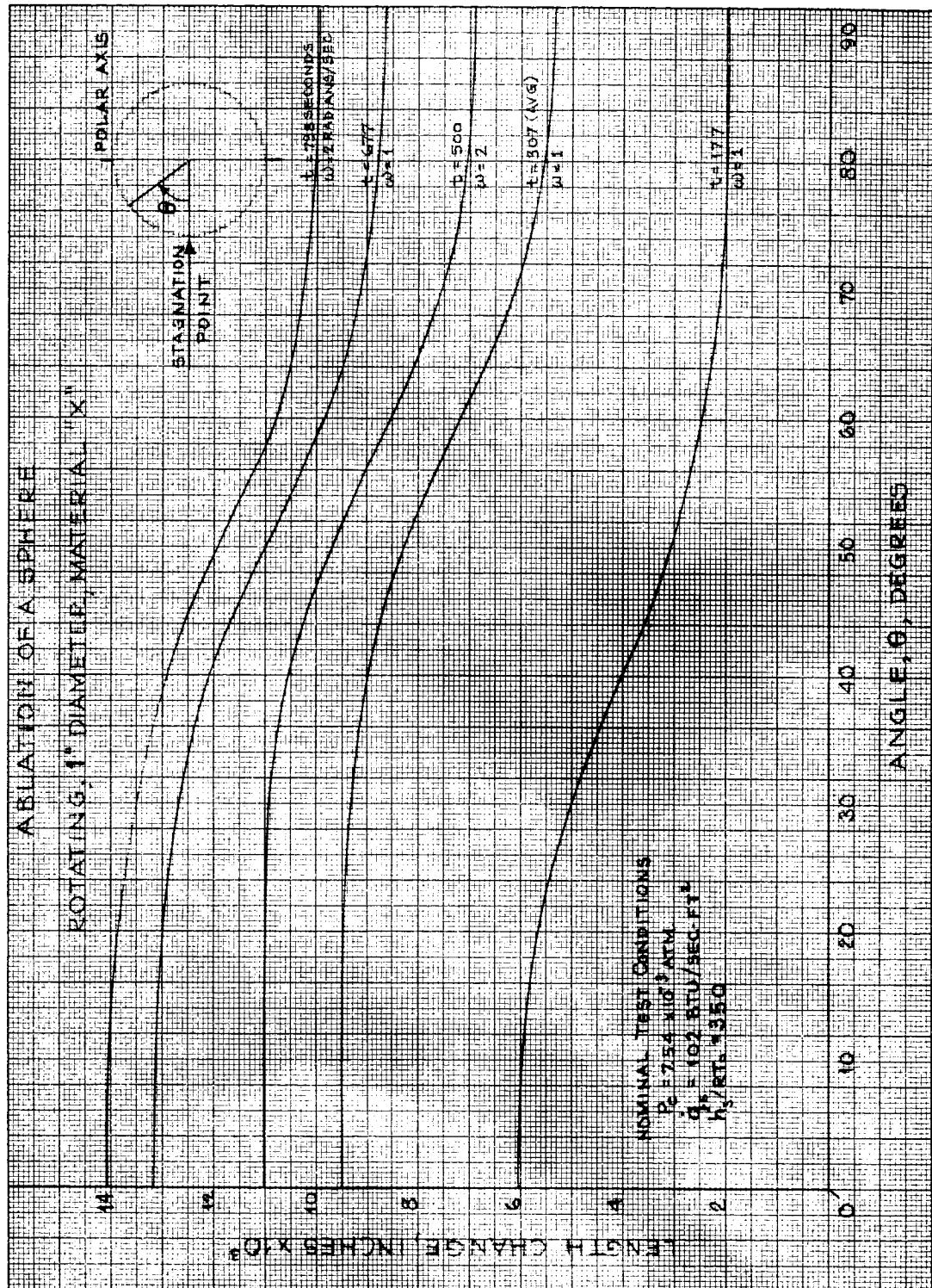


FIGURE 60

~~CONFIDENTIAL~~  
~~RESTRICTED DATA~~

UNCLASSIFIED

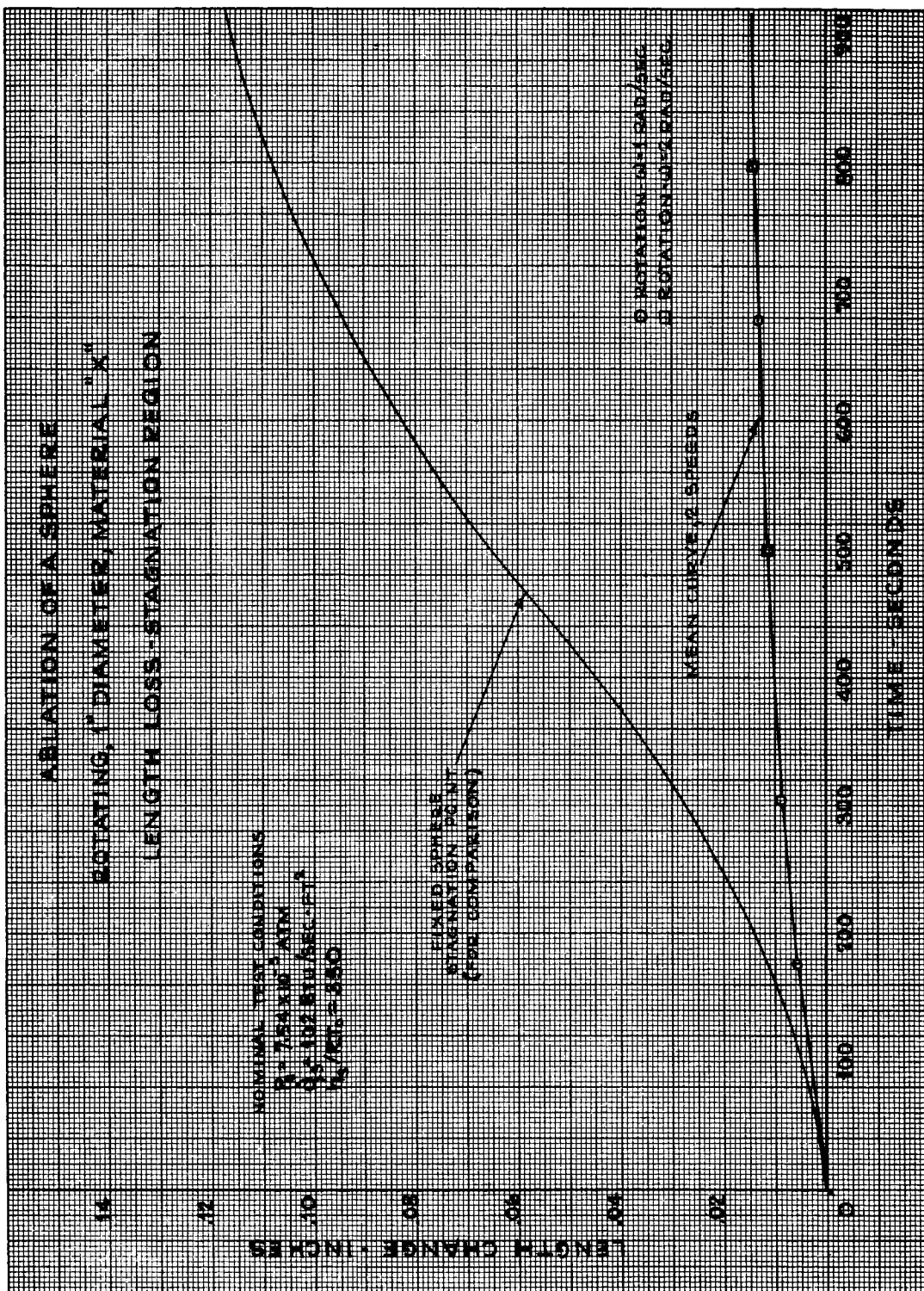


FIGURE 61

~~CONFIDENTIAL~~  
~~RESTRICTED DATA~~  
~~Atomic Energy Act of 1946~~

UNCLASSIFIED

PROFILES OF 250 IN. DIA. STATIONARY SPHERES OF  
MATERIAL "X"

HIGH ENTHALPY ENVIRONMENT:  $h_s = 350 \text{ RT}_0$

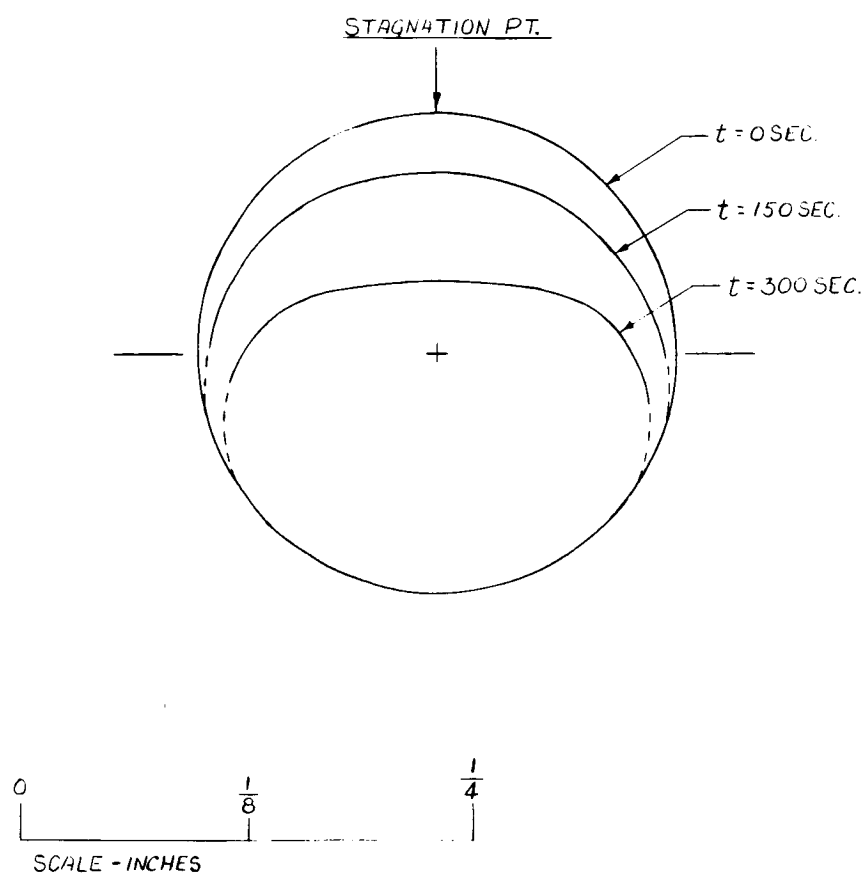


FIGURE 62

~~CONFIDENTIAL~~  
~~RESTRICTED DATA~~

UNCLASSIFIED

PROFILES OF .250 IN. DIA. ROTATING SPHERES OF  
MATERIAL "X"

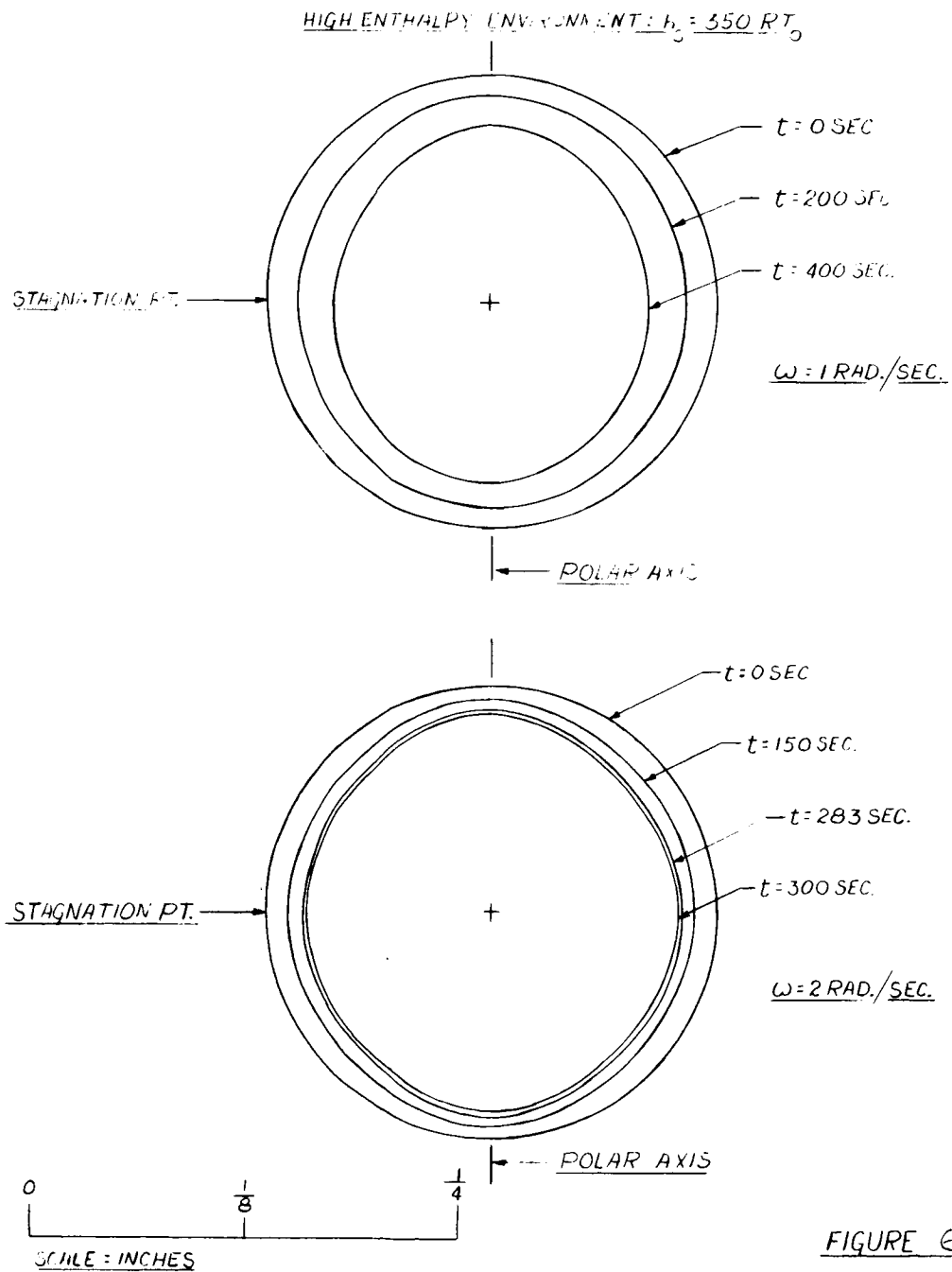


FIGURE 63

~~CONFIDENTIAL~~  
~~RESTRICTED DATA~~  
~~RESTRICTED DATA~~

UNCLASSIFIED



~~CONFIDENTIAL~~  
~~RESTRICTED DATA~~

UNCLASSIFIED

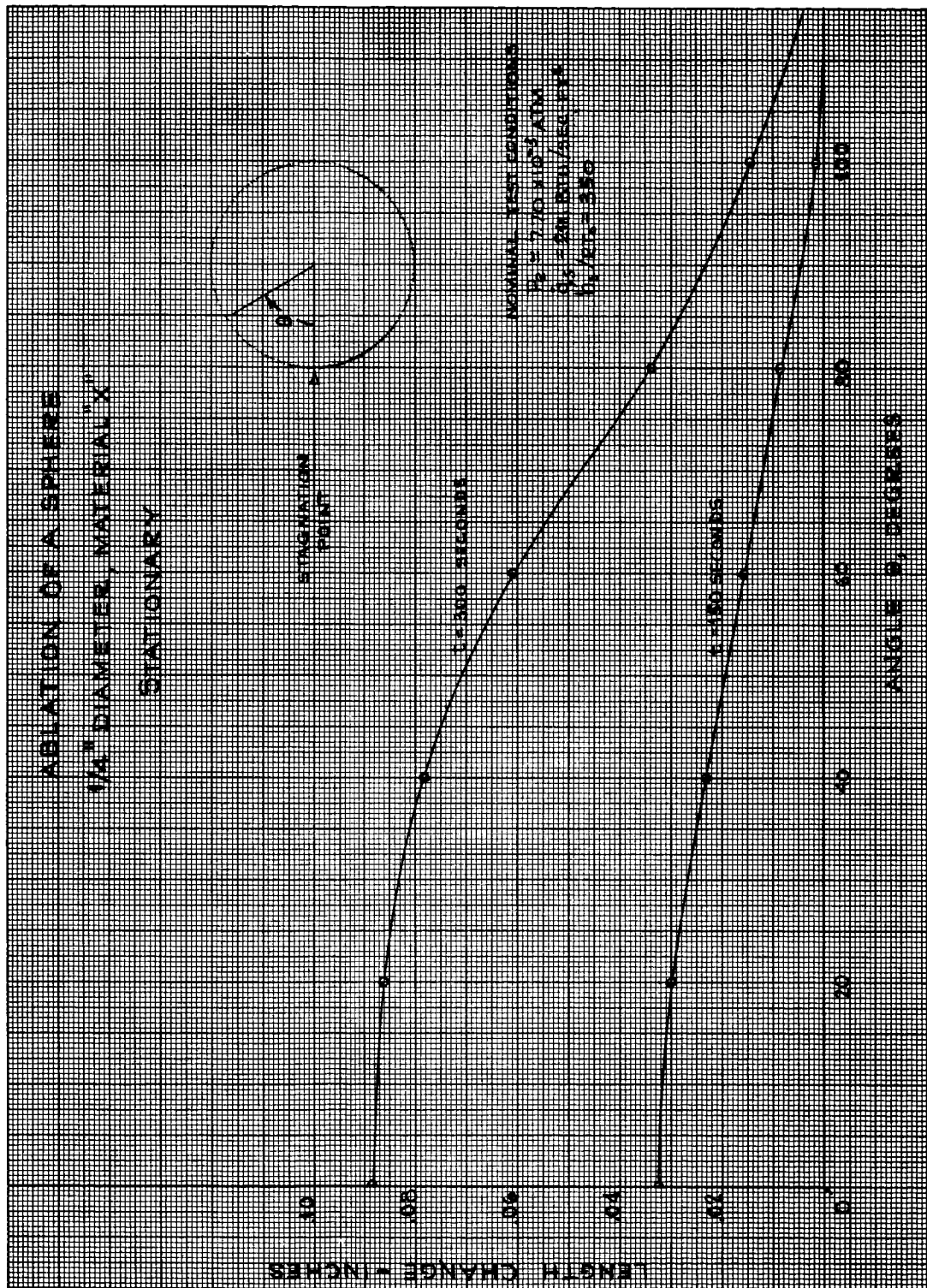


FIGURE 64

~~CONFIDENTIAL~~

~~RESTRICTED DATA~~

~~Atomic Energy Act of 1954~~

UNCLASSIFIED



CONFIDENTIAL  
RESTRICTED DATA

UNCLASSIFIED

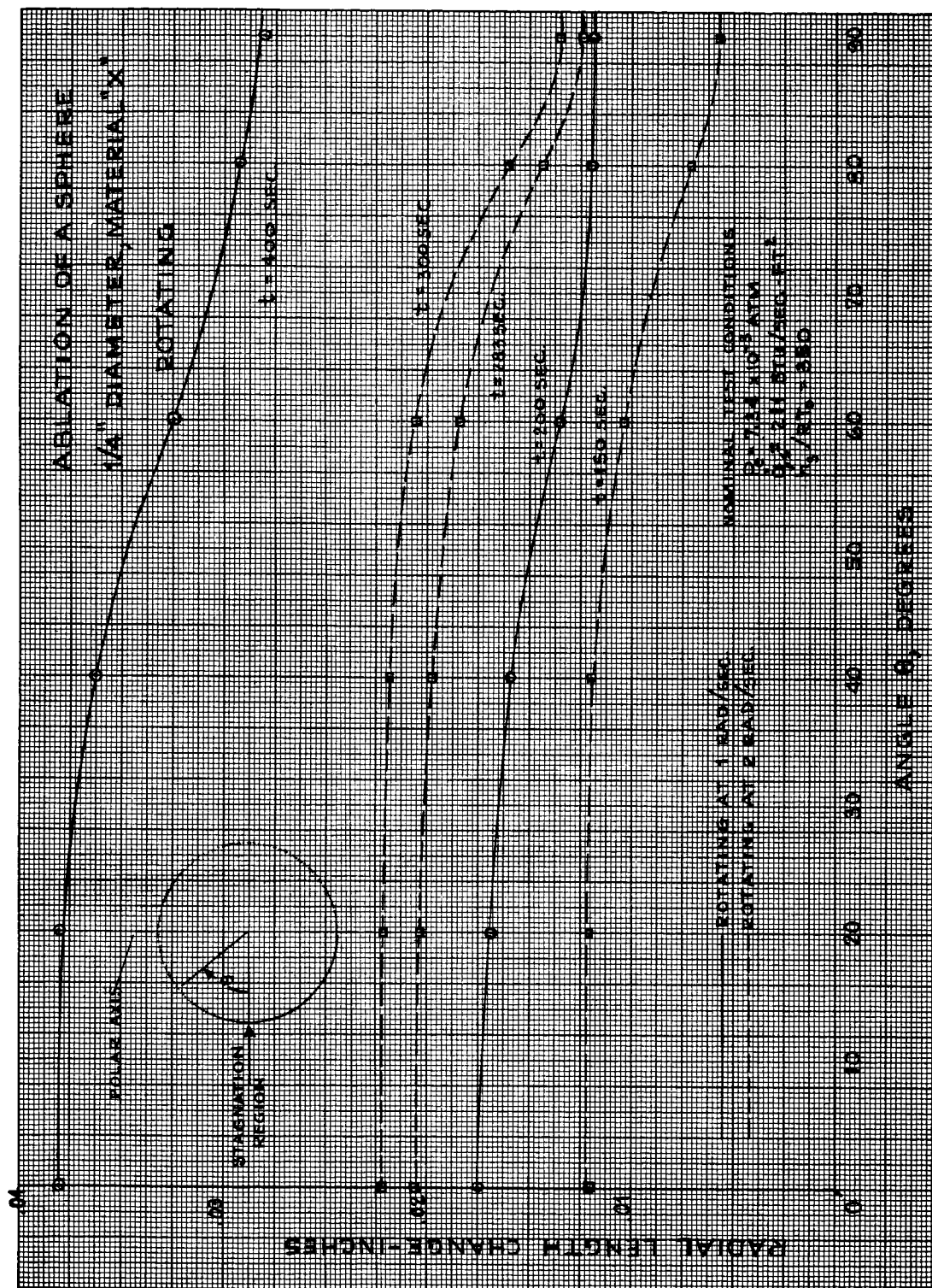


FIGURE 65

CONFIDENTIAL  
RESTRICTED DATA

UNCLASSIFIED

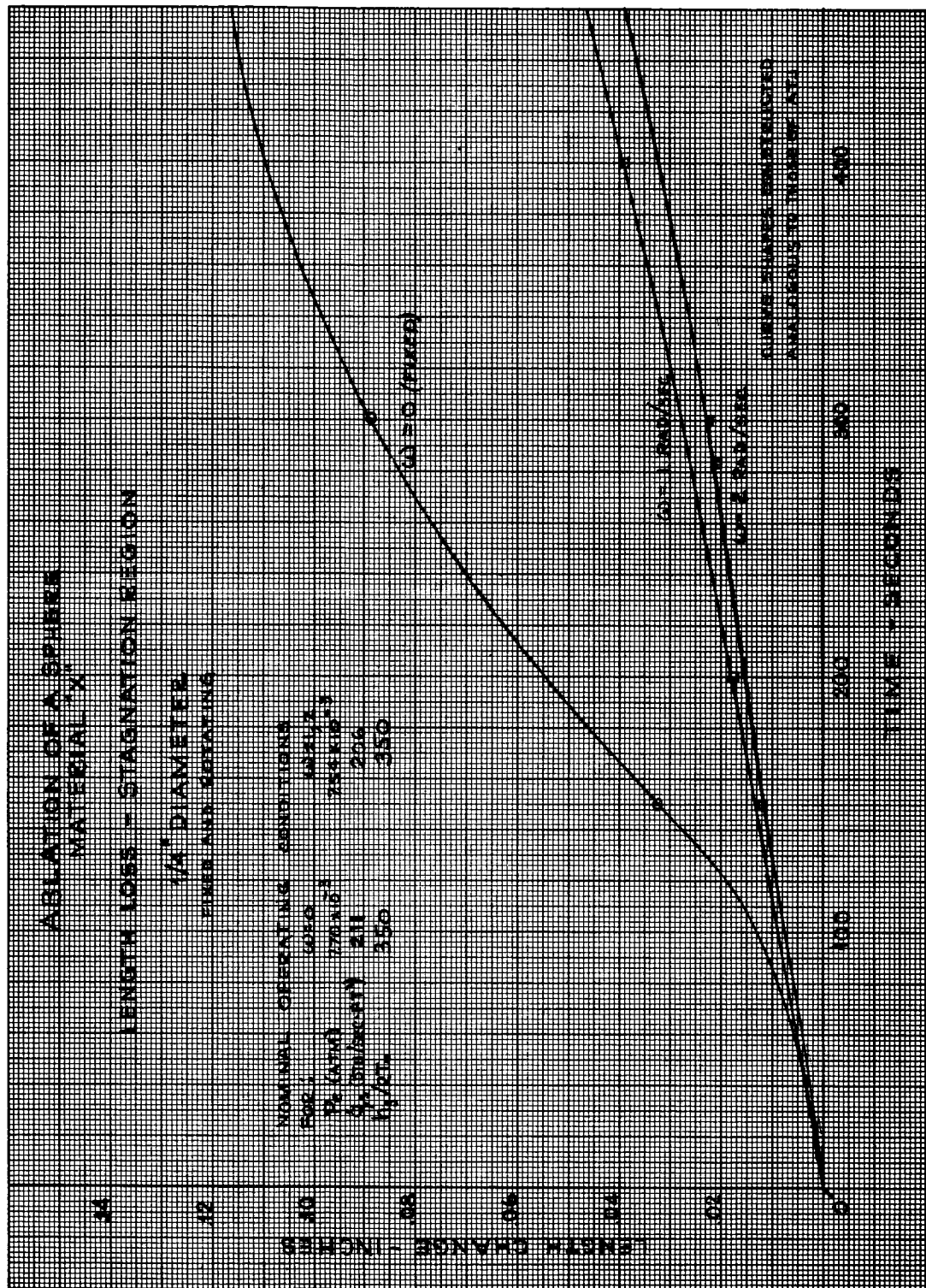


FIGURE 66

~~CONFIDENTIAL~~  
~~RESTRICTED DATA~~

UNCLASSIFIED

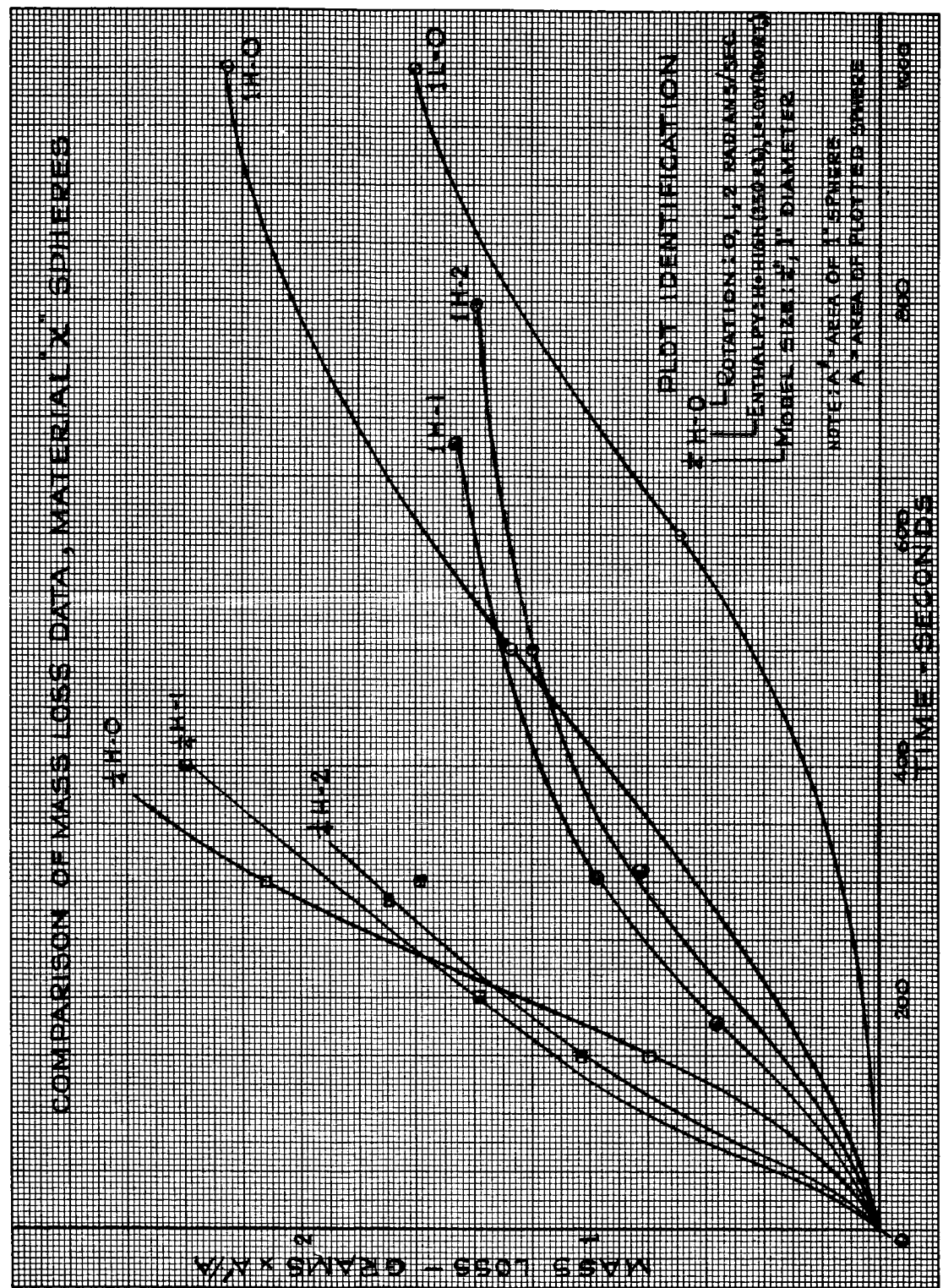


FIGURE 67

~~CONFIDENTIAL~~  
~~RESTRICTED DATA~~  
~~RESTRICTED DATA~~

UNCLASSIFIED

UNCLASSIFIED  
DECLASSIFIED

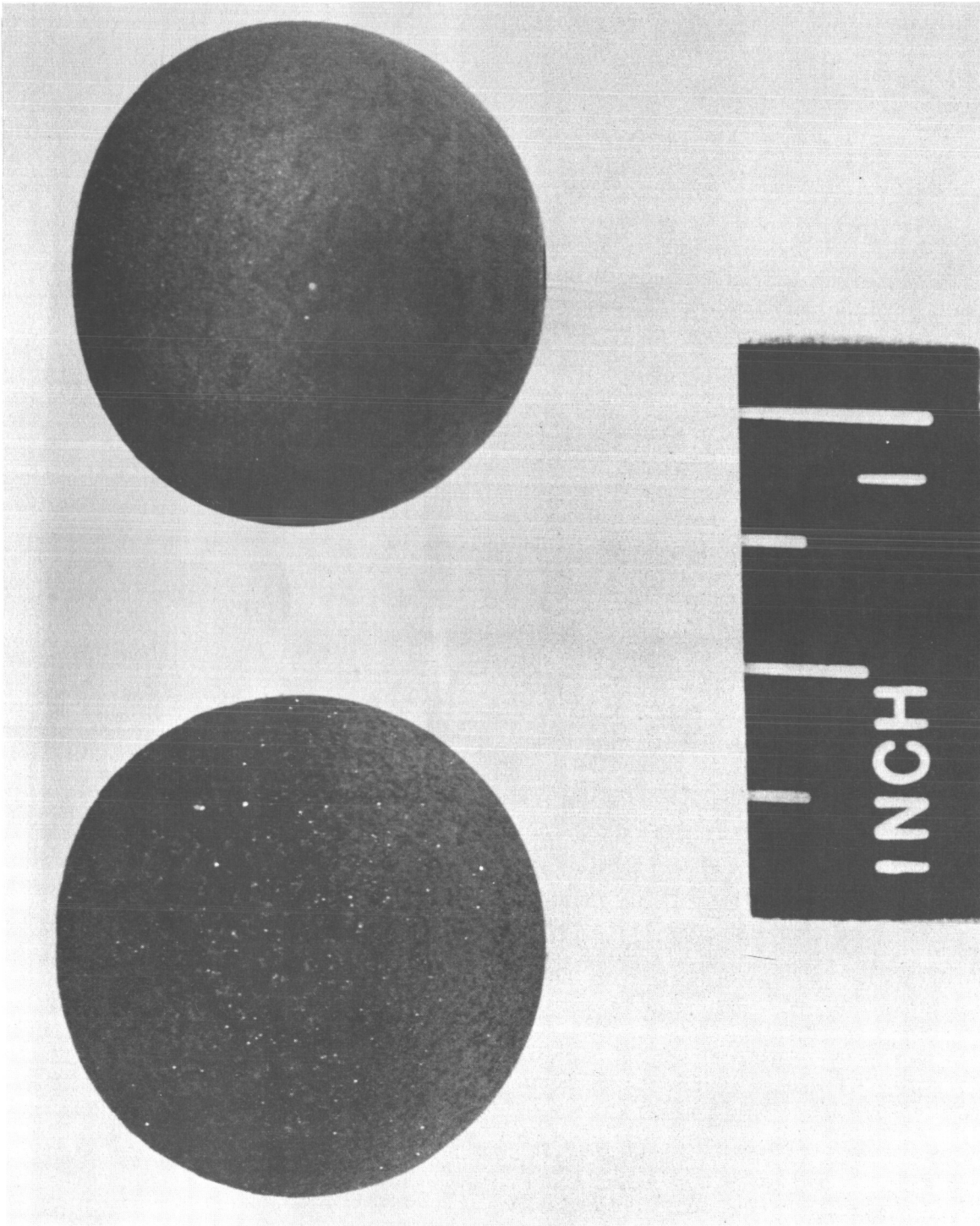


FIGURE 68. COMPARISON OF SURFACE APPEARANCE OF MATERIAL "X" AND ATJ GRAPHITE  
AFTER EXPOSURE (Flow Downward)

UNCLASSIFIED

UNCLASSIFIED



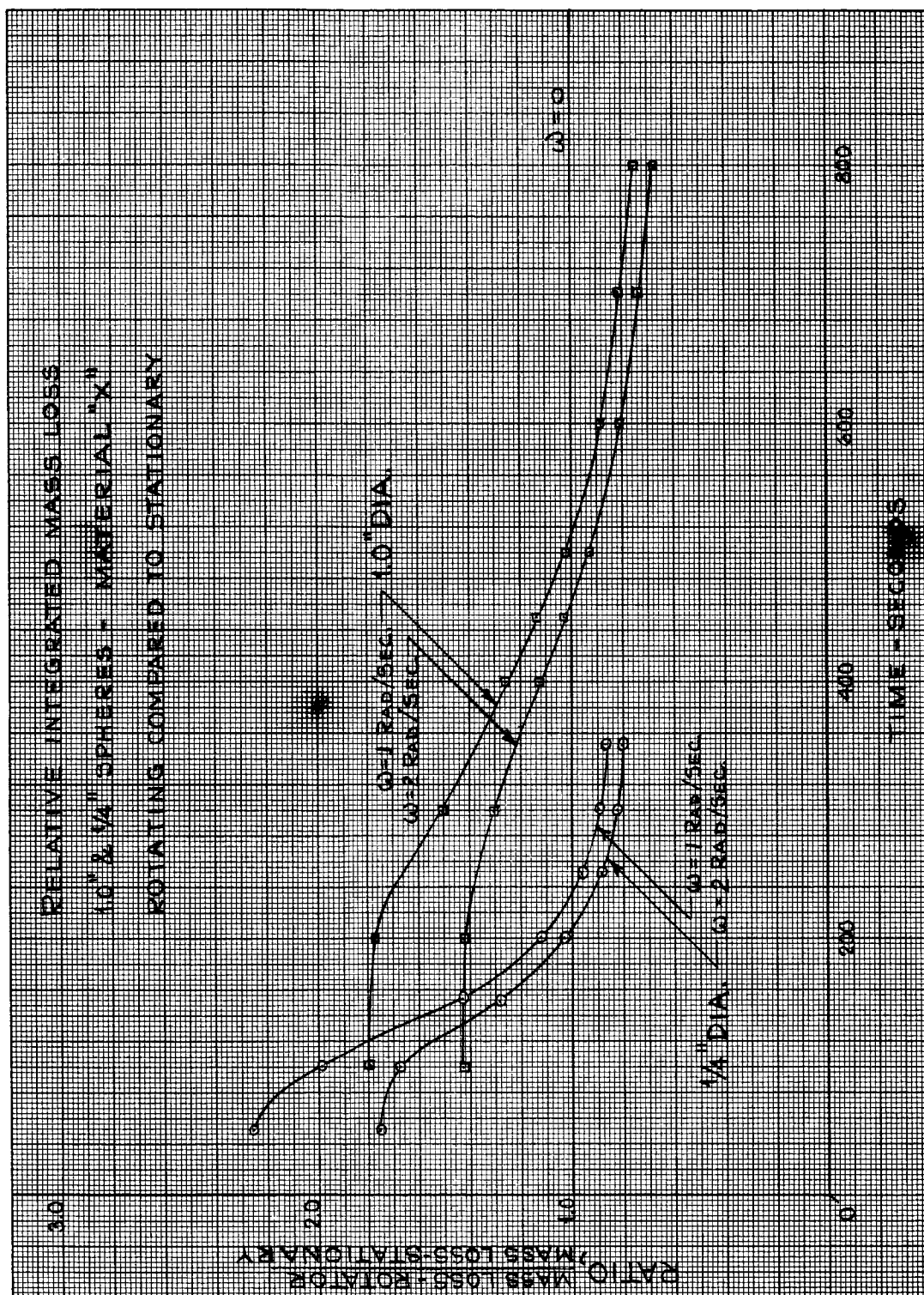


FIGURE 69

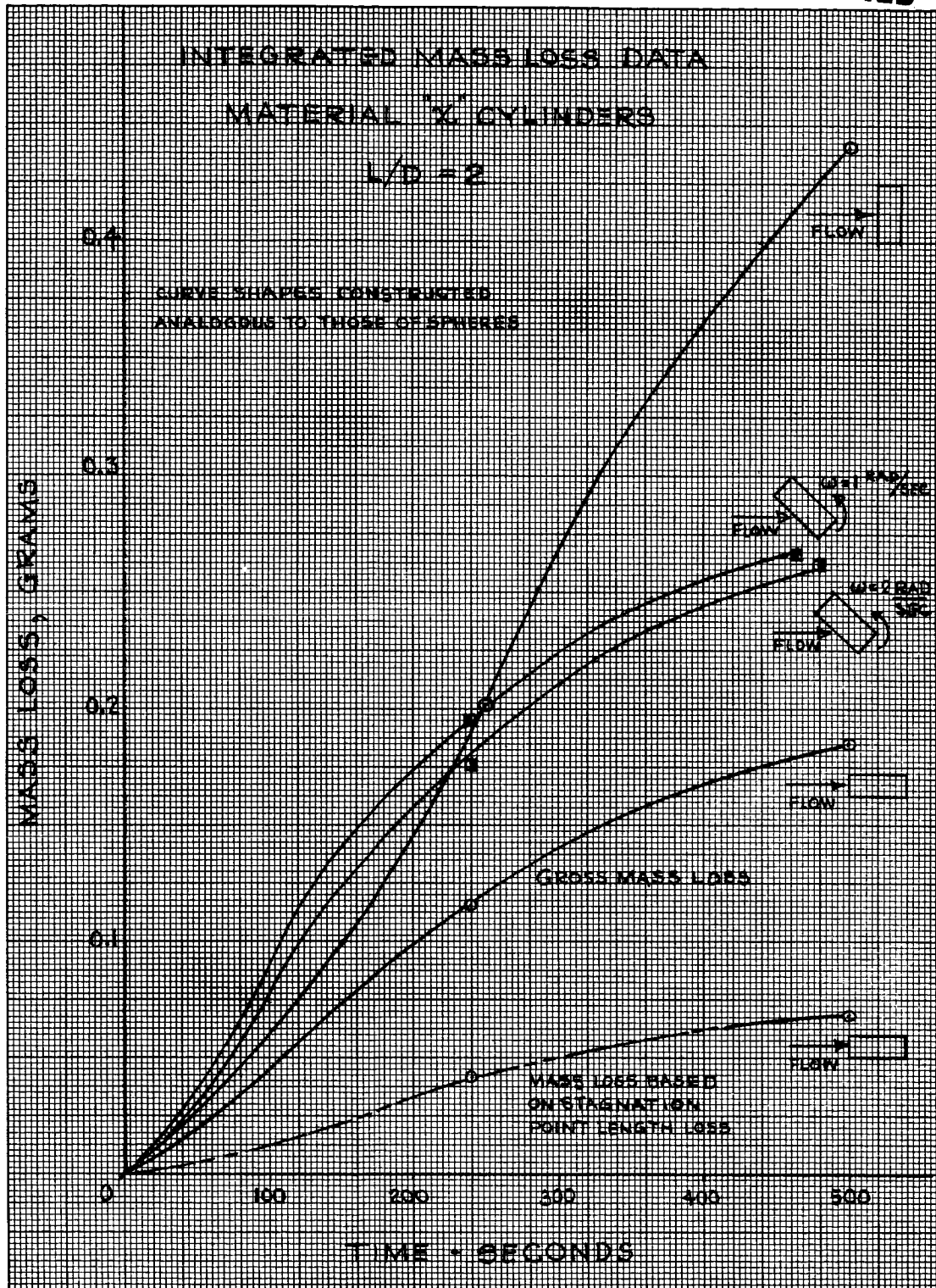



FIGURE 70



REVENUE: REF

**UNCLASSIFIED**

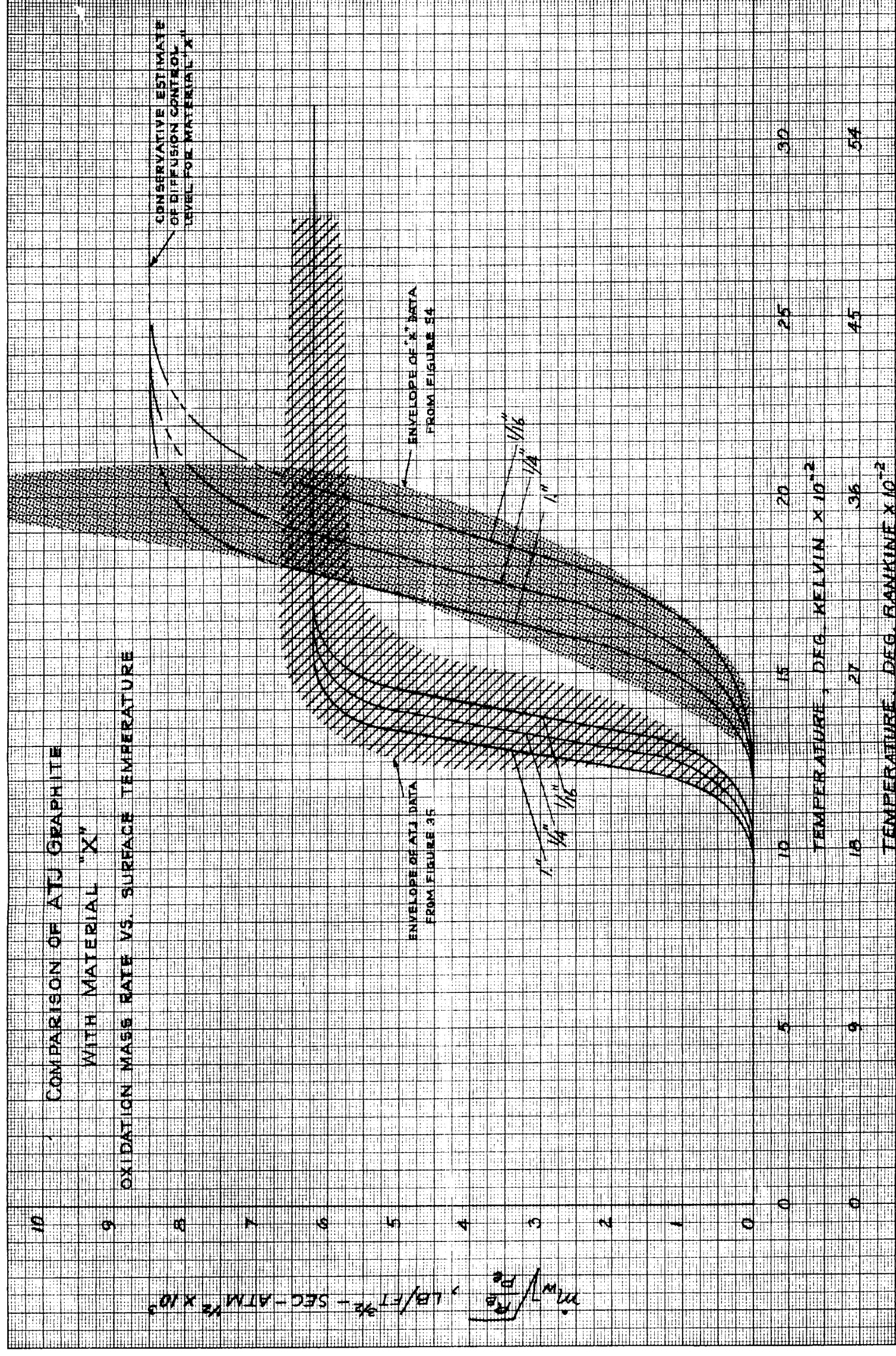


FIGURE 71

264

CONFIDENTIAL  
CONFIDENTIAL  
CONFIDENTIAL  
CONFIDENTIAL

**UNCLASSIFIED**

UNCLASSIFIED  
 DECLASSIFIED

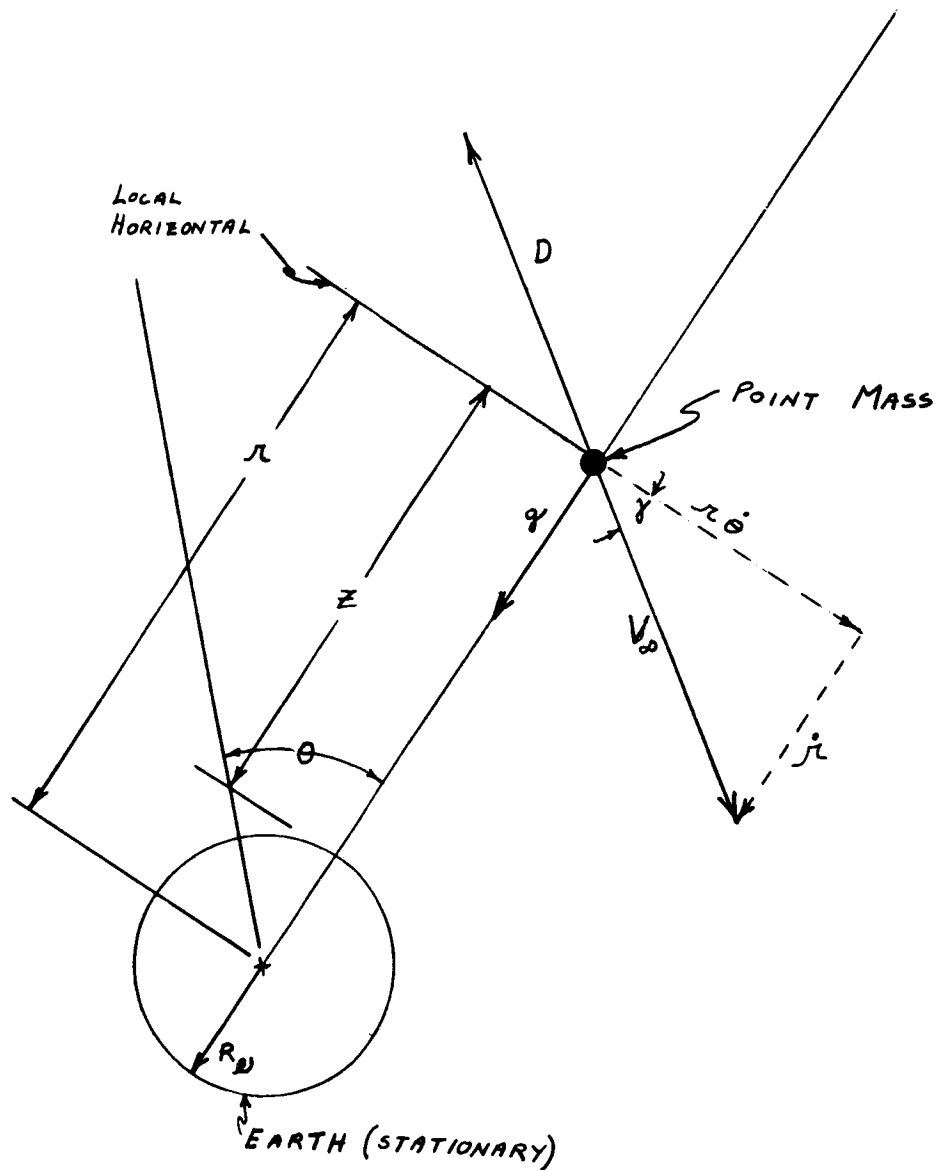


FIGURE 72. MOTION OF A RE-ENTRY FRAGMENT

UNCLASSIFIED



UNCLASSIFIED  
 UNCLASSIFIED  
 UNCLASSIFIED

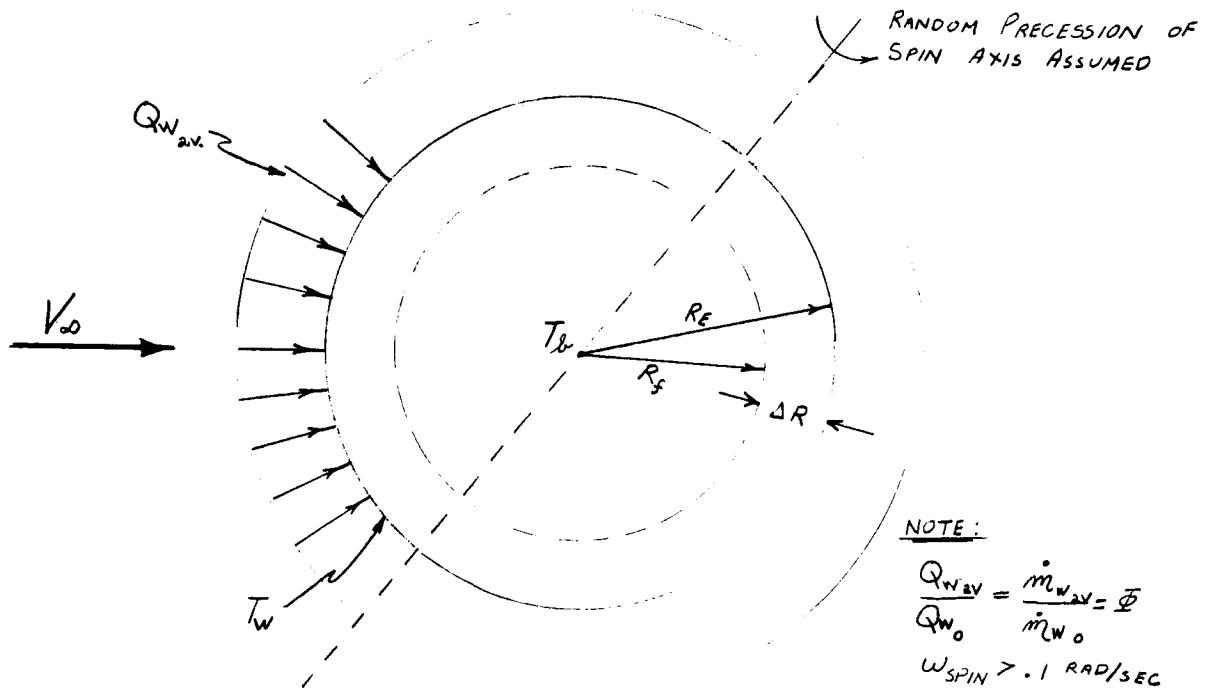


FIGURE 73. MONOTONICALLY SHRINKING SPHERE

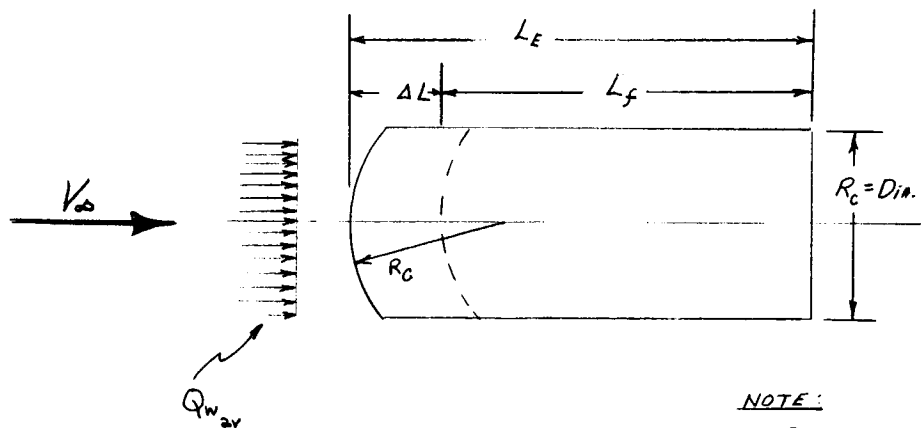


FIGURE 74. ONE DIMENSIONAL CYLINDER

UNCLASSIFIED

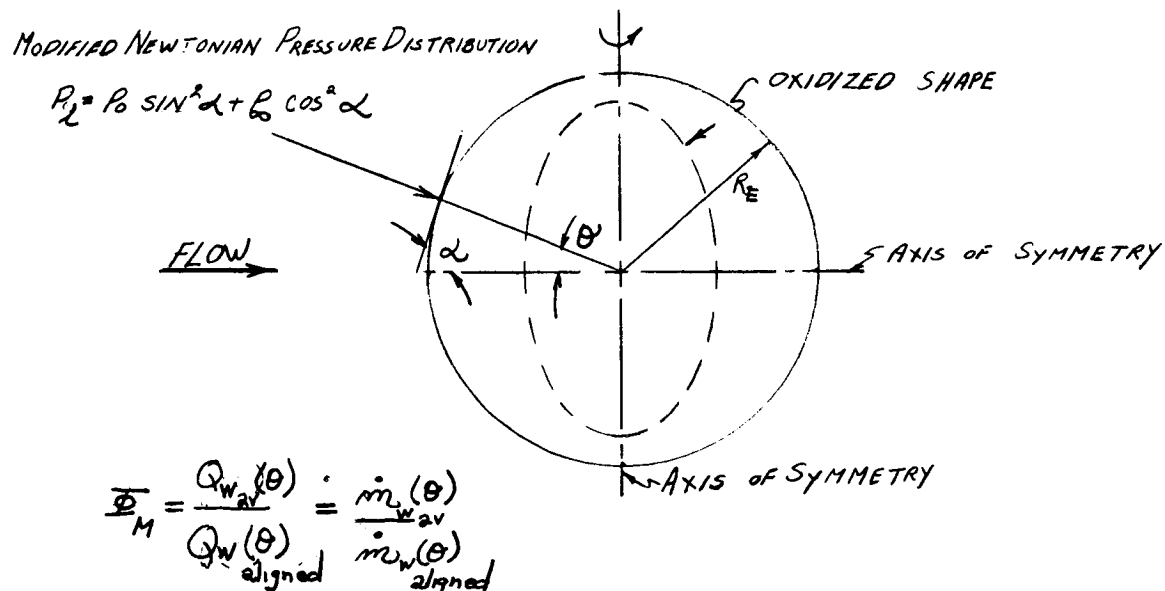


FIGURE 75. TWO-DIMENSIONAL SPHERE (Rotation About Axis  $90^\circ$  to Flow Direction)

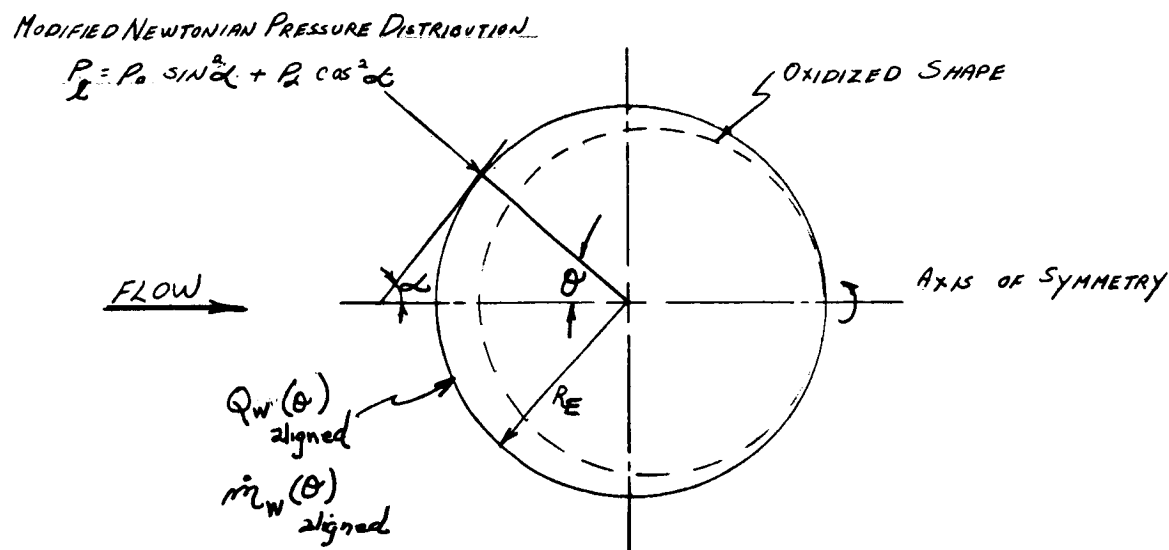


FIGURE 76. TWO-DIMENSIONAL (Rotation About Axis Aligned to Flow Direction)

RESTRICTED DATA

UNCLASSIFIED

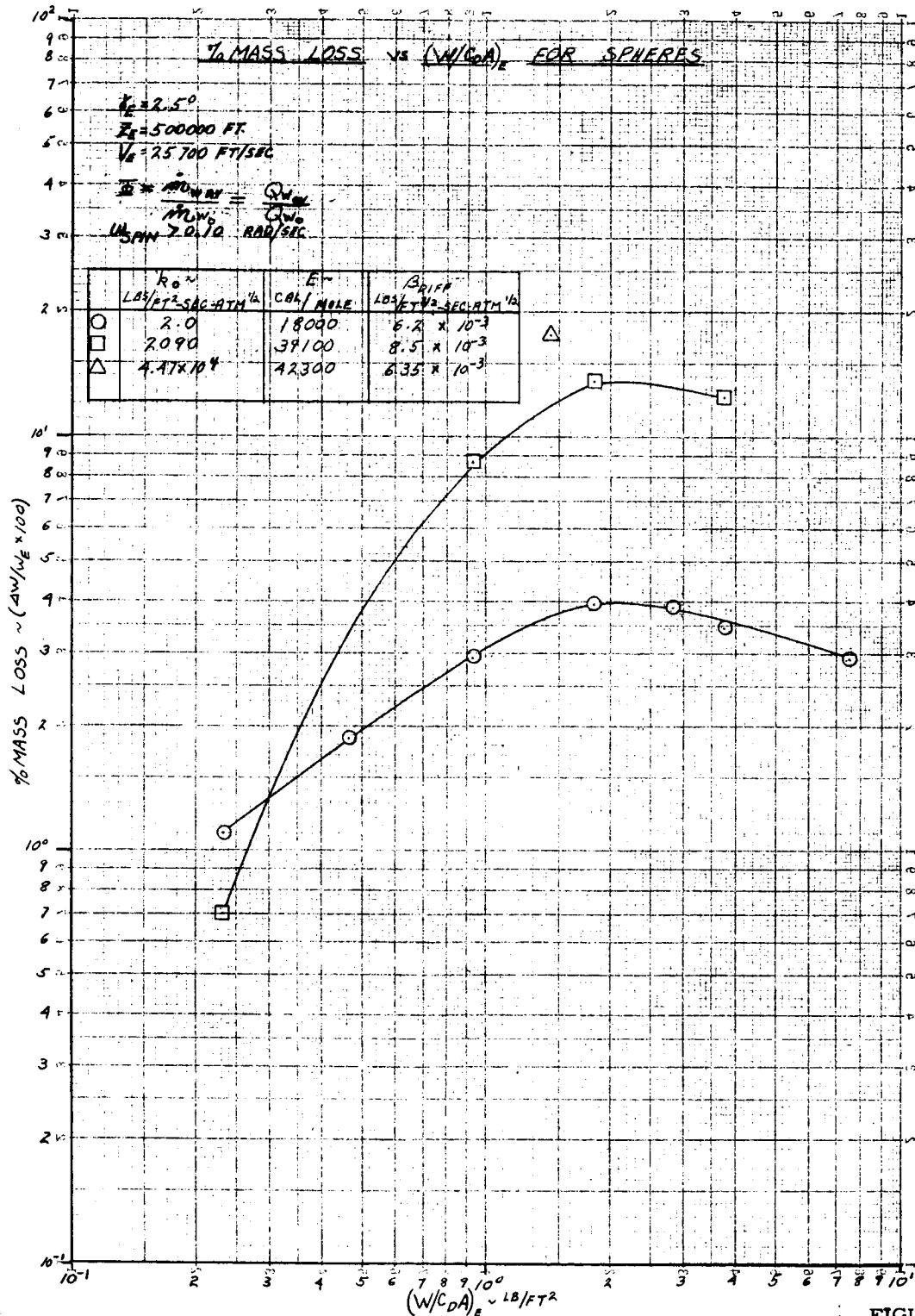


FIGURE 77

RESTRICTED DATA

UNCLASSIFIED

**DECLASSIFIED**



**UNCLASSIFIED**

UNCLASSIFIED.

UNCLASSIFIED.  
DECLASSIFIED

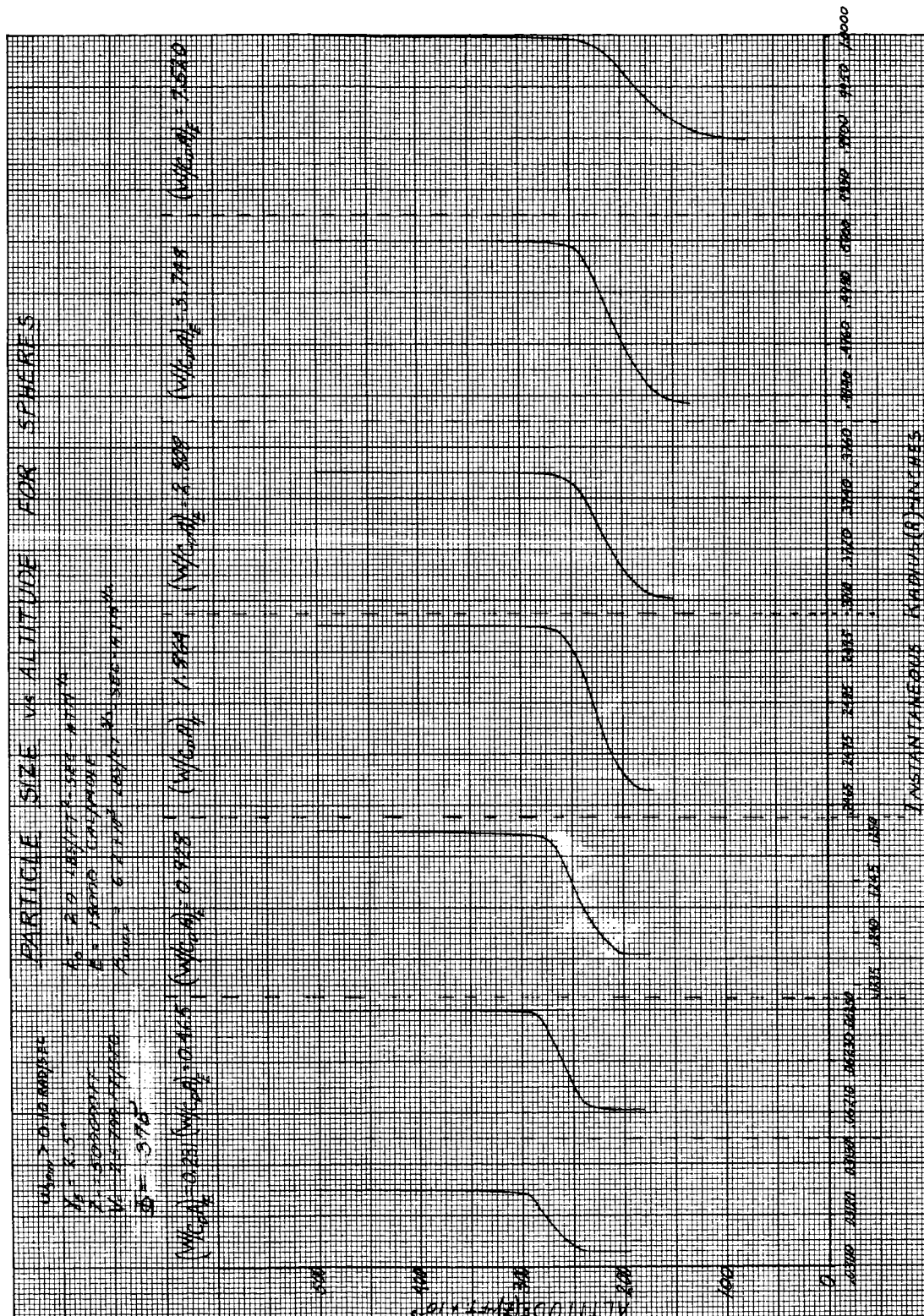


FIGURE 79.

UNCLASSIFIED

~~CONFIDENTIAL~~  
~~RESTRICTED DATA~~

UNCLASSIFIED

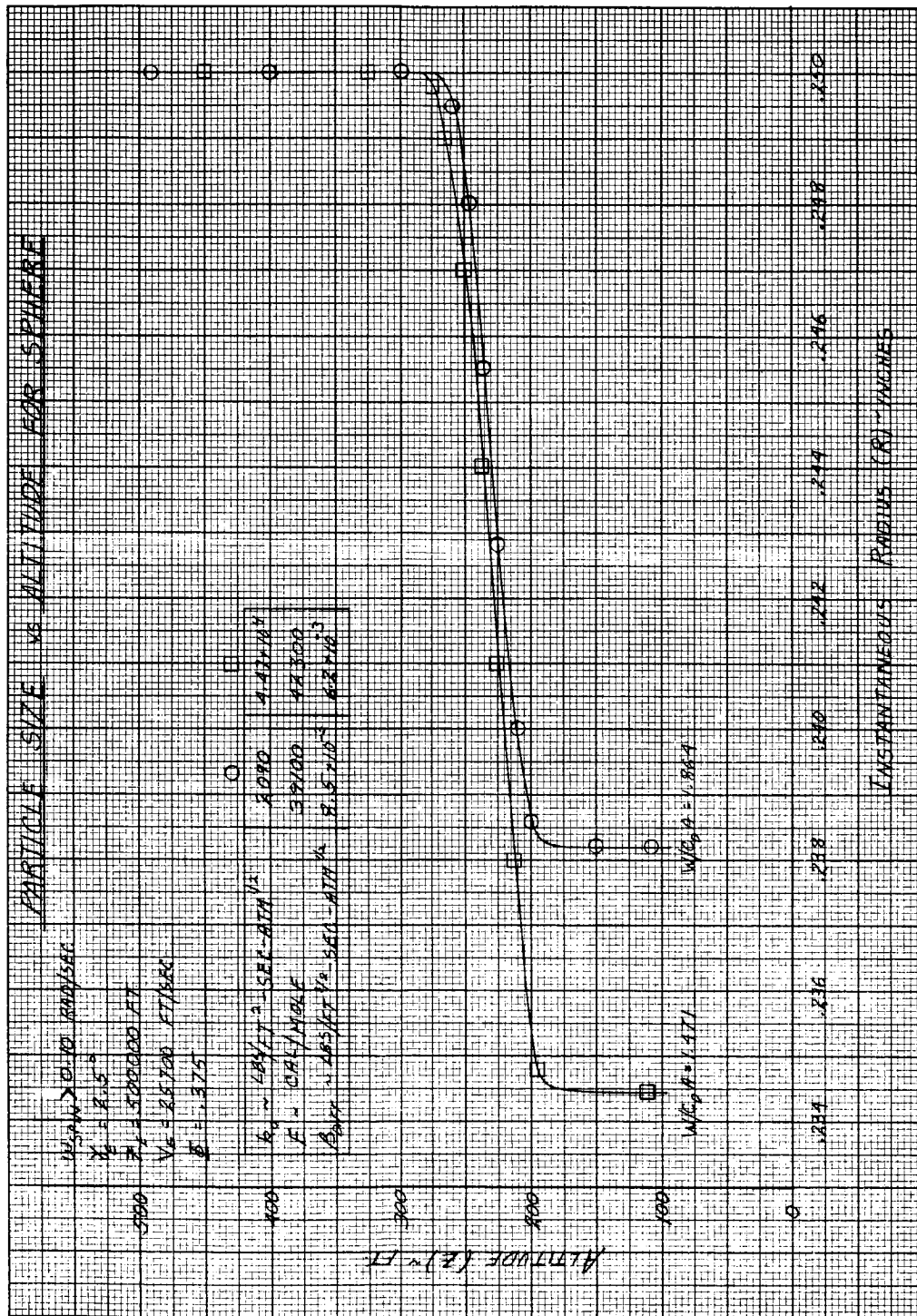
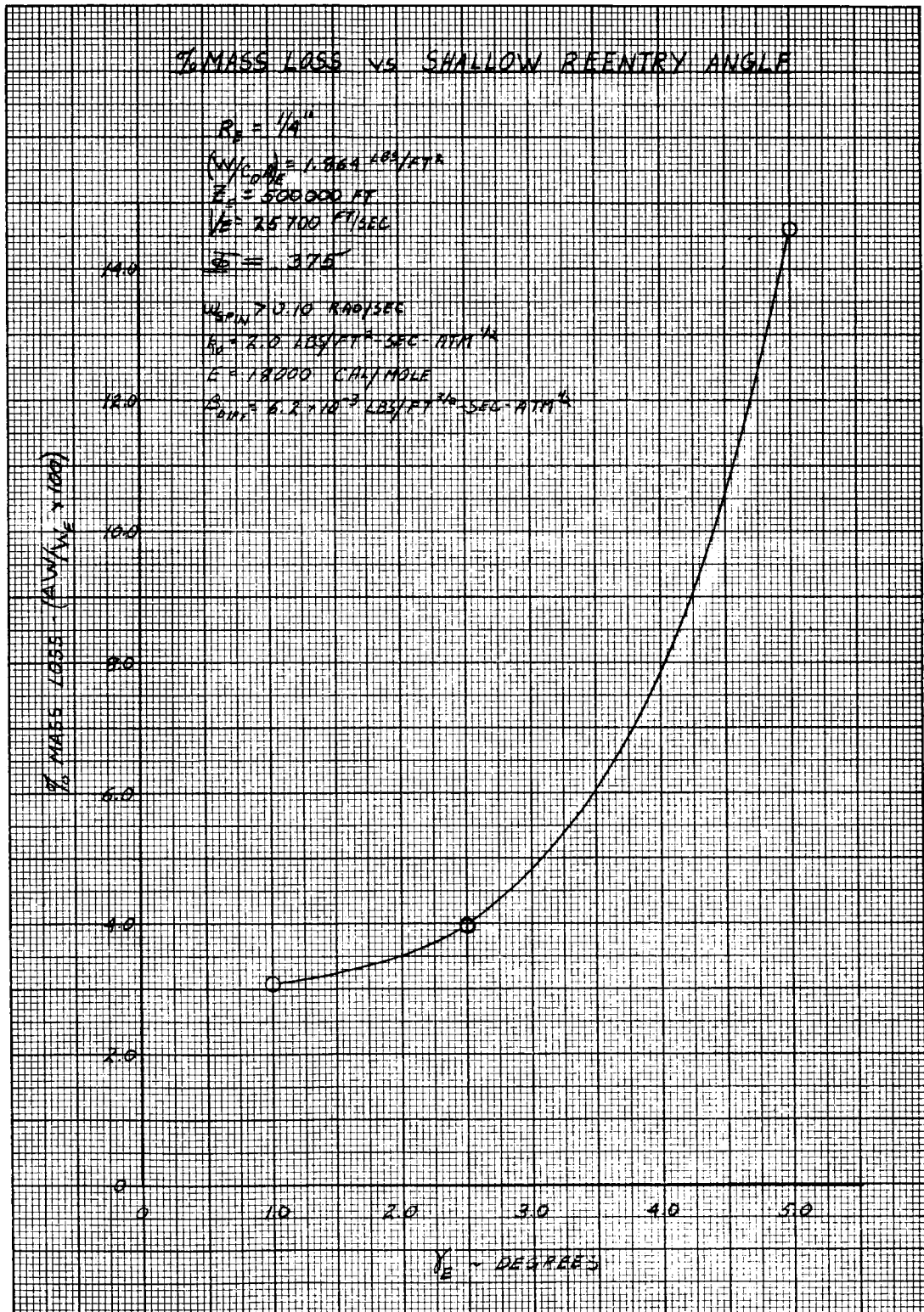


FIGURE 80

~~CONFIDENTIAL~~  
~~RESTRICTED DATA~~  
~~1954~~

UNCLASSIFIED

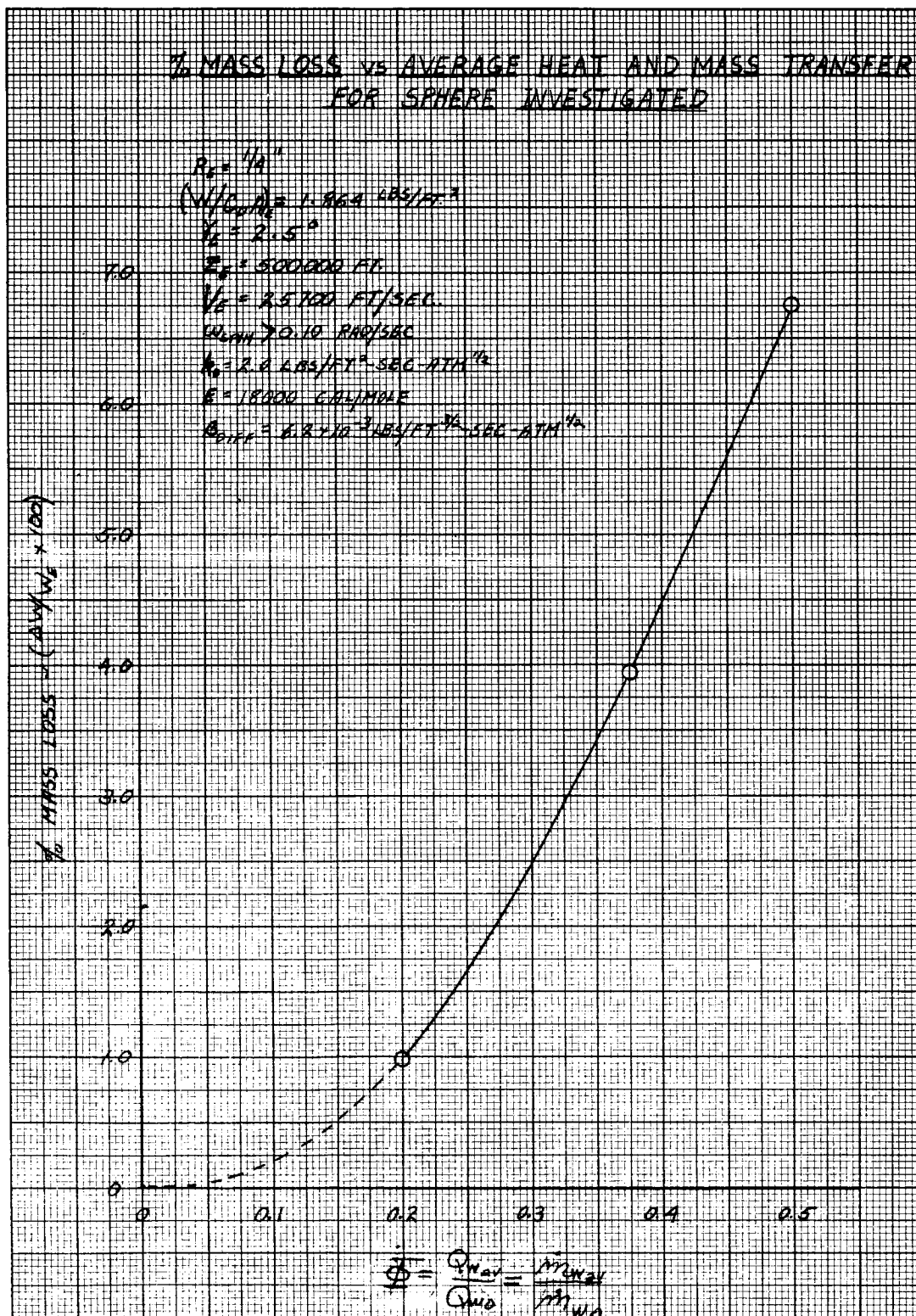
UNCLASSIFIED  
DECLASSIFIED



UNCLASSIFIED



UNCLASSIFIED  
DECLASSIFIED



UNCLASSIFIED











UNCLASSIFIED  
REF ID: A60160

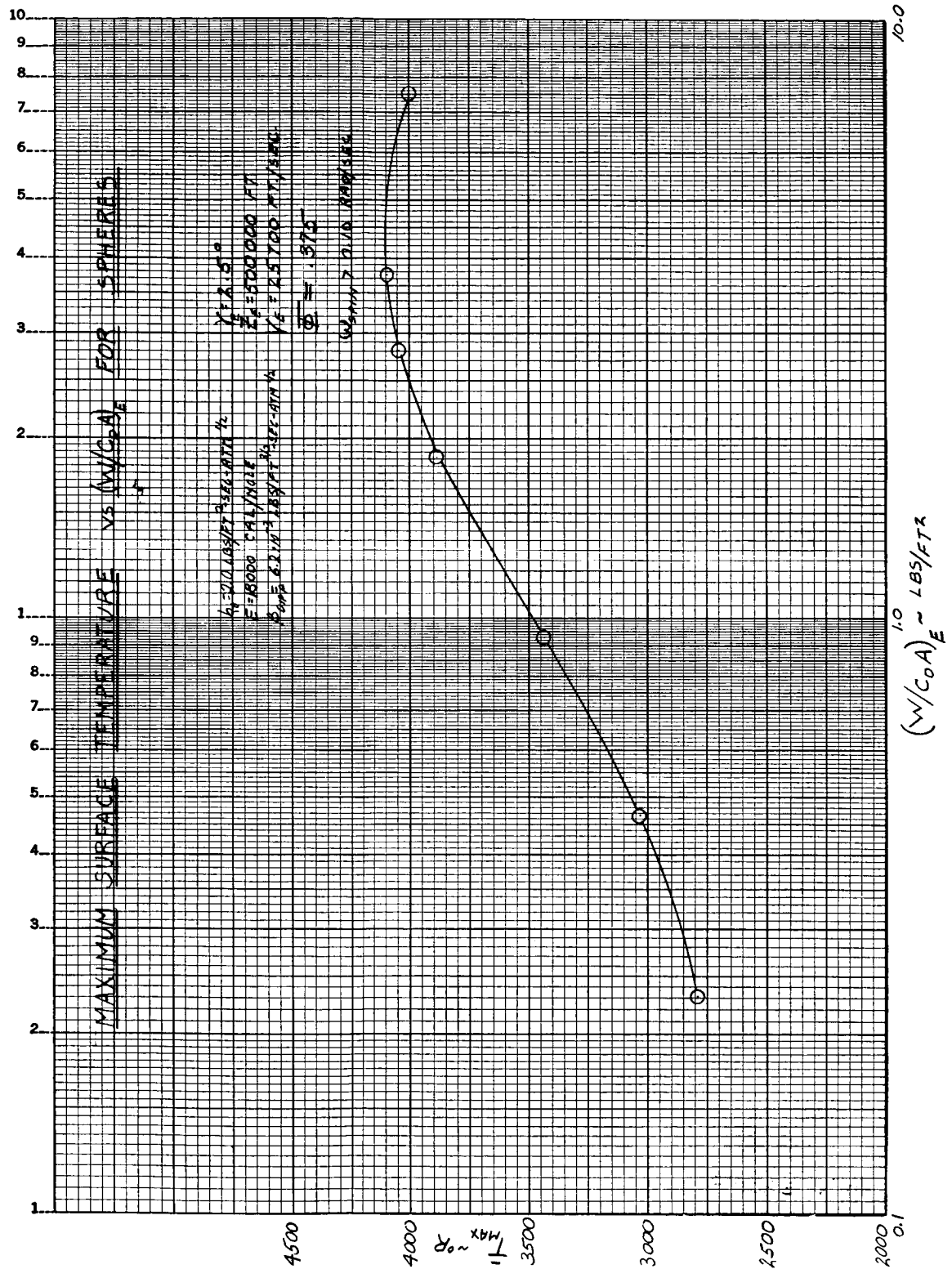
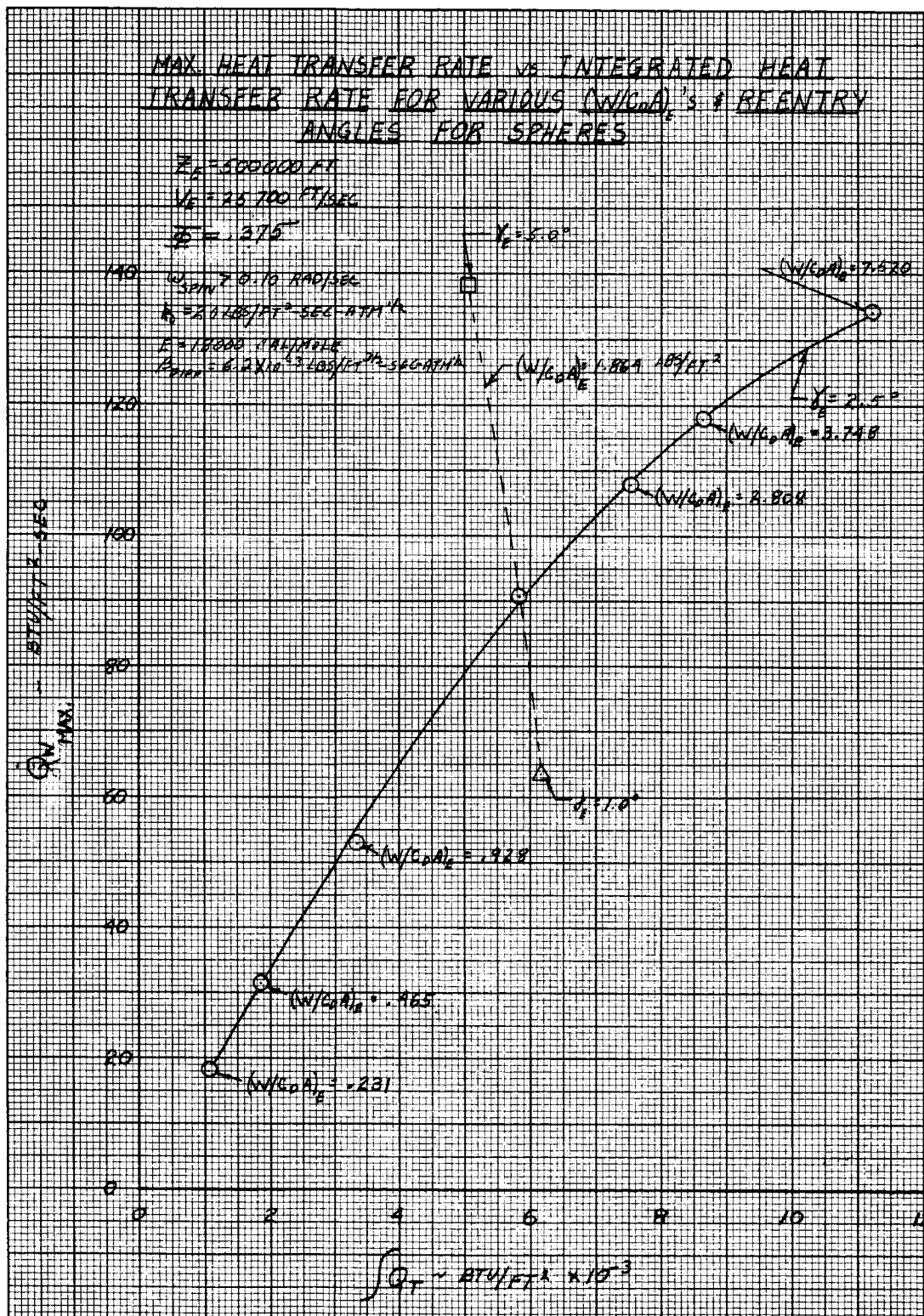
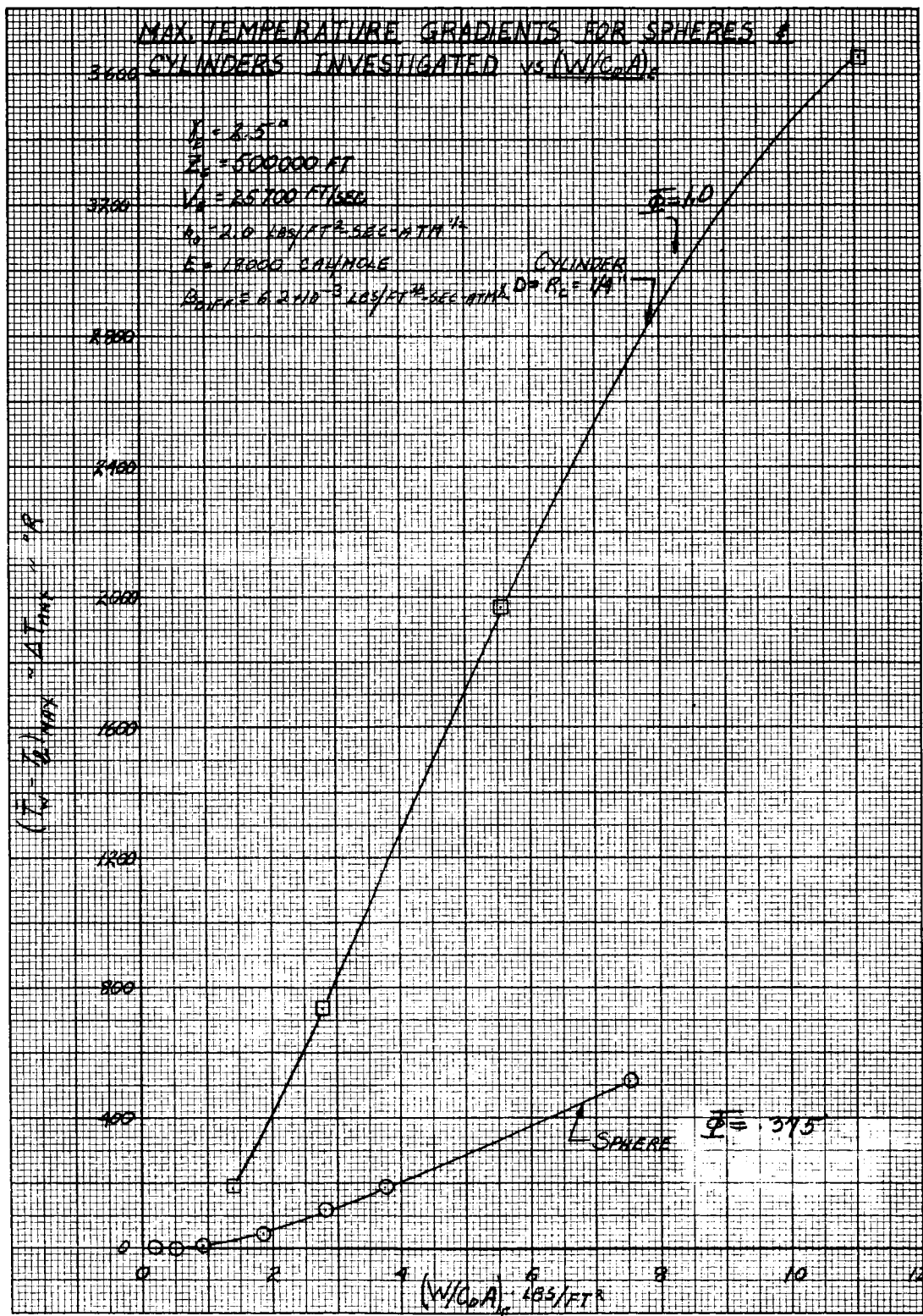


FIGURE 87.

UNCLASSIFIED



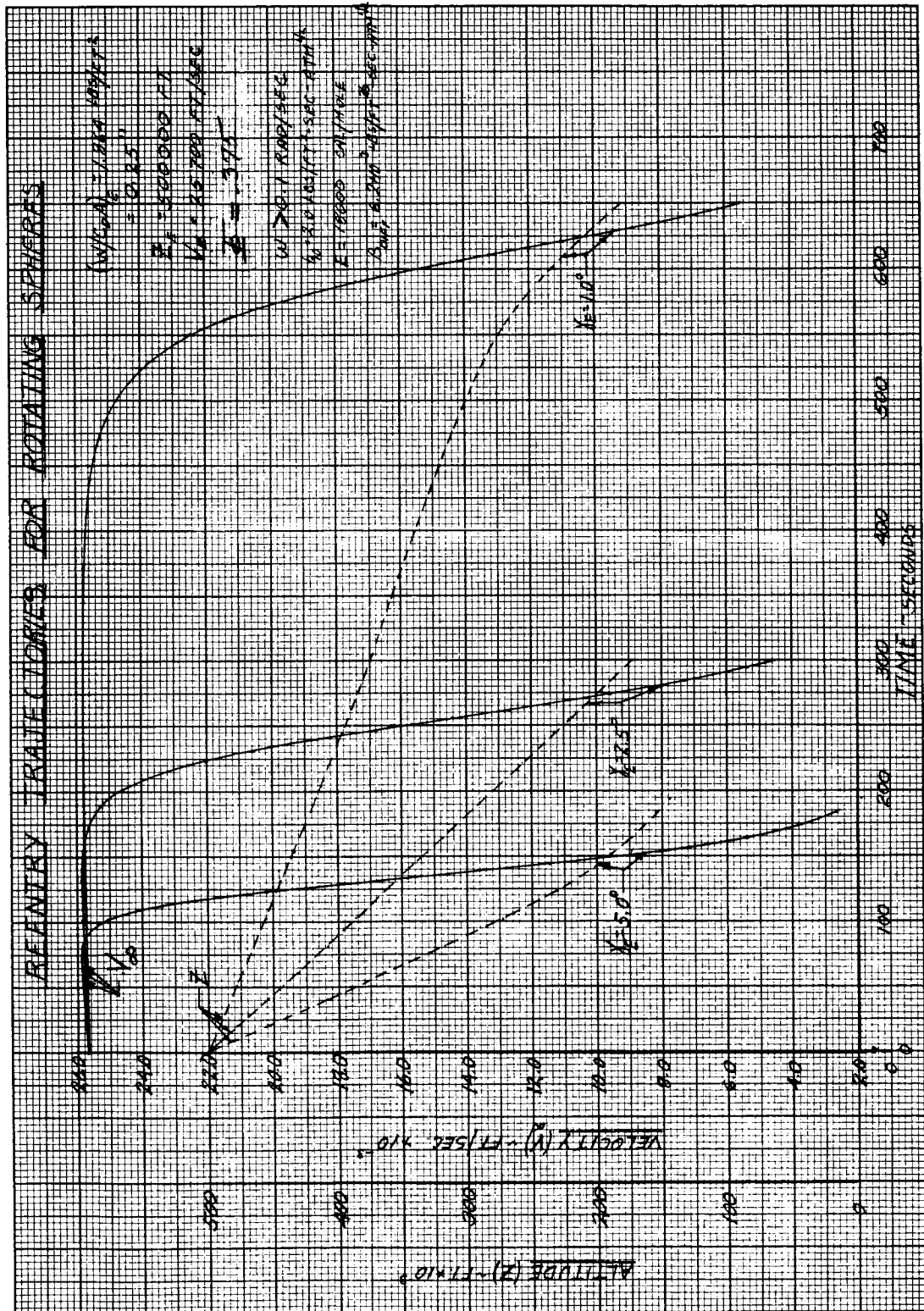


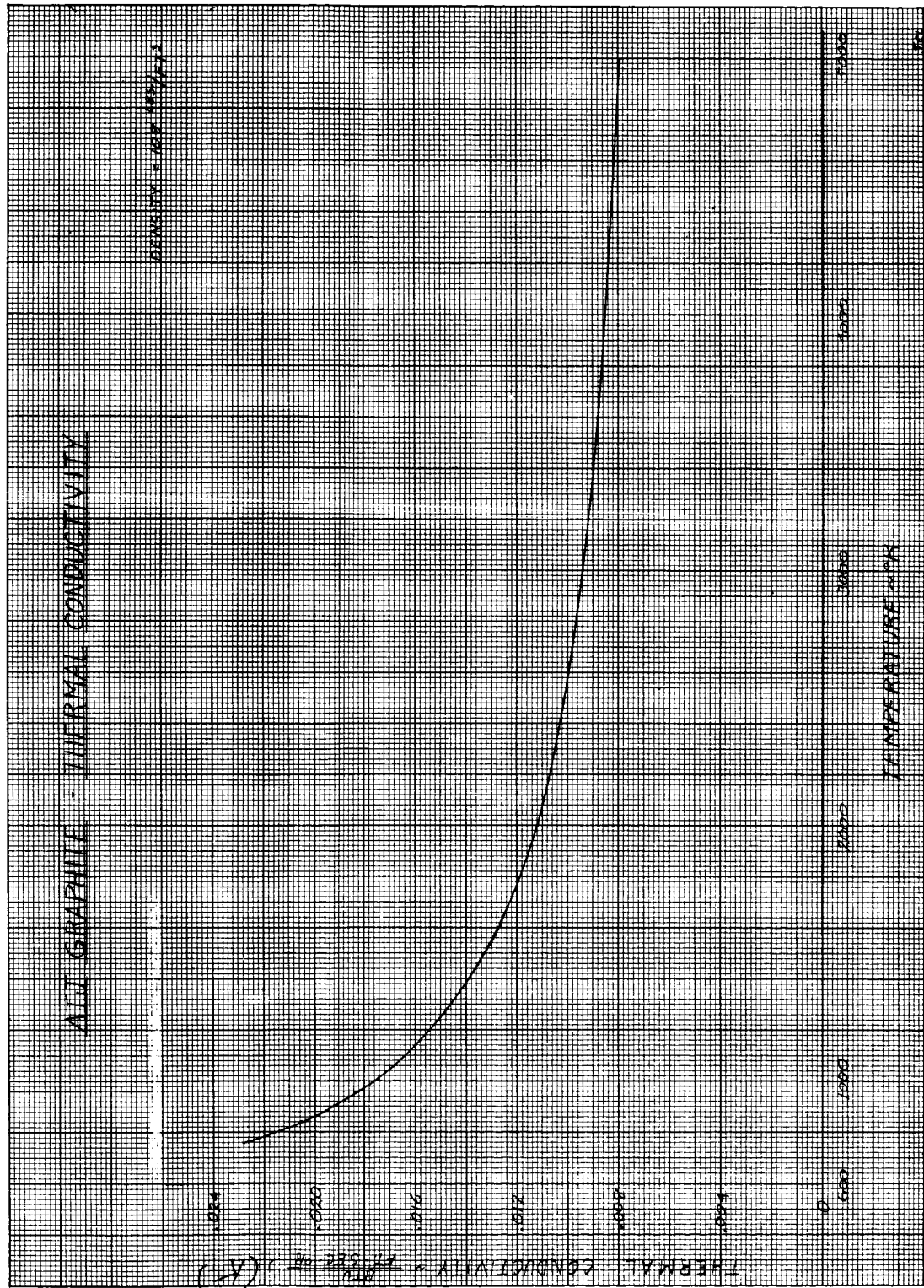


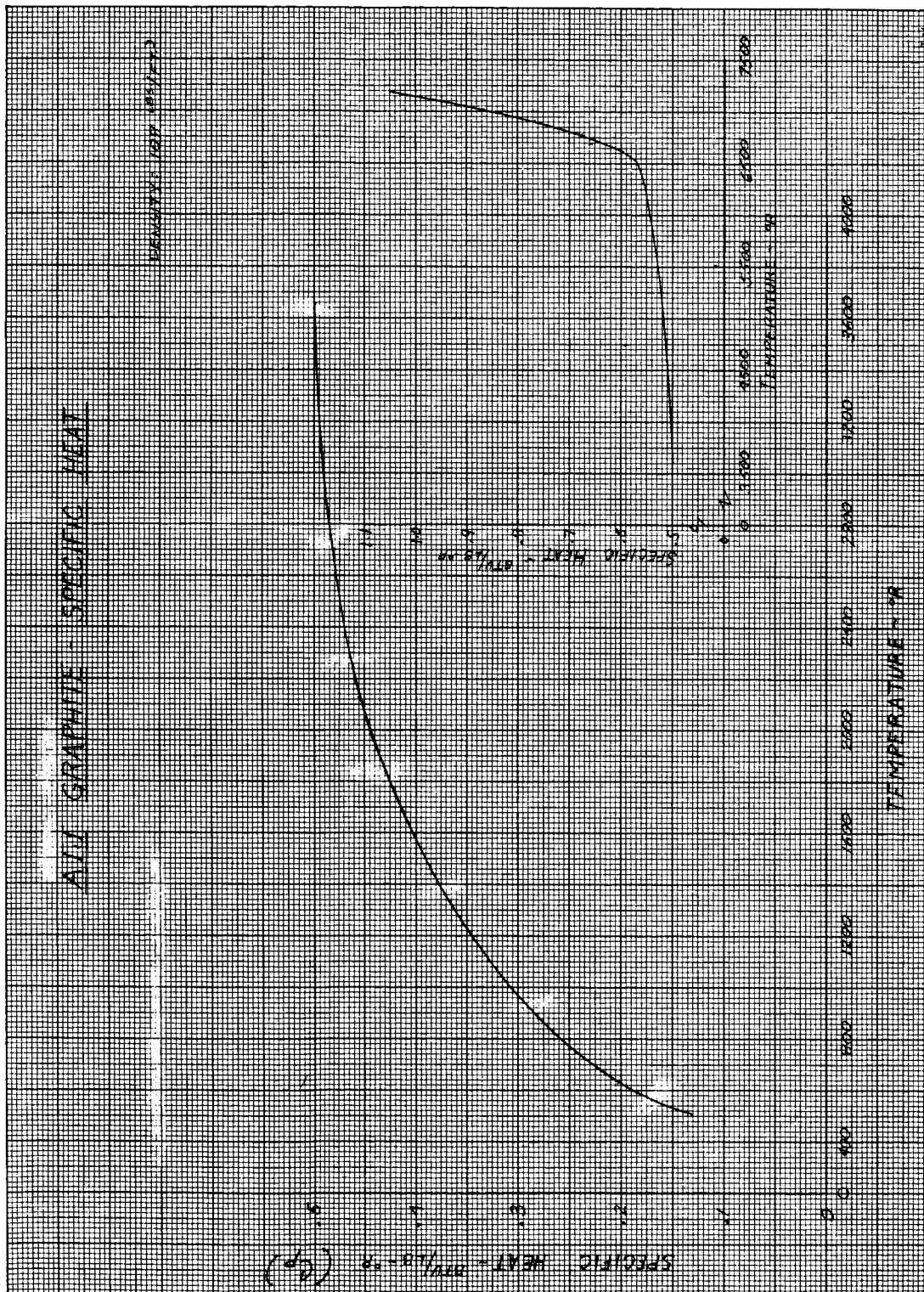
**UNCLASSIFIED**











~~CONFIDENTIAL~~

~~RESTRICTED DATA~~

UNCLASSIFIED

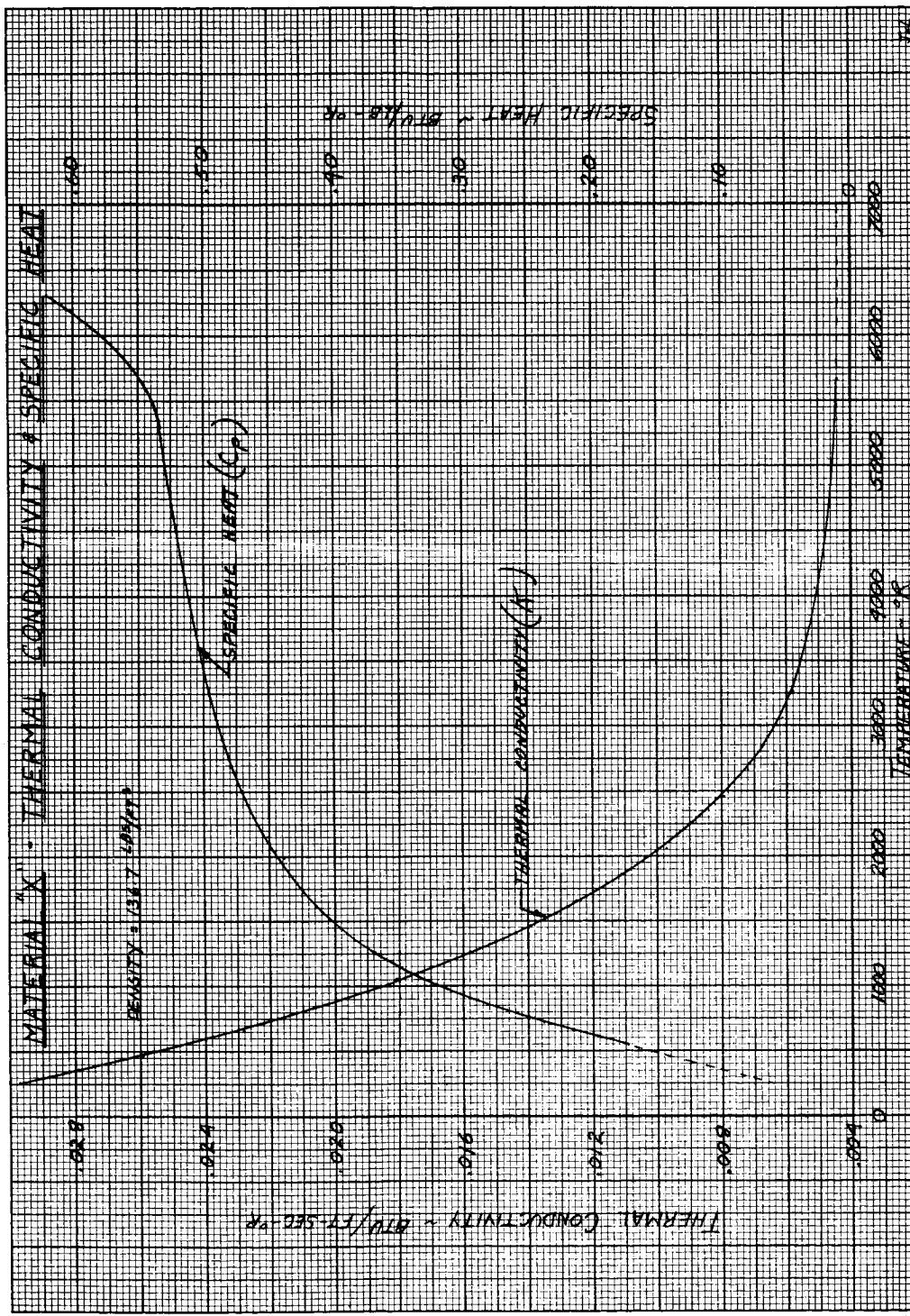


FIGURE 94

~~CONFIDENTIAL~~  
~~RESTRICTED DATA~~  
Atomic Energy Act of 1954

UNCLASSIFIED

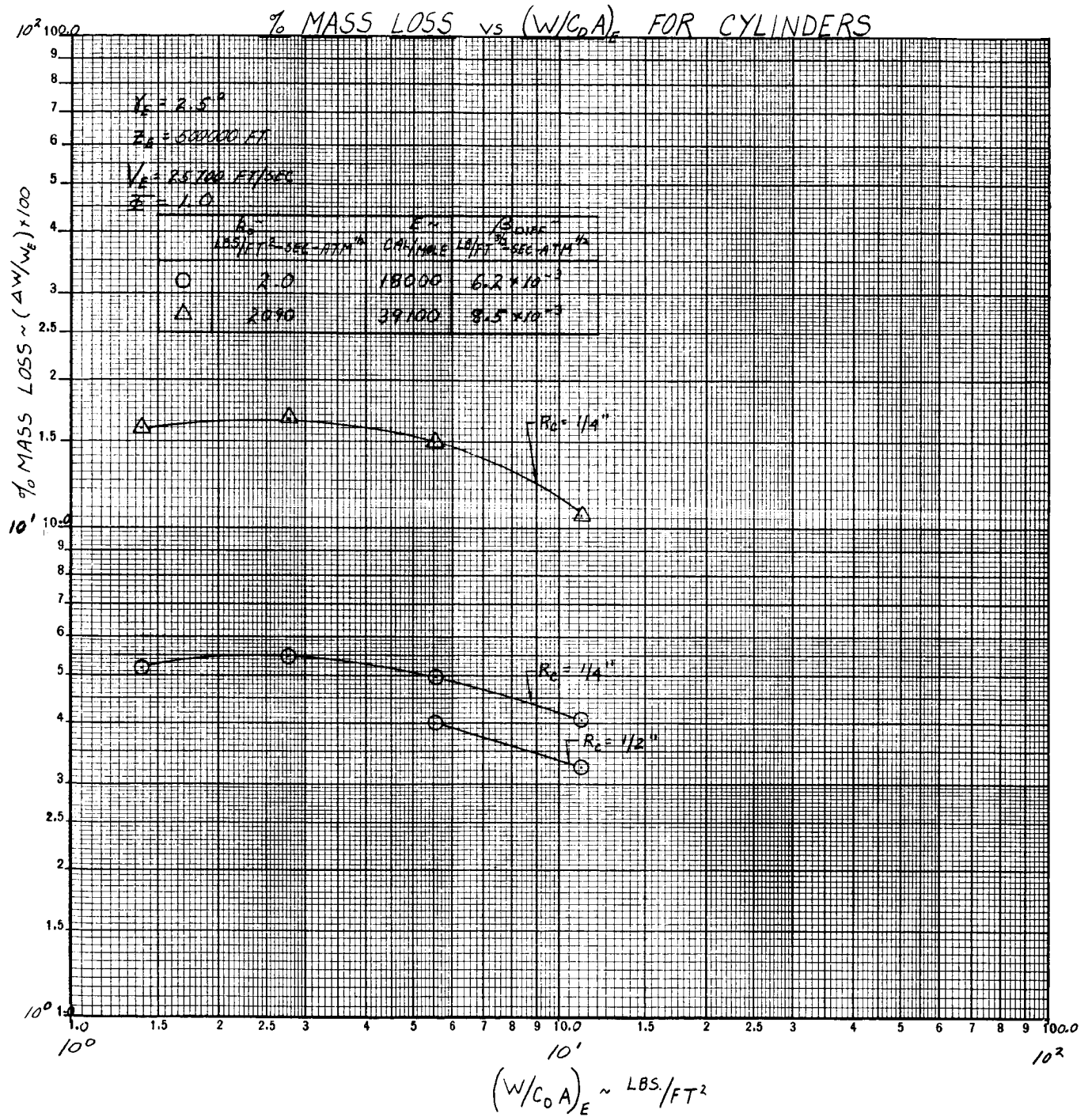


FIGURE 95





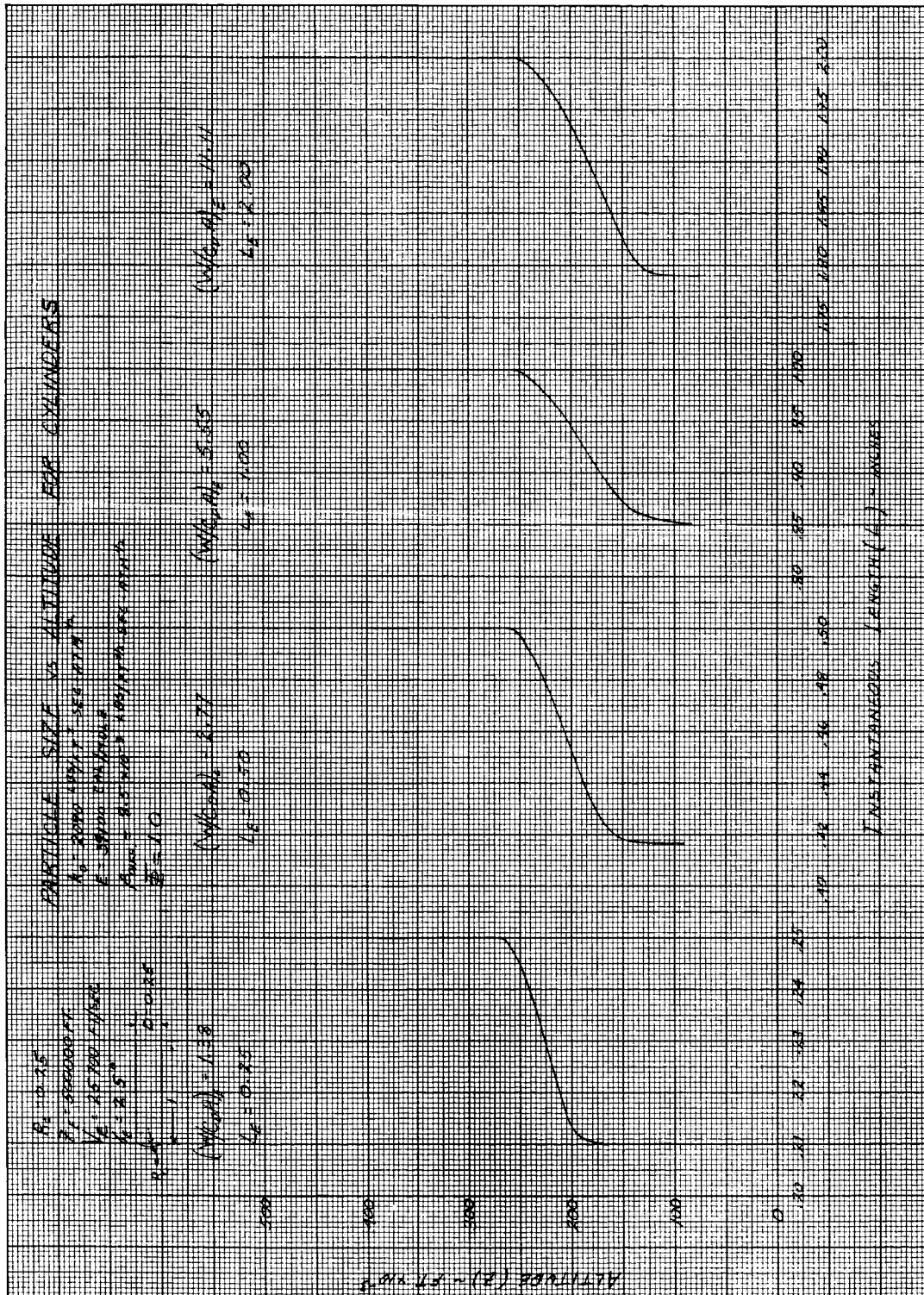


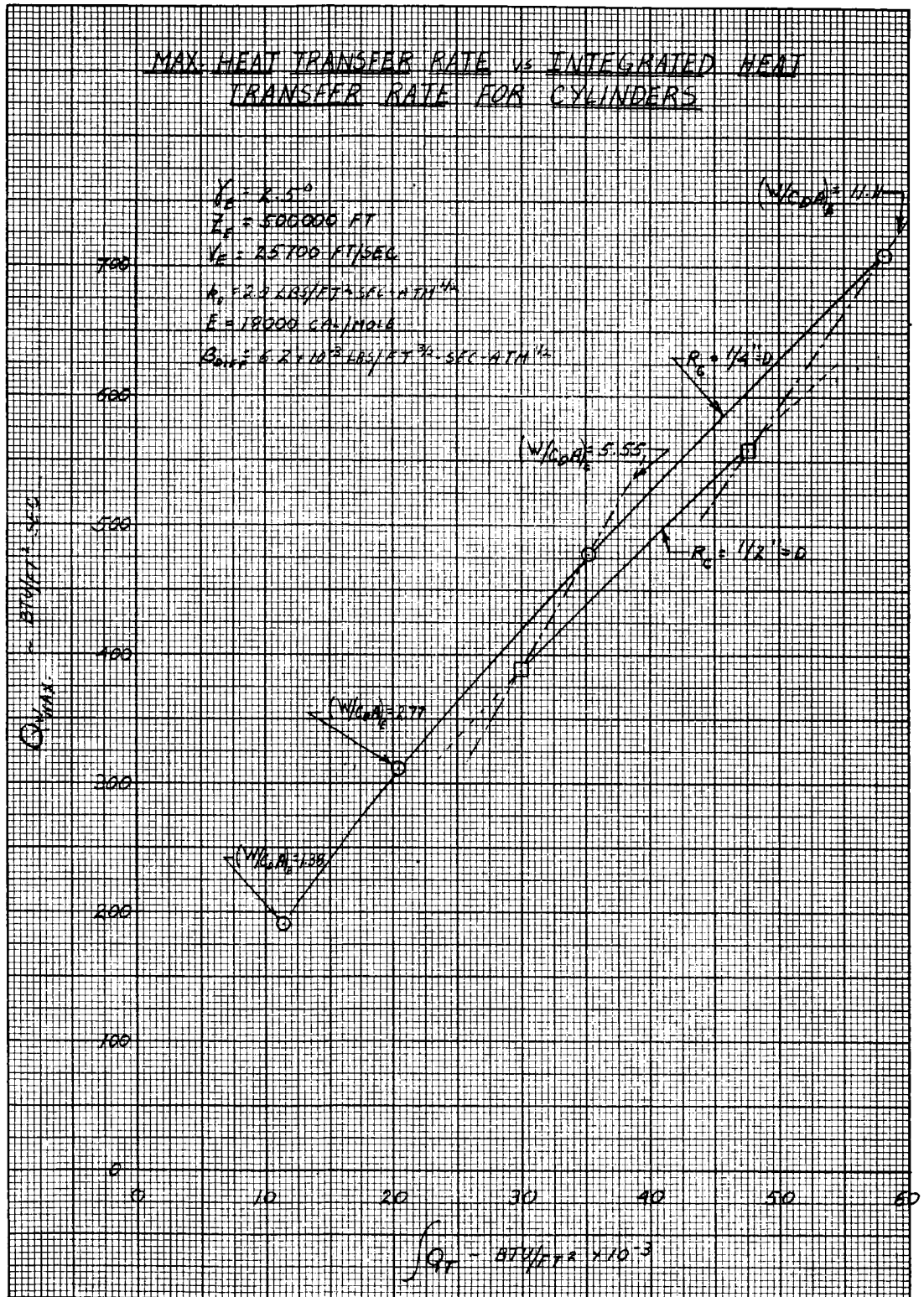
FIGURE 97







UNCLASSIFIED  
DECLASSIFIED



UNCLASSIFIED

**UNCLASSIFIED**



CONFIDENTIAL  
RESTRICTED DATA

UNCLASSIFIED

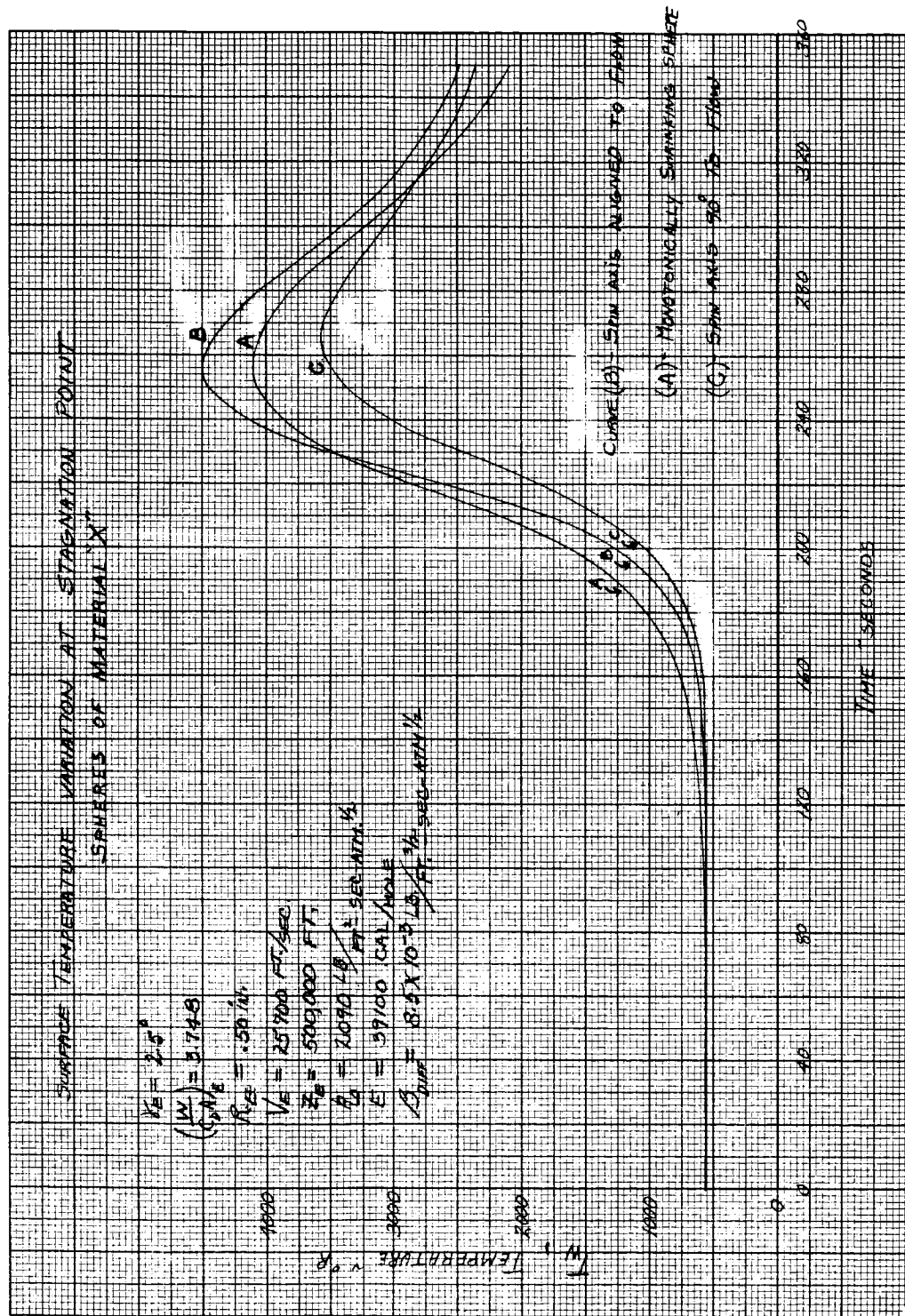
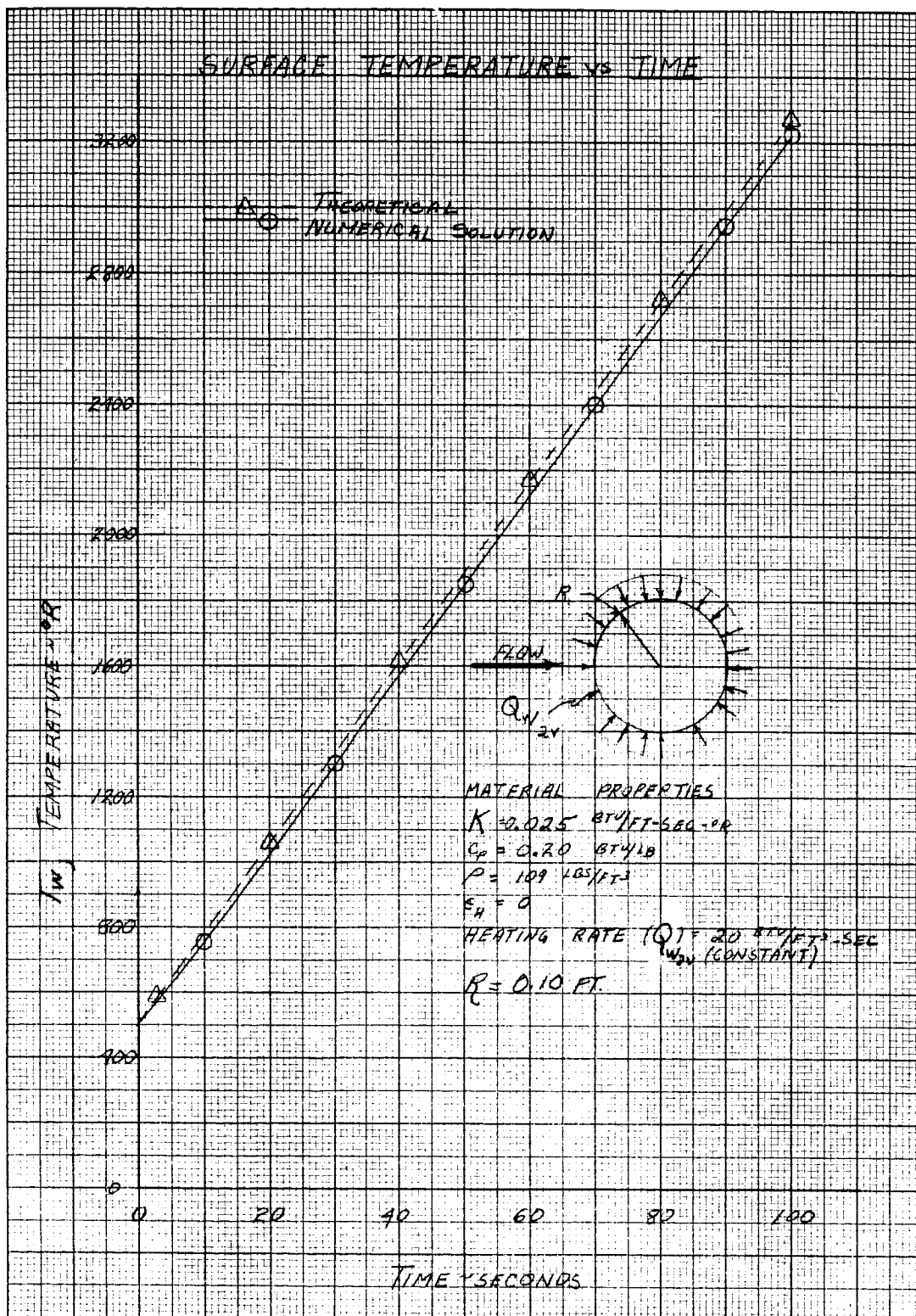


FIGURE 102

CONFIDENTIAL  
RESTRICTED DATA

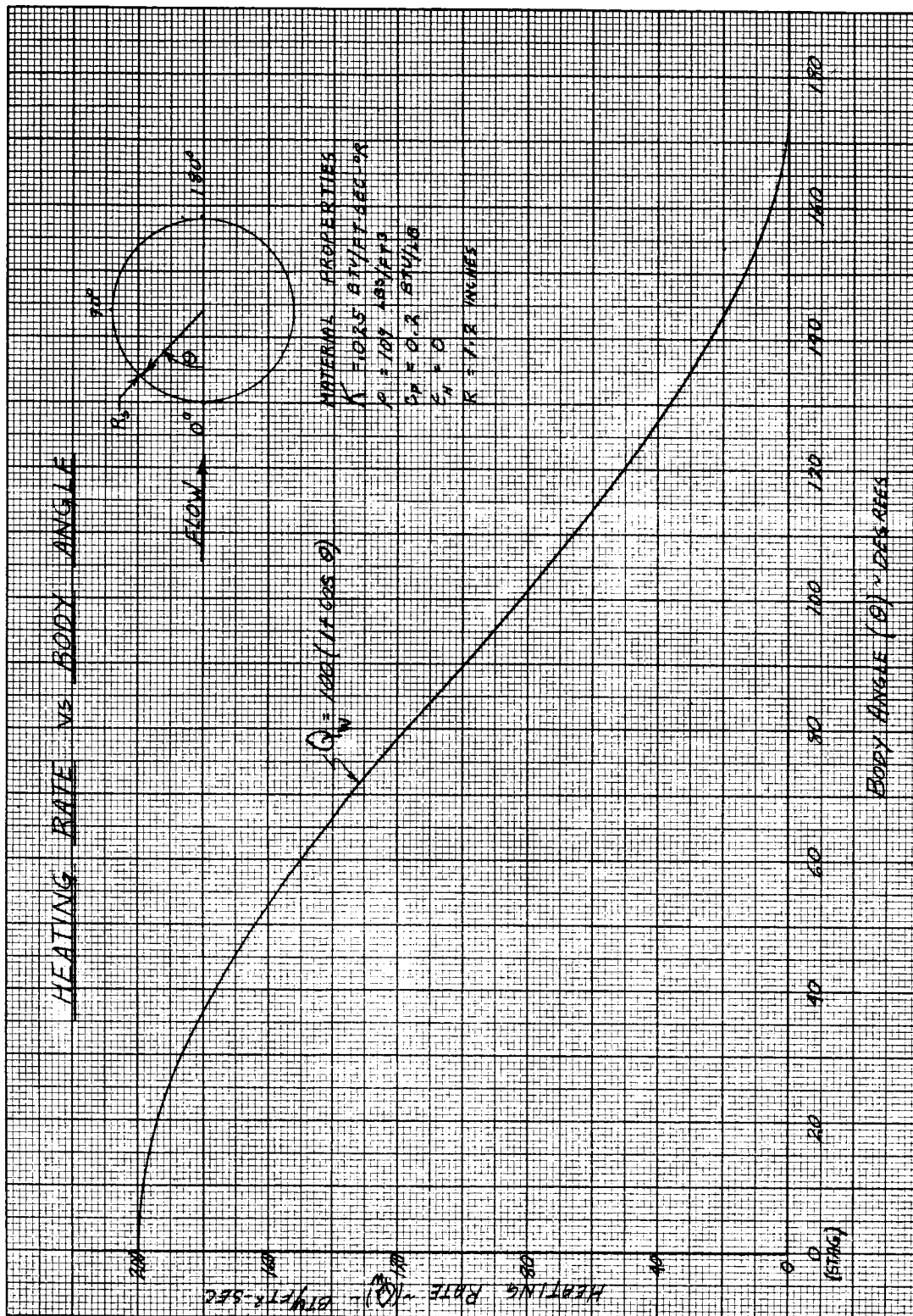
UNCLASSIFIED

UNCLASSIFIED  
DECLASSIFIED

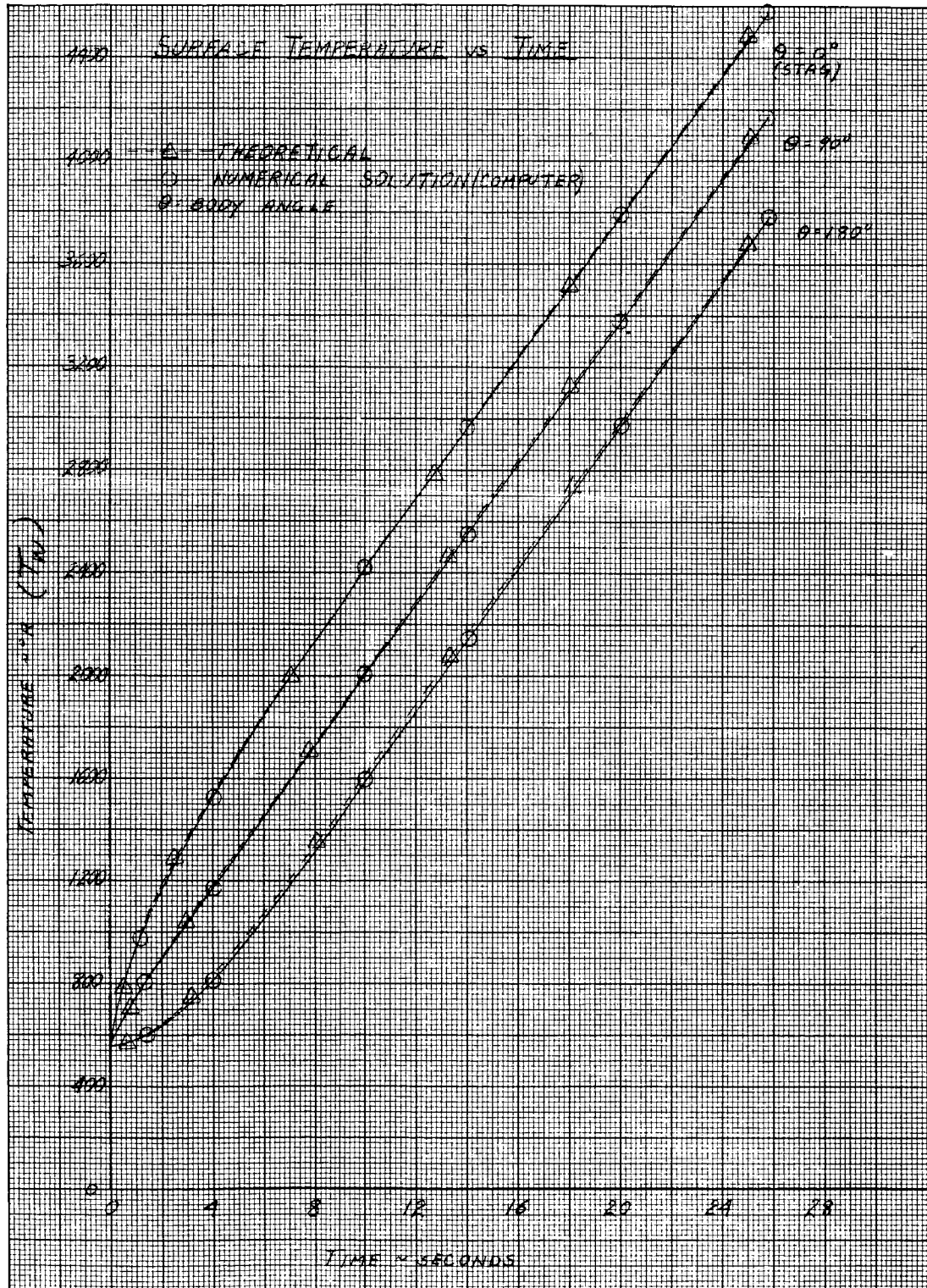


UNCLASSIFIED

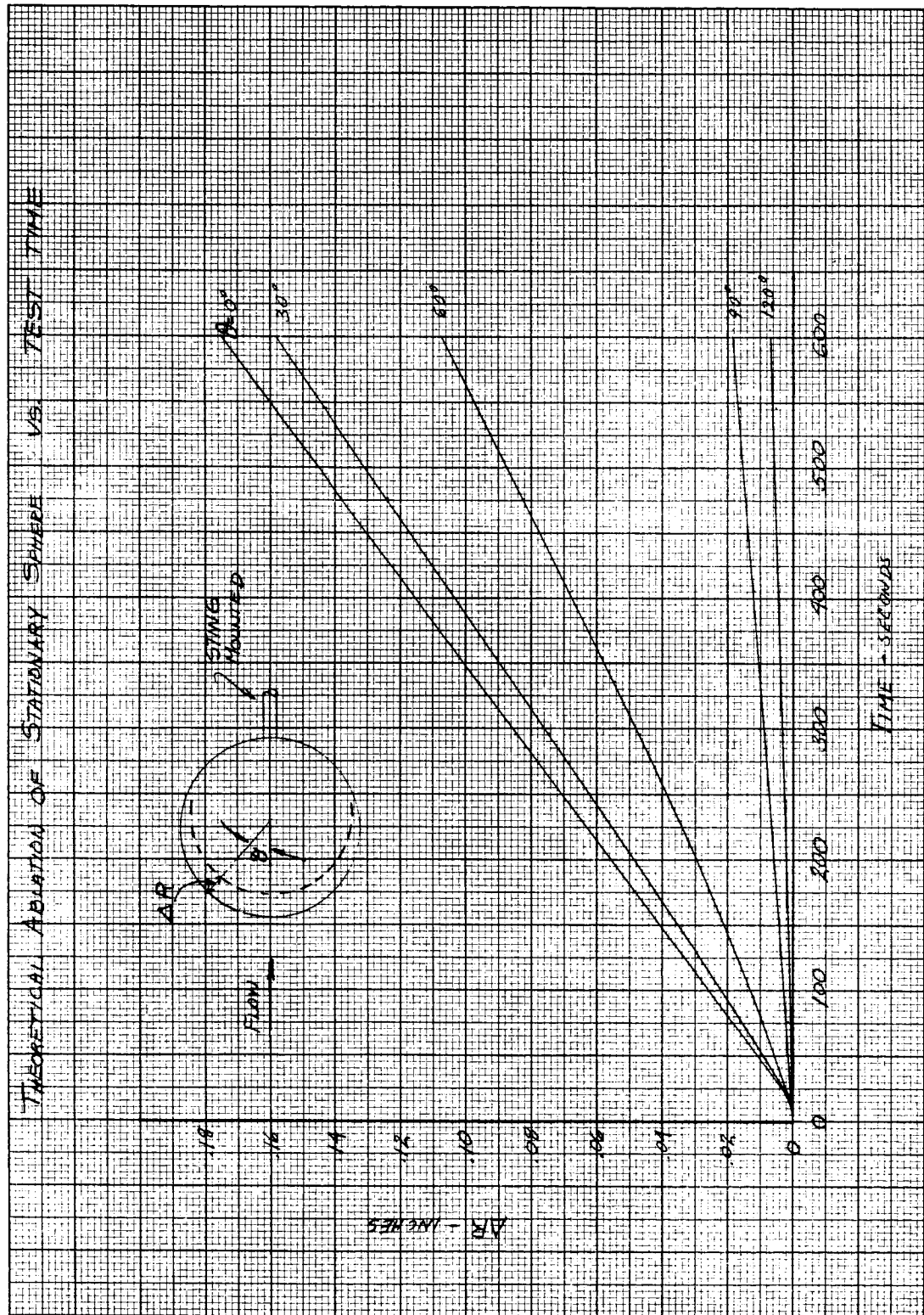




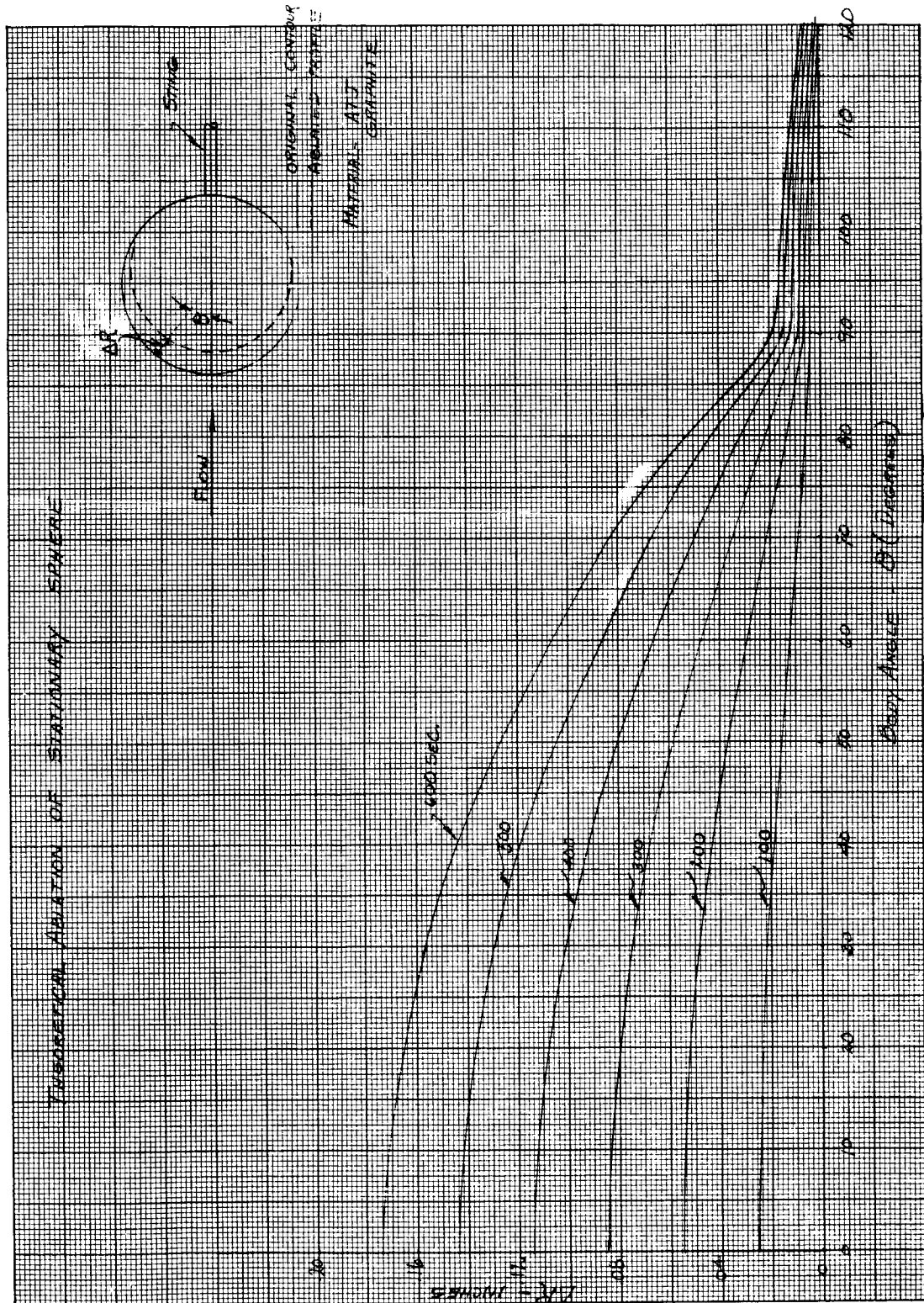
UNCLASSIFIED  
DECLASSIFIED

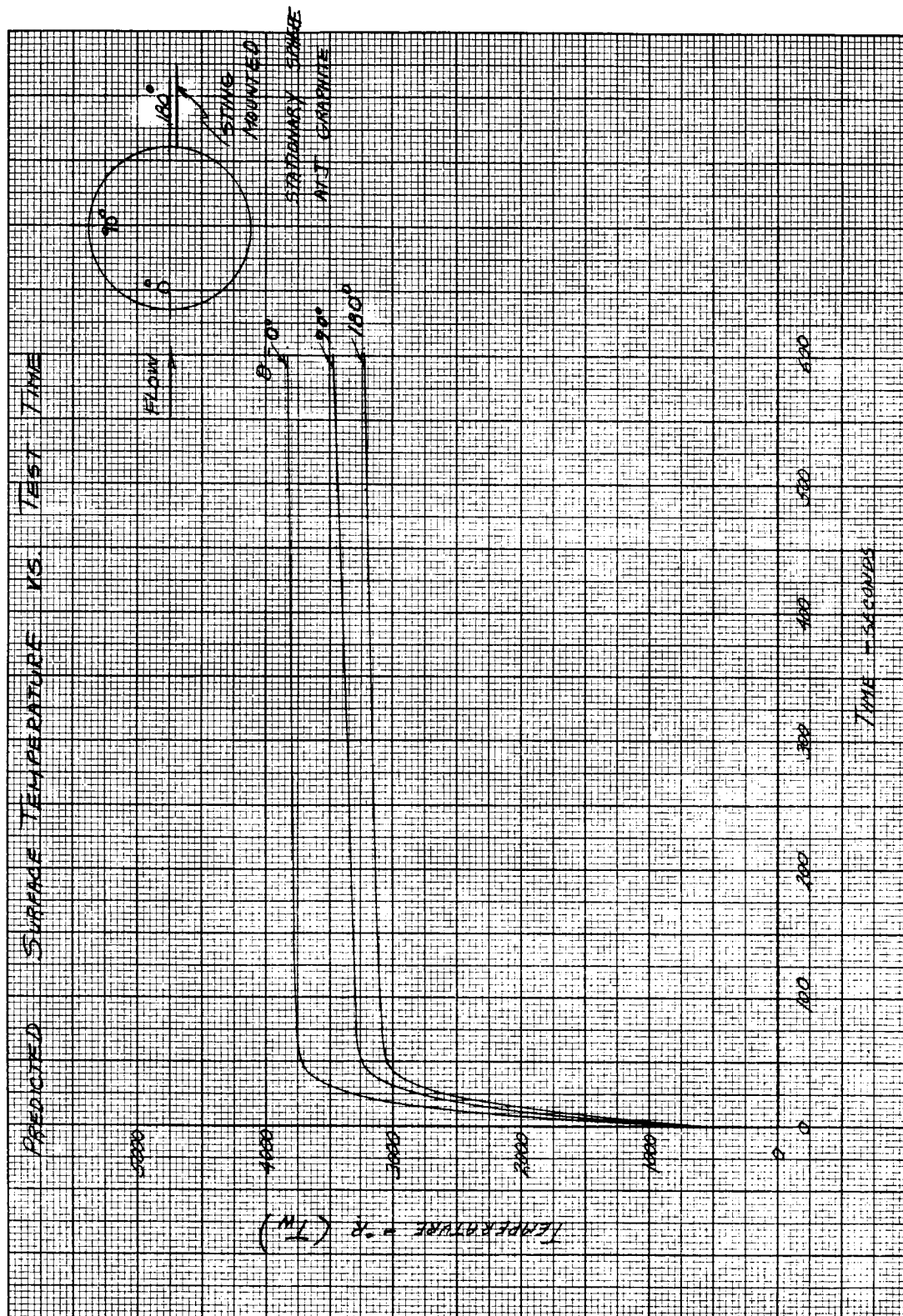


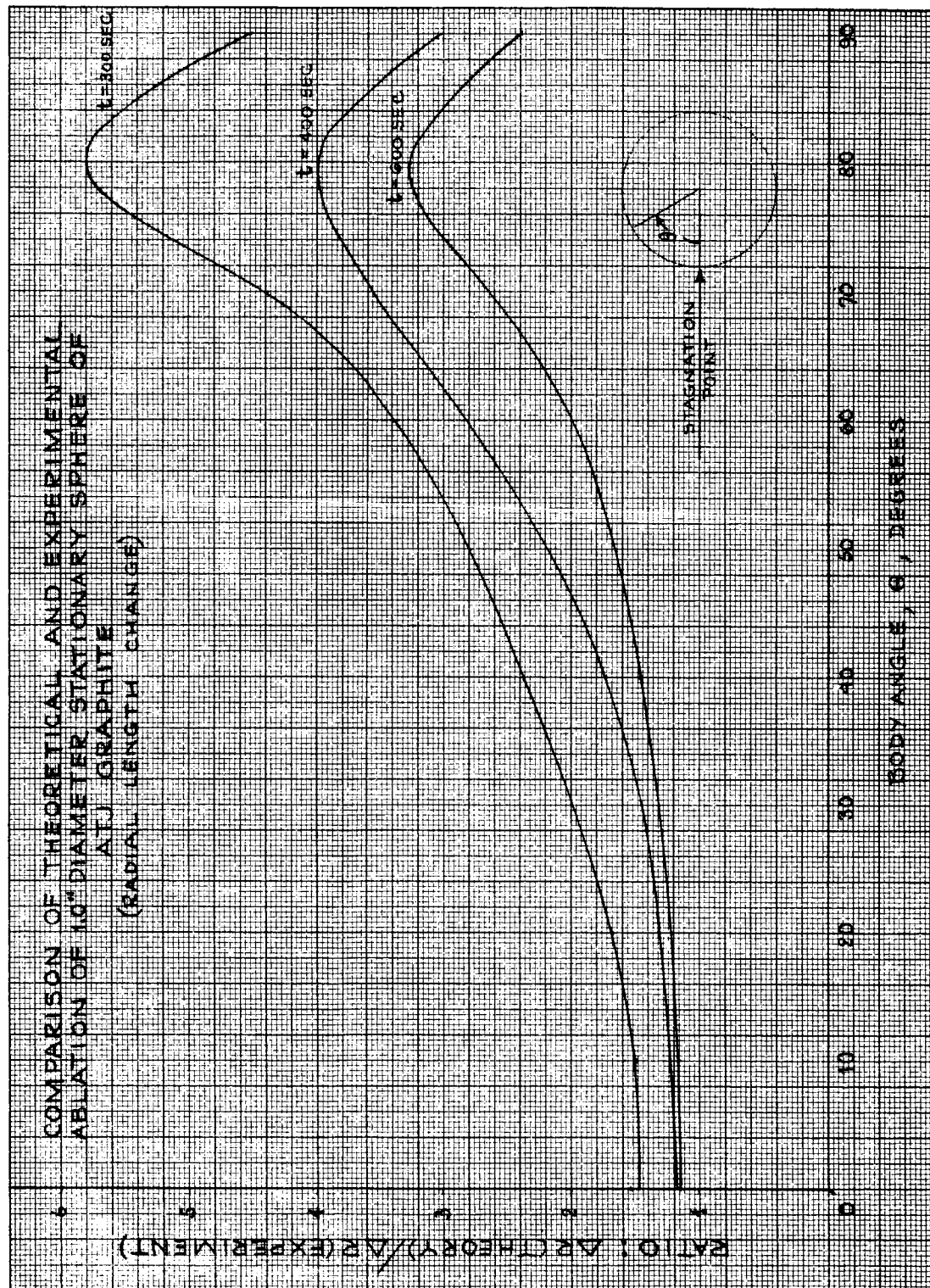
UNCLASSIFIED

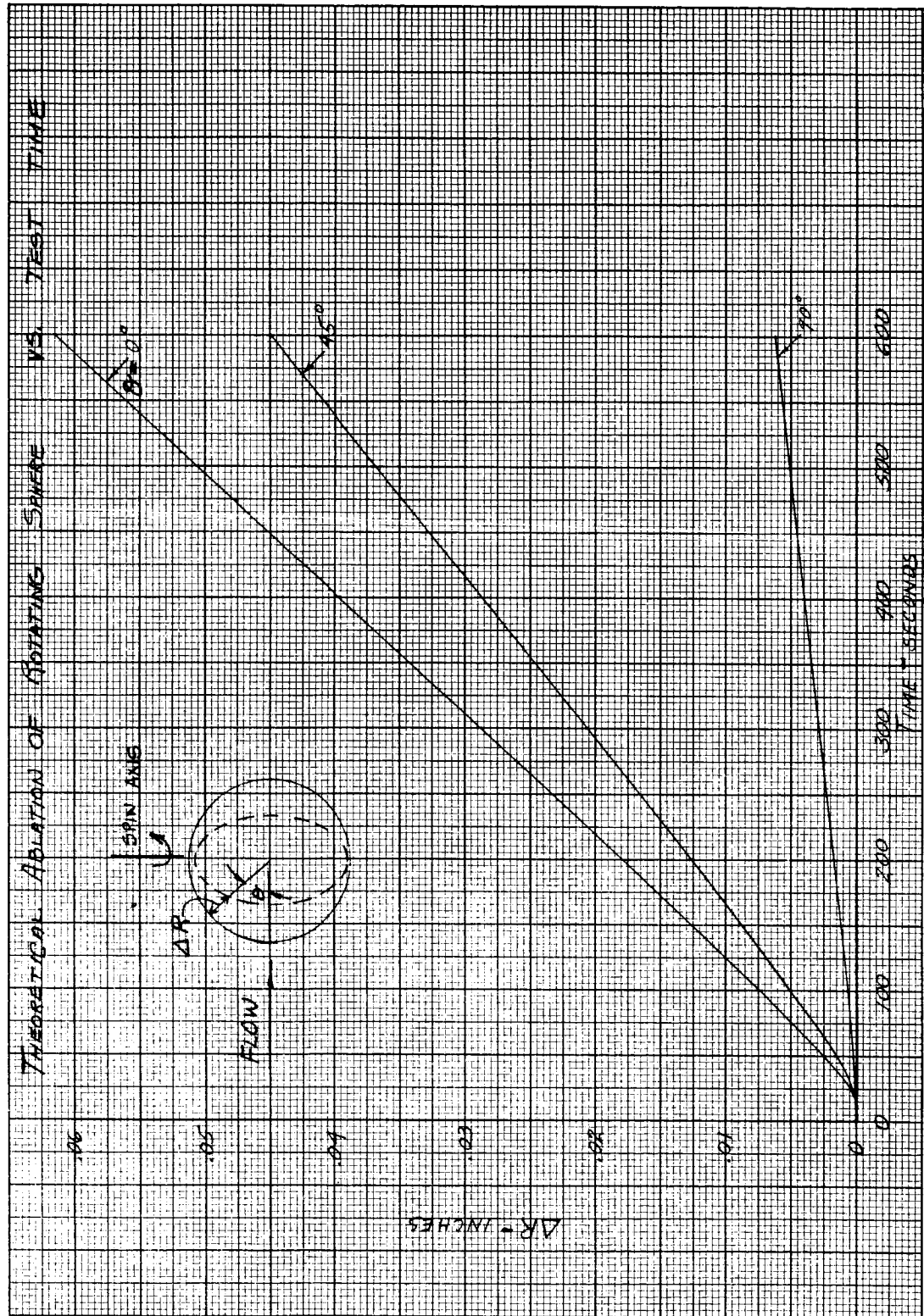




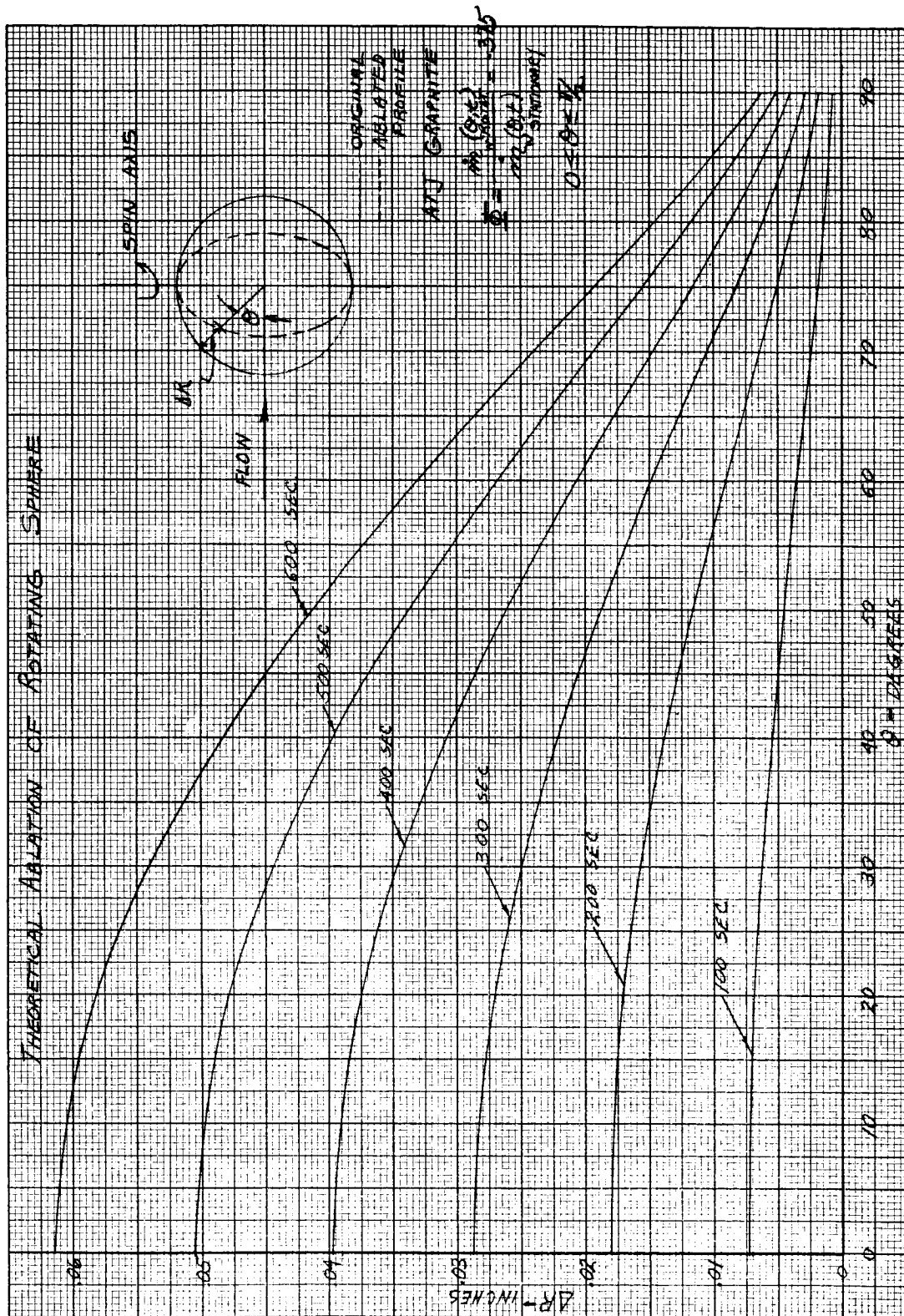




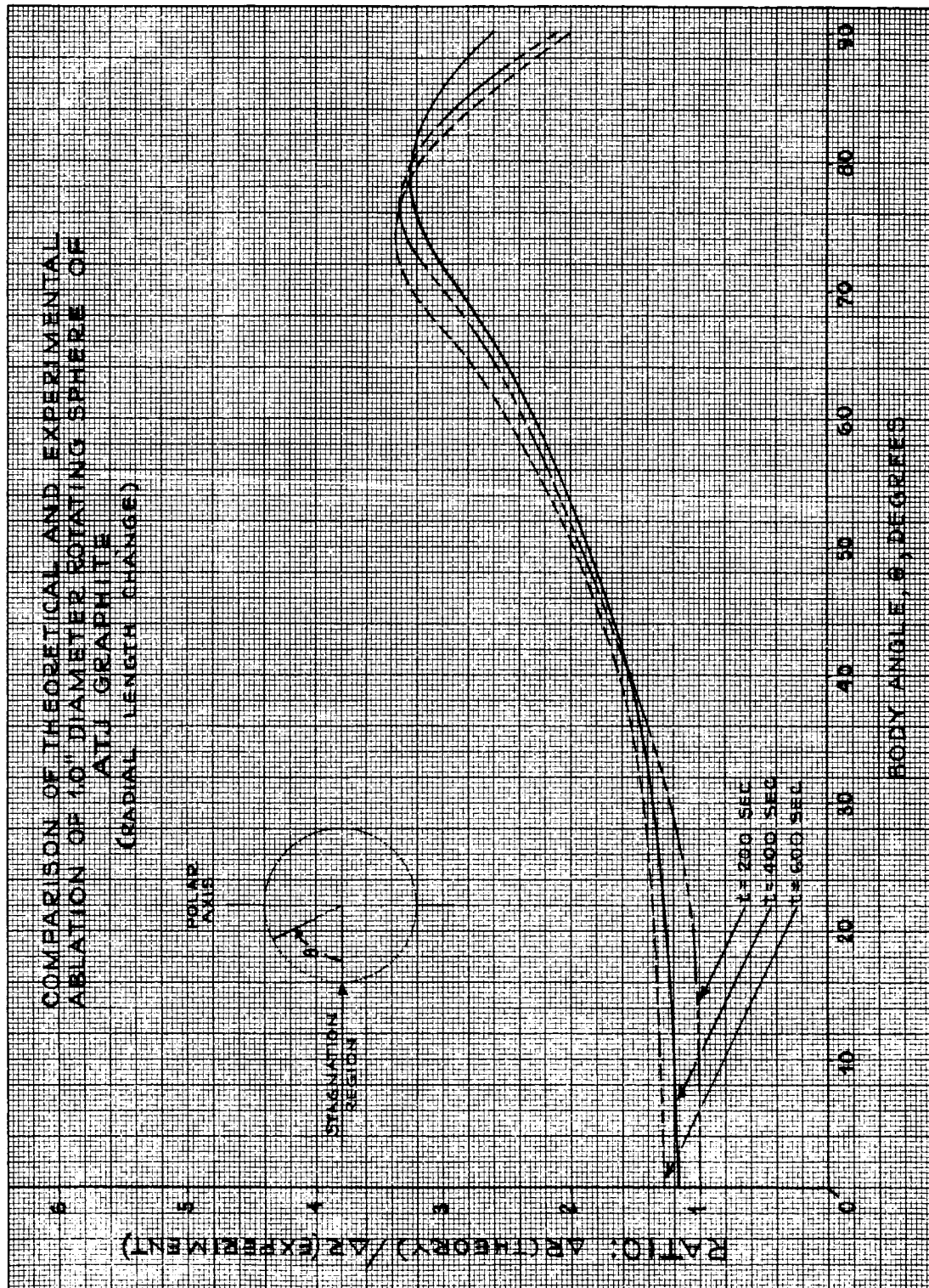












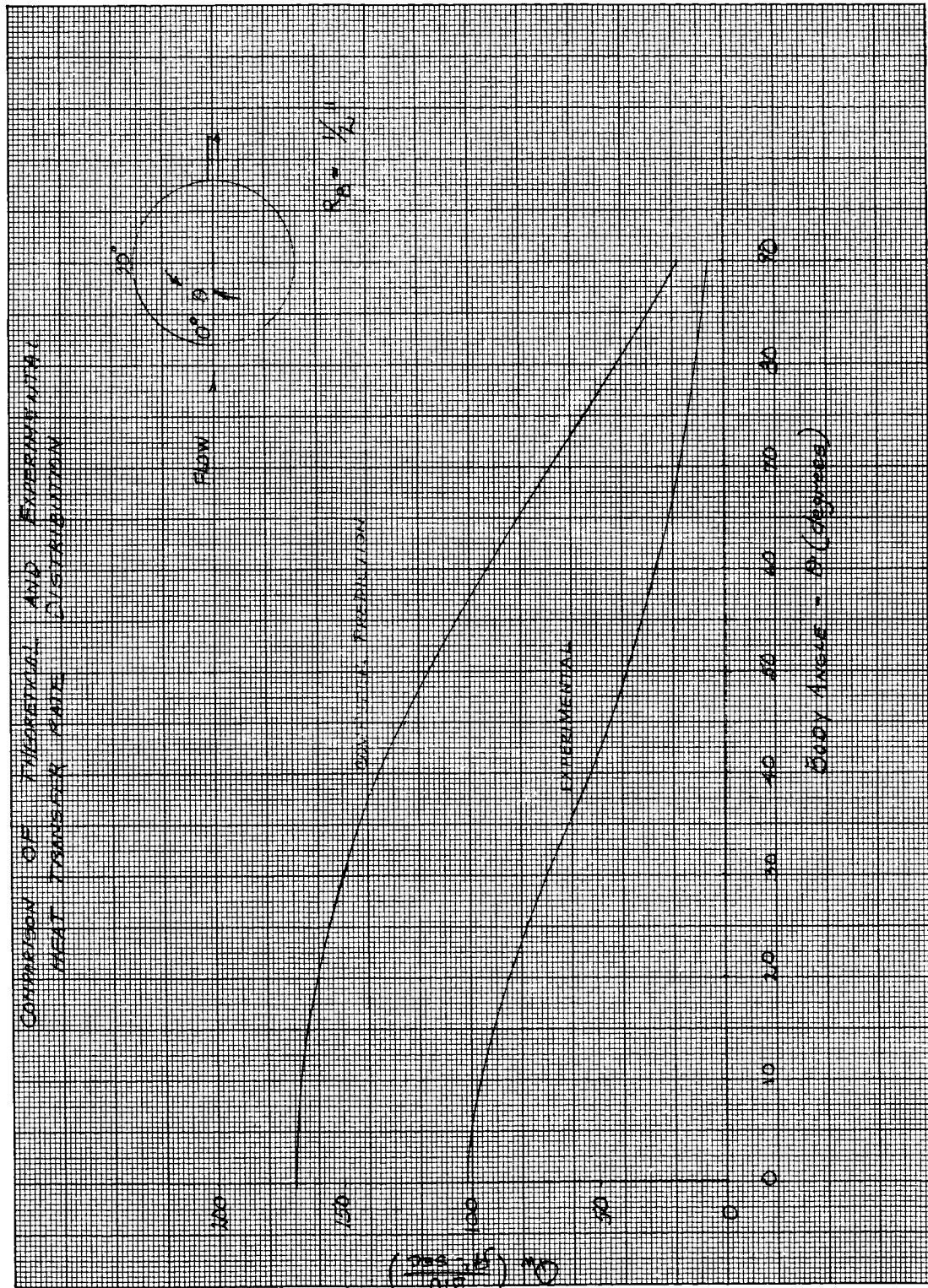
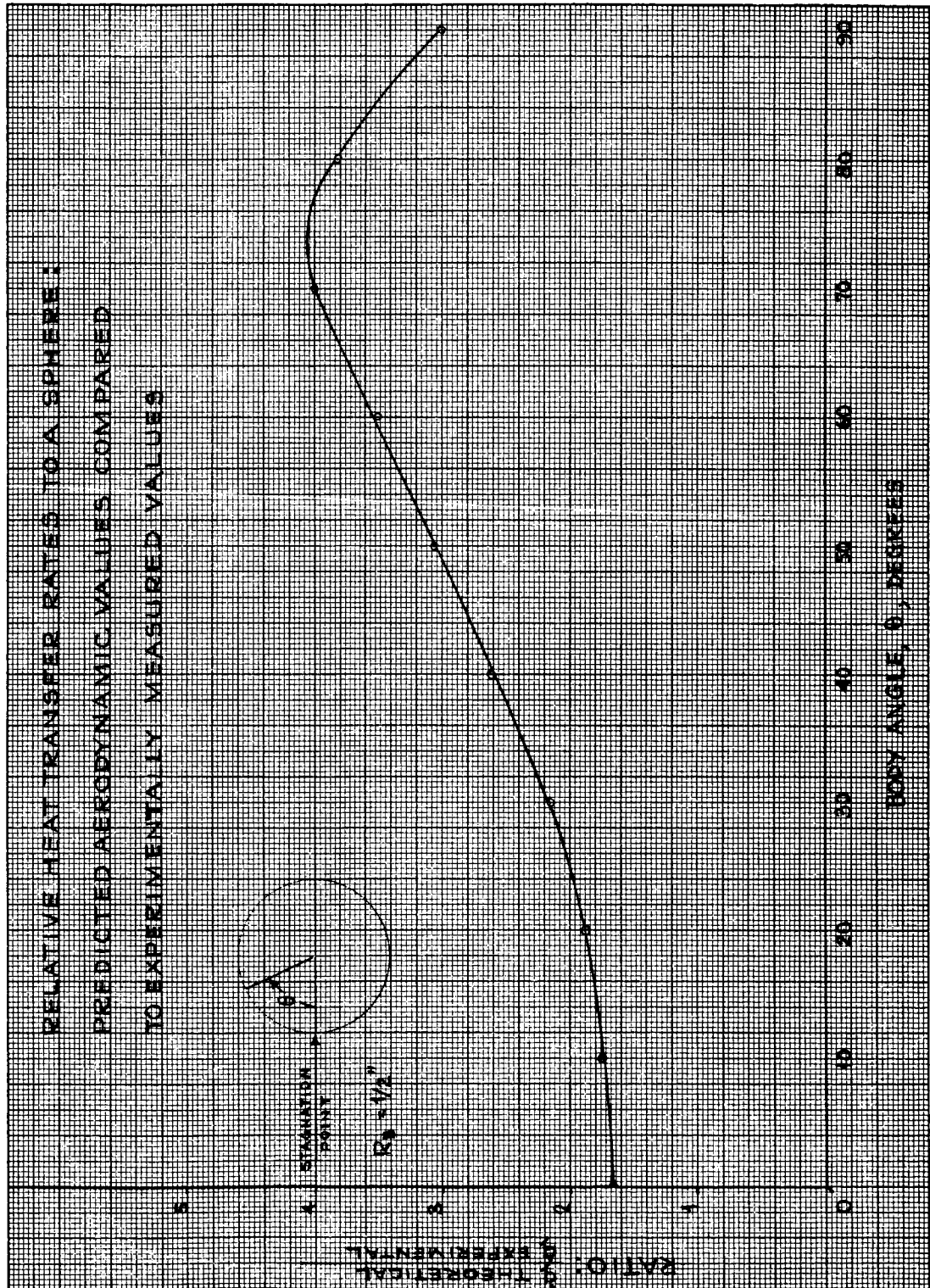


FIGURE 114.





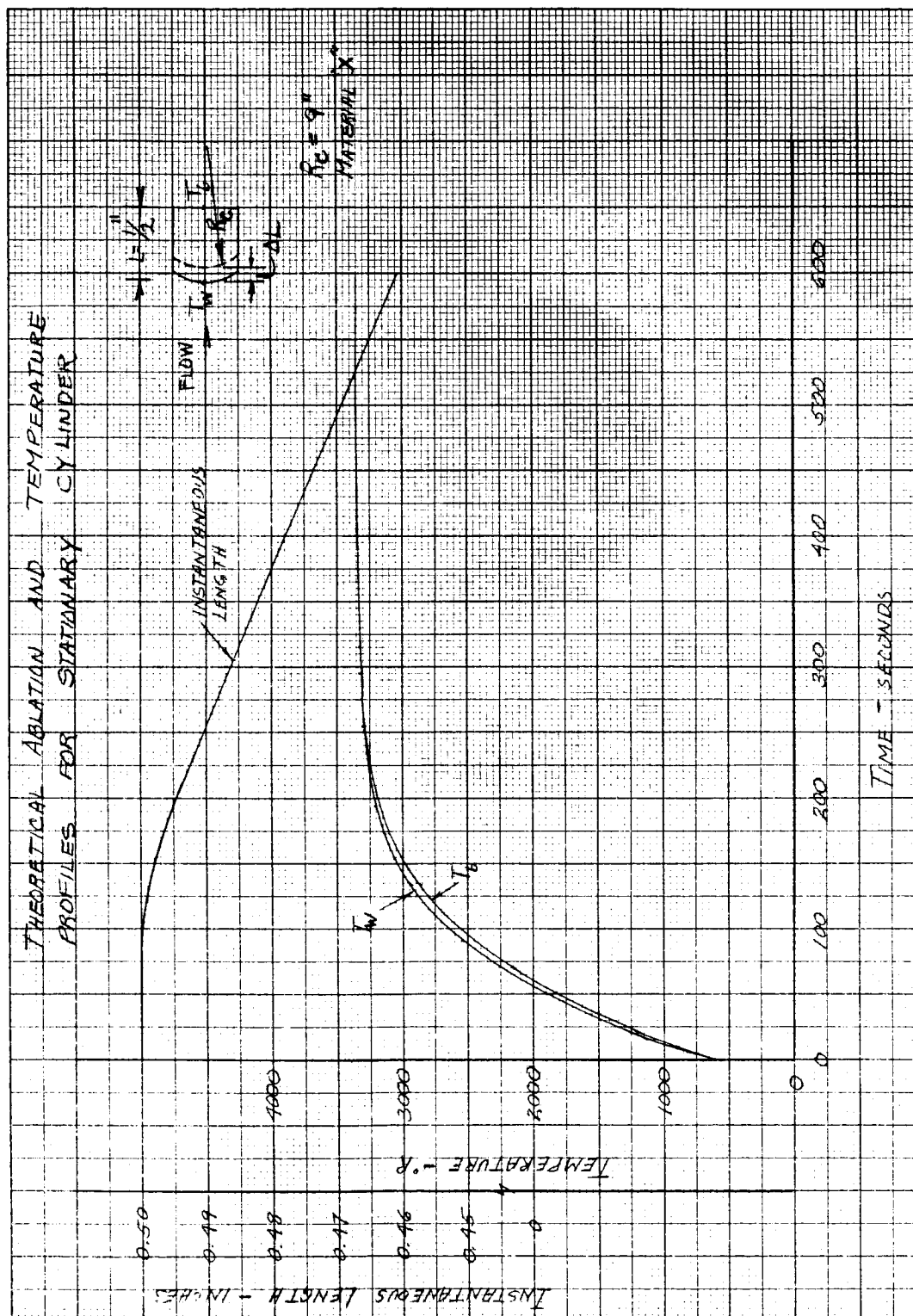
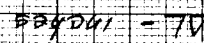


FIGURE 116

CONFIDENTIAL  
DECLASSIFIED IN 1997



~~CONFIDENTIAL~~  
~~RESTRICTED DATA~~  
~~ALL INFORMATION CONTAINED HEREIN IS UNCLASSIFIED~~

**UNCLASSIFIED**